

Tropospheric ozone columns retrieval from SCIAMACHY limb-nadir-matching observations



Vom Fachbereich für Physik und Elektrotechnik
der Universität Bremen

zur Erlangung des akademischen Grades eines
Doktor der Naturwissenschaften (Dr. rer. nat.)
genehmigte Dissertation

vorgelegt von

B. Tech, MSc. Phys. Ebojie Felix
aus Edo state, Nigeria

1. Gutachter: Prof. Dr. John P. Burrows

2. Gutachter: Prof. Dr. Otto Schrems

Eingereicht am: 27 August 2014

Kolloquium am: 15 October 2014

Acknowledgements

I am deeply indebted to my supervisor Prof. Dr. Christian von Savigny and co-supervisor PD Dr. Annette Ladstätter-Weißmayer for their excellent guidance, insightful advice and encouragement. Thank you both for the series of meetings, discussions and time spent in reading the draft of my thesis. The feedback I received from you are very helpful. Despite the fact that my supervisor moved to another university, he still finds time to discuss with me on my thesis. I am thankful to Prof. Dr. John Burrows for giving me the opportunity to work in his group as well as for his supervisory role. Your words of motivation was a source of encouragement throughout the research period. I would like to thank Prof. Dr. Otto Schrems for dedicating his time to be second reviewer of this thesis. I would like to thank every member of the limb group for the resourceful discussions we had during meetings. I am thankful to Alexei Rozanov for helping me out, mostly toward the end of this research and for his time in reading the draft of my thesis. I am also thankful to Mark Weber, Katja Weigel, Andreas Richter, Andreas Hilboill, Klaus Bramstedt, Stefan Noël, Patricia Liebing and Kai-Uwe Eichmann for their time, suggestions and illuminating discussions that contributed to my research. I would like to thank Claus Gebhardt for his help and series of discussions on trend analysis. I am thankful to the members of my examining committee for their time. I cherish the time, ideas and knowledge shared with my office mates, Raulf Bauer and Florian Ernst. I would also like to appreciate all my colleagues in the tropospheric ozone group, Stefan Bötzel and Jia Jia for their discussions and wonderful contributions during meetings. I thankfully acknowledge ESA and the German Aerospace DLR for providing SCIAMACHY level 1 data sets used in this thesis. In addition, I would like to thank DLR and the University and State of Bremen, Germany, for their financial support.

I am deeply grateful to my wife, Mandy Ebojie and children, Joshua and Josephine. Their unconditional love, patience, and persistent support have giving me the drive to aim high and achieve high. My kids Joshua and Josephine missed their dad most of the time and are joyous when daddy comes back home.

I would like to thank Petra Horn, Birgit Tauchert, Geraldine Schmiechen and Anja Gatzka for their administrative support during the course of this research. I am also thankful to Heiko

ACKNOWLEDGEMENTS

Schellhorn and Heiko Schröter for IT support and helping me fix my computer.

Finally, I give praise and thanks to the Almighty God for helping me during this research and in every areas of my life. I appreciate pastors Alabi Adeolu and Lambert Fandegla, as well as all the members of the Deeper Christian Life Ministry Bremen region.

Never tell a young person that anything cannot be done. God may have been waiting centuries for someone ignorant enough of the impossible to do that very thing – G. M. Trevelyan

Zusammenfassung

Troposphärisches Ozon (O_3), hat zwei Hauptquellen: Transport aus der Stratosphäre und photochemische Produktion in der Troposphäre. Es spielt wichtige Rollen für die Chemie der Atmosphäre und den Klimawandel. Ozonmenge und Abbau stehen unter dem Einfluss anthropogener Aktivitäten. Globale Messungen werden benötigt, um unser Verständnis über dessen Quellen und Senken zu testen. Diese Dissertation stellt eine Methode vor, mit welcher Säulen troposphärischen O_3 (TOCs) aus einem globalen Satellitendatensatz ermittelt werden können. Die Methode beinhaltet eine Kombination aus Limb und Nadir Beobachtungen (im weiteren als Limb-Nadir-Matching (LNM) bezeichnet) des SCanning Imaging Absorption spectroMeter for Atmospheric CHartographY (SCIAMACHY) Instruments, welches als Teil der Zuladung an Bord des Satelliten Envisat (2002-2012) der Europäischen Weltraumorganisation (ESA) flog. Die in dieser Studie verwendete LNM Methode ist ein differenzieller Ansatz, der die stratosphärische O_3 Säulen (SOCs), bestimmt aus den Limb-Beobachtungen, von den Gesamtsäulen des O_3 (TOZs), bestimmt aus den Nadir-Beobachtungen, subtrahiert. Für diese Methode wird eine genaue Kenntnis der SOCs, TOZs, Tropopausenhöhe und ihrer jeweiligen Ungenauigkeiten benötigt. Die SOCs wurden aus den stratosphärischen O_3 Profilen bestimmt, die aus den Hartley- und Chappuis- Banden der SCIAMACHY Limb-Streumessungen extrahiert wurden. Die TOZs wurden auch aus SCIAMACHY Messungen abgeleitet, jedoch in diesem Fall aus dem Nadir-Beobachtungsmodus mittels der Methode der Weighting Function Differential Optical Absorption Spectroscopy (WFDOAS) in der Huggins-Bande. Es werden detaillierte Sensitivitätsstudien an den TOC Ableitungen durchgeführt. Die Sensitivitätsstudien zeigten TOC Fehler bis zu 15 %, 19 % und 20 % in der Nördlichen Hemisphäre (NH), den Tropen und der Südlichen Hemisphäre (SH). Zum grössten Teil liegt die Ursache der TOC Fehler in Unsicherheiten der SOCs und TOZs. Die SOC Fehler liegen in der NH, in den Tropen und in der SH bei ungefähr 1,5 %, 2,1 % und 1,7 %, während die Fehler für TOZ global meist um 1 % liegen. Die Auswirkung von Ungenauigkeiten der Tropopausenhöhe auf die TOC wurde ebenfalls analysiert und mit $<0,4$ % jährlich ermittelt. Der globale Fehleranteil der SOCs wurde aus Fehlern berechnet, die aus Unsicherheiten im Temperaturprofil (-0.3 %), der Tangentenhöhenbestimmung (< 1.4 %), dem O_3 Absorptionsquerschnitt (0.1 %), Annahmen des Oberflächenalbedo (<-0.8 %),

ZUSAMMENFASSUNG

der Aerosol-Extinktionsprofile ($<0.5\%$) und des Druckprofils (0.7%) resultieren. Des Weiteren wurde der Einfluss des Nadir-Wolkenanteils auf die TOC Werte analysiert. Die Analyse zeigt, dass eine Erhöhung des Schwellenwertes des Nadir-Wolkenanteils um 10% das SCIAMACHY troposphärische O_3 durchschnittlich um 1 DU ($1\text{ DU} = 2.69 \times 10^{16}\text{ Moleküle cm}^2$) reduzieren kann. Dies wird meist in solchen Fällen beobachtet, wo Verschmutzung troposphärisches O_3 über das klimatologische O_3 ansteigen lässt. Vergleiche der TOCs aus SCIAMACHY und Vergleichsmessungen durch Ozonsonden in beiden Hemisphären zwischen Januar 2003 und Dezember 2011 zeigen prinzipielle Übereinstimmung mit Abweichungen von $<3\text{ DU}$. SCIAMACHY TOC Werte wurden auch mit den Ergebnissen des Troposphärischen Emissions-Spektrometers (TES) und der LNM Methode für Daten des Ozone Monitoring Instrument (OMI) und des Microwave Limb Sounder (MLS) (hiernach benannt als OMI/MLS) verglichen. Alle verglichenen Datensätze stimmen mit den angegebenen Datenprodukt-Fehlerbereichen überein und weisen ähnliche saisonale Variationen auf, die sich jedoch in der Amplitude unterscheiden. Die Klimatologie des SCIAMACHY troposphärischen O_3 zeigt große zeitliche und räumliche Variabilität auch in Akkumulationsregionen von O_3 alljährlich im tropischen südatlantischen Ozean und in der subtropischen Mittelmeerregion während des nördlichen Sommers. Hohe Werte troposphärischen O_3 verbleiben in den mittleren Breiten auf der NH während des nördlichen Frühlings und Sommers. Beobachtet wird dies über dem östlichen nordamerikanischen Kontinent bis hin über den Atlantischen Ozean sowie über dem ostasiatischen Kontinent bis über den Pazifik. Ähnlich hohe O_3 Werte werden über den Tropen und mittleren Breiten der SH während des südlichen Frühlings beobachtet. Eine Trendanalyse des globalen SCIAMACHY TOC mittels eines multivariaten Regressionsmodells, deutet auf einen bedeutsamen Anstieg über Regionen des südlichen Asien ($1 - 4\%/yr$), des südamerikanischen Kontinent ($0 - 2\%/yr$) sowie im zentralen Afrika und der westafrikanischen Küste ($0 - 2\%/yr$) hin. Der steigende Trend über diesen Regionen kann der steigenden Emission von O_3 -Vorläufern zugeschrieben werden. Über den maritimen Regionen ist ein signifikant positiver O_3 Trend über dem Pazifischen Ozean ($1 - 3\%/yr$) und dem Indischen Ozean mit Ausdehnung nach Australien ($1 - 3\%/yr$) zu sehen. Der beobachtete Trend über dem Pazifischen Ozean kann mit dem transpazifischen Transport asiatischer Verschmutzung verbunden werden, während der signifikant positive O_3 Trend über dem Indischen Ozean dem advektiven Transport zugeschrieben werden kann, der durch die dynamische Kopplung zwischen den Tibetanischen Hochplateau auf der NH und dem synoptischen Wellenregime auf der SH erklärt werden kann. Bedeutsame Verringerungen im O_3 Trend ($1 - 3\%/yr$) werden über einigen Regionen Europas und den USA beobachtet, was mit der Verringerung von NO_x und anderen troposphärischen O_3 Vorläufern assoziiert werden kann. Signifikante Verringerungen im O_3 Trend ($1 - 3\%/yr$) werden auch über maritimen Regionen wie

dem Atlantischen Ozean, dem Pazifischen Ozean und dem Indischen Ozean beobachtet. Die Verringerung des O_3 über diesen Regionen steht möglicherweise mit meteorologischen Veränderungen sowie einer Reduzierung des Einflusses von O_3 -Vorläufern in Verbindung. Die räumliche Verteilung des troposphärischen O_3 im SCIAMACHY LNM TOC Produkt zeigt charakteristische Variationen, verbunden mit Stratosphären-Troposphären Austauschprozessen (STE), anthropogenen Aktivitäten und biosphärischen Emissionen. Der SCIAMACHY Datensatz troposphärischen Ozons, der in dieser Studie erstellt wurde, ist wichtig um unser Verständnis über die Prozesse, die troposphärische O_3 Menge bestimmen, zu beurteilen und um chemischen Transport und Chemie-Klimamodelle während der Dekade 2002-2012 zu evaluieren.

ZUSAMMENFASSUNG

Abstract

Tropospheric ozone (O_3), has two main sources: transport from the stratosphere and photochemical production in the troposphere. It plays important roles in atmospheric chemistry and climate change. Its amount and destruction are being modified by anthropogenic activity. Global measurements are needed to test our understanding of its sources and sinks. This dissertation presents a method for retrieving tropospheric O_3 columns (TOCs) from a global satellite data set. The method involves the combination of limb and nadir observations (hereinafter referred to as limb-nadir-matching (LNM)) of the SCanning Imaging Absorption spectroMeter for Atmospheric CHartography (SCIAMACHY) instrument, which flew as part of the payload onboard the European Space Agency (ESA) satellite Envisat (2002 - 2012). The LNM technique used in this study, is a residual approach that subtracts stratospheric O_3 columns (SOCs), retrieved from the limb observations, from the total O_3 columns (TOZs), derived from the nadir observations. The technique requires accurate knowledge of the SOCs, TOZs, tropopause height, and their associated errors. The SOCs were determined from the stratospheric O_3 profiles retrieved in the Hartley and Chappuis bands from SCIAMACHY limb scattering measurements. The TOZs were also derived from SCIAMACHY measurements, but in this case from the nadir viewing mode using the Weighting Function Differential Optical Absorption Spectroscopy (WFDOAS) technique in the Huggins band. Detailed sensitivity studies are performed on the TOCs retrievals. The sensitivity studies showed TOC errors of up to 15 %, 19 %, and 20 % in the Northern Hemisphere (NH), tropics, and Southern Hemisphere (SH), respectively. The largest source of TOCs errors are uncertainties in the SOCs and TOZs. The SOCs errors in the NH, tropics, and SH are approximately 1.5 %, 2.1 %, and 1.7 %, respectively while the TOZs errors are mostly 1 % globally. The effect of the shift of the tropopause height on the TOC was also analyzed and found to be <0.4 % globally. The global error contribution from the SOCs was computed from errors resulting from uncertainties in the temperature profile (-0.3 %), tangent height registration (<1.4 %), O_3 absorption cross section (0.1 %), assumed surface albedo (-0.8 %), aerosol extinction profile (<0.5 %), and pressure profile (0.7 %). The impact of the nadir cloud fraction on TOCs retrieval was analyzed. The analysis

ABSTRACT

showed that an increase in nadir cloud fraction threshold by 10 % can on average reduce SCIAMACHY tropospheric O₃ by about 1 DU (1 DU = 2.69 × 10¹⁶ molecules cm⁻²). This is mostly observed in cases where pollution increases tropospheric O₃ to values above the climatological O₃. Comparisons of the TOCs from SCIAMACHY and collocated measurements from ozonesondes in both hemispheres between January 2003 and December 2011 show agreement to within 3 DU. TOC values from SCIAMACHY have also been compared to the results from the Tropospheric Emission Spectrometer (TES) and from the LNM technique exploiting Ozone Monitoring Instrument (OMI) and Microwave Limb Sounder (MLS) data (hereinafter referred to as OMI/MLS). All compared data sets agree within the given data product error range and exhibit similar seasonal variations, which however, differ in amplitude. The SCIAMACHY tropospheric O₃ climatology exhibits large temporal and spatial variability, including O₃ accumulation regions in the tropical south Atlantic Ocean year-round and in the subtropical Mediterranean region during boreal summer. High levels of tropospheric O₃ persist in the NH mid-latitudes during boreal spring and summer. This is observed over eastern North America continent extending across the Atlantic Ocean as well as over eastern Asian continent extending across the Pacific Ocean. Similar higher O₃ values are observed in the SH tropics and mid-latitudes during austral spring. Trend analysis of SCIAMACHY global TOC using multivariate regression model indicate significant increase over regions of South Asia (1 - 4 %/yr), the South American continent (up to 2 %/yr), North America, especially around Alaska (1 - 3 %/yr), in the Australia outflow region (1 - 2 %/yr) as well as over regions of the central African and west African coast (up to 2 %/yr). The increasing trend over these regions can be attributed to increasing emissions of NO_x and other O₃ precursors as well as the influence of intercontinental transport of O₃ and its precursors. Over the marine regions, significant increase in TOC is derived over South East Pacific region (up to 3 %/yr), the Indian Ocean (1 - 2 %/yr) and the Atlantic Ocean (up to 2 %/yr). The observed increase in TOC over the Oceanic regions can be associated with dynamical processes such as advection, entrainment and transport of O₃ and its precursors from the source regions. Significant decrease in TOC is observed over some regions of the European and North American continents (2 - 4 %/yr), which can be attributed to reduction in the emissions of O₃ precursors. Over the Oceanic regions including the Pacific, Atlantic and Indian Oceans, significant decrease in TOC (1 - 5 %/yr) are observed. The observed decrease over these regions can be associated with photochemical reactions involving hydroxyl (OH) and hydroperoxy (HO₂) radicals. Meteorological changes and increase in the growth of marine algae (phytoplankton) could be an additional source of volatile halocarbons contributing to the destruction of O₃. In general, the spatial distributions of tropospheric O₃ in the SCIAMACHY LNM TOC product show characteristic variations related to anthropogenic activities, stratosphere-troposphere exchange (STE) processes and biospheric emissions. The SCIAMACHY tropospheric O₃ data set

derived in this study is important to assess our understanding of the processes controlling tropospheric O₃ abundances and to evaluate chemical transport and chemistry climate models during the decade 2002 – 2012.

Publications and conference proceedings

F. Ebojie, J. P. Burrows, C. von Savigny, A. Ladstätter-Weißmayer, A. Rozanov, M. Weber, H. Bovensmann: Tropospheric ozone trends and variability from 2002 - 2012 as seen by SCIAMACHY Atmos. Chem. Phys. 2014 (in progress).

F. Ebojie, C. von Savigny, A. Ladstätter-Weißmayer, A. Rozanov, M. Weber, K. Eichmann, S. Bötzel, N. Rapp, H. Bovensmann, and J. P. Burrows: Tropospheric column amount of ozone retrieved from SCIAMACHY limb-nadir-matching observations, Atmos. Meas. Tech., 7, 2073-2096, 2014.

F. Ebojie, C. von Savigny, A. Ladstätter-Weißmayer, S. Bötzel, M. Weber, H. Bovensmann, and J. P. Burrows: Second Tropospheric Ozone Workshop - Tropospheric Ozone Changes: observations, state of understanding and model performances (Météo France, Toulouse, France, 11-13 April 2011), 226 pp. September 2011.

F. Ebojie, C. von Savigny, A. Ladstätter-Weißmayer, S. Bötzel, M. Weber, H. Bovensmann, and J. P. Burrows: Seasonal variability of tropospheric ozone derived from SCIAMACHY limb-nadir matching observations, ACCENT-plus symposium on air quality and climate change: interactions and feedback, Urbino, Italy, 13 - 16 September, 2011.

Kanakidou M., Mihalopoulos N., Kindap T., Im U., Vrekoussis M., Gerasopoulos E., Dermizaki E., Unal A., Kocak M., Markakis K., Melas D., Kouvarakis G., Youssef A.F., Richter A., Hatzianastassiou N., Hilboll A., Ebojie F., von Savigny C., Ladstätter-Weißmayer A., Burrows J., Moubasher H.: Megacities as hot spots of air pollution in the East Mediterranean. Atmos. Env., 2010.

Selected conference contributions

F. Ebojie, C. von Savigny, A. Ladstätter-Weißmayer, S. Bötzel, H. Bovensmann, and J. P. Burrows: Tropospheric ozone columns retrievals and validation from SCIAMACHY limb-nadir-matching observations, ATMOS, 7th International Atmospheric Limb Conference, Bremen, Germany, 17 - 19 June 2013.

F. Ebojie, C. von Savigny, A. Ladstätter-Weißmayer, S. Bötzel, H. Bovensmann, and J. P. Burrows: (1) Validation of tropospheric ozone columns from SCIAMACHY, (2) Intercomparison of the distribution of tropospheric ozone, ATMOS, Bruges, Belgium, 18 - 22 June, 2012.

F. Ebojie, C. von Savigny, A. Ladstätter-Weißmayer, A. Rozanov, M. Weber, K. Eichmann, S. Bötzel, N. Ralpoe, H. Bovensmann, and J. P. Burrows: Tropospheric ozone column retrievals from SCIAMACHY limb-nadir-matching observations, Quadrennial Ozone Symposium, Toronto, August 27-31, 2012.

F. Ebojie, C. von Savigny, A. Ladstätter-Weißmayer, S. Bötzel, H. Bovensmann, and J. P. Burrows: Retrieval of tropospheric ozone from SCIAMACHY limb-nadir matching observations, EGU General Assembly, Vienna, Austria, 22 - 27 April, 2012.

F. Ebojie, C. von Savigny, A. Ladstätter-Weißmayer, S. Bötzel, S. Sinkadar H. Bovensmann, and J. P. Burrows: Tropospheric ozone using SCIAMACHY limb-nadir matching observations: First results, EGU General Assembly, Vienna, Austria, 4 - 8 April, 2011.

F. Ebojie, C. von Savigny, A. Ladstätter-Weißmayer, S. Bötzel, S. Sinkadar H. Bovensmann, and J. P. Burrows: Investigation of the spatial and temporal variation of tropospheric ozone using SCIAMACHY limb-nadir matching observations, EGU General Assembly, Vienna, Austria, 4 - 8 April, 2011.

F. Ebojie, C. von Savigny, A. Ladstätter-Weißmayer, S. Bötzel, S. Sinkadar H. Bovensmann, and J. P. Burrows: Tropospheric ozone climatology derived from SCIAMACHY limb-nadir matching observations, Workshop on tropospheric ozone trends, Toulouse, France, 11 - 13 April, 2011.

F. Ebojie, C. von Savigny, A. Ladstätter-Weißmayer, S. Bötzel, H. Bovensmann, and J. P. Burrows: Retrieval and Interpretation of global tropospheric ozone distributions using SCIAMACHY limb-nadir-matching observations: first steps and results, 38th COSPAR Scientific Assembly, Bremen, Germany, 18 - 25 July 2010.

PUBLICATIONS

Contents

Acknowledgements	i
Zusammenfassung	iii
Abstract	vii
Publications	x
List of Figures	xvii
List of Tables	xxiii
Motivation and objectives	1
SECTION I Fundamentals, ozone chemistry and dynamics	7
1 The Earth's atmosphere, ozone, its role and measurement	9
1.1 The Earth's Atmosphere	9
1.1.1 Structure of the Atmosphere	9
1.2 Atmospheric Ozone	12
1.2.1 Discovery and measurements of Ozone	12
1.2.1.1 Balloon-borne observations: Ozonesonde	13
1.2.2 Satellite based observations of ozone	15
1.2.2.1 The SCIAMACHY instrument	17
1.2.2.2 TES, OMI and MLS	20
2 Chemistry and dynamics of ozone	21
2.1 Tropospheric ozone chemistry and dynamics	21
2.1.1 Ozone production regime	23
2.1.1.1 NO _x -sensitive regime	23
2.1.1.2 VOC-sensitive regime	23

CONTENTS

2.1.1.3	Sources and sinks of odd hydrogen	23
2.1.1.4	Oxidation and photolysis of VOCs and hydrocarbons	26
2.1.2	Transport of O ₃ from the stratosphere	29
2.2	Stratospheric ozone chemistry and dynamics	29
2.2.1	Stratospheric ozone production and loss cycles	29
2.3	Upper troposphere and lower stratosphere (UT/LS)	31
2.3.1	Stratosphere-Troposphere Exchange	32
2.3.2	Brewer-Dobson circulation (BDC)	34
2.3.3	The synoptic and mesoscale processes	36
2.3.3.1	Tropopause folds	36
2.3.3.2	Cutoff lows	36
2.3.3.3	Filamentation and fragmentation of stratospheric streamers	37
2.3.3.4	Thunderstorms and mesoscale convective systems (MCS)	37
2.3.3.5	Breaking gravity waves	38
	SECTION II Methodology	39
3	The tropopause and its role	41
3.1	Concepts of the tropopause	41
3.2	Determination of the tropopause	43
3.3	Thermal Tropopause	43
3.4	Dynamic Tropopause	45
3.4.1	Combination of the Thermal and Dynamic Tropopauses	46
3.5	Determination of tropopause height from ozonesonde temperature profile measurement	47
3.6	Intercomparison of ECMWF and ozonesonde tropopause heights	48
3.7	Global zonal averaged ECMWF tropopause heights	50
4	Ozone Profile and Total Ozone Column retrieval algorithm	53
4.1	Ozone profile retrieval algorithm	53
4.2	Total ozone column retrievals	55
5	Tropospheric ozone column retrievals from satellite and ozonesonde instruments	59
5.1	Combination of SCIAMACHY limb and nadir measurements	61
5.2	Theory of limb-nadir matching algorithm	62
5.3	Tropospheric ozone from OMI/MLS, TES and ozonesondes	65
5.3.1	Tropospheric ozone from OMI/MLS and TES	65
5.3.2	Tropospheric ozone from ozonesondes	66

5.3.2.1	Uncertainties in ozonesonde data	67
5.4	Sensitivity studies for the retrieval of tropospheric ozone column from SCIAMACHY	69
5.4.1	Derivation of SOC error parameters and the effect of tropopause height	70
5.4.2	Derivation of TOZ error parameters	73
5.4.3	Combination of the SOC and TOC errors	74
5.4.3.1	Influence of nadir cloud fraction on TOC errors	77
SECTION III Results		79
6	Validation of SCIAMACHY tropospheric ozone columns	81
6.1	Tropospheric ozone columns retrieved from SCIAMACHY measurements and inter-comparison with ozonesondes and other satellite instruments	81
6.2	Intercomparison of tropospheric ozone columns from SCIAMACHY with TES, OMI/MLS and ozonesondes	89
6.2.1	SCIAMACHY global TOC climatology maps	100
6.2.2	SCIAMACHY zonal mean TOC, TOZ and SOC climatologies	103
6.2.3	Zonal distribution of tropospheric ozone columns from SCIAMACHY	105
6.2.4	Intercomparison plots of the zonal distribution of TOCs from SCIAMACHY, TES and OMI/MLS	107
6.3	Seasonal cycles and trends analysis of SCIAMACHY tropospheric ozone columns	110
6.3.1	Seasonal cycles of SCIAMACHY tropospheric O ₃	110
6.3.2	SCIAMACHY tropospheric ozone timeseries and trends	112
6.3.2.1	QBO, solar cycle, and ENSO signatures in ozone	113
6.3.2.2	Zonal means tropospheric O ₃ changes	115
6.3.2.3	Timeseries and trends of tropospheric O ₃ over megacities	118
6.3.2.4	Timeseries and trends of tropospheric O ₃ comparison between SCIAMACHY and ozonesondes	123
6.3.2.5	Timeseries and trends of tropospheric O ₃ over regions and countries	125
6.3.2.6	Changes in SCIAMACHY global tropospheric O ₃ columns	127
7	Summary and conclusion	131
7.1	Outlook	134
Appendix		137
References		141

CONTENTS

List of Figures

1.1	The vertical structure of the atmosphere and ozone mixing ratio typical of the mid-latitudes.	10
1.2	Schematics of the electrochemical concentration cell (ECC) (A) ozonesonde and (B) sensing cell developed by Komhyr (1969), image after Smit (2002).	14
1.3	Schematics of SCIAMACHY's Total Clear Field of View (TCFoV) and observation geometries (Courtesy of DLR-IMF).	19
1.4	Illustration of SCIAMACHY limb and nadir observation geometries.	20
2.1	Illustration of the lower atmosphere, showing the relevant dynamical aspects of the stratosphere-troposphere exchange (STE) that influences the structure of the UT/LS, modified after Holton <i>et al.</i> (1995) and Hintsa <i>et al.</i> (1998).	33
3.1	Temperature profile over Alert (82.50°N, 62.30°W) at 23:34:00 UTC on 14.04.2010: smoothed temperature profile (red) and original temperature profile (black), a typical tropopause height of about 9 km.	47
3.2	Comparison of monthly mean tropopause height time series in km between ECMWF (red) and ozonesondes (blue) over Alert (82.50°N, 62.30°W), from left to right: time series and scatter plot.	48
3.3	Same as Figure 3.2 but over Bratt's Lake (50.20°N, 104.00°W).	48
3.4	Same as Figure 3.2 but over Barajas (40.40°N, 3.58°W).	49
3.5	Same as Figure 3.2 but over Broadmeadows (37.60°S, 144.00°E).	49
3.6	Same as Figure 3.2 but over Macquarie Island (54.50°S, 158.80°E).	49
3.7	Same as Figure 3.2 but over Marambio (64.20°S, 56.60°W).	49
3.9	The zonal average time series tropopause height in km from ECMWF between 2002 and 2012.	52

LIST OF FIGURES

3.10	The zonal means bias (solid) and standard deviation (dotted) between ozonesondes (44 stations) and ECMWF tropopause heights for the different seasons (DJF: December - February; MAM: March - May; JJA: June - August; SON: September - November, from 2003 - 2011) at 10° latitude \times 10° longitude resolutions.	52
5.1	Illustration of ray crossing in a plane.	62
5.2	Illustration of the crossing number method.	63
5.3	Illustration of ray-edge and ray-vertex intersections.	64
5.4	Simple schematic of the different possible orientations of the limb scans that can be matched with the corresponding nadir scan.	64
5.5	Illustration of SCIAMACHY swath for limb and nadir observations in orbit 09501.	65
5.6	For ECC-ozonesondes: contribution of different instrumental factors to the O_3 partial pressure P_{O_3} (silver dashed line) for (A) a typical mid-latitude profile and (B) a typical tropical profile. Adapted from Smit <i>et al.</i> (2011).	69
5.7	Monthly mean zonal mean error in SOCs parameter error in January 2004. From left to right; top panels: temperature and O_3 absorption cross section, middle panels: Aerosol loading and Tangent height registration, and bottom panels: albedo and pressure.	73
5.8	Same as Figure 5.7 but for July 2004.	73
5.9	Top panels from left to right: Zonal variation of the monthly mean error in tropospheric ozone columns (TOCs) and total ozone (TOZ). Bottom panels from left to right: Zonal variation of the monthly mean error of stratospheric ozone column (SOC) and contribution from error in tropopause height (TPH) to the error in TOC in January 2004.	76
5.10	Same as Figure 5.9 but for July 2004.	76
6.3	Tropospheric O_3 distributions (in Dobson Units (DU)) for December-January-February (DJF) in 2003 – 2011 from SCIAMACHY. The colors in the panels going from blue to red represent smallest to largest values, respectively.	85
6.6	Same as Figure 6.3 but for March-April-May (MAM).	86
6.9	Same as Figure 6.3 but for June-July-August (JJA).	87
6.12	Same as Figure 6.3 but for September-October-November (SON).	88
6.13	World map showing ozonesonde stations (station numbers are listed in Table 4) used in this study.	89

6.14 Monthly mean tropospheric O ₃ column (TOC) in Dobson Units (DU) of tropical stations from SCIAMACHY (black), ozonesondes (red), TES (violet), and OMI/MLS (green).	91
6.15 Monthly mean tropospheric O ₃ column anomaly (TOCA) in Dobson Units (DU) of tropical station from SCIAMACHY (black), ozonesondes (red), TES (violet), and OMI/MLS (green).	92
6.16 Same as Figure 6.14 but for some extratropical ozonesonde stations.	95
6.17 Same as Figure 6.14 but for some extratropical ozonesonde stations.	96
6.18 Same as Figure 6.15 but for some extratropical ozonesonde stations.	97
6.19 Same as Figure 6.15 but for some extratropical ozonesonde stations.	98
6.20 Tropospheric O ₃ climatology (in DU) for the months, January - June from SCIAMACHY limb-nadir matching measurements. The colours in the panels going from blue to red represent smallest to largest values, respectively.	101
6.21 Same as Figure 6.20 but for July - December.	102
6.22 Zonal mean tropospheric O ₃ column climatology (in DU) derived from January 2003 to December 2011 from SCIAMACHY measurements for 5° latitude bins.	104
6.23 Same as Figure 6.22 but for total O ₃ column (TOZ).	104
6.24 Same as Figure 6.22 but for stratospheric O ₃ column (SOC)	105
6.25 Tropospheric O ₃ climatology from 2002 - 2011 as a function of longitude from SCIAMACHY for the latitude bands 10°S - 0, 30°S - 40°N and 30°N - 40°N for October, April and July, respectively. Also included in the plots are ±2σ vertical bars used as estimates of the combination of errors and real atmospheric variability, where σ is the calculated 9-year RMS standard deviation of the individual values.	106
6.26 Tropospheric O ₃ column as a function of longitude from SCIAMACHY for the latitude bands 60°S - 40°S, 20°S - 20°N and 40°N - 60°N for the different seasons between December 2002 and November 2011. Also included in the plots are ±2σ vertical bars used as estimates of the combination of errors and natural variability of monthly zonal means, where σ is the calculated 9-year RMS standard deviation of the individual values.	106
6.27 Calculated zonal mean TOC climatology as a function of latitude at three-month intervals (January, April, July, and October) from January 2003 to December 2011. The zonal mean values are derived from the 10° latitude × 10° longitude gridded TOCs.	107

LIST OF FIGURES

6.28	Plots of TOC (in DU) as a function of longitude from OMI/MLS, SCIAMACHY and TES for the latitude bins 60°S – 40°S between December 2005 and November 2011; from the top panels, left to right: December-January-February, March-April-May, from the bottom panels, left to right: June-July-August and September-October-November. Also included in the plots are $\pm 2\sigma$ vertical bars used as estimates of the combination of errors and real atmospheric variability, where σ is the calculated 9-year RMS standard deviation of the individual values.	108
6.29	Same as figure 6.28 but for the latitude bins 20°S - 20°N.	109
6.30	Same as figure 6.28 but for the latitude bins 40°N - 60°N.	109
6.34	Seasonal distribution of the SCIAMACHY TOC from 2003 - 2011 in selected urban regions.	111
6.35	Time series of the TOC (in Dobson Units (DU)) from SCIAMACHY for 50°S - 30°S (black) with overlaid fitting curve (blue) in top panel and fit residuals (second panel). Below, the components of the fitting curve are shown individually (from top to bottom): harmonic (pink), QBO (light green), solar cycle (yellow), linear change (orange), and ENSO (brown). Each of these terms is overlaid by the time series with all other components of the fitting curve subtracted, e.g., the harmonic terms by the time series with QBO, solar cycle, and linear terms subtracted.	116
6.36	Same as Figure 6.35 but for 30°N - 50°N.	117
6.37	Same as Figure 6.35 but for 20°S - 20°N.	117
6.38	World map showing cities (station numbers are listed in Table 6.3) used in trend analysis.	118
6.39	Time series of the TOC (in DU) from SCIAMACHY in black with overlaid fitting curve in blue and linear trend in violet over Istanbul (41°N, 28°E). The x-axis label represents the start of each year.	119
6.40	Same as Figure 6.39 but for Madrid (40°N, 3°W)	120
6.41	Same as Figure 6.39 for New York (40°N, 73°W)	120
6.42	Same as Figure 6.39 for Los Angeles (33°N, 117°W)	120
6.43	Same as Figure 6.39 for Mexico City (19°N, 99°W)	120
6.44	Same as Figure 6.39 for Shanghai (31°N, 121°E)	121
6.45	Same as Figure 6.39 for Nam Co (31°N, 91°E)	121
6.46	Same as Figure 6.39 for Xinglong (40°N, 117°E)	121
6.47	Same as Figure 6.39 for Tehran (36°N, 51°E)	121
6.48	Same as Figure 6.39 for Beijing (39°N, 116°E)	121
6.49	Same as Figure 6.39 for New Delhi (28°N, 78°E)	122

6.50 Changes in SCIAMACHY tropospheric O₃ columns (%/yr) derived from 2003 - 2011 for 5° latitude × 5° longitude resolution. The regions with cross signs describe statistically significant change and the white colored areas represent places with no trend data. 127

6.51 Changes in SCIAMACHY tropospheric O₃ columns (DU/yr) derived from 2003 - 2011 for 5° latitude × 5° longitude resolution. The regions marked with crosses describe statistically significant trends and the white colored areas represent places with no trend data. 129

LIST OF FIGURES

List of Tables

1.1	Overview of the SCIAMACHY spectrometer channels. The last column on the right shows the list of a number of atmospheric trace gases with strong absorption or emission features in the corresponding wavelength range from which they can be retrieved.	17
3.1	Comparisons of tropopause heights from ECMWF with some selected sondes stations over the entire time series (2002-2011).	50
4.1	The lowest (h_{low}) and reference (h_r) tangent heights for the wavelengths used. . . .	54
4.2	Parameter space of the look-up-tables. The value indicated by (*) in the min/max column of the Relative Azimuth Angle depend on the SZA and LOS.	57
5.1	Pump efficiency correction factors as a function of pressure. NOAA/CMDL values are listed as average correction factors obtained from the individual pump flow calibrations during JOSIE 1996 (Smith-Kley1996).	68
5.2	Zonal monthly averaged uncertainties (σ) due to change in temperature (Temp.), tangent height registration (Tght), O ₃ absorption cross sections (Cr), albedo (Alb), aerosol extinction (Aer) and pressure (Press) for 20°S - 20°N in 2004.	71
5.3	Same as Table 5.2 but for 60°S - 30°S in 2004.	72
5.4	Same as Table 5.2 but for 30°N - 60°N in 2004.	72
5.5	Zonal monthly average and errors in tropospheric O ₃ columns (TOCs), stratospheric O ₃ columns (SOCs), total O ₃ columns (TOZs), and the contribution of the tropopause height (TPH) error to the TOCs error from 20°S - 20°N in 2004.	75
5.6	Same as Table 5.5 but from 60°S - 30°S in 2004.	75
5.7	Same as Table 5.5 but from 30°N - 60°N in 2004.	76

LIST OF TABLES

6.1	Comparisons of tropospheric O ₃ columns from SCIAMACHY, ozonesondes, TES and OMI/MLS for some selected stations over the entire time series (2004-2011). Mean value and standard deviation (stdev) as well as the relative difference of each satellite data product using ozonesonde as the reference are shown. The TOC product is for 10 % cloud fraction threshold at 5° latitude × 10° longitude resolution.	99
6.2	Trend analysis of SCIAMACHY tropospheric O ₃ for different latitude ranges.	118
6.3	Trends in SCIAMACHY tropospheric O ₃ in %yr ⁻¹ over megacities. Bold text signifies statistically significant changes in TOC.	123
6.4	Trends in SCIAMACHY and ozonesondes tropospheric O ₃ in %yr ⁻¹ . SCIAMACHY TOC data are binned in 5° latitude and 5° longitude. Bold text indicates statistically significant changes in TOC.	124
6.5	Trends in SCIAMACHY tropospheric O ₃ in %yr ⁻¹ over some regions and countries of the world. Bold text indicates statistically significant changes in TOC.	126
7.1	Same as table 6.1 but for 0 % cloud fraction threshold.	137
7.2	Same as table 6.1 but for 5 % cloud fraction threshold.	138
7.3	Same as table 6.1 but for 15 % cloud fraction threshold.	139
7.4	Same as table 6.1 but for 30 % cloud fraction threshold.	140

Motivation and objectives

Approximately 90 % of the total ozone in the atmosphere is located in the stratosphere while about 10 % is found in the troposphere. In the troposphere, small amounts of natural O₃ can be found close to the Earth's surface, which originate from hydrocarbons released from soil and plants (Guenther *et al.*, 1993). In addition, O₃ is transported from the stratosphere to the troposphere (e.g., Pfister *et al.*, 2008; Roelofs & Lelieveld, 1997; Thompson *et al.*, 2007b). Anthropogenic activities have led to an increase in the amount of tropospheric O₃ precursors. These precursors include nitrogen oxides (NO_x = NO + NO₂), carbon monoxide (CO), and peroxy radicals generated by the photochemical oxidation of the Volatile Organic Compounds (VOCs), such as hydrocarbons and aldehydes (e.g., Crutzen, 1971; Fishman & Crutzen, 1978; Jacob *et al.*, 1999; Kalabokas *et al.*, 2000).

The earliest quantitative measurements of tropospheric O₃, which occurred from 1876 – 1910 at the Montsouris Observatory near Paris, showed an annual average of 6 – 15 ppb (parts per billion by volume), with an average value of 10 ppb (Volz & Kley, 1988). Measurements at Arkona, on the Baltic coast showed an increase from ~15 ppb to 20 – 27 ppb between 1956 and 1983 (Feister & Warmbt, 1987). This increase was attributed to increase in O₃ precursor emission due to human activities (e.g., Cofala *et al.*, 2007; Olivier *et al.*, 1998; Vestreng *et al.*, 2009). Measurements of tropospheric O₃ over Arosa showed an increase by a factor of two between the 1950s and early 1990s (Stahelin *et al.*, 1994). Similar increases were found in measurements over Hohenpeissenberg in southern Germany from 1971 – 2000 (Gilge *et al.*, 2010). Measurements made over Mauna Loa and Barrow indicated an average increase in O₃ of 4.8 (±1.7) %/decade during the period 1973 – 1984, with the largest increase occurring during summer (e.g., Oltmans *et al.*, 1996a, 2006). Present day surface measurements show that anthropogenic emissions have increased the tropospheric O₃ burden by 38 % compared to preindustrial times (IPCC, 2007).

Tropospheric O₃ has significant adverse effects on human health, ecosystem, and the climate and it is important for the following reasons:

- In the lower troposphere and mostly during summer, O₃ is a pollutant and a major constituent of photochemical smog (Lippmann, 1989). Photochemical smog develops when primary pollu-

MOTIVATION AND OBJECTIVES

tants (O_3 precursors) interact under the influence of sunlight to produce a mixture of several hazardous chemicals known as the secondary pollutants of which O_3 is the most important one. This condition is extremely harmful and can lead to death. Excess of O_3 is toxic to the ecosystem, animal and human health. Studies have shown that exposure to tropospheric O_3 can lead to respiratory diseases, skin inflammation, and increased mortality (see e.g., Bell *et al.*, 2007; Gryparis *et al.*, 2004; Ito *et al.*, 2005; Mudway & Kelly, 2000; WMO, 2003). It has also been found that tropospheric O_3 and its precursors are responsible for most of the damage to vegetation caused by air pollution. Ozone enters through the stomata openings in the leaf surface to attack plants by producing by-products that reduce the efficiency of photosynthesis, thus affecting plants yield (see e.g., Ashmore, 2005; Heck *et al.*, 1982; Olszyk *et al.*, 1988b; Wang & Mauzerall, 2004).

- Tropospheric O_3 is a strong oxidant and its enhancement in the troposphere as a result of emission of pollutants (Bates, 1994; Kalabokas *et al.*, 2000) can affect air quality. Its oxidative capability makes it detrimental to life on earth as it can readily react and alter many biological molecules (e.g., Kalabokas *et al.*, 2000; USEPA, 1986). It is involved in the production of other oxidants such as hydroxyl (OH) radicals in the presence of water vapour (Crutzen, 1995; Fishman *et al.*, 1979; Ramanathan & Dickinson, 1979). Although the OH radical initiates the creation of components of smog such as Peroxyacetyl nitrate (PAN) ($CH_3O_3NO_2$), it is regarded as the detergent of the atmosphere as it leads to the oxidation of most of the species (e.g., CO, CH_4 and other hydrocarbons) found in the troposphere, into water-soluble products that are washed out by rain and snow. Thus, tropospheric O_3 plays an important role in contributing to the ability of the ecosystem to clean itself (see e.g., Crutzen, 1973; Finlayson-Pitts & Pitts Jr., 1997; Levy, 1971; Logan *et al.*, 1981). Despite some of the beneficial roles, its detrimental effects far outweigh its beneficial effects, hence it is termed bad O_3 .
- In the middle and upper troposphere and also around 50 – 55 km, O_3 absorbs in the thermal infrared, primarily in the 9.6 μm band. Therefore, it acts as a greenhouse gas in the troposphere, thus contributing to global warming and has an estimated globally averaged radiative forcing of $0.40 \pm 0.20 \text{ W m}^{-2}$ (IPCC, 2013; Ramaswamy *et al.*, 2001).
- Due to the variation of tropospheric O_3 lifetime with altitude, its local production may imply (near) global pollution.

The objectives of this PhD thesis are to retrieve tropospheric O_3 from the combined limb and nadir measurements from SCIAMACHY and quantify tropospheric O_3 present day distribution

and trends. The generated data can provide insight into the processes controlling tropospheric O₃ abundances and can be used to evaluate chemical transport and chemistry climate models. The data set will provide an understanding of the global tropospheric O₃ by characterizing quantitatively its distribution and changes on different temporal and spatial scales. Important information on tropospheric O₃ sources, sinks, transport, and seasonal behaviour can be acquired from satellite measurements by coupling with chemistry (climate/transport) models. One major challenge in the retrieval of tropospheric O₃ from space observations is that it requires accurate knowledge of stratospheric O₃, which accounts on average for ~90 % of the total O₃ columns (TOZs). In addition, O₃ is highly variable, as a result of the changes in its chemistry (i.e., sources, reactions and sinks) and dynamics. For example, diurnal variation of O₃ in the boundary layer can be significant. However, Stevenson *et al.* (2006) have estimated a mean lifetime of O₃ in the free troposphere to be about 22 days. In general, spatial and temporal sampling of parameters must be finer than the spatial and temporal scale of the physico-chemical phenomenon being investigated. Nyquist sampling theory indicates that significant changes from scales of twice the temporal and/or spatial sampling can be retrieved in principle. The sampling of tropospheric O₃ by the SCIAMACHY instrument, which reaches the global coverage in the tropics within 6 days, results in significance being achieved conservatively at the monthly mean scale.

The advent of the current generation of hyperspectral atmospheric sensors has led to the development of techniques and algorithms that is used to derive tropospheric O₃ retrieved from the measured spectral. The retrieval of tropospheric O₃ from satellite instruments using the residual approach started in the late 1980s (Fishman & Larsen, 1987). In this method, the tropospheric O₃ columns (TOCs) were obtained by subtracting the stratospheric O₃ columns (SOCs) retrieved from SAGE (Stratospheric Aerosol and Gas Experiment) measurements from the TOZs derived from TOMS (Total Ozone Mapping Spectrometer) observations. Several other residual-based approaches have been developed over the years (e.g., Fishman & Balok, 1999; Fishman *et al.*, 1990; Ladstätter-Weißmayer *et al.*, 2004; Schoeberl *et al.*, 2007; Thompson & Hudson, 1999; Ziemke *et al.*, 1998, 2006, 2011). Some of these data products can only give meaningful information within the tropics or involve the use of two different satellite instruments, which may have different spectral ranges at which they acquire data, thus engendering calibration issues.

The retrieval of tropospheric amounts of such species as O₃ by using the LNM technique was one of the principal objectives of the SCIAMACHY instrument (Bovensmann *et al.*, 1999; Burrows *et al.*, 1995; Gottwald & Bovensmann, 2011). Tropospheric amounts of species are obtained by subtracting their stratospheric amounts, which are retrieved from the limb viewing measurements, from the total amounts obtained from the nadir observations performed by the same instrument. This approach is similar in concept to that developed in the late 1980s (Fishman & Larsen, 1987; Fishman *et al.*,

1990). One unique aspect of the retrieval is that the total column (nadir) and stratospheric profile (limb) data from the same instrument are used. This reduces some of the uncertainties due to instrumental issues and SCIAMACHY provides a dense sampling of tropospheric O_3 on a global scale. The global retrieval of tropospheric O_3 from SCIAMACHY using the LNM technique is advantageous, because it does not require any further assumptions, such as zonal homogeneity of stratospheric O_3 or an estimate from model data. The algorithm extracts tropospheric O_3 information from observations of nearly the same air mass, probed in both nadir and limb geometry.

Outline

The remainder of this thesis is divided into three sections:

- Section I comprises chapters 1 & 2. Chapter 1 provides the background information on ozone, its role and measurements in the Earth's atmosphere. This entails a brief description of the Earth's atmosphere and its structure. It introduces atmospheric ozone, its discovery and measurements. It provides the description of ozonesonde, TES, OMI and MLS instruments with regards to this study. It also describes the SCIAMACHY instrument and provides an insight into the limb-nadir-matching (LNM) observations. Chapter 2 discusses the chemistry and dynamics of ozone and its role in the climate system. It covers the description of both tropospheric and stratospheric ozone chemistry and dynamics as well as the coupling mechanism of the upper troposphere/lower stratosphere (UT/LS).
- Section II describes in detail the methodology applied in this work to derive tropospheric O_3 columns from SCIAMACHY LNM observations. This section consists of chapters 3, 4 & 5. Chapter 3 discusses the derivation of tropopause heights from the European Center for Medium Range Weather Forecasts (ECMWF) reanalyses (ERA)-Interim data as well as from the temperature profile measurements by ozonesondes. Chapter 4 gives a brief description of the stratospheric O_3 profile retrievals from the limb and TOZs retrievals from the nadir measurements, while chapter 5 gives a detailed description of the SCIAMACHY LNM algorithm and culminates in sensitivity studies, estimating both systematic and random errors from all relevant error sources.
- Section III consists of chapter 6, which discusses the results of the retrieval. It provides the validation of SCIAMACHY TOC with ozonesonde data products. It also compares the TOC from SCIAMACHY with those from TES and OMI/MLS. Chapter 6 also deals with the analysis of SCIAMACHY TOC and TOCA (TOC anomaly) time series, global distributions, time-latitude morphologies, longitudinal variation of the complete SCIAMACHY tropospheric

O₃ datasets as well as SCIAMACHY TOC trends. The thesis closes with the summary of principal findings and proffers suggestions for future investigations.

MOTIVATION AND OBJECTIVES

SECTION I

Fundamentals, Ozone chemistry and dynamics

Chapter 1

The Earth's atmosphere, ozone, its role and measurement

1.1 The Earth's Atmosphere

The Earth is surrounded by a layer of gases and suspended solid and liquid particles called atmosphere. The atmosphere, which is retained by Earth's gravity, has made the Earth habitable for life by absorbing harmful solar ultraviolet (UV) radiation and regulates the surface temperature of the Earth. It consists of a mixture of gases composed primarily of nitrogen (78.08 %), oxygen (20.95 %), argon (0.93 %) by volume and many other less abundant but important trace gases amongst which are carbon dioxide (CO₂), ozone (O₃), water vapour (H₂O), methane (CH₄), oxides of nitrogen (e.g., N₂O, NO₂), helium (He), chlorofluorocarbons (CFCs) and numerous others. Although these trace gases comprise less than 0.1 % of the atmosphere, they are still a very important component of the atmosphere, as they play important roles in its chemical, thermodynamical and radiative properties. For example, O₃ obstructs harmful UV radiation; H₂O, CO₂ and O₃ play a key role in the earth radiation balance; CFCs and other halogen compounds play crucial roles in O₃ depletion. Apart from gaseous components in the atmosphere, there also exist some solid or liquid particles with diameters between 0.002 μm and 100 μm , which are called aerosols.

1.1.1 Structure of the Atmosphere

The atmosphere has a total mass of about 5×10^{18} kg with about 50 % of the mass lying below 6 km and 99 % below about 30 km. It extends some 500 km above the surface of the Earth and it is divided into layers based on the distribution of its vertical temperature structure (Figure 1.1). In this thesis, the discussion of the importance and challenge in conducting O₃ retrieval in the atmosphere will be limited to below 100 km because virtually all of the atmospheric mass (~ 99.99 %) is found below

1. THE EARTH'S ATMOSPHERE, OZONE, ITS ROLE AND MEASUREMENT

this altitude. The temperature of the Earth varies greatly vertically, horizontally and temporally throughout the atmosphere. These variations in temperature are produced by differences in the radiation budget and chemical composition of the atmosphere at different altitudes. Despite the horizontal and temporal variations, the average temperature profile of the atmosphere (see figure 1.1) is used to characterize the Earth's atmosphere into concentric spherical shells because it gives a better identification of the regions where the vertical temperature gradient has the same sign (e.g., troposphere, stratosphere, mesosphere, thermosphere and exosphere). The vertical temperature profile is also used to identify the pauses (tropopause, stratopause, mesopause, thermopause), that is, the regions where the gradient between layers with opposite signs is approximately zero.

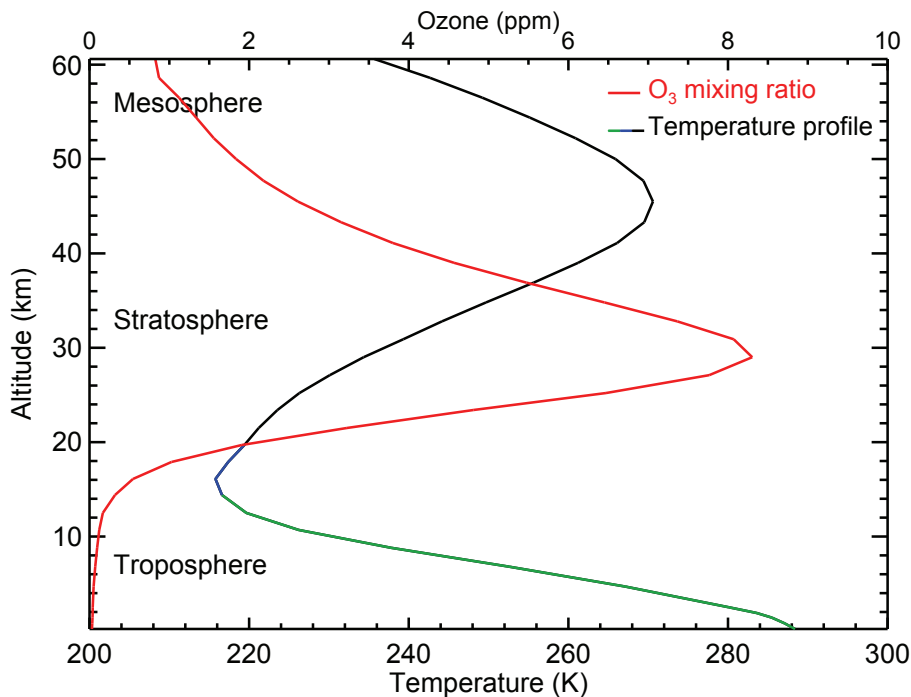


Figure 1.1: The vertical structure of the atmosphere and ozone mixing ratio typical of the midlatitudes.

The different atmospheric components are not uniformly distributed throughout the atmosphere. They can absorb or scatter solar and terrestrial radiation, thereby leading to the storage and re-emission of energy in the atmosphere. These different processes together with oceanic and surface interaction with radiation help to maintain the radiative balance between incoming and outgoing radiation. In the troposphere (green line in Figure 1.1), temperature decreases with altitude up to the tropopause (blue line in Figure 1.1), because the atmosphere is heated from the surface. Above the tropopause is the stratosphere, which is characterized by temperature increase with altitude due to the dissociation of molecular oxygen and O₃ by solar radiation at UV wavelengths. The temperature at the top of the stratosphere is as high as 270 K (see figure 1.1), which

is about the same as the ground level temperature. Above the stratosphere, and extending to approximately 90 km, is the mesosphere where the temperature decreases again due to radiative cooling by CO₂. The layer above the mesosphere is called the thermosphere, which extends from between 90 and 100 km to about 400 km above the Earth's surface.

In addition to temperature, two other atmospheric parameters that play important role in atmospheric chemistry are pressure and density. The relationship between these three main atmospheric parameters (equation 1.1b) can be derived from the ideal gas law (equation 1.1a).

$$PV = nRT, \tag{1.1a}$$

$$PV = \frac{m}{M}RT, \Rightarrow P = \frac{m}{VM}RT = \frac{\rho}{M}RT. \tag{1.1b}$$

Where P is the pressure, V is the volume, n is the number of moles, m is the mass, M is the molar mass, T is the air temperature, ρ is the mass density of the gas and R is the ideal gas constant (for dry air $R = 287 \text{ J/kg/K}$).

It should be noted that while temperature behaves differently in the different regions of the atmosphere, density and pressure decrease with altitude in the terrestrial atmosphere. The reason for the decrease in density with altitude is due to the gravitational attraction between the earth and air molecules, which is greater for those molecules closer to the earth than those farther away. The decrease in pressure with altitude is as a result of the reduced air mass with increasing altitude. This can be illustrated from the hydrostatic equation for a column of air, which is given as:

$$dp = -\rho g dh. \tag{1.2}$$

Where g is the acceleration due to gravity. Dividing equation 1.2 by equation 1.1b yields the so called barometric formula (equation 1.3c), which explains the dependency of barometric pressure on altitude.

$$\frac{dP}{P} = \frac{Mg}{RT} dh, \tag{1.3a}$$

$$\int_{P_o}^P \frac{dP}{P} = -\frac{Mg}{RT} \int_{h_o=0}^h dh, \tag{1.3b}$$

$$P = P_o \exp\left(\frac{-Mgh}{RT}\right), \tag{1.3c}$$

Equation (1.3c) can also be written as:

$$P = P_o \exp\left(\frac{-Mgh}{KT}\right), \tag{1.4a}$$

$$P = P_o \exp\left(\frac{-h}{H}\right). \tag{1.4b}$$

1. THE EARTH'S ATMOSPHERE, OZONE, ITS ROLE AND MEASUREMENT

Where K is the Boltzmann constant and $H = \frac{kT}{Mg}$ is referred to as the scale height, which ranges from 3 to 8 km throughout the lowest 100 km. This signifies that $\sim 99.99\%$ of the atmospheric mass lies below 100 km. The above barometric formula is useful for estimating the height of various pressure levels in the atmosphere, because the pressure at a given height in the atmosphere is a measure of the mass that lies above the level.

1.2 Atmospheric Ozone

Ozone is the allotropic form of oxygen. It is a colourless, toxic, unstable gas, and in standard conditions, condenses to a dark blue liquid at -112°C . Ozone is a highly reactive compound and capable of oxidizing many organic compounds. It is one of the most extensively studied and best understood atmospheric trace constituents and has played important roles in the development of atmospheric chemistry.

1.2.1 Discovery and measurements of Ozone

Measurements of gases in the atmosphere have formed the basis of our knowledge and understanding of the atmosphere. The history of ozone began in the 19th century when Christian Friedrich Schönbein in 1840 (Schönbein, 1858) discovered that a gas with a particular strong odor was produced in the electrolysis of water as well as in discharges of frictional electricity in air (Leeds, 1880). In 1858, André Houzeau through a quantitative technique, discovered that ozone is present in natural air. Ozone was assigned the chemical formula O_3 in 1865 by Jacques-Louis Soret and finally confirmed by Schönbein in 1867 (Leeds, 1880). In 1879, a few years after the discovery of atmospheric O_3 , measurements of the solar spectrum by Marie Alfred Cornú showed that solar radiation dropped off rapidly at wavelengths below about 300 nm. He stated that the wavelength of the "cutoff" increased during sun set and at long pathlength in the atmosphere. He also demonstrated that the cutoff was as a result of an absorber located in the Earth's atmosphere (Cornú, 1879). One year later, in 1880, Sir Walther Noel Hartley described the strong UV O_3 absorptions between 200 and 300 nm. Thus, confirming that the observed spectrum at about 300 nm was influenced by the presence of O_3 in the stratosphere (Hartley, 1880). Chappuis Jean in 1880, discovered the much weaker absorption in the visible range at about 400 and 800 nm (Chappuis band) in liquid O_3 . The highly structured O_3 absorption between 300 and 360 nm (Huggins bands) in spectra of Sirius was discovered by Sir William Huggins in 1890. The characteristic absorption features of the Huggins bands make it suitable for the identification and quantification of atmospheric O_3 absorption in measured spectra. Balloon-borne spectroscopic measurements over Berlin performed by Albert Wigand in 1913 showed that the O_3 layer was located above 9 km altitude. The altitude was later

shown to be around 25 km (Dobson & Harison, 1926; Götz *et al.*, 1934). The first spectrometric measurements of the “thickness” of O₃ layer was carried out by Charles Fabry in 1919.

Immediately after the discovery of the optical properties of O₃, towards the end of the 19th century, a technique based on the capability of O₃ to absorb solar radiation differently at specific wavelengths, was used to determine the total O₃ column (TOZ) above the surface (Dobson, 1931; Dobson & Harison, 1926). The wavelengths used by Dobson spectrometer fall within the Huggins bands. The cross section in the Hartley band quickly becomes so large that no radiation is transmitted to the ground, thus making measurements impossible. Therefore, only limited information on O₃ profile can be deduced.

The abundance of O₃ in the atmosphere is measured by a variety of techniques based on its unique optical and chemical properties. Ozone reacts with various chemicals, gases, and some lubricating oils to produce faint luminescence that can be detected by a sensitive photomultiplier tube. Due to its absorption potential in the UV, visible, and infrared, as well as emission in the microwave or infrared region, electronic sensors in these wavelength regions are incorporated in several high-technology O₃ detectors. These detectors can be classified into ground based, balloon-borne, airborne or satellite platforms. The development of satellite platforms has led to the expansion in the measurement of atmospheric O₃ from just an isolated ground station to daily global coverage and O₃ profile retrievals in the atmosphere. In this work, O₃ measurements from balloon-borne and satellite platforms are used.

1.2.1.1 Balloon-borne observations: Ozonesonde

An ozonesonde, schematically shown in figure 1.2, is a lightweight O₃ measuring instrument carried aloft a small balloon. It comprises an electrochemical cell filled with a Potassium Iodide (KI) solution and a meteorological radiosonde (Komhyr, 1967). When ambient air is pumped through the cell, O₃ present in the air undergoes redox reactions with the KI solution as illustrated by equations 1.5 & 1.6, and generates an electric current, which is considered to be proportional to the concentration of O₃ in the sampled air after correcting for background effects.



The radiosonde also measures the ambient air temperature, pressure, relative humidity and transmits all the acquired information back to a ground receiving station during the balloon ascent before bursting at an altitude typically of around 35 km, depending on the state of the atmosphere.

1. THE EARTH'S ATMOSPHERE, OZONE, ITS ROLE AND MEASUREMENT

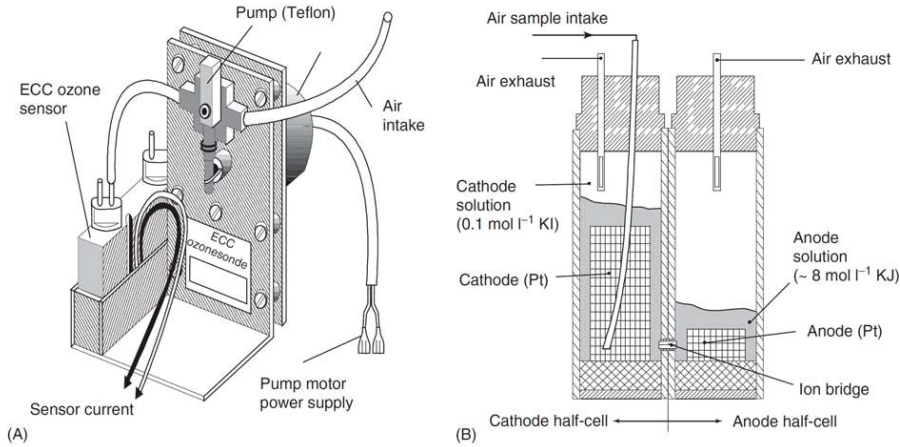


Figure 1.2: Schematics of the electrochemical concentration cell (ECC) (A) ozonesonde and (B) sensing cell developed by Komhyr (1969), image after Smit (2002).

The relationship between the measured O_3 partial pressure and the cell current can be derived from the combination of the ideal gas law and Faraday's law of electrolysis as shown in equation 1.7,

$$P_{O_3} = \frac{R}{2 \times F} \times T \times \eta \times Q(I_m - I_B). \quad (1.7)$$

Where P_{O_3} is the measured O_3 partial pressure in millipascal (mPa), T is the temperature of the sampled air in Kelvin (K), η is the pump efficiency correction, Q is the flow rate, R is the universal gas constant, $F = 9.64853399 \times 10^4 C mol^{-1}$ is Faraday's constant, I_m is the cell current in microampere (μA) and I_B is the cell background current (typically $0.1 \mu A$).

Ozonesonde provides information on the vertical distribution of O_3 as well as on the TOZs up to the burst altitude. The derivation of the TOZs is based on integrating the O_3 number density profiles from the ground to the burst altitude and adding a residual amount obtained from climatological O_3 tables (McPeters *et al.*, 1997). Ozonesondes can provide useful information on O_3 close to the polar region mostly during low sun and polar night, when satellite observations in the optical spectral range are not possible. However, the balloon often bursts at about 16 km due to extremely harsh and cold weather conditions. Another limitation of this instrument is that the trajectory of balloon-borne ozonesonde can not be controlled because the balloons are not powered. Several ozonesonde instruments have been in use to measure O_3 in the atmosphere since the early 1960s. Examples of major types of ozonesondes in use today are:

- Electrochemical Concentration Cell (ECC) (Komhyr, 1969; Komhyr & Harris, 1971),
- Brewer-Mast (BM) (Brewer & Milford, 1960),
- Carbon iodine cell (KC96) (Kobayashi & Toyama, 1966).

These different types of ozonesondes operate on similar principles as discussed above but differ in instrumental layouts and design (Smit, 2002). The Jülich Ozone Sonde Intercomparison Experiment (JOSIE) (Smit & Straeter, 2004b; Smit *et al.*, 2007) is aimed at quantifying systematically the influence of various sonde solution strengths on instrument performance and serves as a facility for calibrating ozonesondes.

1.2.2 Satellite based observations of ozone

Since the launch of the first satellite (Sputnik) in 1957 (Cadbury, 2006; Krieger, 1958), space borne platforms have been instrumental in providing measurements at various spectral intervals, thus allowing the retrieval of a variety of atmospheric species as well as surface properties. Satellite measurements of O₃ are essential to derive comprehensive data everyday over the entire globe. Satellite instruments use a passive spectroscopic method to measure solar radiation that has been scattered, transmitted, and reflected by the atmosphere and the Earth's surface. They are capable of providing information on O₃ vertical profiles, TOZs, tropospheric O₃ columns (TOCs) as well as on other constituents in the atmosphere.

The determination of the vertical distribution of O₃ by monitoring back scattered radiation in the Hartley and Huggins bands was first proposed by Springer and Wentworth in 1957 (Singer & Wentworth, 1957). This technique has been applied to recent satellite instruments that are capable of measuring the spectrum of limb scattered sun-light at UV, visible and near-infrared wavelengths (e.g., Ultraviolet Spectrometer (UVS) on the Solar Mesospheric Explorer (SME) (Rusch *et al.*, 1984), the Shuttle Ozone Limb Sounding Experiment/Limb Ozone Retrieval Experiment (SOLSE/LORE) (McPeters *et al.*, 2000), the Optical Spectrograph and Infrared Imager System (OSIRIS) on the Odin satellite (Llewellyn *et al.*, 2004; Warshaw *et al.*, 1998) and SCIAMACHY on Envisat (Bovensmann *et al.*, 1999)). Thus, allowing the retrieval of atmospheric species at a high vertical resolution and near global coverage. Satellite instruments such as Global Ozone Measurement by Occultation of Stars (GOMOS) on Envisat (Bertaux *et al.*, 1991), The Ozone Mapping and Profiler Suite (OMPS) on Suomi National Polar-orbiting Partnership satellite (Flynn *et al.*, 2006), Stratospheric Aerosol and Gas Experiment III (SAGE III) on the Meteor-3M spacecraft (McCormick *et al.*, 1991), Halogen Occultation Experiment (HALOE)(Russell III *et al.*, 1993) and Polar Ozone and Aerosol Measurement (POAM) (Lucke *et al.*, 1999) also have the ability to provide information on O₃ vertical profiles. Vertical distribution of O₃ has also been derived from passive thermal emission instruments, which are not limited to measuring in the sunlit atmosphere. Such instruments include Microwave Limb Sounder (MLS) on UARS (Baray *et al.*, 1993), Michelson Interferometer for Passive Atmospheric Sounding (MIPAS) on Envisat (Fischer & Oelhaf, 1996) and Submillimeter and Millimeter Radiometer (SMR) on the Odin satellite (Frisk *et al.*, 2003).

1. THE EARTH'S ATMOSPHERE, OZONE, ITS ROLE AND MEASUREMENT

Apart from the vertical distribution of ozone, information on the TOZ can also be derived from satellite instruments. TOZ is the number of O_3 molecules per unit area in the atmospheric column below the satellite instruments expressed in Dobson Units (DU). The first feasibility study on the determination of TOZ from satellite measurements of the solar UV radiation was presented by Dave and Carlton in 1967 (Dave & Mateer, 1967), which was later implemented on the measured attenuated backscattered UV radiation observed by Nimbus IV satellite instruments (Mateer *et al.*, 1971). Over the years, different satellite instruments and algorithms have been developed to infer TOZ from backscattered UV radiance. Examples of such satellite instruments include Total Ozone Mapping Spectrometer (TOMS)(Nimbus-7, Meteor 3, Earth Probe, and ADEOS), SBUV (Nimbus-7)(Heath *et al.*, 1975), SBUV/2s (NOAA-9, NOAA-11, NOAA-14, NOAA-16 and NOAA-17) (Frederick *et al.*, 1986; Hilsenrath *et al.*, 1995), GOME (ERS-2) (Burrows *et al.*, 1999), SCIAMACHY (Envisat)(Bovensmann *et al.*, 1999), OMI (EOS-Aura)(Levelt *et al.*, 2006), and GOME-2 (Metop-A)(Callies *et al.*, 2000).

Tropospheric O_3 has also been retrieved from satellite instrument as discussed in section 5. However, measuring tropospheric O_3 from space is very challenging, because the backscattered radiation from the troposphere to the satellite instrument travels through the stratosphere and mesosphere where about 90 % of the atmospheric O_3 is located, and is thus affected strongly by extinction through this upper level O_3 absorption. This poses a great problem in separating the contribution of tropospheric ozone, which is about 10 % to the measured radiance signal. Another problem is the uncertainty in the spectroscopic O_3 data for wavelengths > 315 nm. This is an issue as limiting the O_3 retrievals to wavelengths less than or equal to 315 nm will limit the tropospheric O_3 information for larger solar zenith angles. The GOME instrument on the European Remote Sensing satellite (ERS-2), is the first satellite instrument that shows the potentiality of measuring tropospheric O_3 from space (Chance *et al.*, 1997). The advent of current generation of satellite hyperspectral atmospheric sounders, which are capable of making simultaneous radiance measurements with high spectral resolution and sampling rate, covering the UV-visible (e.g., SBUV instruments, GOME, GOME-2, SCIAMACHY and OMI) and IR (e.g., TES, IASI) spectral ranges, have greatly enhanced the capability to develop algorithms that can detect and quantify tropospheric O_3 on a global scale (see section 5). The SCIAMACHY instrument provided the main data products used in this study. Other satellite data products used in this work include TES, OMI and MLS.

1.2.2.1 The SCIAMACHY instrument

SCIAMACHY (Greek: $\sigma\kappa\iota\alpha\mu\alpha\chi\eta$, analogously: “chasing or hunting shadows”) (Bovensmann *et al.*, 1999; Burrows *et al.*, 1995), was a passive spectrometer, and part of the payload for ESA’s Environmental Satellite (Envisat), launched into orbit on 28th February, 2002. Unfortunately, on 8th April, 2012 contact was lost with Envisat and thus far, ESA has failed to re-establish contact. Envisat orbited the earth in a sun-synchronous, near-polar orbit at a mean altitude of typically about 800 km, but was lowered by 17 km in late 2010. It had an inclination relative to the equatorial plane of 98.5° with an orbital period of about 100 minutes, thus completing about 14.3 orbits per day (Gottwald & Bovensmann, 2011). Its local equator crossing time was 10:00 a.m. at the descending node.

The SCIAMACHY instrument was an eight-channel passive imaging grating spectrometer that measured the transmitted, reflected and scattered solar radiation in the UV, visible, and near infrared (NIR) wavelength regions (214 - 2386 nm) with a spectral resolution varying between 0.22 nm and 1.48 nm. The observations were contiguous from 214 nm to 1750 nm with two additional channels: 1940 - 2040 nm and 2265 - 2380 nm (e.g., Gottwald & Bovensmann, 2011). The spatial resolution of the scan mode depended on the scan velocity and the integration time of the detectors. The scan velocity along track was determined by the satellite velocity, which was approximately 7.5 kms^{-1} while the across track velocity was determined by the geometry scan mirror rate on ground. Useful information on a wide range of trace gases (e.g., O_2 , O_3 , O_4 , NO , N_2O , NO_2 , NO_3 , CO , CO_2 , HCHO , CH_4 , H_2O , SO_2 , BrO , OCIO), clouds (e.g., PSCs, NLC), surface parameters, and aerosols have been provided by the SCIAMACHY instrument (see Table 1.1) (Gottwald & Bovensmann, 2011).

Channels	Spectral range (nm)	Resolution (nm)	Detector material	Temperature range (K)	Retrieval targets
1	214 - 334	0.24	Si	204.5 - 210.5	O_3 , ClO , NO , Metals, Noctilucent clouds
2	300 - 412	0.26	Si	204.0 - 210.0	NO_2 , OCIO , BrO
3	383 - 628	0.44	Si	221.8 - 227.8	O_3 , NO_2 , O_4 , Aerosols
4	595 - 812	0.48	Si	222.9 - 224.3	O_3 , NO_3 , H_2O , Aerosols
5	773 - 1063	0.54	Si	221.4 - 222.4	H_2O , Aerosols
6	971 - 1773	1.48	InGaAs	197.0 - 203.8	H_2O , Aerosols
7	1934 - 2044	0.22	InGaAs	145.9 - 155.9	H_2O , CO_2
8	2259 - 2386	0.26	InGaAs	143.5 - 150.0	H_2O , CO_2 , CO

Table 1.1: Overview of the SCIAMACHY spectrometer channels. The last column on the right shows the list of a number of atmospheric trace gases with strong absorption or emission features in the corresponding wavelength range from which they can be retrieved.

1. THE EARTH'S ATMOSPHERE, OZONE, ITS ROLE AND MEASUREMENT

1.2.2.1.1 SCIAMACHY measurement geometries

The scan mirror system enabled three different viewing geometries: nadir, limb, and solar/lunar occultation as shown in figure 1.3, with each geometry having its particular advantage. The daylight measurements can be performed in the limb and nadir viewing geometries while the instrument can also observe atmospheric transmission in solar and lunar light in the occultation mode. A typical orbit starts with a limb measurement of the twilight atmosphere, followed by the solar occultation measurement during sunrise at high northern latitudes and an optimized limb-nadir sequence. If the moon is visible in the southern hemisphere ($30^\circ - 90^\circ\text{S}$), lunar occultation measurements are performed in every second orbit.

1.2.2.1.1.1 The nadir viewing geometry

In the nadir mode (figure 1.3), the field of view (FOV) of the instrument was directed near-perpendicular to the earth's surface. This geometry allowed the instrument to scan the region underneath the spacecraft, thus, detecting upwelling solar radiation that has been scattered in the atmosphere and reflected by the Earth's surface. The field of view of the nadir mirror was $25 \text{ km} \times 0.6 \text{ km}$ across the satellite track with the across track velocity rate approximately 240 km s^{-1} on ground. Thus, the typical spatial resolution was approximately 240 km across track and 30 km along track with the footprint of a single observation being typically $30 \text{ km} \times 60 \text{ km}$. The across track resolution depends on the integration times and the data readout rate of the satellite instrument. The actual penetration depth of the nadir scans depends on the wavelength range that was employed. For instance, total column information obtained by employing the UV channel ($214 - 300 \text{ nm}$) do not extend to the ground, as O_3 absorption in the Hartley band prevents radiation within this wavelength range from penetrating deep into the atmosphere as in the case of visible radiation.

1.2.2.1.1.2 The limb viewing geometry

In the limb mode (figure 1.3), the instrument line of sight was directed tangentially to the Earth surface as the instrument scanned in the horizontal and vertical direction with elevation steps of approximately 3.3 km at the tangent point (Gottwald & Bovensmann, 2011). The tangent height was raised in discrete steps from the surface up to about 100 km , thus providing vertically resolved information on the atmospheric state. The instantaneous field of view at the tangent point was about 110 km (horizontally) $\times \sim 2.6 \text{ km}$ (vertically). For every limb state, a horizontal scan with a cross track coverage of 960 km and typically four readouts in the visible part of the spectrum were performed. This resulted in a typical horizontal resolution of 240 km . This viewing geometry

was strongly affected by surface albedo, aerosol extinction, and clouds, particularly in the spectral ranges with small gaseous absorption.

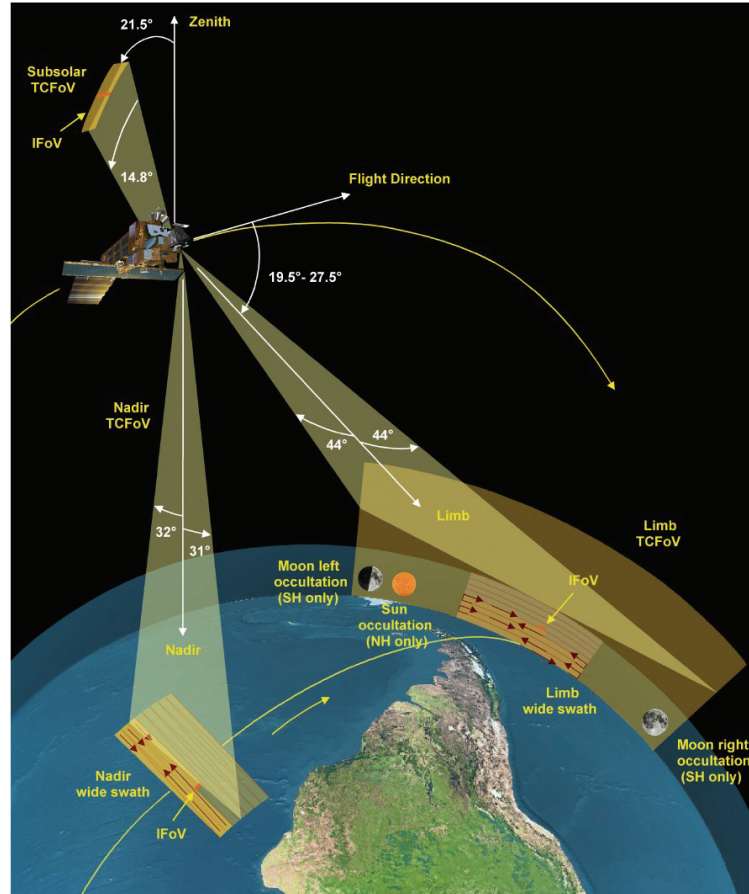


Figure 1.3: Schematics of SCIAMACHY's Total Clear Field of View (TCFoV) and observation geometries (Courtesy of DLR-IMF).

1.2.2.1.2 The limb-nadir measurement mode

A special feature of SCIAMACHY was the combined limb-nadir measurement mode illustrated by figure 1.4, which enables the instrument to observe the same atmospheric volume first in limb and then after about 7 minutes in nadir geometry. This mode of observation was introduced to facilitate the separation of the tropospheric abundance of absorbing constituents from that in the middle atmosphere. The separation of tropospheric columns from the middle atmospheric columns of important atmospheric trace gases was one of the scientific goals of the SCIAMACHY project. The inversion of the combination of limb and nadir measurements enables tropospheric column amounts of trace gases including ozone to be determined as described in section 5.1

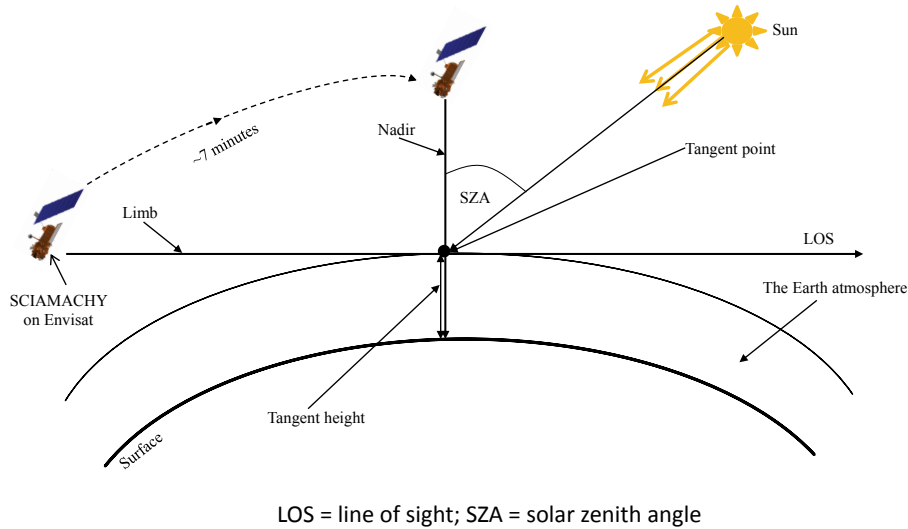


Figure 1.4: Illustration of SCIAMACHY limb and nadir observation geometries.

1.2.2.2 TES, OMI and MLS

TES, OMI and MLS are satellite instruments aboard the Aura spacecraft, which was launched into a sun-synchronous polar orbit in July 2004 at an inclination angle of 98.2° and an altitude of about 705 km. The spacecraft has an equatorial crossing time of approximately 01:45 p.m. in ascending node and takes about 98.8 minutes to cover an orbit, thereby completing about 14.6 orbits per day.

TES is a Fourier transform IR spectrometer, covering the spectral range of $650 - 3050 \text{ cm}^{-1}$ ($3.3 - 15.4 \mu\text{m}$) at a spectral resolution of 0.1 cm^{-1} in the nadir viewing mode (Beer, 2006). The nadir vertical profiles are 1.6° apart along the orbital track with a footprint of about $5 \times 8 \text{ km}^2$ (Beer *et al.*, 2001). TES covers the globe in 16 days in the cross-track mode.

OMI is a UV-visible nadir viewing spectrometer, detecting backscattered solar radiation over the 270 – 500 nm wavelength range with a spectral resolution of 0.42 – 0.63 nm (Levelt *et al.*, 2006). It has a spatial resolution of 13 km x 24 km at nadir and covers the globe in one day, thus providing daily information on the TOZs.

The MLS instrument is a thermal-emission microwave limb sounder that measures vertical profiles of O_3 , providing information on the SOC. The spatial resolution of MLS is 5 km cross-track \times 500 km along-track \times 3 km vertically, depending on the parameter under observation (Waters *et al.*, 2006). Details on the instrument description and measurement techniques are discussed by Waters *et al.* (2006).

Chapter 2

Chemistry and dynamics of ozone

2.1 Tropospheric ozone chemistry and dynamics

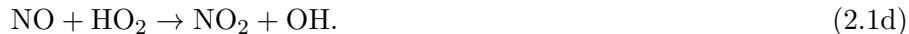
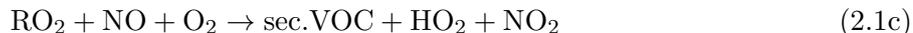
The tropospheric O₃ budget is determined by several processes including its photochemical production, downward transport from the stratosphere via stratosphere-troposphere exchange (STE) processes (e.g, Fusco & Logan, 2003; Hsu & Prather, 2009; Roelofs & Lelieveld, 1997), long range transport of O₃ and its precursors from the upwind regions into the downwind regions (Jacob *et al.*, 1999), destruction and dry deposition. Photochemistry in the lower troposphere is the major source of tropospheric O₃ (Hogrefe *et al.*, 2004; Young *et al.*, 2013), which is highly dependent on the presence of carbon monoxide (CO), methane (CH₄), non methane hydrocarbons (NMHCs) and volatile organic compounds (VOCs), controlled and catalyzed by NO_x (Fishman *et al.*, 1979). Therefore, a high amount of O₃ in a particular region is primarily associated with O₃ precursors, sunlight and high temperatures. Relatively light winds and conditions that suppress vertical mixing in the atmosphere such as thermal inversions or subsidence layers also play a role.

The sources of NO_x in the troposphere are either anthropogenic or natural. Natural sources of NO_x include lightning (Kaynak *et al.*, 2008; Price *et al.*, 1997), transport from the stratosphere (Wang *et al.*, 1998), and soil emission resulting from microbial reactions (Stewart *et al.*, 2008; Wayne, 2000), which is enhanced by the application of fertilizers. Other natural sources are oxidation of biogenic ammonia initiated by OH radicals (Delon *et al.*, 2008; Stewart *et al.*, 2008), biomass burning and wildfires (savannah burning, tropical deforestation, temperate wildfire and agricultural waste burning) (Crutzen & Andreae, 1990). Anthropogenically, NO_x is produced from aircraft emissions (Gauss *et al.*, 2006a), industrial, thermal, and fossil fuel combustion processes (Benkovitz *et al.*, 1996; Dignon, 1992). Studies have shown that the concentrations of natural or biogenic NO_x are far smaller compared to the concentrations of anthropogenic NO_x (Pierce *et al.*, 2009).

2. CHEMISTRY AND DYNAMICS OF OZONE

VOCs are emitted either naturally or anthropogenically. Natural sources of VOCs are mainly from vegetation (forest, grasslands and wetlands), e.g., isoprene and terpenes, as well as from cattle and termites (Brasseur *et al.*, 1999b; Hewitt, 1999; Lemieux *et al.*, 2004). Dimethylsulphide (DMS) is an important VOC in the marine air mass. It is produced by biological processes from phytoplankton in surface water (Andreae *et al.*, 1985). The anthropogenic sources of VOCs include hydrocarbons such as alkanes (e.g., ethane, butane), alkenes (e.g., butene, propene), aromatics (e.g., toluene, xylene, benzene), alcohol (e.g., methanol, ethanol), aldehydes (formaldehyde), etc. (Warneke *et al.*, 2007). Home and personal care products (air fresheners), building materials and household utilities (e.g., carpets, vanishes, paints) are anthropogenic sources of VOCs (Hewitt, 1999). Biogenic VOCs are highly reactive and form a significant fraction of the total ambient VOC that exist in suburban and rural regions (Pierce *et al.*, 1998).

The formation of O₃ in the troposphere can be initiated through the reaction of VOCs or CO with OH radicals to form organic peroxy radicals (RO₂) or hydroperoxy radical (HO₂), which then react with NO to form NO₂ (Chameides & Davis, 1982), as shown below.



The NO₂ is photolyzed at wavelengths less than 424 nm to produce NO and atomic oxygen. The atomic oxygen combines with O₂ to form O₃, which combines with NO to form NO₂ (Crutzen, 1970; Fabian & Pruchniewicz, 1977; Wayne, 2000), as shown in equations 2.2a – 2.2c.



Where M in 2.2b is any body with mass, primarily N₂ and O₂. M absorbs the energy of the reaction as heat, which helps in the completion of the reaction. The set of equations (2.2a - 2.2c) is called the NO_x photostationary state (Null cycle) as there is no net production of O₃. It leads to the recycling of NO₂ due to NO_x titration (equation 2.2c), which occurs mainly at night and in the presence of high NO concentrations (e.g., from power plants). In the daytime, equation 2.2c is balanced by the photolysis of NO₂ (equations 2.2a and 2.2b). Equation 2.2c contributes to the reason why tropospheric O₃ amount is depressed in the vicinity of the production sources and elevated as the plume travels further downwind. Equations 2.2a – 2.2c suggest that net O₃ production would be

very limited, unless there is a process that can turn NO into NO₂ without simultaneously destroying O₃. VOCs play this important role when they are oxidized by OH radicals (see equations 2.1a and 2.1b) as described in section 2.1.1.2.

2.1.1 Ozone production regime

From the relation between O₃, NO_x and VOC, two regimes with different O₃-NO_x-VOC sensitivity can be identified. NO_x-sensitive regime (limited NO_x and high VOC) and VOC-sensitive regime (saturated NO_x and low VOC). In the NO_x-sensitive regime, O₃ concentrations increase with increasing NO_x and exhibit a little response to increasing VOC. In the VOC-sensitive regime, O₃ concentrations decrease with increasing NO_x and increase with increasing VOC. Therefore, while the NO_x-sensitive regime is associated with high VOC/NO_x ratios, the VOC-sensitive regime is associated with low VOC/NO_x ratios.

2.1.1.1 NO_x-sensitive regime

The condition is NO_x-sensitive when peroxides (RO₂) represent the dominant radical sink. In this condition, the concentrations of HO₂ and RO₂ radicals will be determined by the balance between equations 2.3c & 2.6d with equations 2.8c & 2.8d. Because the rate of peroxide formation is quadratic in HO₂, the ambient concentrations of HO₂ and RO₂ show little variation in response to changes in NO_x and VOC. Therefore, the rate of O₃ formation is determined by the reaction of HO₂ and RO₂ with NO (equations 2.1c and 2.1d). This rate increases with increasing NO_x. In polluted regions, the rate of O₃ formation is usually slightly affected by changes in VOC, but in remote regions the rate of O₃ formation increases with increasing VOC.

2.1.1.2 VOC-sensitive regime

In the VOC-sensitive regime, nitric acid (HNO₃), PAN (peroxyacetyl nitrates) and other organic nitrates serve as the principal radical sink. During this condition, the concentrations of OH radicals will be determined by the balance between equations 2.3c & 2.6d with equation 2.8e. Because the rate of the formation of HNO₃ increases with NO₂, OH decreases with increasing NO₂. The rate of O₃ formation is therefore determined by the rate of the reaction of VOC and CO with OH (equations 2.1a and 2.1b). This rate increases with increasing VOC and decreases with increasing NO_x.

2.1.1.3 Sources and sinks of odd hydrogen

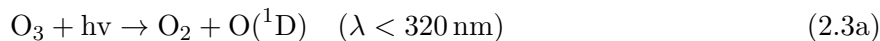
The O₃-NO_x-VOC regimes are driven by the chemistry of odd hydrogen radicals (mainly free radicals such as H, OH, HO₂ and other RO₂ species), which consist of two main sinks: RO₂ and

2. CHEMISTRY AND DYNAMICS OF OZONE

HNO₃. The O₃ production rates depend on the abundance of OH, which is part of the sources and sinks of odd hydrogen radicals. Peroxy radicals are mainly produced in two ways: reaction of free radicals such as the alkyl radicals (R, H or RO, OH), NO, NO₃ and O₃ with VOCs in the presence of oxygen and secondly, through the photolysis of carbonyls like formaldehyde (CH₂O).

2.1.1.3.1 Sources of odd hydrogen

Sources of odd hydrogen radicals include the photolysis of O₃, CH₂O, and other secondary VOCs. The main source of OH in the troposphere is the photolysis of O₃ at wavelengths less than 320 nm, leading to the production of a singlet oxygen atom O(¹D) as shown in equation 2.3a. The O(¹D) then reacts with water vapour to yield two molecules of OH radicals as shown below (e.g., Atkinson, 1979; Finlayson-Pitts & Pitts Jr., 1986).



The O(¹D) formed in equation 2.3a can get quenched to a ground-state oxygen O(³P) atom, which further reacts with O₂ to regenerate O₃ as shown in equations 2.4a - 2.4c

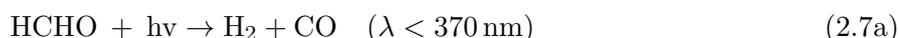
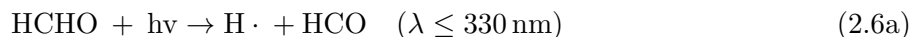


Another source of OH or alkoxy radicals in the troposphere is the photolysis of nitrous acid (HONO) at a wavelength of less than 370 nm (e.g., Platt, 1985). They are also formed from the photolysis of CH₂O and other carbonyls in the presence of NO, as well as in the dark reactions of NO₃ and O₃ with alkenes as shown in equations 2.5a - 2.5g. (e.g., Collins *et al.*, 2002; Platt *et al.*, 1990; Singh *et al.*, 2004):



2.1 Tropospheric ozone chemistry and dynamics

Photolysis or oxidation of CH₂O yields important sources of HO_x (OH + HO₂), H₂ and CO as shown in equations 2.6a - 2.7b.



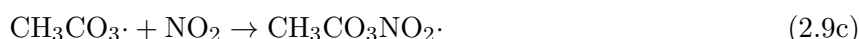
The formyl radical (HCO) and atomic hydrogen (H) react with O₂ to produce HO₂, which then combines with nitric oxide (NO) to form OH and NO₂. NO₂ is again photolyzed to produce more O₃, thus beginning another cycle of O₃ production.

2.1.1.3.2 Sinks of odd hydrogen

The sinks of odd hydrogen radicals include hydrogen peroxide (H₂O₂), organic peroxides (ROOH), HNO₃, PAN (CH₃COONO₂) and other organic nitrate (see equations 2.8a - 2.8e and 2.9a - 2.9c).



PAN is formed by the reaction of aldehydes with OH radicals in the presence of NO₂ as shown in equations below.



PAN formation acts as a sink for NO_x (Singh *et al.*, 1994, 1995), thus serving as a long range transport vehicle for HO_x and NO_x to remote regions due to its stability at the cold temperatures

2. CHEMISTRY AND DYNAMICS OF OZONE

of the upper troposphere. It is decomposed photochemically as shown in equation 2.10 to form NO_2 . Thus, it plays a significant role in urban air pollution. It also has impact on ozone-temperature sensitivity as well as on rural chemistry.



2.1.1.4 Oxidation and photolysis of VOCs and hydrocarbons

Two major sources of O_3 production in the remote oceanic boundary layer and free troposphere are the oxidation of CO and CH_4 (Crutzen, 1974).

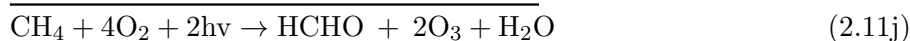
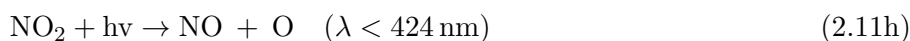
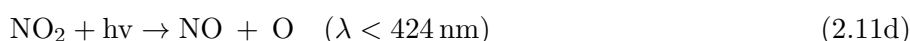
2.1.1.4.1 Oxidation of Methane

The main natural source of CH_4 in the atmosphere is wetlands. Other natural sources include termites, oceans, vegetation and CH_4 hydrates. Anthropogenic sources of CH_4 are the combustion of coal and natural gas, waste disposal in landfills, livestock (cattle, sheep), rice cultivation, and biomass burning. Studies have shown that anthropogenic sources of CH_4 are far more important than natural sources (IPCC, 2007, 2013). CH_4 has a life time of about 8 years. Its major sink is OH radical while its minor sinks include uptake by soils and destruction in the stratosphere.

2.1.1.4.1.1 High NO_x condition

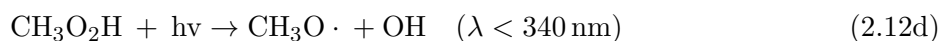
In the presence of high NO_x concentration, CH_4 is oxidized in the troposphere by OH radicals to yield methylperoxy radicals (CH_3O_2) (Finlayson-Pitts & Pitts Jr., 1986). CH_3O_2 reacts with NO to form methyloxy (CH_3O) radicals and NO_2 (equation 2.11c). The NO_2 is photolyzed to produce O_3 (equations 2.11d and 2.11e), while the CH_3O is oxidized to form CH_2O and HO_2 (equation 2.11f). HO_2 reacts with NO to produce NO_2 and OH radical, thus generating another pathway for the production of O_3 (equations 2.11g - 2.11i). This set of reactions leads to net formation of two molecules of O_3 and one molecule of CH_2O and water vapour (equation 2.11j).

2.1 Tropospheric ozone chemistry and dynamics

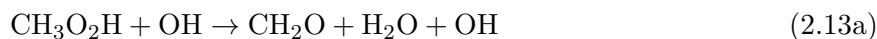


2.1.1.4.1.2 Low NO_x condition

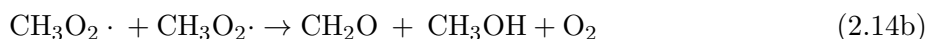
At low NO_x concentrations, CH_4 is oxidized by OH radicals to yield methyl hydroperoxide ($\text{CH}_3\text{O}_2\text{H}$) (equation 2.12c). During this condition, there is the loss of RO_2 and a subsequent loss of OH radicals (equations 2.12a to 2.13b)



$\text{CH}_3\text{O}_2\text{H}$ in equation 2.12d can also be oxidized as shown in equations 2.13a - 2.13b.



CH_3O_2 molecules can collide with each other to either form methoxy radicals (CH_3O) or methanol (CH_3OH) and CH_2O , with the release of oxygen as shown in equations 2.14a & 2.14b.



2. CHEMISTRY AND DYNAMICS OF OZONE

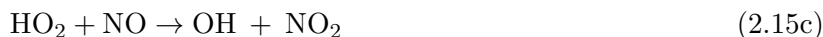
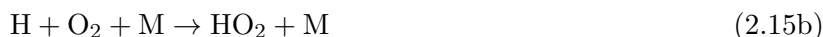
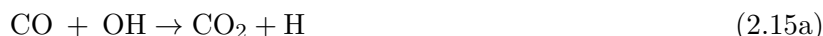
However, $\text{CH}_3\text{O}_2\text{H}$ and CH_3OH are partly removed from the atmosphere by dry deposition, thus reducing the total yield of CH_2O from the oxidation of CH_4 . The major photochemical loss processes of CH_2O in the remote atmosphere are photolysis and oxidation by OH radical as described by equations 2.6a - 2.7b.

2.1.1.4.2 Oxidation of Carbon monoxide

Tropospheric O_3 can also be produced from the oxidation of CO by the OH radical 2.15a - 2.16d. Besides the production of CO from the photolysis and oxidation of CH_2O , it is also produced from the incomplete combustion of organic materials.

2.1.1.4.2.1 High NO_x condition

At high NO_x concentrations, O_3 is produced via equations 2.15a to 2.15f



2.1.1.4.2.2 Low NO_x condition

In a low NO_x environment, despite the presence of CO, O_3 is lost in the presence of hydroxy radicals as shown in equations 2.16a to 2.16d:

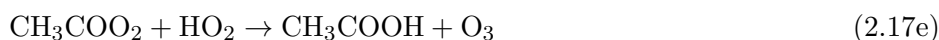
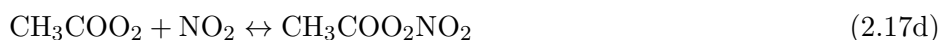
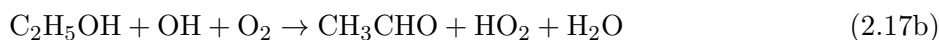
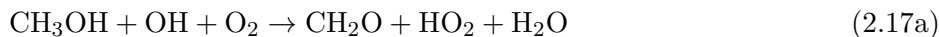


2.1.1.4.3 Photolysis and oxidation of other VOCs

In the upper troposphere, O_3 production is influenced by the photolysis and oxidation of VOCs such as alcohol and acetone (CH_3COCH_3), leading to the formation of HO_x , peroxy and alkoxy radicals

2.2 Stratospheric ozone chemistry and dynamics

(equations 2.17a - 2.17c). These reactions have the capability of changing the partitioning of odd-nitrogen between NO_x and reservoir species such as HONO and PAN (Singh *et al.*, 1994, 1995).



2.1.2 Transport of O_3 from the stratosphere

Although there has been an observed increase in the photochemical production of tropospheric O_3 due to enhanced emissions of anthropogenically produced O_3 and its precursor species (Marenco *et al.*, 1994; Shindell *et al.*, 2006b; Volz & Kley, 1988), the tropospheric O_3 budget is also influenced by downward transport from the stratosphere during the STE events and deposition to the surface (Collins *et al.*, 2003; Ganguly & Tzanis, 2011; Holton *et al.*, 1995; Sprenger *et al.*, 2007). Previous studies showed that STE is one of the important sources of tropospheric O_3 (Collins *et al.*, 2003; Roelofs *et al.*, 2003), but it is still uncertain as to how much it contributes to tropospheric O_3 budget. For example, comparisons between global models show that STE fluxes vary by a factor of 4 (340 - 1440 $\text{Tg}(\text{O}_3) \text{ yr}^{-1}$) (Wild, 2007) while observations show different estimates of STE fluxes (510 $\text{Tg}(\text{O}_3) \text{ yr}^{-1}$ (450–590) (Gettelman *et al.*, 1997), $550 \pm 140 \text{ Tg}(\text{O}_3) \text{ yr}^{-1}$ (Olsen *et al.*, 2001)).

2.2 Stratospheric ozone chemistry and dynamics

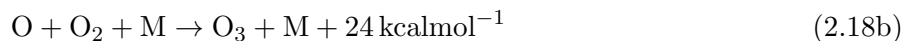
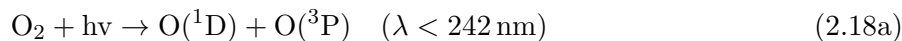
The stratosphere is characterized by rapid horizontal mixing of gaseous components and strong coupling between dynamical, radiative and chemical processes, such that any changes in the stratospheric circulation can have general effects on the atmospheric circulation and in particular on the tropospheric weather and climate.

2.2.1 Stratospheric ozone production and loss cycles

The production of O_3 in the stratosphere is mainly due to the photolysis of O_2 at UV wavelengths of less than 242 nm ($\lambda < 242 \text{ nm}$). The understanding of stratospheric O_3 chemistry began with

2. CHEMISTRY AND DYNAMICS OF OZONE

the steady-state photochemical model proposed by Chapman in 1930. The model is based on oxygen-only reactions as shown in equations 2.18a - 2.18f,



Where M is a third body collision partner that absorbs the excess kinetic energy. The reactions in 2.18a - 2.18f can be classified into three different groups namely:

1. Those that produce odd-oxygen (the combination of [O] and [O₃]), e.g., equation 2.18a
2. Those that balance the ratio of atomic oxygen (O) and O₃ concentrations, e.g., equations 2.18b and 2.18c.
3. Those that destroy odd oxygen, e.g., equations 2.18d – 2.18f.

The production mechanism for O₃ can be described by combining equations 2.18a and 2.18b to give equation 2.19c.



At steady state, the rate of creation of O₃ from three body collisions will be equal to the rate of photodissociation of O₃ by sunlight as expressed in 2.20,

$$K_{(o,o_2)}[\text{O}][\text{O}_2][\text{M}] = J_{o_3}[\text{O}_3]. \quad (2.20)$$

Where the brackets [] around a chemical symbol indicate the concentration of the chemical in molecules cm⁻³, K is the reaction rate coefficient in cm⁶ molecule⁻² sec⁻¹ and J is the photodissociation coefficient in molecule⁻¹ sec⁻¹.

Apart from the O_x catalytic chemical loss cycle, additional loss cycles are attributed to highly reactive catalysts that are primarily produced in the stratosphere by photolytic decomposition. Some of these species may also be transported from the troposphere into the stratosphere. An example of catalytic O₃ destruction cycle in the stratosphere is illustrated by equations 2.21a - 2.21c,

2.3 Upper troposphere and lower stratosphere (UT/LS)



Where X represents a catalyst such as HO_x (Bates & Nicolet, 1950), NO_x (Crutzen, 1970; Johnston, 1971) and halogen species (e.g., Cl_x and Br_x) (Rowland & Molina, 1975; Stolarski & Cicerone, 1974). HO_x are mainly generated from the decomposition of CH₄ and H₂O while NO_x are generated from N₂O produced in the biosphere. Sources of N₂O in the troposphere include fertilizers, oceans and soil. Cl_x and Br_x are mainly by-products of Freons and Halons, respectively, which are anthropogenic. The catalytic cycles involving Br_x are more efficient than those of Cl_x but bromine compounds are much less abundant in the atmosphere than the Cl compounds.

The efficiency of the loss cycles varies with altitude, latitude and season. The variation in either the rate of O₃ production, the strength of stratospheric circulation or the rate of chemical O₃ loss may alter the distribution of O₃ in the stratosphere. This can lead to its depletion or loss. O₃ depletion, which is the decrease in local concentration of TOZ over time, occurs due to either a chemical or dynamical process or both. The depletion of stratospheric O₃ layer results to a phenomenon called the O₃ hole, which occurs mostly at the polar regions (e.g., Farman *et al.*, 1985; Solomon *et al.*, 1986). The catalytic O₃ destruction cycle involving Cl_x became an important issue in stratospheric chemistry in the 1980s when Antarctic O₃ hole was discovered (Farman *et al.*, 1985).

2.3 Upper troposphere and lower stratosphere (UT/LS)

The tropopause is not a hard boundary but acts as a lid that opposes massive exchange of air between the convectively dominated and unstable troposphere and the stably stratified stratosphere. Between these two spheres is a transition zone referred to as the upper troposphere and lower stratosphere (UT/LS). The UT/LS is located in the region of ± 5 km around the tropopause (Gettelman *et al.*, 2011), and lies roughly between 5 and 20 km depending on season and latitude.

The UT/LS is a highly coupled region where the concentration of many trace constituents or greenhouse gases of tropospheric or stratospheric origin (such as H₂O and O₃) is controlled by both dynamical and chemical processes (Holton *et al.*, 1995). This leads to the sensitivity of the UT/LS to climate change (Shepherd, 2002). The interaction of greenhouse gases and particles in this region has a strong influence on the Earth's radiative balance (Foster & Shine, 1997). Highly reactive particles such as cirrus clouds, which can facilitate heterogeneous and multiphase reactions

2. CHEMISTRY AND DYNAMICS OF OZONE

are formed in the UT/LS region. The UT/LS exhibits some distinct characteristics which influence the Earth's climate. For instance, the coldest part of the lower atmosphere, which occurs as a result of dynamics and radiative cooling, lies in the UT/LS region. The low temperatures in this region do not only have influence on the dynamical evolution of the stratosphere but also affect the course of chemical reactions as well as photochemical processes, thereby making the distribution of trace gases relevant to climate change sensitive to radiative forcing (Shepherd, 2007).

2.3.1 Stratosphere-Troposphere Exchange

Stratosphere-Troposphere Exchange (STE) involves the transport, mixing and exchange of air between the troposphere and stratosphere, which may be important for the chemical balance of the atmosphere. These transport processes occur with different strengths and by a number of different mechanisms (Holton *et al.*, 1995; Toumi *et al.*, 1994). The STE process can either be shallow or deep, depending on whether the events connect points within the tropopause or outside the tropopause (Stohl *et al.*, 2003; Wernli & Bourqui, 2002). The understanding of the stratosphere-troposphere transport of O₃ is important for the analysis of the overall tropospheric O₃ climatology, its budget and long-term trends (Lin *et al.*, 2000; Naja *et al.*, 2003; Terao *et al.*, 2008). STE is one of the key components that controls the concentrations and distributions of O₃, water vapour, and hydroxyl radicals (Levy, 1971), and determines the chemical composition of both the stratosphere and the troposphere (Cristofanelli *et al.*, 2003; Roelofs *et al.*, 2003; Seo & Bowman, 2001). The troposphere and stratosphere have different physical and chemical properties. For example, the troposphere has low O₃ number densities, high water vapour number densities, it is turbulent and unstable due to decrease in temperature with altitude, whereas the stratosphere has high O₃ number densities, low water vapour number densities and it is relatively stable due to increase in temperature with height. As a result of the differences in the physical and chemical properties between these two regions, exchange between them affect their radiative flux balance (e.g., Holton *et al.*, 1995; Ramaswamy *et al.*, 1992; Toumi *et al.*, 1994), and also plays a significant role in the radiative forcing of the global climate (Holton *et al.*, 1995). STE is a vital process in climate predictions (Collins *et al.*, 2003; Sudo *et al.*, 2003) due to the effect of the residence time and exchange rates between the troposphere and stratosphere.

An increase or a decrease in STE can significantly change the composition of both the stratosphere and troposphere (Levy *et al.*, 1980). The atmospheric species at the lower troposphere or stratosphere influence the atmospheric behaviour of the UT/LS region. For example, the near-surface emissions of gases, particles and almost all the materials necessary for photochemical production of O₃ in the UT have their sources or origin in the lower troposphere. These components are transported via synoptic scale uplift (warm conveyor belts) and deep convection through the

2.3 Upper troposphere and lower stratosphere (UT/LS)

UT to the LS, where they can be converted to more reactive gases and initiate the chemistry responsible for the depletion of stratospheric O_3 (e.g., WMO, 2007). Conversely, the downward transport constitutes a significant input of O_3 and other reactive species into the troposphere (e.g., Hoskins *et al.*, 1985; Levy *et al.*, 1980). This constitute the main removal mechanism for many stratospheric species, including the halogen gases that were initially transported from the surface or at some altitudes, which play vital role in O_3 depletion (Tilmes *et al.*, 2009, 2012). The downward transported species can remain in the troposphere for some time before they are lost via wet and dry deposition processes. In the stratosphere, the fraction of these substances depends mainly on the rate of chemical break down versus the time taken for the chemical to arrive in the stratosphere.

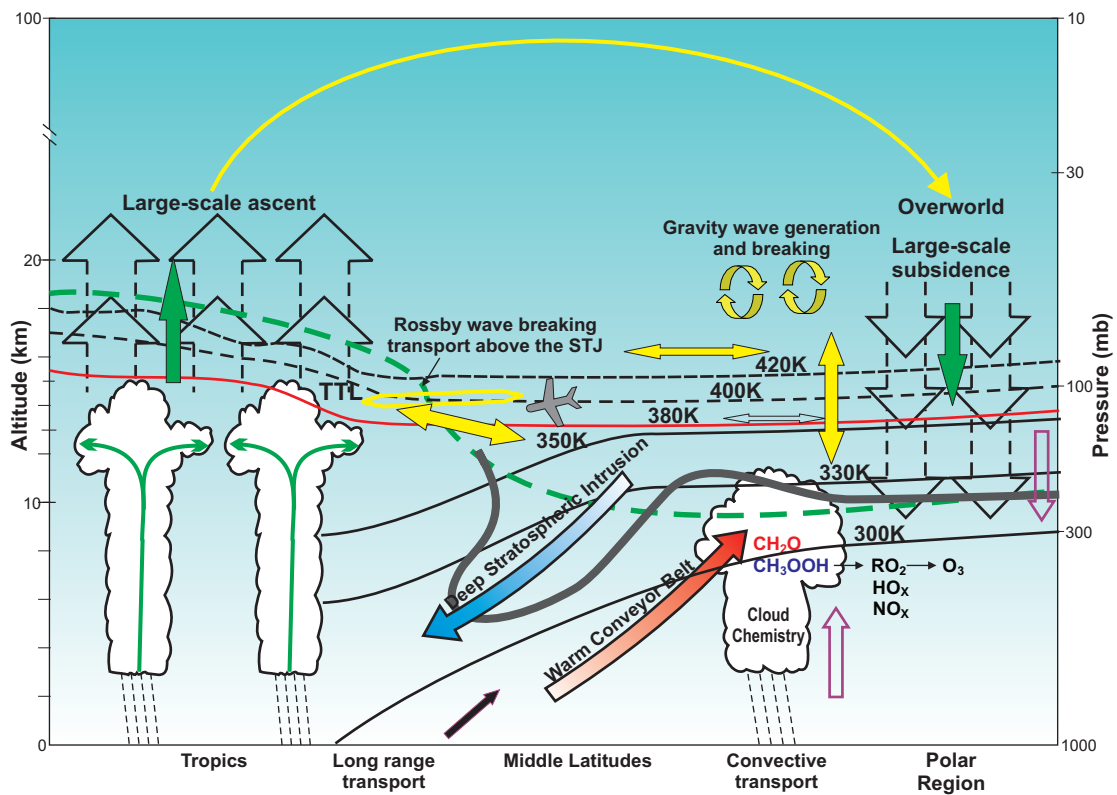


Figure 2.1: Illustration of the lower atmosphere, showing the relevant dynamical aspects of the stratosphere-troposphere exchange (STE) that influences the structure of the UT/LS, modified after Holton *et al.* (1995) and Hintsa *et al.* (1998).

To analyze the transport and mixing processes depicted in figure 2.1, isolines of constant potential temperature are used as vertical coordinate. Atmospheric flow tends to follow isentropes or routes over which entropy is conserved. With the isentropes, the lower atmosphere can be divided into three different parts, such as the overworld, middleword, and underworld (Holton *et al.*, 1995; Hoskins, 1991).

2. CHEMISTRY AND DYNAMICS OF OZONE

The overworld is the region of the atmosphere that lies entirely within the stratosphere, that is, where the potential temperature is above 380 K. Due to quasi-horizontal isentropic transport, the air parcels within the overworld cannot reach the troposphere directly, except by descent through diabatic cooling across isentropic surfaces to the lower stratosphere and troposphere. Conversely, isentropes in the underworld are entirely within the troposphere, therefore tropospheric air parcels have to rise diabatically to reach the stratosphere.

The middleword is characterized by isentropes that connect the tropical troposphere with the extratropical stratosphere. Since these isentropes cross the extratropical tropopause (see, Hoskins, 1991), there is the possibility of bidirectional exchange between both parts of the middleword (Holton *et al.*, 1995). The stratospheric part of the middleword, referred to as the lowermost stratosphere is located between the tropopause and the 380 K isentropes, thus, serving as a convergence zone between the tropospheric and stratospheric air (Holton *et al.*, 1995; Hoskins, 1991). The transport from the troposphere to the lowermost stratosphere causes strong gradients for many chemical species above the tropopause. The lowermost stratosphere differs from the overlying stratospheric overworld in the way surfaces of equal potential temperature cross the tropopause, thereby allowing isentropic transport between the troposphere and the lowermost stratosphere (Dessler *et al.*, 1995).

The transport of trace gases and their precursors from either the troposphere or the upper stratosphere to the lower stratosphere is strongly determined by both large and small scale transport processes, which play major roles in determining the chemical composition and radiative properties of the troposphere and stratosphere. The processes that govern the exchange of air masses between the stratosphere and the troposphere involve a balance of the net upward mass flux from the tropical troposphere to the stratosphere (upward green arrow in figure 2.1), and a net downward flux from the extratropical stratosphere to the troposphere (downward green arrow in figure 2.1). This processes involve vertical mixing of trace gases into the tropical tropopause layer (TTL), which couples the Hadley circulation in the tropical troposphere with the much slower Brewer-Dobson circulation (BDC) (Brewer & Roy, 1949) in the stratosphere (Atticks & Robinson, 1983; Fueglistaler *et al.*, 2009; Plöger *et al.*, 2009). The vertical exchange between the troposphere and stratosphere takes hours to days (Fischer *et al.*, 2003; Poulida *et al.*, 1996). STE is related to the general atmospheric meridional circulation that involves the upward transport of air in the tropics to the stratosphere, where it travels poleward and downward at the midlatitudes and in polar regions, which is described by the BDC.

2.3.2 Brewer-Dobson circulation (BDC)

The large-scale upwelling in the tropical stratosphere, poleward transport and downwelling in the extratropical stratosphere is described by the so-called BDC (yellow curved arrow in figure 2.1)).

2.3 Upper troposphere and lower stratosphere (UT/LS)

The BDC is based on model studies conducted based on water vapour measurements (Brewer, 1949) and O₃ column measurements (Dobson, 1956). BDC is driven by breaking Rossby (planetary) and gravity waves that are induced by extratropical disturbances in the middle and upper stratosphere, which are called extratropical wave pump (Collins *et al.*, 2003; Holton *et al.*, 1995; Seo & Bowman, 2001).

During the STE events, relatively dry and O₃-rich air masses, with a higher potential vorticity are transported from the stratosphere into the troposphere via the BDC mechanism. Due to this large scale circulation in the stratosphere, O₃, CFCs and other trace gases are transported poleward and downward in the extratropics, thereby leading to low O₃ concentration within the source region in the tropical lower stratosphere and high O₃ concentration within the middle and polar lower stratosphere. In the lower stratosphere, the O₃ distribution is mainly dominated by transport processes because of its photochemical lifetime, which is up to a few months (Sankey & Shepherd, 2003; Shepherd, 2007).

The equator-to-pole hemispheric BDC consists of a relatively shallow cell in the lowermost stratosphere that extends from the tropics to the mid-latitudes and a deeper cell that extends to the polar latitudes (Birner & Bönisch, 2011). While the shallow cell is driven primarily by both breaking equatorial planetary waves and synoptic-scale waves (e.g., Held & B. J. Hoskins, 1985; Zhou *et al.*, 2012), the deeper cell is driven by planetary-scale wave breaking in the extratropical stratosphere (e.g., Haynes *et al.*, 1994; Holton *et al.*, 1995; Zhou *et al.*, 2012). Planetary waves are mainly generated in the troposphere and propagate upward to the stratosphere (Holton *et al.*, 1995) where they aid in shaping the O₃ hole (Austin & Butchart, 1992; Solomon, 1999) and its recovery (e.g., Li *et al.*, 2009; Oman *et al.*, 2009), through their effect on the polar vortex and the BDC. Since these planetary waves require westerly winds to propagate upward, the BDC only occurs in the winter hemisphere, when the stratospheric polar vortex has formed. The BDC has great impact on the global climate by influencing temperatures and concentrations of trace gases in the entire stratosphere (e.g., Butchart *et al.*, 2010; Li *et al.*, 2008).

The diabatic vertical bidirectional mixing on isentropes across the extratropical tropopause is associated with both synoptic scale baroclinic eddies (Chen, 1995; Dethof *et al.*, 2000) and dynamical processes. These synoptic and mesoscale processes occur at the downward part of the BDC in the extratropics, where net irreversible transport from the stratosphere to the troposphere takes place. This forms the key features of cross-tropopause exchange especially in the subtropics and polar region, where the tropopause folds in the vicinity of the subtropical and polar jet streams (Danielsen, 1968; Shapiro, 1980; Sprenger *et al.*, 2003). These processes contribute to the seasonal variability of the middleworld, thus affecting the coupling between the TTL and the subtropical jet streams to the mid-latitudes and polar regions. These localized exchange processes between the

2. CHEMISTRY AND DYNAMICS OF OZONE

troposphere and the stratosphere can lead to net irreversible mixing in the extratropical UT/LS and therefore, contribute to the formation of the mixing layer around the extratropical tropopause (Dessler *et al.*, 1995; Fischer *et al.*, 2000; Hoor *et al.*, 2004). This mixing layer is characterized by several factors, including the photochemical processes of both the stratosphere and the troposphere, change in the gradient of climate relevant trace gases and large seasonal variability that is more pronounced in summer than in winter (Brioude *et al.*, 2008; Fischer *et al.*, 2000).

2.3.3 The synoptic and mesoscale processes

Synoptic and mesoscale processes play vital roles in the exchange of air masses between the stratosphere and the troposphere. These processes include: Tropopause folds (Holton *et al.*, 1995; Shapiro, 1980), cutoff lows (Sprenger *et al.*, 2007; Wirth, 1995), filamentation and fragmentation of stratospheric streamers (Appenzeller & Davies, 1992; Sprenger *et al.*, 2007), thunderstorms and mesoscale convective systems (e.g., Poulida *et al.*, 1996), and breaking gravity waves (Lamarque *et al.*, 1996).

2.3.3.1 Tropopause folds

Tropopause folds are associated with frontal regions that are characterized with horizontal boundaries between air masses where the tongue of the stratospheric air can intrude into the troposphere. The flow in a frontal region typically occurs either along the front or across the front. Ageostrophic flow, which occurs along the front on the cyclonic (poleward) side of the jet streams, creates a cross frontal movement of closed circular loops. This leads to frequent dynamical instability due to high levels of vertical shear across the boundary of the tropopause folds, which contains elevated potential vorticity (Rao *et al.*, 2008). It is in this region that most of the intrusion of stratospheric air into the troposphere along strongly tilted isentropes occurs (Appenzeller & Davies, 1992; Holton *et al.*, 1995; Seo & Bowman, 2002). Measurements have shown that high O₃ content is associated with regions of tropopause folds during spring and early summer (Van Haver *et al.*, 1996) and also that not all baroclinic systems and tropopause folds transport the same amount of O₃ into the troposphere (Olsen *et al.*, 2002). Records have also shown that tropopause folds exhibit an annual cycle, with smaller frequency during summer than every other season (Elbern *et al.*, 1998; Sprenger *et al.*, 2003).

2.3.3.2 Cutoff lows

Cutoff lows are isolated cyclonic vortices in the upper level flow, which can be identified by isolated regions of high PV (Price & Vaughan, 1993). They are conceived as polar air masses that are

2.3 Upper troposphere and lower stratosphere (UT/LS)

subsequently cut off as they are advected toward the tropics (Hoskins *et al.*, 1985). Cutoff lows occur more frequently during summer in the NH due to the weakening of the mid level westerlies (Price & Vaughan, 1992) and during winter in the SH (Fuenzalida *et al.*, 2005). The weak seasonality in the SH implies that other factors could be responsible for the occurrence of cutoff lows. The location of the jet stream determines the location of cutoff lows as they are either formed equatorwards of the jet or as an extension of the jet stream (Price & Vaughan, 1993).

There is a strong link between cutoff lows and tropopause folds. In the presence of intense upper level frontogenesis, tropopause folds are formed at the edge of cutoff lows (Ancellet *et al.*, 1994). The only difference is that while cutoff lows emphasize the horizontal structure in which stratospheric intrusion may occur, tropopause folds accentuate on the vertical structure.

2.3.3.3 Filamentation and fragmentation of stratospheric streamers

Downward transport of air masses from the lowermost stratosphere into the troposphere can result from small scale processes associated with anticyclones and filamentation. The stratospheric or tropospheric potential vorticity streamers are narrow filaments of high or low potential vorticity air that can extend far toward the equator or pole, respectively, which can eventually break up into distinct high or low PV cutoffs. Filamentation by synoptic scale-eddies correlates with stirring processes and occurs on a relatively short timescale (Stohl *et al.*, 2001). In large-scale cyclonic and anticyclonic disturbances at the extratropical troposphere, the intruding stratospheric air is stirred quasi-adiabatically with the surrounding tropospheric air (Mahlmann, 1997; Zierl & Wirth, 1997). This causes the intruding stratospheric air to form filamentary structures that appear for instance, as laminae in O₃ profiles (Dobson, 1973; Stohl & Trickl, 1999). These filamentary structures are transported through advection to the upper troposphere and can even descend deeply into the mid and lower troposphere (Stohl & Trickl, 1999). The deep ascent of stratospheric air can generate severe weather features, such as high wind speeds at the surface (Goering *et al.*, 2001) before they are destroyed by turbulence and convection.

2.3.3.4 Thunderstorms and mesoscale convective systems (MCS)

Mesoscale convective systems (MCS) are collections of thunderstorms. MCS have a spatial coverage of 20 - 500 km and temporal scale of 3 - 12 hours, and can be classified as either Mesoscale Convective Complexes (MCC) (Corfidi *et al.*, 1996; Maddox, 1980), based on their circular eccentricity or as mesoscale convective vortices (MCV) (Davis & Trier, 2007; Menard & Fritsch, 1989) based on their linear eccentricity when observed from satellite instruments. During thunderstorms and MCS processes, trace gases are transported from the troposphere to the lower stratosphere (Hintsa *et al.*,

2. CHEMISTRY AND DYNAMICS OF OZONE

1998; Poulida *et al.*, 1996; Ray *et al.*, 1999). In the extratropics, these transport processes occur through diabatic means in warm conveyor belts (Stohl *et al.*, 2001; Wernli & Bourqui, 2002; Zierl & Wirth, 1997), which are counter-balanced by the large-scale descent from the overworld (Haynes *et al.*, 1994). The lower stratosphere is highly stable, so to penetrate deep into the stratosphere, an increase in potential temperature is needed.

2.3.3.5 Breaking gravity waves

Gravity waves (Gossard & Munk, 1954; Queney, 1948; Sawyer, 1959) are wave motions in a stratified fluid that balance the downward acting gravity forces with the upward acting buoyant forces in a vertically displaced fluid parcel. As the wave propagates upward, its amplitude increases due to exponential decrease in atmospheric density with height before breaking. At the breaking point the amplitude is so large that the atmospheric transformation attained becomes irreversible such that the waves deposit energy and momentum into the mean flow. This contribute mainly to atmospheric circulation as they aid in the transport of energy away from their source region. For instance, transport and mixing processes due to inertia-gravity waves in the lower stratosphere alter the mean stratospheric temperature locally with amplitudes up to 10 K, which can lead to the formation of PSCs at the polar latitudes during winter months (Buss *et al.*, 2004; Dörnbrack *et al.*, 2002).

SECTION II

Methodology

Chapter 3

The tropopause and its role

The existence of the tropopause has been known for over a century (e.g., Hoinka, 1997). Understanding its position is very important in the retrieval of tropospheric O₃, as it generally influences O₃ amount (Vaughan & Price, 1991), as well as the different parameters involved in the study of tropospheric O₃. The tropopause plays a crucial role in the understanding of the dynamics of the atmosphere (Haynes *et al.*, 2001), as well as in the study of STE processes (Holton *et al.*, 1995; Randel *et al.*, 2004). It is a good indicator of climate change because its trend can be easily detected over shorter time-scales compared to that of surface temperature.

3.1 Concepts of the tropopause

The tropopause marks the boundary between the well mixed troposphere and the stably stratified stratosphere. This boundary is primarily characterized by the change in temperature. While the troposphere is characterized by decreasing temperature with height, the stratosphere exhibits increasing temperature with height (Figure 1.1). This creates a great difference in stability and potential vorticity. In fact, the large amount of O₃ produced in the stratosphere is inhibited from entering the troposphere due to a sharp increase in atmospheric stability at the tropopause. The tropopause can also be observed by the strong gradients in trace gases, such as O₃, CH₄, H₂O, and Hydrogen Fluoride (HF). The tropopause can be referred to as the cold-trap because rising water vapour and warm air masses are trapped in this region of the atmosphere.

The height of the tropopause varies with the amount of solar energy that reaches the Earth. In a zonal-mean sense, the tropopause height decreases from the tropical region toward the polar regions (Hoinka, 1998). For instance, the tropical tropopause is roughly at ~ 18 km and slopes down toward the polar regions at ~ 7 km. Increase in tropopause heights are associated with warming of the troposphere and a cooling of the stratosphere, hence it is an essential indicator of

3. THE TROPOPAUSE AND ITS ROLE

global climate change (e.g., Randel *et al.*, 2000; Santer *et al.*, 2003b, 2004). The primary cause for its observed increase has been found to be due to increase in well-mixed greenhouse gases (e.g., Santer *et al.*, 2004). It may also be controlled by interacting processes such as variation in radiation, baroclinic eddies and the stratospheric mean meridional circulation. While the height of the tropical tropopause can be determined by deep convection (Reid & Gage, 1981), the height of the extratropical tropopause can be determined by baroclinic waves, cyclones and anticyclones (Held, 1982; Lindzen, 1993).

There are several concepts that can be used to define the tropopause, including the temperature lapse rate (thermal tropopause) (WMO, 1986), potential vorticity (PV) gradient (dynamical tropopause) (Reed, 1955; Shapiro, 1978) and O₃ gradient and values (chemical tropopause) (Bethan *et al.*, 1996; Zahn & Brenninkmeijer, 2003). Each of the different definition of the tropopause may not be applicable globally due to the characteristics of the tropopause.

The thermal based criterion works well in the tropics but fails in the extratropical and polar regions. It is not able to identify the tropopause during polar nights. During polar winter, temperature may keep decreasing into the stratosphere without any inversion, thus making it difficult to appropriately define the thermal tropopause (Zangl & Hoinka, 2001). In addition, studies have shown that the arctic thermal tropopause can be located at ~ 300 hpa (8 - 10 km) throughout the year (Highwood *et al.*, 2000), but during austral winter and spring, the temperature can continue to decrease with height up to about 20 km in the southern hemisphere polar vortex, thus inhibiting proper definition of the thermal tropopause (Highwood *et al.*, 2000; Roscoe, 2004). Secondly, the tropopause can also become deformed in the vicinity of the polar and subtropical jet streams through diabatic ascent or descent due to convection or stratospheric intrusion, respectively. This occurs when the jet becomes strong and the associated front at low levels increases, causing it to fold down to about 550 hpa or even lower, behind a well defined cold front. Since the vertical temperature gradient is not a conserved quantity, the thermal criterion will not be able to characterize the different air masses, thereby leading to multiple or inaccurate computation of the tropopause heights (Pan *et al.*, 2004; Wirth, 2001). The PV based criterion gives reliable tropopause values at the extratropics but fails at the tropics because the PV surfaces (isentropes) become vertical close to the Equator (potential vorticity becomes zero at the equator). Similarly, the definition based on tracer gradients is ill-poised mostly in regions where there is strong mixing. There is great difficulty in translating the chemical tropopause in tracer-space back into physical height as it does not produce a clear peak.

3.2 Determination of the tropopause

In this thesis, a similar approach as introduced by Zangl & Hoinka (2001) is followed in the determination of the global tropopause from the European Center for Medium Range Weather Forecasts (ECMWF) reanalyses (ERA)-Interim data, which uses cycle 31R1 of the Integrated Forecasting System (IFS)(Dee *et al.*, 2012). The approach involves the combination of both the thermal and dynamical tropopauses. The ECMWF ERA-interim data comprise three-dimensional fields of pressure, temperature, and wind vectors on a latitude/longitude grid of 1.5° resolution with 91 levels and 4 analysis times (00, 06, 12, 18) daily. It is advantageous to use ECMWF ERA-interim data because it has been directly interpolated from full vertical resolution model level data to the surface. Otherwise, error could be introduced when using the dynamic tropopause criterion.

3.3 Thermal Tropopause

The conventional definition of the tropopause is based on the thermal structure of the atmosphere. According to the World Meteorological Organization (WMO), the tropopause is defined as the lowest level where the temperature lapse rate decreases below 2 K km^{-1} , and the lapse rate averaged between this level and all higher levels within 2 km has to remain below 2 K km^{-1} (WMO, 1957, 1986). The lapse rate, Γ , is the change in temperature with respect to altitude,

$$\Gamma = -\frac{\partial T}{\partial z}, \quad (3.1)$$

where T is the parcel temperature and z is the altitude above the surface of the Earth (Wallace & Hobbs, 2006). To determine the thermal tropopause, the vertical temperature gradient (Γ) is first calculated between each two adjacent model levels i and $i + 1$ as follows:

$$\Gamma_{i+1/2} = \frac{T_{i+1} - T_i}{Z_{i+1} - Z_i}. \quad (3.2)$$

Assigning equation 3.2 to the mean geometric height of the model levels will lead to the determination of the centered difference as shown in equation 3.3,

$$Z_{i+1/2} = \frac{Z_{i+1} + Z_i}{2}. \quad (3.3)$$

The tropopause search criterion is set at between $\sim 2 \text{ km}$ and 90 hPa , to avoid the influence of surface inversion. In the next step, the the lowest level that fulfills the conditions in equations 3.4 and 3.5 are checked.

$$\Gamma_{i+1/2} \geq \Gamma_{tp}, \quad (3.4)$$

3. THE TROPOPAUSE AND ITS ROLE

$$\Gamma_{i-1/2} < \Gamma_{tp}, \quad (3.5)$$

where $\Gamma_{tp} = -2 K km^{-1}$ is the threshold value base on WMO thermal tropopause criterion (WMO, 1957). Equations 3.2 - 3.5 can be combined to determine the tropopause as follows:

$$Z_{tp} = \left(\frac{\Gamma_{tp} - \Gamma_{i+1/2}}{\Gamma_{i+1/2} - \Gamma_{i-1/2}} \right) (Z_{i+1/2} - Z_{i-1/2}) + Z_{i-1/2}, \quad (3.6)$$

where Z_{tp} is the height of the basic state tropopause. The following step involves the determination of the depth of the tropopause by searching for its pressure and temperature based on the following criteria, $Z_{tp} > Z_i$ and $Z_{tp} < Z_i$ as shown in equations 3.7 and 3.8 for the tropopause pressure and 3.9 and 3.10 for the tropopause temperature. To calculate the tropopause pressure, it is assumed that the logarithm of the pressure vary linearly with z (i.e., $z \approx \ln p$). Therefore, for $Z_{tp} > Z_i$, the tropopause pressure is given as,

$$P_{tp} = p_i \exp \left(\ln \left(\frac{p_{i+1}}{p_i} \right) \frac{Z_{tp} - Z_i}{Z_{i+1} - Z_i} \right), \quad (3.7)$$

and for $Z_{tp} < Z_i$, the tropopause pressure becomes,

$$P_{tp} = p_i \exp \left(\ln \left(\frac{p_i}{p_{i-1}} \right) \frac{Z_{tp} - Z_i}{Z_i - Z_{i-1}} \right). \quad (3.8)$$

Similarly, we can find the tropopause temperature as follows, for $Z_{tp} > Z_i$, tropopause temperature is given as,

$$T_{tp} = T_i + \Gamma_{i-1/2} (Z_{tp} - Z_i), \quad (3.9)$$

and for $Z_{tp} < Z_i$, the tropopause temperature is given as,

$$T_{tp} = T_i + \Gamma_{i+1/2} (Z_{tp} - Z_i). \quad (3.10)$$

In the last step, the height of the tropopause can be determined for all i for all higher levels within 2 km that should remain below $2 K km^{-1}$ ($0 < z_i - z_{tp} \leq 2 km$) by using the thermal tropopause criterion (WMO, 1957) as follows,

$$\frac{T_i - T_{tp}}{z_i - z_{tp}} > -2 K km^{-1}. \quad (3.11)$$

The height of the thermal tropopause varies depending on latitude and season. For instance, in the tropics, due to strong surface heating, the annual mean of the tropopause coincides roughly with an isentropic surface with a potential temperature of 380 K at a height of 15 - 18 km and slopes downwards at the extratropical regions close to a potential vorticity surface and further downwards toward the poles, where it may be at a potential temperature of 290 - 320 K and as low as 6 - 10 km due to less surface heating (Holton *et al.*, 1995; Seidel *et al.*, 2001).

3.4 Dynamic Tropopause

The definition of the dynamic tropopause is based upon stability criteria. The surface between the transition of tropospheric and stratospheric air masses is usually characterized by a sharp gradient of PV. A single PV surface within this gradient defines the tropopause. The usage of the PV criterion involves the consideration of the stability of the atmosphere, its density and circulation.

The potential vorticity in isentropic coordinates is given by:

$$P = -g(\zeta_{\Theta} + f)\frac{\partial\Theta}{\partial p}, \quad (3.12)$$

where P is the potential vorticity, g is gravitational acceleration, ζ_{Θ} is the relative isentropic vorticity, f is the Coriolis parameter, p is the pressure, and Θ is the potential temperature. Equation 3.12 shows that the potential vorticity consist of two terms, the component of absolute vorticity normal to an isentropic surface ($\zeta_{\Theta} + f$) and the static stability ($\frac{\partial\Theta}{\partial p}$), which corresponds to the dynamical and thermodynamical elements, respectively. Assuming that the ERA model levels are quasi-horizontal in the tropopause region, the hydrostatic form of PV in z can be expressed as,

$$P = \frac{1}{\rho} (fk + \nabla \times \nu) \cdot \nabla \theta, \quad (3.13)$$

where ρ is the density, k is the local vertical unit vector, ν is the horizontal wind vector. Similar to equations 3.2 and 3.3, the PV between each two adjacent model levels i and $i + 1$ can be calculated by first setting the centered differences as shown in equation 3.14,

$$Z_{i+1/2} = \frac{Z_{i+1} + Z_i}{2}. \quad (3.14)$$

Therefore, equation 3.13 can be reformed as follows,

$$\begin{aligned} P_{i+1/2} &= \left(\frac{R(T_i + T_{i+1})}{2\sqrt{P_i P_{i+1}}} \right) = - \left(\frac{\partial v}{\partial z} \right)_{i+1/2} \left(\frac{\Delta \theta}{\Delta x} \right)_{i+1/2} \\ &+ \left(\frac{\partial u}{\partial z} \right)_{i+1/2} \left(\frac{\Delta \theta}{\Delta y} \right)_{i+1/2} + \left(f + \frac{s_i + s_{i+1}}{2} \right) \left(\frac{\partial \theta}{\partial z} \right)_{i+1/2}, \end{aligned} \quad (3.15)$$

where Δ represents the centered horizontal differences and R is gas constant for air. Since the relative vorticity (ς) is one of the prognostic variables in a spectral model, it can be obtained directly. Similar to the approach available in the literature, a dynamical tropopause threshold (P_{tp}) of 3.0 PVU was used (1 PVU equals $1.0 \times 10^{-6} \text{ m}^2 \text{ s}^{-1} \text{ K kg}^{-1}$) (Highwood *et al.*, 2000; Hoerling *et al.*, 1991; Zangl & Hoinka, 2001) and a search for where equations 3.16 and 3.17 are fulfilled is established.

$$P_{i-1/2} < P_{tp}, \quad (3.16)$$

3. THE TROPOPAUSE AND ITS ROLE

$$P_{i+1/2} \geq P_{tp}. \quad (3.17)$$

The tropopause height is then set to,

$$Z_{tp} = Z_{i-1/2} + \left(Z_{i+1/2} - Z_{i-1/2} \right) \left(\frac{P_{tp} - P_{i-1/2}}{P_{i+1/2} - P_{i-1/2}} \right). \quad (3.18)$$

The dynamic tropopause is not a constant height or pressure but a level at which the gradients of potential vorticity on an isentropic surface are maximized. It is advantageous to use potential vorticity to define the tropopause because it provides information on both the dynamical and thermodynamical behavior of the tropopause. The dynamic tropopause is conserved in adiabatic, frictionless three-dimensional flow (see e.g., Hoskins, 1991). In other words, it is a material surface under conservative conditions (Stohl *et al.*, 2003; Wirth, 2001) and it is also invertible, thereby allowing the derivation of similar meteorological fields such as geopotential, wind, temperature and the static stability, when the potential temperature at the surface, the distribution of the PV and the boundary conditions are known. However, there are debates on which PV values best describe the dynamic tropopause. For example, WMO (1986) defines the dynamic tropopause to be at 1.6 PVU and several other studies defined their PV levels at the range of 1 to 5 PVU (e.g., Holton *et al.*, 1995; Sprenger *et al.*, 2003; Wernli & Bourqui, 2002). Records have shown that these definitions agree qualitatively on the large scale, but differ significantly when the location of the tropopause is investigated in detail (Pan *et al.*, 2004).

3.4.1 Combination of the Thermal and Dynamic Tropopauses

The combination of the dynamical and thermal tropopauses enabled a clear definition of the boundary between the troposphere and the stratosphere at all latitudes. For the tropics (i.e. $\pm 20^\circ$ latitude from the equator) the thermal criterion was applied and from the subtropics to the poles (latitudes higher than 30° in both hemispheres) the dynamical criterion was applied. In the transition region between the two regimes (20° - 30° in both hemispheres), the tropopause was linearly interpolated between the thermal and dynamic tropopause. Based on this, the deficiencies associated with each criterion and the properties of the air-mass in the transition region were accounted for. The derived tropopause heights were compared with the tropopause heights derived from ozonesonde temperature profile measurement.

3.5 Determination of tropopause height from ozonesonde temperature profile measurement

The tropopause heights from ozonesonde data were determined using the thermal definition of the tropopause described in section 3.3. Therefore, the lapse rate (Γ) was calculated using equation 3.19,

$$\Gamma_i = -\frac{T_{i+1} - T_i}{H_{i+1} - H_i}, \quad (3.19)$$

where T is the temperature, H is the altitude and i is the index. Concisely, the tropopause height computation start by setting a search range from 4 to 18 km . Starting from lower to higher altitude levels, the tropopause height is the first point where the vertical temperature gradient, $\frac{\partial T}{\partial z}$ exceeds $-2 K km^{-1}$ and the average lapse rate between this level and all higher levels within 2 km does not fall below $-2 K km^{-1}$. The search criteria is brought down to 4 km so as to account for the influence of high static stability, mostly during Antarctic winter (Bethan *et al.*, 1996).

Figure 3.1, shows a plot of the altitude against temperature for a sample temperature profile measured with an ozonesonde at Alert and interpolated on a 50 m grid. To minimize noise, the data is smoothed using a 5-point running mean filter. The fitting of the lapse rate involves iterating between three data points and fitting a straight line across them. The iteration is repeated until all the data are considered. Choosing the step-wise slope from the first point of iteration to the last point of iteration yield $N/2$ data points for fitting the lapse rate.

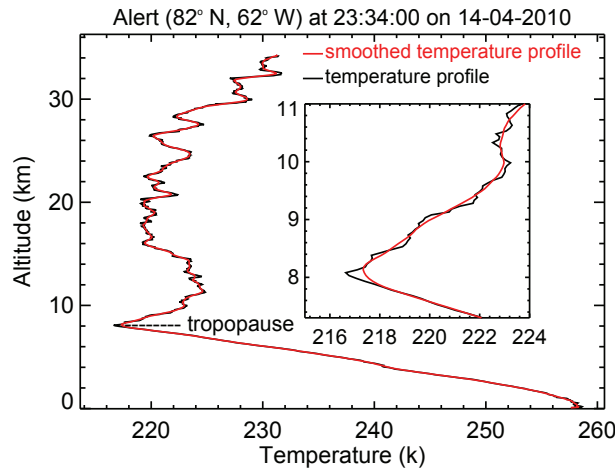


Figure 3.1: Temperature profile over Alert (82.50°N, 62.30°W) at 23:34:00 UTC on 14.04.2010: smoothed temperature profile (red) and original temperature profile (black), a typical tropopause height of about 9 km.

3. THE TROPOPAUSE AND ITS ROLE

3.6 Intercomparison of ECMWF and ozonesonde tropopause heights

Figures 3.2 to 3.7 show the comparison plots of the monthly mean tropopause heights from the temperature profile measurements of ozonesondes and collocated meteorological model data from ECMWF. The analysis show good agreement between both data sets with strong correlation, but slight variations in their amplitudes. The scatter plots on the right of each timeseries show a positive correlation with few scattered points, which are close to the mean in some regions. Over Alert (Figure 3.2), the tropopause height values derived from both ozonesonde and ECMWF show good agreement except between 2003 and 2006. In addition, ECMWF measurements show too low values around December 2006. Observation over Bratt's Lake (Figure 3.3), shows that the tropopause height data from both ECMWF and ozonesondes show different values before January 2005 but good agreement afterwards except in 2008 and 2009 where ECMWF values show maxima and between January and March 2011 where ECMWF tropopause height values are too low.

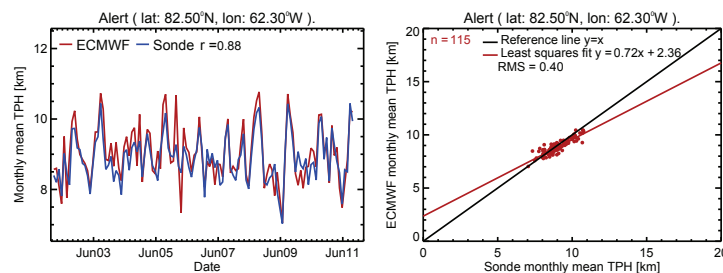


Figure 3.2: Comparison of monthly mean tropopause height time series in km between ECMWF (red) and ozonesondes (blue) over Alert (82.50°N, 62.30°W), from left to right: time series and scatter plot.

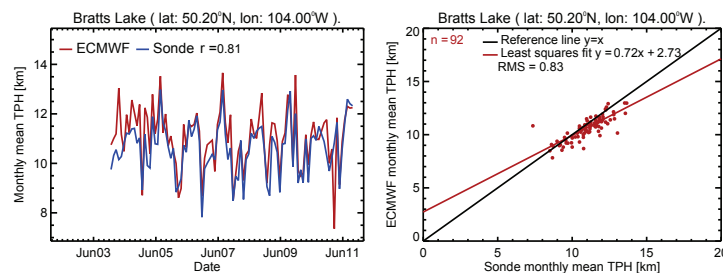


Figure 3.3: Same as Figure 3.2 but over Bratt's Lake (50.20°N, 104.00°W).

Above Barajas (Figure 3.4), measurements from ECMWF show higher values in late 2004 and early 2005 as well as in early 2007. Above Broadmeadows (Figure 3.5), Macquarie Island (Figure 3.6), and Marambio (Figure 3.7), the tropopause height values derived from both ECMWF reanalysis and ozonesondes measurements show good agreement but the peak values from ECMWF analysis are higher than those from ozonesondes in some months. The variability of less than 1.5 km with a relative uncertainty of less than 100 m is observed in all the stations investigated. A

3.6 Intercomparison of ECMWF and ozonesonde tropopause heights

relative difference with respect to ozonesondes for all considered stations is about 2 % as explicitly summarized in table 3.1.

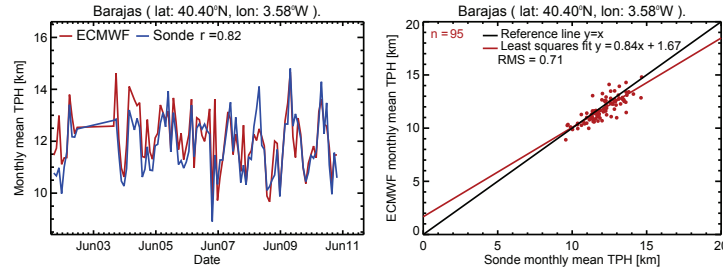


Figure 3.4: Same as Figure 3.2 but over Barajas (40.40°N, 3.58°W).

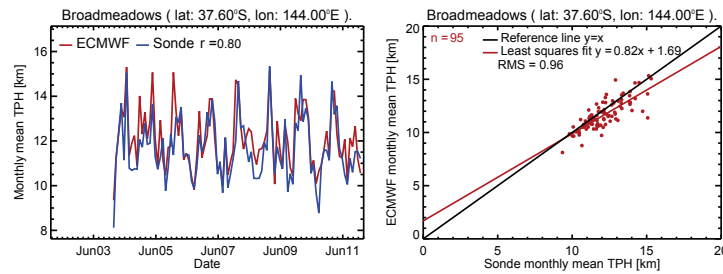


Figure 3.5: Same as Figure 3.2 but over Broadmeadows (37.60°S, 144.00°E).

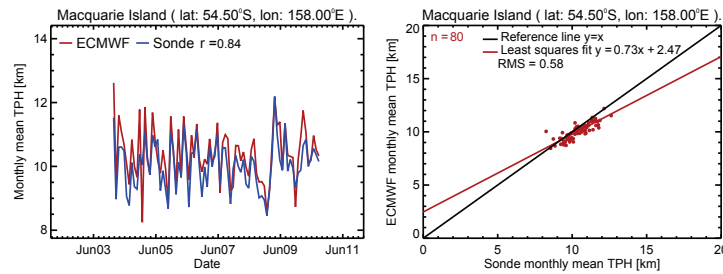


Figure 3.6: Same as Figure 3.2 but over Macquarie Island (54.50°S, 158.80°E).

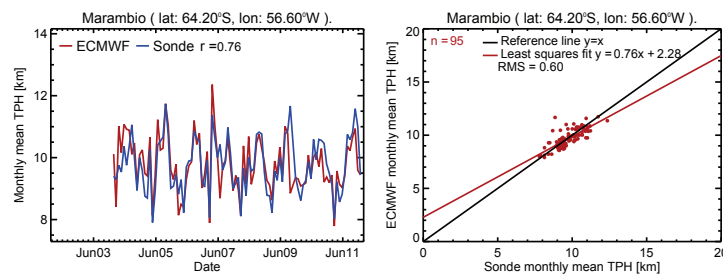


Figure 3.7: Same as Figure 3.2 but over Marambio (64.20°S, 56.60°W).

3. THE TROPOPAUSE AND ITS ROLE

Station name	No of points	Lat.[°N]	Long.[°E]	Mean value of trop. hgt. (ECMWF[km])	Mean value of trop. hgt. (Sondes[km])	Absolute diff.[km]	Relative diff.[km]
Alert	115	82.50	-62.30	9.02±0.79	8.89±0.65	0.13	0.01
Eureka	116	79.90	-85.90	8.84±0.81	8.52±0.92	0.32	0.04
Ny Aalesund	56	78.90	11.90	9.50±0.69	9.25±0.68	0.25	0.03
Resolute	106	74.70	-94.90	8.87±0.88	8.87±0.63	0.01	0.00
Sodankyla	56	67.30	26.60	10.19±0.86	9.86±0.72	0.33	0.03
Lerwick	99	60.10	-1.18	10.46±0.95	10.33±0.80	0.13	0.01
Churchill	111	58.70	-94.00	9.97±1.23	9.64±1.05	0.33	0.03
Stonyplain	115	53.50	-114.00	10.69±1.06	10.38±0.93	0.31	0.03
Goose Bay	113	53.30	-60.30	10.00±1.07	9.91±1.03	0.09	0.01
Legionowo	109	52.40	20.90	11.04±1.01	10.75±0.79	0.29	0.03
DeBilt	119	52.10	5.18	11.32±1.00	10.97±0.78	0.35	0.03
Valentia	63	51.90	-10.20	11.07±0.99	10.79±0.89	0.28	0.03
Uccle	102	50.80	4.35	11.36±0.72	10.98±0.59	0.38	0.03
Bratt's Lake	92	50.20	-104.00	11.05±1.20	10.63±1.06	0.42	0.04
Praha	39	50.00	14.40	10.80±0.61	10.38±0.49	0.41	0.04
Paramaribo	104	5.81	-55.20	16.77±0.44	16.41±0.43	0.37	0.02
Kelowna	93	49.90	-119.00	11.07±1.13	10.69±0.98	0.38	0.04
Payerne	103	46.40	6.57	11.54±0.83	11.18±0.74	0.36	0.03
Egbert	88	44.20	-79.70	11.56±1.57	11.23±1.58	0.32	0.03
Yarmouth	78	43.80	-66.10	11.63±1.58	11.39±1.39	0.25	0.02
Sapporo	25	43.00	141.00	11.05±1.68	11.17±1.99	-0.12	-0.01
Barajas	95	40.40	-3.58	12.06±1.09	11.79±1.11	0.26	0.02
Ankara	98	39.90	32.80	11.84±1.46	11.87±1.86	-0.03	-0.00
Wallops	105	37.80	-75.40	13.09±1.51	12.65±1.68	0.44	0.04
Huntsville	71	35.20	-86.50	13.87±1.55	13.54±1.59	0.33	0.02
Naha	38	26.20	127.00	16.67±0.60	16.25±0.39	0.43	0.03
Hong Kong	118	22.30	114.00	17.25±0.38	16.63±0.36	0.62	0.04
Sepang Airport	97	2.73	101.00	16.88±0.50	16.33±0.58	0.55	0.03
Hilo	103	19.40	-155.00	16.47±0.60	15.70±0.71	0.77	0.05
San Cristobal	40	0.90	-89.60	16.88±0.50	16.44±0.51	0.44	0.03
Neumayer	118	-70.60	-8.26	9.49±0.62	9.67±1.04	-0.18	-0.02
Ascension	63	-7.98	-14.40	16.89±0.43	16.40±0.50	0.50	0.03
Watukosek	82	-7.50	112.00	16.89±0.53	16.56±0.45	0.33	0.02
Syowa	21	-69.00	39.50	9.26±0.65	9.93±1.41	-0.66	-0.07
Marambio	95	-64.20	-56.60	9.79±0.87	9.76±0.87	0.03	0.00
Macquarie	80	-54.50	158.00	10.38±0.85	10.04±0.74	0.34	0.03
Natal	90	-5.42	-35.30	16.81±0.38	16.26±0.40	0.55	0.03
Lauder	83	-45.00	169.00	11.49±0.97	10.90±0.85	0.59	0.05
Broadmeadows	95	-37.60	144.00	12.08±1.32	11.64±1.37	0.44	0.04
Irene	61	-25.90	28.20	16.24±1.13	15.67±1.12	0.58	0.04
La Reunion	85	-21.00	55.40	16.81±0.37	16.14±0.65	0.67	0.04
Suva	31	-18.10	178.00	17.09±0.36	16.30±0.50	0.79	0.05
Samoa	91	-14.20	-170.00	16.83±0.48	16.37±0.48	0.46	0.03
Nairobi	72	-1.27	36.80	16.88±0.49	16.46±0.53	0.41	0.03
Mean value of tropopause height				12.66± 0.9	12.68± 0.9	0.31	0.02

Table 3.1: Comparisons of tropopause heights from ECMWF with some selected sondes stations over the entire time series (2002-2011).

3.7 Global zonal averaged ECMWF tropopause heights

Figure 3.8a shows the averaged tropopause heights for each year between 2002 and 2012. Similar patterns are observed throughout the entire period with little or no difference between each yearly global measurements. The averaged tropopause height (black line) of the entire period ranges

3.7 Global zonal averaged ECMWF tropopause heights

from about 8 - 10 km at the poles, 10 - 14 in the mid-latitudes and 16 - 18 at the tropics. It is on average slightly higher in the northern mid and higher latitudes than in the southern mid and higher latitudes. The global mean tropopause height acts as a natural filter that removes much of the ENSO (El Nino/Southern Oscillation) variability that makes the interpretation of tropospheric and surface temperature difficult (Sausen & Santer, 2003). These properties make the tropopause height an interesting tool for the detection of temperature variabilities and changes in the troposphere as well as in the lower stratosphere (Santer *et al.*, 2003a).

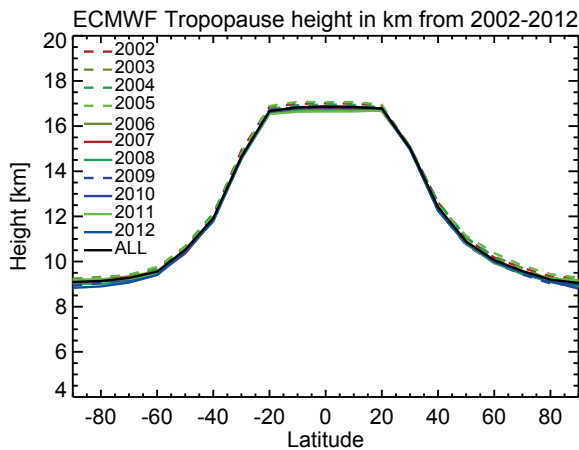


Figure 3.8(a): The zonal average, annual-mean tropopause heights in km from ECMWF between 2002 and 2012 at 10° latitude \times 10° longitude resolutions.

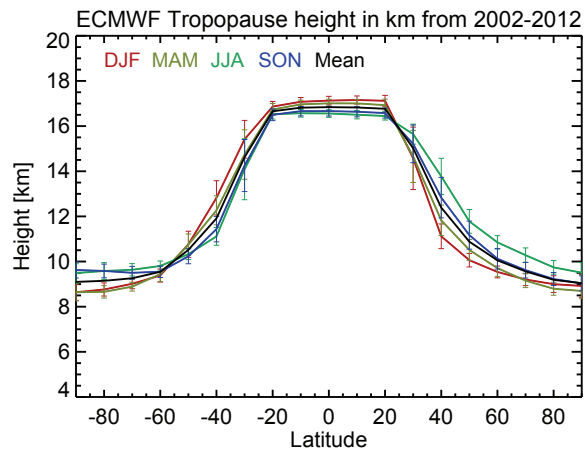


Figure 3.8(b): The zonal average, seasonal-mean tropopause heights in km from ECMWF between 2002 and 2012 at 10° latitude \times 10° longitude resolutions.

The zonal means tropopause heights from ECMWF for different seasons between 2002 and 2012 at 10° latitude \times 10° longitude resolutions is shown in figure 3.8b. Strong meridional structure during all the seasons are observed. In the tropics, the tropopause heights are nearly constant, but with the highest values between 16 and 18 km during NH winter in the deep tropics. This is clearly observed in the zonal average time series tropopause height plot shown in figure 3.9. The strongest gradients in tropopause heights occur between 20° and 45° on both hemispheres as shown in figure 3.9. The extratropical tropopause height is higher during summer than in winter time with the exception of the SH polar region as shown in figure 3.8b.

Figure 3.10 shows the zonal mean bias and standard deviation from ECMWF and ozonesonde for the different seasons (DJF: December - February; MAM: March - May; JJA: June - August; SON: September - November, from 2003 - 2011). The two data sets show agreement better than about 30 m at most latitudes. The variability of the biases in the southern and northern hemispheres subtropics are similar, although it is higher during boreal summer/autumn in the southern/northern subtropics. The high variability of the bias in the tropics during boreal winter is due to the increased

3. THE TROPOPAUSE AND ITS ROLE

response of tropopause height in this region. On average the variability of the biases in the SH polar regions is higher compared with the NH polar region.

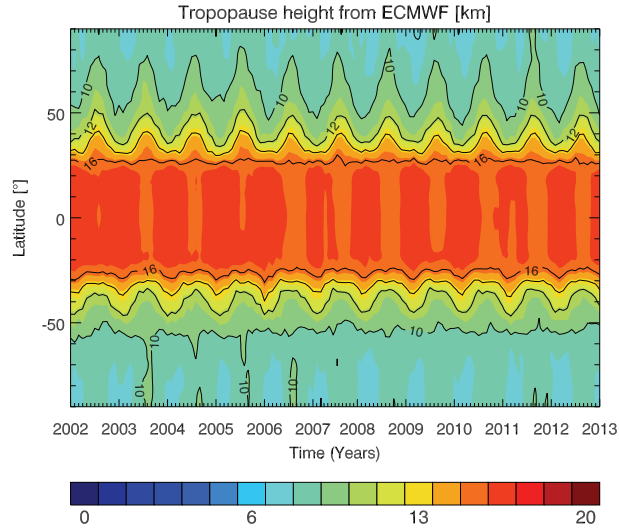


Figure 3.9: The zonal average time series tropopause height in km from ECMWF between 2002 and 2012.

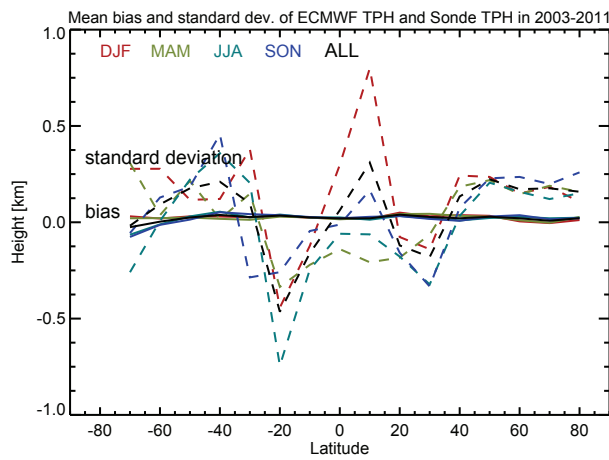


Figure 3.10: The zonal means bias (solid) and standard deviation (dotted) between ozonesondes (44 stations) and ECMWF tropopause heights for the different seasons (DJF: December - February; MAM: March - May; JJA: June - August; SON: September - November, from 2003 - 2011) at 10° latitude \times 10° longitude resolutions.

Chapter 4

Ozone Profile and Total Ozone Column retrieval algorithm

4.1 Ozone profile retrieval algorithm

The retrievals of the vertical profiles of ozone number density from satellite measurements of limb-scattered sunlight in the UV-Visible spectral range is conducted by exploiting the Hartley, Huggins, or Chappuis absorption bands. The limb-scatter technique has been applied to retrieve mesospheric ozone profiles using single scattering theory in the UV Hartley bands from measurements made by UV spectrometers such as SME (Solar Mesosphere Explorer)(Rusch *et al.*, 1984). Ozone profiles in the upper stratosphere and lower mesosphere have been retrieved from SCIAMACHY limb scatter measurements in the Hartley bands (Rohen *et al.*, 2006). The limb-scatter technique has also been used to retrieve vertical profiles of ozone in the near UV Huggins bands from observation made by the Shuttle Ozone Limb Scattering Experiment/Limb Ozone Retrieval Experiment (SOLSE/LORE) flown on the space shuttle in 1997 and 2003 (Flittner *et al.*, 2000; McPeters *et al.*, 2000).

The Chappuis band in the visible range has also been exploited in the retrieval of vertical ozone profile in the stratosphere from observations derived from SOLSE/LORE, the Optical Spectrograph and InfraRed Imager System (OSIRIS) on Odin, the Stratospheric Aerosol and Gas Experiment (SAGE III) on Meteor-3, and SCIAMACHY (Flittner *et al.*, 2000; Haley *et al.*, 2004; McPeters *et al.*, 2000; Rault, 2005; Roth *et al.*, 2007; Rozanov *et al.*, 2007; von Savigny *et al.*, 2003).

The retrieval of the vertical distributions of ozone used in this study is described by Sonkaew *et al.* (2009). It involves the combination of spectral information from the Hartley, Huggins and Chappuis bands to simultaneously retrieve ozone profile information.

This is implemented by using normalized limb radiance profiles in the UV and the triplet method (Flittner *et al.*, 2000; von Savigny *et al.*, 2003) in the visible wavelength range. The normalized limb

4. OZONE PROFILE AND TOTAL OZONE COLUMN RETRIEVAL ALGORITHM

radiance profiles in the Chappuis, Hartley, and Huggins bands are used in a simultaneous retrieval to obtain the ozone number density and extend the ozone profile to about 80 km. Independent of the latitude, the retrieved O₃ profile is determined by UV absorption above 40 km and by visible wavelengths below 35 km, while both spectral channels contribute in the transition region. To avoid airglow emissions and Fraunhofer lines, only selected wavelengths (264, 267.5, 273.5, 283, 286, 288, 290, and 305 nm) in the UV Hartley-Huggins band were used.

The UV wavelengths are measured in SCIAMACHY channels 1 and 2. To increase the signal to noise ratio, the limb radiance is averaged over 2 nm spectral intervals around each central wavelength. Similar to the approach employed by Rohen *et al.* (2006), three wavelengths (250, 252, and 254 nm) were ignored so as to avoid the usage of data that are contaminated with noise and two wavelengths (307 and 310 nm) were ignored to avoid the influence of multiple scattering and surface reflection on the retrievals (Sonkaew *et al.*, 2009). To reduce the impact of instrument calibration errors as well as light scattering in the lower atmospheric layers, the limb radiance profiles at each wavelength are normalized by the limb radiance measured at an upper tangent height, which is commonly referred to as the reference tangent height as shown in equation 4.1,

$$I_N(\lambda_k, h_l) = \frac{I(\lambda_k, h_l)}{I(\lambda_k, h_r)}, \quad (4.1)$$

where $I(\lambda_k, h_l)$ and $I(\lambda_k, h_r)$ represent the limb radiance at 8 wavelengths listed in table 4.1 at the current (h_l) and reference (h_r) tangent heights, respectively. At each wavelength only limb radiances observed in a selected tangent height range are used.

Wavelength (nm)	264	267.5	273.5	283	286	288	290	305	525	602	675
h_{low} (km)	52	52	52	45	45	45	45	35	9	9	9
h_r (km)	71	71	71	68	65	65	61	55	41	41	41

Table 4.1: The lowest (h_{low}) and reference (h_r) tangent heights for the wavelengths used.

The spectral information obtained in the visible spectral range are combined together to build the Chappuis triplet (equation 4.2) (Flittner *et al.*, 2000; von Savigny *et al.*, 2003), which exploits the limb radiance profiles at three wavelengths: $\lambda_1 = 525$ nm at a relatively weak ozone absorption in the short-wavelength wing of the Chappuis band, $\lambda_2 = 602$ nm at a strong ozone absorption near the center of the Chappuis band, and $\lambda_3 = 675$ nm at a weaker ozone absorption in Chappuis bands. The Chappuis band wavelengths are measured in channels 3 and 4 of SCIAMACHY. Similar to the UV wavelengths, the limb radiance is averaged over 2 nm spectral intervals around each central wavelength and normalized by the limb radiance at the reference tangent height.

$$I_{Ch}(h_l) = \frac{I_N(\lambda_2, h_l)}{\sqrt{I_N(\lambda_1, h_l) I_N(\lambda_3, h_l)}}. \quad (4.2)$$

Finally, both the normalized limb radiances at UV wavelengths (equation 4.1) and the Chappuis triplet (equation 4.2) are then implemented in the SCIATRAN radiative transfer model in order to determine the limb radiance profiles for the considered wavelengths and tangent height ranges as required by the inversion routine. The temperature and pressure profiles needed as input for the retrieval of ozone number density by SCIATRAN RTM are obtained from the ECMWF operational analysis for the matching day, time and location of each individual SCIAMACHY measurement.

The *a priori* ozone volume mixing ratio profiles required for the optimal estimation retrieval, as the first guess in the forward model for the evaluation of the retrieval vector is taken from the ozone climatology provided by Prather & Remsberg (1993). The diagonal elements of the *a priori* covariance matrix are set to standard deviations of 1000 % to ensure that the retrieval is completely independent of the *a priori* information. The off-diagonal elements of the *a priori* covariance matrix are determined assuming a correlation length of 1.5 km over the whole atmosphere. The diagonal elements of the measurement covariance matrix are calculated from the squares of the measured radiance random errors. An aerosol database, ECSTRA (Extinction Coefficient for STRatospheric Aerosol) climatological (Fussen & Bingen, 1999) and albedo data base (Matthews, 1983) were used in the analysis. Clouds are detected in the limb viewing mode using the SCIAMACHY Cloud Detection Algorithm (SCODA) (Eichmann *et al.*, 2009). SCODA uses colour index ratios in the vertical radiance profiles at different wavelength pairs in the visible and near infrared to determine the cloud top height and cloud thermodynamic phase (ice, liquid).

Comparison of the SCIAMACHY stratospheric O₃ data product with the results from MLS, SABER, SAGE II and ACE-FTS show an agreement of typically better than 10 % globally, although larger biases exist around 30 km in the tropics and below 20 km at all latitudes (Mieruch *et al.*, 2012).

4.2 Total ozone column retrievals

The Weighting Function Differential Optical Absorption Spectroscopy (WFDOAS) algorithm (Coldewey-Egbers *et al.*, 2005; Weber *et al.*, 2005) is used to retrieve total O₃ columns (TOZs) from the SCIAMACHY nadir-viewing measurements. The WFDOAS algorithm approximates the measured atmospheric optical depth (logarithm of the sun-normalised radiances) by a Taylor expansion around a reference intensity plus cubic polynomial. The fitting parameters are all derived

4. OZONE PROFILE AND TOTAL OZONE COLUMN RETRIEVAL ALGORITHM

using a linear least squares minimization. The WFDOAS equation can be expressed as follows.

$$\begin{aligned} \ln F = & \ln(F_o)_{mod} + \left(\frac{d\ln(F_o)}{dV} \right)_{mod} (V_{fit} - V_{clim}) \\ & + \left(\frac{d\ln(F_o)}{dT} \right)_{mod} (T_{fit} - T_{clim}) + SC_{ring} \times \sigma_{i,ring} \\ & + SC_{usamp} \times \sigma_{i,usamp} + SC_{I_o} \times \sigma_{i,I_o} + Pol. \end{aligned} \quad (4.3)$$

Where F is the sun normalized nadir radiance, V denotes the TOZ, T is the scalar temperature, the parameters with the subscript (mod) indicate the quantities provided by radiative transfer model. Other fit parameters are the ring effect ($ring$) and the under-sampling correction ($usamp$). These fit parameters are both treated as effective absorbers similar to the approach used in standard DOAS. The I_o effect describes the cross-section derived from the highly structured solar spectrum. Pol stands for the polynomial, which accounts for all broadband contributions from surface albedo and aerosols.

In contrast to the standard DOAS technique, which uses the O_3 cross section in the fit procedure, the WFDOAS algorithm exploits the weighting function for the retrieval of TOZ. The latter is estimated by a vertical integration of the altitude dependent weighting function of O_3 (equation 4.3). To obtain the weighting function for the change in the total O_3 including profile shape, solar zenith angle (SOZ), line-of-sight (LOS) azimuth, relative azimuth angle (RAA), and bottom-of-atmosphere (BOA) altitude and albedo, the weighting functions calculated at each altitude using the SCIATRAN radiation transfer code (Rozanov *et al.*, 1998) are integrated vertically. This is an added advantage because only a negligible amount of additional computer effort is required (Rozanov *et al.*, 1998).

Ozone and temperature profiles are obtained from the TOMS (Total Ozone Mapping Spectrometer) V7 climatology (Wellemeyer *et al.*, 1997), see table 4.2. This climatology also contains typical ozone hole profiles. It accounts for seasonal variation and provides different profile shapes for three latitude bands (low, middle and high) as a function of TOZ, which vary from 225 – 475 DU in low latitudes and 125 – 575 DU in mid and high latitudes (Coldewey-Egbers *et al.*, 2005). In the TOMS V7 climatology, the SZA and LOS varies from $15^\circ - 92^\circ$ and $-34.5^\circ - +34.5^\circ$, respectively. The range for the relative azimuth angle is defined by a given combination of both the SZA and LOS (Coldewey-Egbers *et al.*, 2005).

Succinctly, the retrieval of TOZ with the WFDOAS approach, involves the utilization of calibrated SCIAMACHY level 1 radiance and solar spectrum from the same day. Also included in the retrieval are *a-priori* values for total ozone, effective altitude, and effective albedo. The effective altitude is obtained from FRESCO (Fast Retrieval Scheme for Clouds from the oxygen A-Band, (Koelemeijer *et al.*, 2001)). Cloud top pressure and cloud fraction are derived from the oxygen

4.2 Total ozone column retrievals

Atmospheric Parameter	Min	Max	Δ	N
Total Ozone (high latitudes)	125 DU	575 DU	50 DU	10
Total Ozone (mid latitudes)	125 DU	575 DU	50 DU	10
Total Ozone (low latitudes)	225 DU	475 DU	50 DU	6
Solar Zenith Angle	15°	92°	5° if SZA \leq 70° 1° if SZA $>$ 70°	34
Line-Of-Sight	-34.5°	34.5°	11.5°	7
Relative Azimuth Angle	(*)	(*)		3
Surface Albedo	0.02	0.98	\sim 0.2	6
Altitude	0 km	12 km	2 km	7

Table 4.2: Parameter space of the look-up-tables. The value indicated by (*) in the min/max column of the Relative Azimuth Angle depend on the SZA and LOS.

transmittance assuming a highly reflecting boundary representing the cloud top. Surface albedo is taken from minimum spectral reflectances derived from SCIAMACHY data record. The effective height ($ehgt$) is the sum of the ground altitude ($shgt$) and the retrieved cloud top height (cth) weighted by the fractional cloud cover (cf) as illustrated by equation 4.4 (Coldewey-Egbers *et al.*, 2005),

$$ehgt = cf \times cth + (1 - cf) \times shgt. \quad (4.4)$$

The Lambertian Equivalent Reflectivity LER (Herman & Celarier, 1997) defines the effective albedo obtained from SCIAMACHY sun-normalised radiances at 377.6 nm, where variations with respect to the Ring effect are small and can be easily checked. The LER are retrieved using the look-up-table (table 4.2) that was pre-calculated using SCIATRAN to find the best match between calculated and measured top of atmosphere (TOA) reflectance by inverse search in the multidimensional table as described in Coldewey-Egbers *et al.* (2005). The Raman correction to scattered intensity also called the Ring spectra (Solomon *et al.*, 1987) were calculated using the ozone profiles taken from the climatology. These parameters are stored in look-up tables and a fitting window of 326.6 – 334.5 nm is used for the TOZ retrieval. At the end of the iteration, the ghost vertical column (GVC) (equation 4.5), which is hidden below the (partial) cloud, is determined from an ozone climatology and then added to the retrieved column to obtain the final total ozone amount as illustrated by equation 4.6,

$$GVC = cf \times \int_{p(ho)}^{p(hp)} O_3(p) dp, \quad (4.5)$$

$$TOZ = ROC + GVC. \quad (4.6)$$

Where TOZ is the total ozone column, ROC is the retrieved ozone column, $p(ho)$ is the pressure at the surface altitude (ho), $p(hp)$ is the cloud top pressure and $O_3(p)$ is the ozone profile, which is also

4. OZONE PROFILE AND TOTAL OZONE COLUMN RETRIEVAL ALGORITHM

pressure dependent. To account for partial cloudiness, the integrated partial column ($\int_{p(h_o)}^{p(h_p)} O_3(p)$) is multiplied by the cloud fraction (cf). In the TOZ retrieval, clouds are treated as Lambertian reflecting surfaces (Coldewey-Egbers *et al.*, 2005). Cloud-top-height and cloud fraction (cf) from SACURA as applied to SCIAMACHY (Kokhanovsky & Rozanov, 2004) are used to determine an effective BOA height. In case of a clear-sky scene, this becomes the surface height. For a fully cloudy scene, the cloud-top-height is the BOA. The effective albedo of the BOA is determined using the LER at 377 nm. The missing O_3 below the cloud is corrected by adding a GVC to the ROC derived from an O_3 profile climatology to obtain the TOZ. In cases of very high clouds, the tropospheric contribution to the total column is then solely determined by climatological O_3 .

The validation of the TOZ with ground based measurements from the WOUDC (World Ozone and UV Radiation Data Centre) shows good agreement to within $\pm 1\%$ with small seasonal differences (Bracher *et al.*, 2005; Weber *et al.*, 2007). In the polar regions, and at very high solar zenith angles, biases can be larger (Weber *et al.*, 2005).

Chapter 5

Tropospheric ozone column retrievals from satellite and ozonesonde instruments

Over the years, several techniques have been proposed for retrieving the tropospheric O₃ amount from satellite instruments. The retrieval of tropospheric O₃ from satellite instruments using the residual approach started in the late 1980s (Fishman & Larsen, 1987). In this method, the TOCs were obtained by subtracting the SOCs retrieved from SAGE measurements from the TOZs derived from TOMS (Total Ozone Mapping Spectrometer) observations. This approach was prone to uncertainties due to the coarse temporal resolution and limited spatial coverage of the SAGE instrument. Different residual based approaches have been developed over the years with each method dealing with the subtraction of SOC from TOZs (e.g., Fishman & Balok, 1999; Fishman *et al.*, 1990; Schoeberl *et al.*, 2007; Thompson & Hudson, 1999; Ziemke *et al.*, 1998, 2006, 2011). Ziemke *et al.* (1998) used the Convective Cloud Differential (CCD) method to retrieve TOC, an approach that is based on using the knowledge of the cloud top pressure to separate the stratosphere from the troposphere. This technique is applicable only at the tropical region and in the presence of deep convective clouds. In this technique, TOZ are derived from low reflectivity ($R < 0.2$) measurements and the SOC are derived from a near-by column O₃ measurements taken above the tops of very high tropopause-level clouds under the conditions of high reflectivity ($R > 0.9$). This technique is based on the condition that the tropical stratospheric O₃ is zonally invariant, therefore, the monthly mean TOC was computed from the minimum O₃ above high-reflectivity clouds points (reflectivity $> 90\%$) in every 5° bands across the Pacific ocean from 120°E to 120°W. An extension of this technique called the cloud slicing method (Ziemke *et al.*, 2003) has also been used to retrieve upper tropospheric O₃ between 100 and 400 *hPa*, but unlike CCD technique, this method involves

5. TROPOSPHERIC OZONE COLUMN RETRIEVALS FROM SATELLITE AND OZONESONDE INSTRUMENTS

the simultaneous/co-located measurements of both above-cloud column O_3 and cloud-top pressure by utilizing the advantage that water vapour clouds are opaque to UV radiation. Ladstätter-Weißmayer *et al.* (2004) used the Tropospheric Excess Method (TEM) also called the reference sector method (RSM) to compute TOCs by finding the difference between TOZ from polluted and unpolluted areas (e.g., data from pacific region) at similar latitudes. This method assumes negligible tropospheric O_3 over clean areas and that stratospheric O_3 do not vary zonally (Chance *et al.*, 2000; Fishman *et al.*, 1990; Leue *et al.*, 2001), such that the TOZ measured on the same day at the same latitude over a clean air region can be used as an approximation of the SOC over the region of interest. Kim *et al.* (2001) used the scan angle geometry technique to retrieve tropical tropospheric O_3 , a method that requires multi-angle measurements.

A retrieval of tropospheric O_3 from near simultaneous nadir measurements in the Hartley and Huggins bands of O_3 has been shown to be feasible. This approach exploits the different penetration depths at different wavelengths to obtain information on the vertical distribution of O_3 . It was first described by Singer & Wentworth (1957) and then used by Bhartia *et al.* (1996, 2013), Munro *et al.* (1998), Hoogen *et al.* (1998, 1999), and Liu *et al.* (2006, 2010) among others to retrieve O_3 profiles at a moderate to low vertical resolution. This method, however, requires very accurate measurements between 250 and 350 nm of the upwelling radiation at the top of atmosphere, which changes in this range by several orders of magnitude. As shown by theoretical studies (Natraj *et al.*, 2011), additional information on the vertical distribution of ozone in the lower atmosphere is obtained by combining measurements in the visible and UV spectral range. This, however, makes the retrieval more sensitive to the spectral characteristics of the surface reflection and weaker absorption features like chlorophyll and liquid water (e.g., Vountas *et al.*, 2007).

Tropospheric O_3 has also been retrieved from nadir measurements of thermal infrared (TIR) emission (Aumann *et al.*, 2003; Beer, 2006). However, as the signal in the thermal infrared depends on the thermal contrast, sensitivity is poor in the lower troposphere and maximizes in the upper troposphere and lower stratosphere.

Another approach to retrieve tropospheric O_3 is the use of simultaneous observations in the UV, visible and TIR spectral ranges, as first proposed in the GeoTROPE studies (Burrows *et al.*, 2004). The TIR O_3 signal is dependent on the temperature and O_3 profiles. The capabilities of this technique have been demonstrated by synthetic retrievals in Natraj *et al.* (2011) and Worden *et al.* (2007). A similar technique has also been applied to retrieve tropospheric O_3 using infrared radiance spectra recorded by the Infrared Atmospheric Sounding Interferometer (IASI) and GOME-2 ultraviolet measurements (Cuesta *et al.*, 2013).

Data assimilation in combination with chemistry/transport models have been used to derive TOC (e.g., Doughty *et al.*, 2011). Tropospheric O_3 amounts have also been determined using

neural network (NN) algorithms (e.g., Di Noia *et al.*, 2013; Sellitto *et al.*, 2011). The NN approach combines reflectances obtained in satellite nadir viewing measurements with temperature and tropopause pressure information to yield estimates of TOC.

The retrieval of atmospheric trace gases using the residual approach through the combination of limb and nadir measurements from SCIAMACHY has been previously applied to O₃ and NO₂ (Beirle *et al.*, 2010; Hilboll *et al.*, 2013; Sierk *et al.*, 2006; Sioris *et al.*, 2004). The global retrieval of tropospheric O₃ from SCIAMACHY using the LNM technique is advantageous, because it does not require any further assumptions, such as zonal homogeneity of stratospheric O₃ or an estimate from model data. The algorithm extracts tropospheric O₃ information from observations of nearly the same air mass, probed in both nadir and limb geometries (Ebojie *et al.*, 2014).

5.1 Combination of SCIAMACHY limb and nadir measurements

The objective of the retrievals of the SCIAMACHY LNM measurements is the accurate determination of the tropospheric amount of trace species, which have significant stratospheric absorption. The SCIAMACHY instrument was designed to alternate between limb and nadir geometries so that the region probed during the limb scan can be observed about 7 minutes later during the nadir scan (see figure 1.4). The limb measurements yield the stratospheric vertical profiles of trace gases directly over the region of the nadir measurements of total columns. Integrating the coincident stratospheric profiles from the tropopause upwards determines the stratospheric vertical column density above the target area. The subtraction of the resulting stratospheric column amount from the total column measured in nadir yields the tropospheric column amounts. Combining limb and nadir measurements from the same instrument as in the case of SCIAMACHY (Beirle *et al.*, 2010; Sierk *et al.*, 2006), is expected to be associated with lower uncertainties than those approaches that require different instruments that do not allow exact matches of air masses in space and time. The particular advantage here is that LNM provides large number of tropospheric O₃ and NO₂ (Beirle *et al.*, 2010; Sierk *et al.*, 2006) measurements with global coverage within six days.

The determination of the SOC, involves the computation of the tropopause heights as discussed in chapter 3.2 and then integrating O₃ profiles from the height of the tropopause to about 80 km. At higher latitudes, where the tropopause is below 10 km, the stratospheric O₃ profiles below the lowest retrieval altitude were constructed from ozonesonde climatological profiles (2003 - 2011) scaled to match the lower part of the retrieved SCIAMACHY profile, which is ~10 km. The ground area covered by a single limb measurement is about 400 km (along track) × 240 km (across track) and that of an individual nadir state is approximately 30 km (across track) × 60 km (along track). In order to determine the TOC, the subsequent nadir measurements that matched with the limb

5. TROPOSPHERIC OZONE COLUMN RETRIEVALS FROM SATELLITE AND OZONESONDE INSTRUMENTS

measurement are averaged such that the ground area corresponding to a single tropospheric column value is about $60 \text{ km} \times 240 \text{ km}$. The TOC is obtained by subtracting SOC from TOZ.

Since TOCs constitute only about 10 % of the TOZs, small errors associated with clouds might significantly affect the derived TOCs. Therefore, limb scenes that are contaminated with clouds and nadir measurements that are not near cloud-free scenes were screened out. Furthermore, to minimize uncertainties in the retrieved tropospheric O_3 , the analysis was restricted to measurements from the descending part of the orbit with solar zenith angles (SZAs) less than 80° , because of the decrease in tropospheric sensitivity to O_3 of nadir measurements at higher SZAs.

5.2 Theory of limb-nadir matching algorithm

The LNM technique implemented in the retrieval of tropospheric ozone from SCIAMACHY is based on the method of locating a point in a polygon. To determine whether an arbitrary point Q lies in a closed polygon P , the crossing number (CN) algorithm is used. The polygon with n number of vertices P_0, P_1, \dots, P_{n-1} (see figure 5.1) are sorted in a way that there exists an edge between P_i and P_{i+1} for $0 \leq i < n - 1$ and the polygon is closed by the edge from P_{n-1} to P_0 .

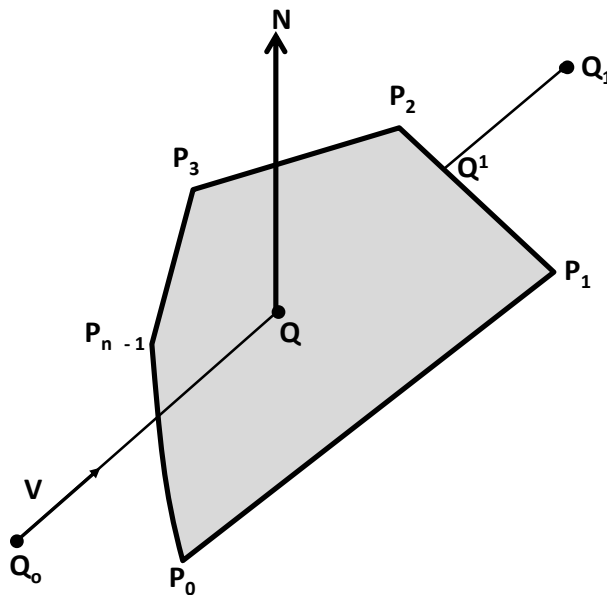


Figure 5.1: Illustration of ray crossing in a plane.

The CN algorithm is based on the Jordan curve theorem (JCT), which asserts that every Jordan curve (a non-self-intersecting continuous loop in the plane) separates the plane into exactly two components (Jordan, 1887). This theorem has been proved (e.g., Hales, 2007; Tverberg, 1980). The CN method is also referred to as the in-out parity or the even-odd test. The CN method works

by casting a ray (line) from the projection of Q along the positive x -axis. Then the number of intersections between the polygon edges and the ray is computed. If the line from Q crosses the edges $e_i = \overline{P_i P_{i+1}}$ of the polygon an odd number of times, then the point is considered to lie inside. Otherwise, it is even, when the point is outside the polygon as illustrated by figure 5.2.

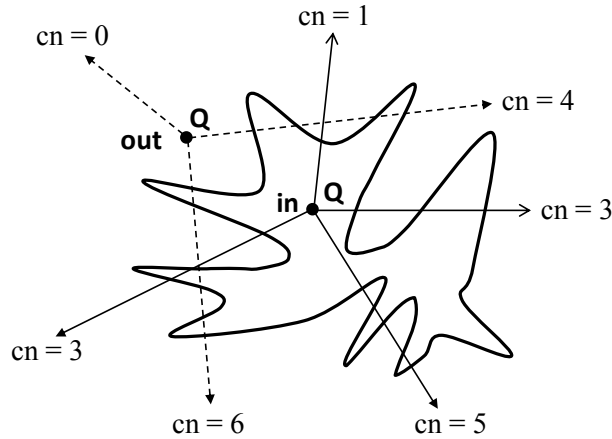


Figure 5.2: Illustration of the crossing number method.

To check whether Q is the origin of the ray, the edges are tested against the positive x -axis (see figure 5.3). In general, if the y -coordinates of the edge of the polygon has the same signs, then the edge cannot cross the x -axis. Otherwise, it crosses it, thus leading to the checking of the x -coordinates. If both are positive, then the number of crossings is incremented. But if they differ in sign, then the x -coordinate of the intersection between the edge and the x -axis is computed. If it is positive, then the number of crossings is again increased. The procedure can be expanded to loop over the edges of P , so that a decision can be made for each edge whether it crosses the line or not, and the corresponding crossings are counted. But there exist some special cases where the ray passes through or intersects a vertex (figure 5.3), this can lead to two crossings (e.g., Galetzka & Glauner, 2012; O'Rourke, 1998). To handle such cases, the vertex is set infinitesimally above the ray (x -axis) by considering all vertices with $y \geq 0$ as lying above the ray.

Figure 5.3 describes the ray-edge and ray-vertex intersections, where the number of crossings with the positive x -axis determines whether Q is inside the polygon or not. Edges e_2, e_3, e_4, e_5, e_6 and e_9 do not cross the x -axis. The intersection between edge e_1 and the x -axis (blue filled circle) is computed, although it will not yield a crossing, since the intersection has a negative x -component. Edges e_0 and e_{10} , which intersect with the positive x -axis of the ray (red filled circles), will each increase the number of crossings, since the vertices of these edges have positive x -components and one negative and one positive y -component. Edges e_7 and e_8 share a vertex where $y = 0$ and $x > 0$, which intersects with the positive x -axis of the ray. Both of them will together increase the

performed to find the minimum and maximum x and y coordinates of each corner, which is checked against the corners of the limb scan box. If the nadir box is confirmed to lie in the limb box, then the TOZs that meet cloud fraction threshold is averaged within a limb box. For the nadir states which are only partially within the limb state, the nadir pixel is weighed based on the distance of its center to nearest corners of the limb pixel. The process is iterated for all nadir pixels measured at about 7 minutes later after the limb scan.

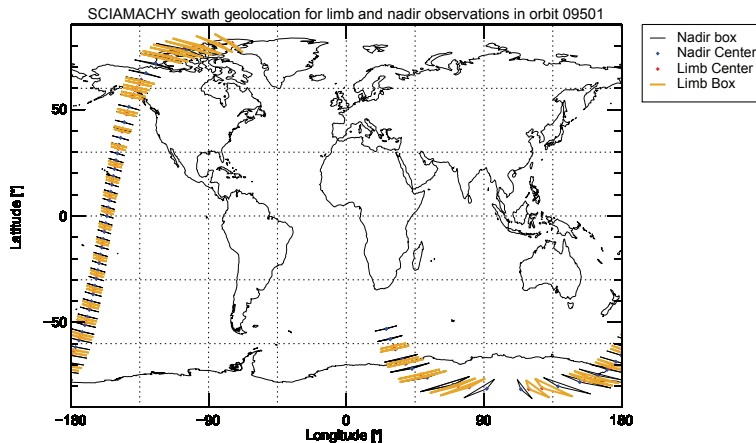


Figure 5.5: Illustration of SCIAMACHY swath for limb and nadir observations in orbit 09501.

5.3 Tropospheric ozone from OMI/MLS, TES and ozonesondes

5.3.1 Tropospheric ozone from OMI/MLS and TES

TES V003 monthly mean tropospheric O_3 data used in this study was downloaded from <http://eosweb.larc.nasa.gov/>. This data set was retrieved using the optimal estimation (OE) technique (Rodgers, 2000) as described in detail by Bowman *et al.* (2006). TES measurements provide O_3 profiles with a vertical resolution of approximately 6 km, corresponding to about 1 - 2 degrees of freedom (DOF) in the troposphere, using NCEP (National Centers for Environmental Prediction) tropopause height data. Tropical and subtropical clear-sky measurements have the highest number of DOFs when the TES instrument can distinguish between lower and upper tropospheric O_3 (Jourdain *et al.*, 2007). The O_3 *a-priori* profiles are derived from the Model of Ozone and Related Tracers (MOZART) CTM (Brasseur *et al.*, 1998) monthly means, which are averaged in 10° latitude \times 60° longitude grid boxes (Bowman *et al.*, 2006). Although the limited profile resolution determined from TES instrument can lead to a bias when comparing with other data products, the TOC is reasonable (Tang & Prather, 2012). A description of TES data product used in this study is given by Osterman *et al.* (2009, 2008).

5. TROPOSPHERIC OZONE COLUMN RETRIEVALS FROM SATELLITE AND OZONESONDE INSTRUMENTS

TES tropospheric O₃ data were screened using the O₃ data quality flag (Osterman *et al.*, 2009), the emission layer flag (Nassar *et al.*, 2008), cloud top pressure and cloud effective optical depth (Eldering *et al.*, 2008; Kulawik *et al.*, 2006). Validation studies showed that TES tropospheric O₃ overestimate the reference data with an average bias of 3 - 11 ppbv (e.g., Boxe *et al.*, 2010). It has been reported that TES O₃ profiles are biased high throughout the troposphere by up to 15 % (Nassar *et al.*, 2008). Comparisons of TES TOCs with ozonesondes, shown in Fig. 3 of Nassar *et al.* (2008), reveal that TES TOCs are high biased by 2.6 DU in the tropics, 5.1 DU in the northern subtropics, 3.3 DU in the northern midlatitudes and about 1.9 DU in the southern low and midlatitudes (Nassar *et al.*, 2008).

OMI provides the TOZs using the OMI-TOMS retrieval algorithms version 8 described in <http://ozoneaq.gsfc.nasa.gov/doc/ATBD-OMI-04.pdf> (Ziemke *et al.*, 2006). For determining tropospheric O₃ in combination with MLS data, the TOZ from OMI have been screened as follows. Clouds are approximated as opaque Lambertian surfaces and scenes with solar zenith angle greater than 84° are screened out (Ziemke *et al.*, 2006). Also surface glint, SO₂ contamination and some other factors are flagged (Ziemke *et al.*, 2006). Furthermore, cloudy scenes are screened by rejecting O₃ measurements with reflectivity greater than 0.3 (Ziemke *et al.*, 2006). This data product has been extensively validated with both ground-based and satellite instruments. Comparisons between the TOZ values from OMI and Dobson spectrometer show a global mean agreement of less than 1 % (Balis *et al.*, 2007).

The MLS instrument provides information on the SOC. An analysis of SOCs derived from MLS version 3.3 and an earlier version 2.2 (Froidevaux *et al.*, 2006, 2008), shows a systematic offset of about +2.5 DU (Ziemke *et al.*, 2011). It has also been documented that a low bias in the AURA tropospheric O₃ is probably due to MLS O₃ being high biased in the lowermost stratosphere (Livesey *et al.*, 2011).

The MLS measurements are made about 7 minutes before OMI views the same location during ascending (daytime) orbital tracks. To determine the TOC and the SOC, tropopause pressure determined from the NCEP analysis based on the thermal tropopause criterion (WMO, 1957) was used. The TOCs are derived by subtracting the vertically integrated MLS O₃ profiles from the OMI TOZ. For our analysis we used OMI/MLS TOC, described in detail by Ziemke *et al.* (2006). This data product has been validated by comparison with ozonesondes. The results indicated an agreement within a few DU.

5.3.2 Tropospheric ozone from ozonesondes

The ozonesonde dataset used in this analysis is obtained with the electrochemical concentration cell (ECC) (Komhyr, 1969), Brewer-Mast (BM) (Brewer & Milford, 1960), and the carbon iodine cell

(KC96) (Kobayashi & Toyama, 1966) detectors. The datasets are available at <http://www.woudc.org/> (WOUDC, 2007) and <http://croc.gsfc.nasa.gov/shadoz/> (Thompson *et al.*, 2003). From the datasets, the tropopause heights were determined from the temperature profile measurements by using the thermal tropopause definition (WMO, 1957) and then the TOC by integrating the O₃ concentration (c_i) from the surface to the tropopause as follows,

$$TOC = \frac{1}{2} \sum_{i=1}^{i_{\max}-1} [(c_{i+1} + c_i)(h_{i+1} - h_i)], \quad (5.1)$$

where c_i is given by

$$c_i = \frac{N_A P_i}{RT_i}, \quad (5.2)$$

where i represents the level index, h is the height, N_A is Avogadro's number, R is the ideal gas constant, and T and P are the temperature and O₃ partial pressure, respectively. Analysis shows that the quality of ozonesonde measurements is well established (WOUDC, 2007) to be used to validate SCIAMACHY tropospheric O₃ (Ebojie *et al.*, 2014).

5.3.2.1 Uncertainties in ozonesonde data

The contribution to overall uncertainties in the ozonesonde data products may be due to a number of factors, including degradation of the pump efficiency at higher altitudes, heat isolation and improper positioning of the thermistor. Enhancement of the conversion efficiency and influence of background signal measured before flight particularly in the case of ECC sondes also play a role.

In the early 1990s it was difficult to measure the actual pump temperature due to the positioning of the thermistor and also as a result of limited information transmitted by the analog radiosonde (Smit, 2002). Thus, a constant pump temperature profile was generally assumed. Modern ECC sondes now have the thermistor inserted in a hole drilled into the Teflon block.

The degradation of the pump efficiency is mainly due to pump leakage or evaporation of the sensing solution as the instrument ascends to higher altitudes (Smit *et al.*, 2007), thus affecting the shape of the upper part of the profile. The need to correct this becomes important at ambient pressure lower than 100 hpa by empirically using tables, for example, for BM sondes (Claude *et al.*, 1987) and ECC sondes (Komhyr, 1986; Komhyr *et al.*, 1995a). The correction tables (e.g. Table 5.1) are based on averages obtained from laboratory experiments. Although there are some exceptions, for example, the NOAA/CMDL (National Oceanic and Atmospheric Administration/Climate Monitoring and Diagnostic Laboratory) corrections are based on individual pump flow calibrations implemented as part of the sonde pre-launch preparation.

5. TROPOSPHERIC OZONE COLUMN RETRIEVALS FROM SATELLITE AND OZONESONDE INSTRUMENTS

Pressure (hPa)	Claude et al., 1986	JMA	Komhyr et al., 1986	Komhyr et al., 1995	NOAA/CMDL
1050	1	1	1	1	1
1000	1	1	1	1	1
500	1	1.002	1.002	1	1
300	1	1.005	1.005	1	1.003
200	1	1.007	1.007	1	1.008
100	1.01	1.02	1.01	1.007	1.018
50	1.035	1.04	1.015	1.018	1.04
30	1.065	1.07	1.024	1.029	1.053
20	1.092	1.11	1.033	1.041	1.071
10	1.17	1.25	1.054	1.066	1.12
7	1.24	1.40	1.068	1.087	1.16
5	1.3	1.66	1.087	1.124	1.21

Table 5.1: Pump efficiency correction factors as a function of pressure. NOAA/CMDL values are listed as average correction factors obtained from the individual pump flow calibrations during JOSIE 1996 (Smith-Kley1996).

Measurements in the upper troposphere where O_3 concentration is lower, may be affected by the background current. As the balloon ascends to higher altitudes the background current changes because the background signal is always correlated with past exposure to O_3 due to a memory effect. The memory effect can be explained by chemical reaction in the cell in two pathways: a fast reaction pathway due to iodine/iodide reaction and a slow minor reaction pathway due to oxidation of iodide by O_3 in the cathode sensing solution (Vömel & Diaz, 2010). There have been different approaches on how to correct for the background current. For example, in the case of ECC sondes, the background current is usually measured three times as part of pre-launch preparations: before exposure to O_3 after flushing the sonde with purified (O_3 free) air; after exposure to O_3 (after ~ 10 minutes), and just prior to flight. The background current after exposure to O_3 is typically larger than before exposure but later decreases with time. As the sensor is exposed to higher concentration of O_3 in the stratosphere, the background current will again begin to increase (Komhyr *et al.*, 1995a). An important instrumental factor that contributes to the overall uncertainty is the conversion efficiency (η). As the solution evaporates, η increases, thus leading to an increase in the sensitivity of the O_3 sensor, which can yield a stoichiometric factor (I_2/O_3) larger than unity. Although this is not a major issue for BM- and KC-sondes because they use much lower solution concentration (Smit *et al.*, 2011) compared to ECC sondes. For ECC sondes, increase in sensitivity of the sensor is significant mostly in the presence of a phosphate buffer (e.g., Johnson *et al.*, 2002).

The contributions of the different factors of equation 1.7 for ECC sondes have been combined

5.4 Sensitivity studies for the retrieval of tropospheric ozone column from SCIAMACHY

using Gaussian error propagation as shown in figure 5.6, with the largest uncertainties found at altitudes of 10 - 14 km for a typical mid-latitude station and 13 - 17 km for a typical tropical station, which coincide closely to the mean tropopause height of the respective stations.

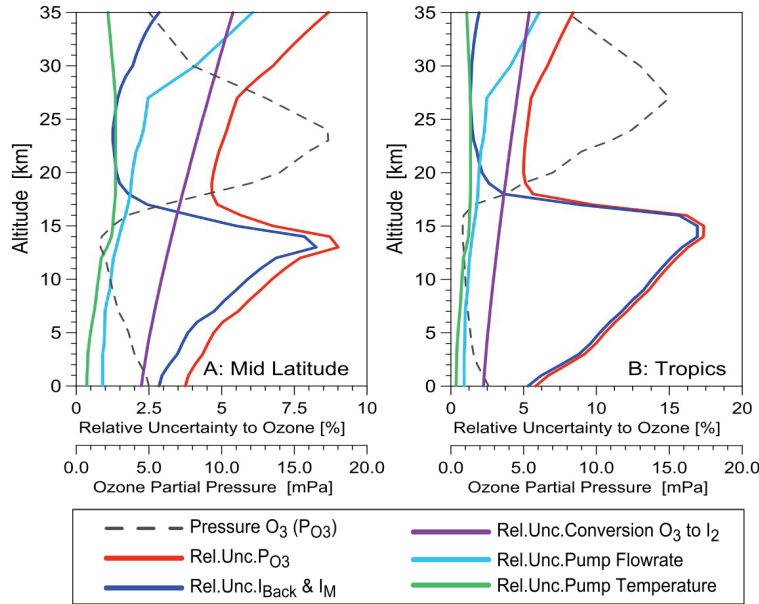


Figure 5.6: For ECC-ozonesondes: contribution of different instrumental factors to the O₃ partial pressure P_{O₃} (silver dashed line) for (A) a typical mid-latitude profile and (B) a typical tropical profile. Adapted from Smit *et al.* (2011).

5.4 Sensitivity studies for the retrieval of tropospheric ozone column from SCIAMACHY

The retrieval of TOCs presented in this thesis is based on measurements from SCIAMACHY limb and nadir observations. While the SOCs were retrieved from the limb observations the TOZs were derived from the nadir observations. Both SOC and TOZ depend on similar geophysical parameters and both are influenced by (different) instrumental effects. Some of the geophysical parameters include aerosol extinction, surface albedo, pressure profile, temperature profile, absorption cross section and clouds while an example of the instrumental effects is tangent height registration, line-of-sight, etc. Accurate simulation of the above mentioned physical parameters and the viewing geometries of the instrument is needed for the estimation of the overall error in the retrieved TOCs as well as the derived global error budget. Clouds are one of the potential error sources, but their effect was minimized by using only near cloud-free limb and nadir scenarios (see section 5.1). Among the other potential error sources, the SOC error dominates. In order to quantify the effects

5. TROPOSPHERIC OZONE COLUMN RETRIEVALS FROM SATELLITE AND OZONESONDE INSTRUMENTS

of the parameters error on the retrieved SOC, sensitivity analyses for the most important effective parameters were performed through forward model runs.

5.4.1 Derivation of SOC error parameters and the effect of tropopause height

The method used in the derivation of the different error parameters in stratospheric O_3 profile retrievals have been discussed by Rahpoe *et al.* (2013). In summary, the contributions from each of the different parameter errors to the retrieved O_3 profiles were computed for both hemispheres at different SZAs by using the synthetic retrievals. This was done by applying the following procedure. For each particular parameter, synthetic limb radiances were calculated using a climatological ozone profile (further referred to as the true profile) and a perturbed value of the parameter. For example, to investigate the influence of the albedo uncertainty, the radiative transfer model was run with the surface albedo increased by 0.1 from its unperturbed value of 0.3. Other model parameters remain the same as used in the routinely retrieval procedure. These simulated radiances were used then as the input for the retrieval instead of the measured spectra and the retrieval was initialized with the unperturbed parameter value. The difference between the ozone profile resulting from this retrieval and the true profile is considered as the contribution from the parameter error (see equation 5.3),

$$\sigma(\delta_{Aer}, z) = \frac{O_3(Y, z) - O_3(r, z)}{O_3(r, z)}. \quad (5.3)$$

Where $O_3(r, z)$ and $O_3(Y, z)$ are the ozone number densities retrieved at altitude z with unperturbed albedo value r and perturbed albedo value Y , respectively. Further details on the synthetic retrievals can be found in (Rahpoe *et al.*, 2013).

The method to estimate the total uncertainty associated with SOC is not straightforward because an assumption of Gaussian distribution for all errors may lead to an underestimation, while the assumption that all errors are additive, overestimates the actual total error. The total uncertainty of the SOC is computed from both the systematic (X_{err_1}) and random (X_{err_2}) errors, where the former error is derived from the upper limit estimation as follows:

$$X_{err_1} = |X_{ac}| + |X_{ae}| + |X_{th}|, \quad (5.4)$$

while the random errors are summed up in accordance with the Gaussian rule:

$$X_{err_2} = \sqrt{X_{ab}^2 + X_{pr}^2 + X_{temp}^2}, \quad (5.5)$$

5.4 Sensitivity studies for the retrieval of tropospheric ozone column from SCIAMACHY

where the X term corresponds to uncertainties in SOC due to uncertainty of a change in absorption cross section (ac), aerosol (ae), tangent height (th), albedo (ab), pressure (pr) and temperature (temp). Finally, the total uncertainty in SOC is estimated as follows:

$$X_{soc} = \sqrt{X_{err_1}^2 + X_{err_2}^2}. \quad (5.6)$$

Table 5.2 shows the zonally averaged monthly uncertainty in SOC due to uncertainty in change of temperature (Temp.), tangent height registration (Tght), O₃ absorption cross sections (Cr), albedo (Alb), aerosol extinction (Aer) and pressure (Press) for the zonal band, 20°S - 20°N in 2004. Similar information is shown in tables 5.3 and 5.4 but for 60°S - 30°S and 30°N - 60°N, respectively. The uncertainty due to a change in O₃ absorption cross sections was estimated by replacing the SCIAMACHY proto-flight model (PFM) cross sections (Bogumil *et al.*, 2003) used in limb retrievals by the GOME flight model (FM) cross sections (Burrows *et al.*, 1999).

The values of the uncertainties derived from the change in the values of each parameter in a zonal band are nearly constant throughout the year. The uncertainty due to change in temperature (-0.8 DU (-0.3 %)), O₃ absorption cross sections (0.2 DU (0.1 %)), albedo (~-1.4 DU (-0.5 %)), and pressure (~1.9 DU (0.7 %)) exhibit similar values in both 60°S - 30°S and 30°N - 60°N zonal bands. The uncertainty contribution from change in tangent height registration is higher in the SH than in the NH (2.8 DU (1 %) versus 1.45 DU (0.5 %)). Conversely, the uncertainty due to a change in aerosol value is higher in the NH than in the SH (1.4 DU (0.5 %)) versus (-0.9 DU (-0.3 %)). The aerosol loading uncertainty depends on the scattering phase function and hence on the scattering angle.

Month	σ of Temp		σ of Tght		σ of Cr		σ of Alb		σ of Aer		σ of Press	
	DU	%	DU	%	DU	%	DU	%	DU	%	DU	%
200401	-0.8	-0.3	3.1	1.4	0.2	0.1	-1.9	-0.8	-0.9	-0.4	1.6	0.7
200402	-0.8	-0.3	3.2	1.4	0.2	0.1	-1.9	-0.8	-0.9	-0.4	1.6	0.7
200403	-0.8	-0.3	3.2	1.4	0.2	0.1	-1.9	-0.8	-0.9	-0.4	1.6	0.7
200404	-0.8	-0.3	3.2	1.4	0.2	0.1	-1.9	-0.8	-0.9	-0.4	1.6	0.7
200405	-0.8	-0.3	3.2	1.4	0.2	0.1	-1.9	-0.8	-0.9	-0.4	1.6	0.7
200406	-0.8	-0.3	3.2	1.4	0.2	0.1	-1.9	-0.8	-0.9	-0.4	1.6	0.7
200407	-0.8	-0.3	3.2	1.4	0.2	0.1	-1.9	-0.8	-0.9	-0.4	1.6	0.7
200408	-0.8	-0.3	3.2	1.4	0.2	0.1	-1.9	-0.8	-0.9	-0.4	1.6	0.7
200409	-0.8	-0.3	3.2	1.4	0.2	0.1	-1.9	-0.8	-0.9	-0.4	1.6	0.7
200410	-0.8	-0.3	3.2	1.4	0.2	0.1	-1.9	-0.8	-0.9	-0.4	1.6	0.7
200411	-0.8	-0.3	3.2	1.4	0.2	0.1	-1.9	-0.8	-0.9	-0.4	1.6	0.7
200412	-0.8	-0.3	3.1	1.4	0.2	0.1	-1.9	-0.8	-0.9	-0.4	1.6	0.7
Mean	-0.8	-0.3	3.2	1.4	0.2	0.1	-1.9	-0.8	-0.9	-0.4	1.6	0.7

Table 5.2: Zonal monthly averaged uncertainties (σ) due to change in temperature (Temp.), tangent height registration (Tght), O₃ absorption cross sections (Cr), albedo (Alb), aerosol extinction (Aer) and pressure (Press) for 20°S - 20°N in 2004.

5. TROPOSPHERIC OZONE COLUMN RETRIEVALS FROM SATELLITE AND OZONESONDE INSTRUMENTS

Month	σ of Temp		σ of Tght		σ of Cr		σ of Alb		σ of Aer		σ of Press	
	DU	%	DU	%	DU	%	DU	%	DU	%	DU	%
200401	-0.9	-0.3	2.8	1.0	0.2	0.1	-1.4	-0.5	-0.9	-0.3	1.9	0.7
200402	-0.9	-0.3	2.8	1.0	0.2	0.1	-1.5	-0.5	-0.9	-0.3	1.9	0.7
200403	-0.9	-0.3	2.8	1.0	0.2	0.1	-1.5	-0.5	-0.9	-0.3	1.9	0.7
200404	-0.9	-0.3	2.8	1.0	0.2	0.1	-1.5	-0.5	-0.9	-0.3	1.9	0.7
200405	-0.9	-0.3	2.8	1.0	0.2	0.1	-1.5	-0.5	-0.9	-0.3	1.9	0.7
200406	-0.9	-0.3	2.8	1.0	0.2	0.1	-1.5	-0.5	-0.9	-0.3	1.9	0.7
200407	-0.9	-0.3	2.8	1.0	0.2	0.1	-1.4	-0.5	-0.9	-0.3	1.9	0.7
200408	-0.9	-0.3	2.9	1.0	0.2	0.1	-1.5	-0.5	-0.9	-0.3	1.9	0.7
200409	-0.9	-0.3	2.8	1.0	0.2	0.1	-1.5	-0.5	-0.9	-0.3	1.9	0.7
200410	-0.9	-0.3	2.8	1.0	0.2	0.1	-1.5	-0.5	-0.9	-0.3	1.9	0.7
200411	-0.9	-0.3	2.8	1.0	0.2	0.1	-1.4	-0.5	-0.9	-0.3	1.9	0.7
200412	-0.9	-0.3	2.7	1.0	0.2	0.1	-1.4	-0.5	-0.9	-0.3	1.9	0.7
Mean	-0.9	-0.3	2.8	1.0	0.2	0.1	-1.4	-0.5	-0.9	-0.3	1.9	0.7

Table 5.3: Same as Table 5.2 but for 60°S - 30°S in 2004.

Month	σ of Temp		σ of Tght		σ of Cr		σ of Alb		σ of Aer		σ of Press	
	DU	%	DU	%	DU	%	DU	%	DU	%	DU	%
200401	-1.0	-0.3	1.4	0.5	0.2	0.1	-1.3	-0.5	1.3	0.5	1.9	0.7
200402	-1.0	-0.3	1.4	0.5	0.2	0.1	-1.3	-0.5	1.4	0.5	2.0	0.7
200403	-1.0	-0.3	1.4	0.5	0.2	0.1	-1.3	-0.5	1.4	0.5	2.0	0.7
200404	-0.9	-0.3	1.4	0.5	0.2	0.1	-1.3	-0.5	1.3	0.5	1.9	0.7
200405	-1.0	-0.3	1.5	0.5	0.2	0.1	-1.3	-0.5	1.5	0.5	2.0	0.7
200406	-0.9	-0.3	1.4	0.5	0.2	0.1	-1.3	-0.5	1.3	0.5	1.9	0.7
200407	-1.0	-0.3	1.4	0.5	0.2	0.1	-1.3	-0.5	1.4	0.5	1.9	0.7
200408	-1.0	-0.3	1.5	0.5	0.2	0.1	-1.3	-0.5	1.5	0.5	2.0	0.7
200409	-1.0	-0.3	1.4	0.5	0.2	0.1	-1.3	-0.5	1.4	0.5	1.9	0.7
200410	-1.0	-0.3	1.5	0.5	0.2	0.1	-1.4	-0.5	1.5	0.5	2.0	0.7
200411	-1.0	-0.3	1.5	0.5	0.2	0.1	-1.4	-0.5	1.6	0.5	2.0	0.7
200412	-1.0	-0.3	1.5	0.5	0.2	0.1	-1.3	-0.5	1.5	0.5	2.0	0.7
Mean	-1.0	-0.3	1.4	0.5	0.2	0.1	-1.3	-0.5	1.4	0.5	1.9	0.7

Table 5.4: Same as Table 5.2 but for 30°N - 60°N in 2004.

Figures 5.7 and 5.8 show the SOC's uncertainties due to uncertainties in the different parameters for January 2004 and July 2004, respectively. The behaviour of the SOC uncertainty parameters is similar in both months except for O₃ absorption cross section and pressure uncertainties. In the tropics, the temperature uncertainty is slightly higher while the pressure, aerosol and albedo uncertainties are lower. The variation of all the parameter uncertainties is out-of-phase between the two hemispheres except for aerosol uncertainty where the variation in the SH is low. As mentioned above, the high contributions of aerosol uncertainty to the SOC uncertainty in the NH and those of the tangent height registration in the tropics and SH are observed.

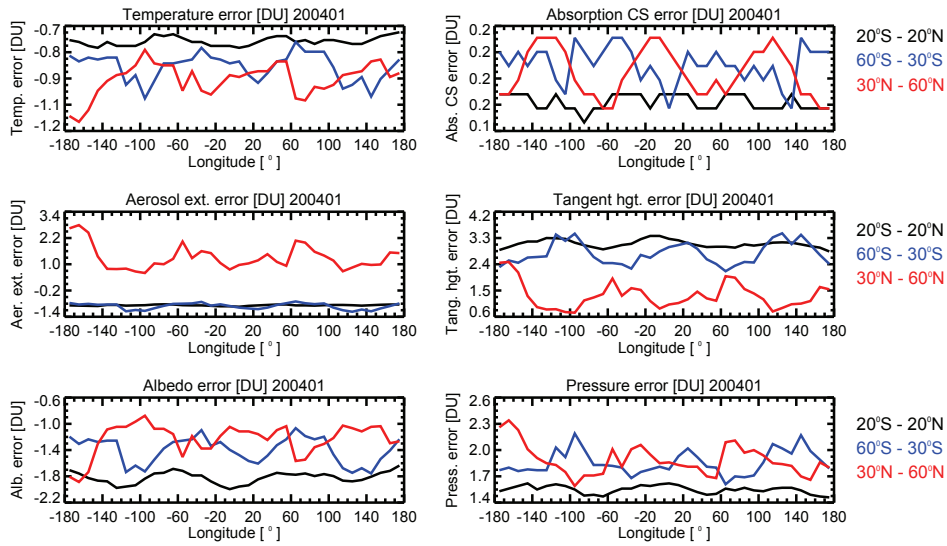


Figure 5.7: Monthly mean zonal mean error in SOCs parameter error in January 2004. From left to right; top panels: temperature and O₃ absorption cross section, middle panels: Aerosol loading and Tangent height registration, and bottom panels: albedo and pressure.

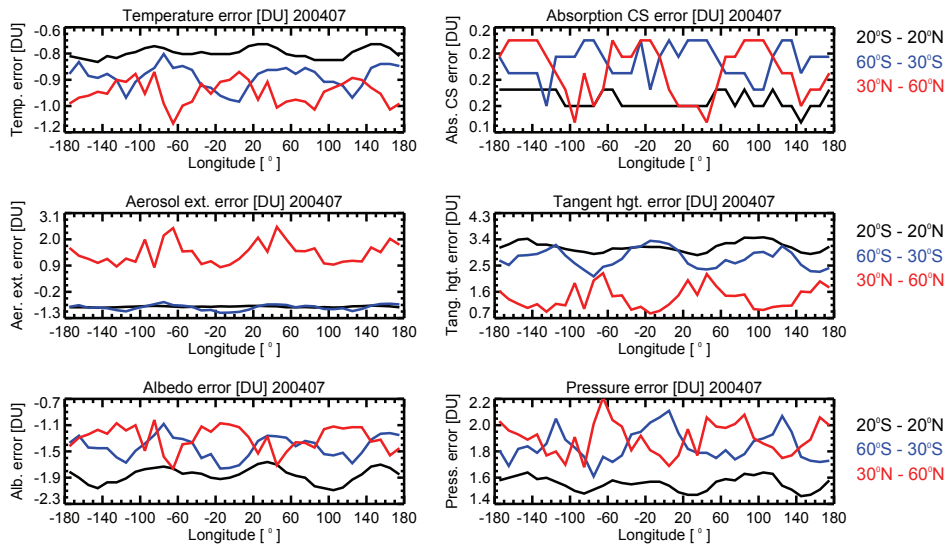


Figure 5.8: Same as Figure 5.7 but for July 2004.

5.4.2 Derivation of TOZ error parameters

The description of the method used to derive the uncertainty of TOZ due to uncertainty in its geophysical parameters has been shown by Coldewey-Egbers *et al.* (2005). The influence of the uncertainty contributions from the different parameters used to generate the reference database were investigated using synthetic radiance spectra. The largest contribution to the error in TOZ was identified to come from the *a-priori* errors associated with the O₃ climatology and from the

5. TROPOSPHERIC OZONE COLUMN RETRIEVALS FROM SATELLITE AND OZONESONDE INSTRUMENTS

uncertainty in the derived effective scene albedo. The effective albedo errors contribute about 1.5 % to the error of the retrieved O₃ column and an assumed effective height of the SCIAMACHY scene of 1 km results to an uncertainty of 1 % error in the TOZ. The interpolation errors from a look-up-table comprising the effective parameters and for SZA less than 80 % is below 0.3 % but may reach 1.5 % for SZA greater than 80°. The error from the GVC is found to be less than 0.2 %. In summary, the precision of the TOZ retrieval is estimated to be below 3 % for SZA less than 80° and better than 5 % up to SZA of 88°. In fact, comparison of SCIAMACHY TOZ with the TOZ derived from TOZs from ground-based and balloon-borne instruments agree typically within 1 % (e.g., Bracher *et al.*, 2005; Weber *et al.*, 2005, 2013). In the polar regions, and at high SZAs, biases can be larger (Weber *et al.*, 2005).

5.4.3 Combination of the SOC and TOC errors

The overall error in the retrieved TOCs as well as the derived global error budget were determined by combining the contributions of the various error sources as follows:

$$X_{toc} = \sqrt{X_{toz}^2 + X_{soc}^2 + X_{tph}^2}, \quad (5.7)$$

where X_{toc} is the TOC error, X_{toz} is the TOZ error, X_{soc} is the SOC error and X_{tph} is the contribution of the tropopause height error to the TOCs error. The influence of the tropopause height on the retrieved TOCs was estimated by using the standard deviation of the tropopause height in a latitude bin as a measure of uncertainty. This approach does not account for the TOC uncertainty resulting from the use of different methods to calculate the tropopause height.

Table 5.5 presents the zonally averaged monthly means and errors in TOC, SOC, TOZ and the effect of tropopause height (TPH) from 20°S - 20°N in 2004. Similar information is shown in tables 5.6 and 5.7 but for 60°S - 30°S and 30°N - 60°N, respectively. The mean value of the SOCs in the tropics is lower than in the NH and SH while its mean error value is higher in the tropics than in the NH and SH. The mean SOCs and their errors for the southern and northern zonal bands are similar, i.e., approximately 276.9 DU ± 4.3 DU (1.6 %). This may be associated with the balance in the error contribution from aerosol loading (maximum in the NH) and tangent height registration (maximum in the SH). For the TOZ, the mean values are lower in the tropics than at the NH and SH. While the mean TOZ value in the NH is higher than in the SH, the TOZ error is similar globally (3.0 DU (1 %)). The mean TOC is higher in the NH and has a lower mean error compared to the other zonal bands. The highest mean TOC error (5.6 DU (20.1 %)) is located in the SH.

Figures 5.9 and 5.10 show the zonal variation of monthly mean zonal mean error in TOCs, TOZs, SOCs and the contribution of the tropopause height error to the TOCs error in January 2004 and July 2004, respectively. The variations of the different errors are mostly out-of-phase

5.4 Sensitivity studies for the retrieval of tropospheric ozone column from SCIAMACHY

Month	Mean TOC	Resulting error in TOC		Mean SOC	Error of SOC		Mean TOZ	Error of TOZ		Mean TPH	Ozone error caused by TPH error	
		DU	%		DU	%		DU	%		DU	%
200401	29.2	5.5	18.9	228.4	4.9	2.1	257.7	2.6	1.0	16.8	0.1	0.3
200402	27.9	5.6	20.0	230.1	5.0	2.2	258.0	2.6	1.0	16.5	0.1	0.4
200403	30.0	5.6	18.8	232.0	5.0	2.1	261.9	2.6	1.0	16.6	0.1	0.4
200404	29.5	5.5	18.8	229.0	4.9	2.1	258.5	2.6	1.0	16.8	0.1	0.3
200405	28.3	5.6	19.6	229.1	4.9	2.1	257.4	2.6	1.0	16.6	0.1	0.4
200406	31.1	5.6	18.0	230.4	5.0	2.1	261.5	2.6	1.0	16.7	0.1	0.4
200407	29.5	5.5	18.8	228.6	4.9	2.1	258.1	2.6	1.0	16.8	0.1	0.4
200408	29.8	5.6	18.8	230.6	5.0	2.2	260.3	2.6	1.0	16.6	0.1	0.4
200409	31.1	5.6	18.0	231.0	5.0	2.1	262.1	2.6	1.0	16.7	0.1	0.3
200410	29.2	5.6	19.0	228.6	4.9	2.1	257.7	2.6	1.0	16.8	0.1	0.4
200411	29.9	5.6	18.9	231.5	5.0	2.2	261.3	2.6	1.0	16.7	0.1	0.4
200412	28.5	5.5	19.4	229.4	4.9	2.1	257.8	2.6	1.0	16.8	0.1	0.4
Mean	29.5	5.6	18.9	229.9	4.9	2.1	259.4	2.6	1.0	16.7	0.1	0.4

Table 5.5: Zonal monthly average and errors in tropospheric O₃ columns (TOCs), stratospheric O₃ columns (SOCs), total O₃ columns (TOZs), and the contribution of the tropopause height (TPH) error to the TOCs error from 20°S - 20°N in 2004.

Month	Mean TOC	Resulting error in TOC		Mean SOC	Error of SOC		Mean TOZ	Error of TOZ		Mean TPH	Ozone error caused by TPH error	
		DU	%		DU	%		DU	%		DU	%
200401	27.9	5.6	19.9	275.5	4.7	1.7	303.4	3.0	1.0	11.0	0.1	0.3
200402	26.3	5.6	21.3	278.1	4.7	1.7	304.3	3.0	1.0	10.9	0.1	0.3
200403	27.9	5.6	20.1	279.2	4.7	1.7	307.1	3.1	1.0	10.8	0.1	0.3
200404	26.9	5.6	20.7	275.9	4.7	1.7	302.8	3.0	1.0	10.9	0.1	0.3
200405	27.0	5.6	20.8	277.9	4.7	1.7	304.9	3.1	1.0	10.8	0.1	0.3
200406	28.9	5.7	19.6	280.7	4.7	1.7	309.6	3.1	1.0	10.8	0.1	0.2
200407	27.4	5.5	20.1	273.1	4.6	1.7	300.5	3.0	1.0	10.9	0.1	0.3
200408	28.3	5.6	19.9	278.3	4.7	1.7	306.6	3.1	1.0	10.8	0.1	0.2
200409	28.9	5.6	19.3	276.0	4.7	1.7	304.9	3.1	1.0	10.9	0.1	0.2
200410	27.5	5.5	20.1	274.1	4.6	1.7	301.6	3.0	1.0	10.6	0.1	0.3
200411	28.7	5.5	19.2	274.8	4.6	1.7	303.4	3.0	1.0	10.9	0.1	0.2
200412	27.1	5.4	19.7	268.3	4.5	1.7	295.4	3.0	1.0	11.0	0.1	0.3
Mean	27.7	5.6	20.1	276.0	4.6	1.7	303.7	3.0	1.0	10.8	0.1	0.3

Table 5.6: Same as Table 5.5 but from 60°S - 30°S in 2004.

between the two hemispheres. The TOZ error is mostly low in the tropics in both months. The mean SOC error is higher in the SH than in the NH in both months. Similar behaviours are also observed in the TOC error. The TOZ error and the contribution of the tropopause height error to the TOC error are similar in both months.

5. TROPOSPHERIC OZONE COLUMN RETRIEVALS FROM SATELLITE AND OZONESONDE INSTRUMENTS

Month	Mean TOC	Resulting error in TOC		Mean SOC	Error of SOC		Mean TOZ	Error of TOZ		Mean TPH	Ozone error caused by TPH error	
	DU	DU	%	DU	DU	%	DU	DU	%	km	DU	%
200401	33.4	5.0	14.9	272.9	3.9	1.4	306.3	3.1	1.0	12.4	0.1	0.3
200402	32.3	5.1	15.9	277.3	4.0	1.5	309.6	3.1	1.0	11.8	0.1	0.3
200403	32.2	5.1	15.9	278.1	4.0	1.4	310.3	3.1	1.0	12.2	0.1	0.3
200404	32.0	4.9	15.3	270.5	3.8	1.4	302.6	3.0	1.0	12.3	0.1	0.3
200405	31.4	5.2	16.6	281.4	4.1	1.5	312.7	3.1	1.0	11.9	0.1	0.3
200406	34.5	4.9	14.2	270.2	3.8	1.4	304.7	3.1	1.0	12.3	0.1	0.3
200407	35.7	5.1	14.3	277.1	4.0	1.4	312.7	3.1	1.0	12.2	0.1	0.3
200408	34.6	5.2	15.1	280.8	4.1	1.5	315.4	3.2	1.0	12.0	0.1	0.3
200409	36.9	5.1	13.8	277.6	4.0	1.4	314.5	3.1	1.0	12.3	0.1	0.3
200410	36.9	5.3	14.5	283.7	4.2	1.5	320.5	3.2	1.0	11.8	0.1	0.3
200411	37.1	5.4	14.4	283.4	4.2	1.5	320.5	3.2	1.0	11.9	0.1	0.3
200412	39.1	5.3	13.4	280.4	4.1	1.5	319.5	3.2	1.0	12.1	0.1	0.3
Mean	34.7	5.1	14.9	277.8	4.0	1.5	312.4	3.1	1.0	12.1	0.1	0.3

Table 5.7: Same as Table 5.5 but from 30°N - 60°N in 2004.

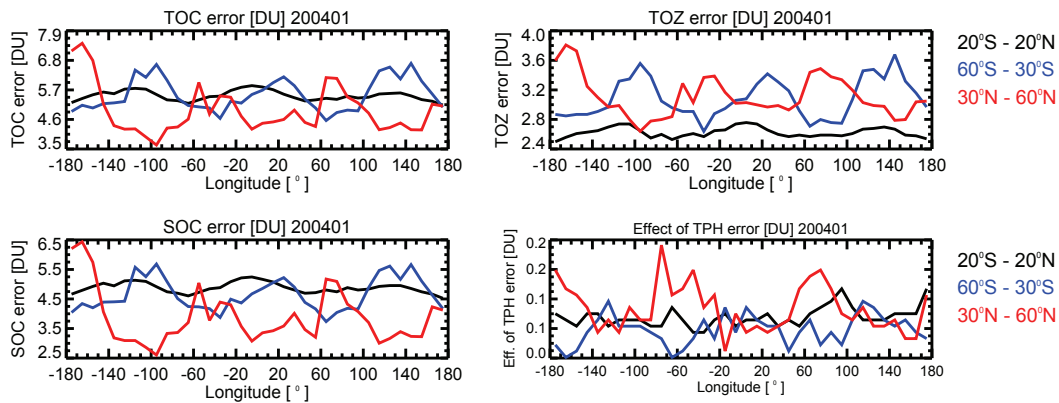


Figure 5.9: Top panels from left to right: Zonal variation of the monthly mean error in tropospheric ozone columns (TOCs) and total ozone (TOZ). Bottom panels from left to right: Zonal variation of the monthly mean error of stratospheric ozone column (SOC) and contribution from error in tropopause height (TPH) to the error in TOC in January 2004.

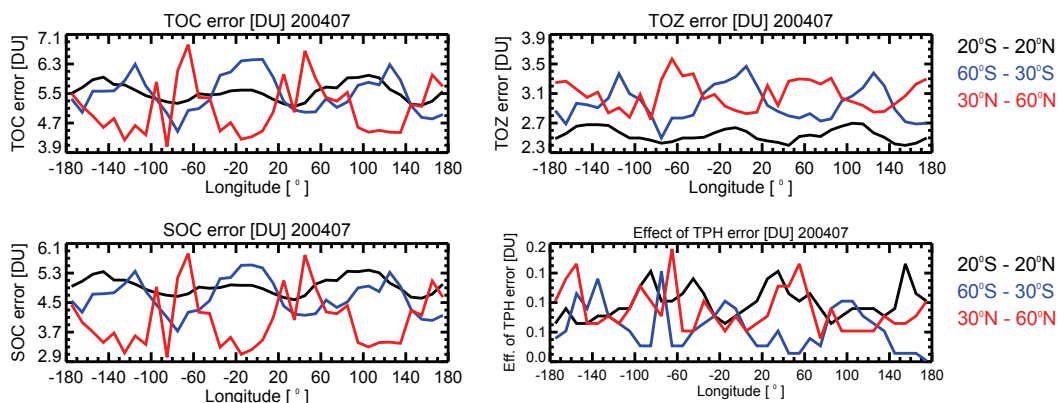


Figure 5.10: Same as Figure 5.9 but for July 2004.

5.4.3.1 Influence of nadir cloud fraction on TOC errors

To further quantify the influence of the vertical ghost column (GVC) on the retrieved TOC, a sensitivity analysis on the impact of the nadir cloud fraction (cf) threshold was performed. The TOC retrieval was derived first by setting the nadir cf threshold at $\leq 0\%$. The retrieval process was then repeated for other cf thresholds ($\leq 5\%$, $\leq 10\%$, $\leq 15\%$, $\leq 30\%$). From the analysis, it was found that $cf \leq 10\%$ is optimal for statistical analysis. The error value estimated from a global TOC mean using $cf \leq 0\%$ is higher than that of $cf \leq 10\%$ because of less measurements. For $cf \leq 30\%$, questionable TOC values were derived at the high latitudes. The results of the comparisons of the SCIAMACHY TOCs retrieved at different cloud fractions with those of the ozonesonde and other satellite instruments are discussed in section 6.2

5. TROPOSPHERIC OZONE COLUMN RETRIEVALS FROM SATELLITE AND OZONESONDE INSTRUMENTS

SECTION III

Results



Chapter 6

Validation of SCIAMACHY tropospheric ozone columns

6.1 Tropospheric ozone columns retrieved from SCIAMACHY measurements and intercomparison with ozonesondes and other satellite instruments

Global measurements of tropospheric O₃ are needed to test our understanding of its sources, seasonal variations, and long-range transport (Creilson *et al.*, 2003, 2005). They also allow for the generation of temporally extended records that are vital for the investigation of long term trends (Fishman *et al.*, 2005; Kim & Newchurch, 1996; Valks *et al.*, 2003).

Tropospheric O₃ is a strongly seasonal pollutant, exhibiting usually higher concentrations in the spring and summer months. The tropospheric O₃ seasonality is caused by variation in tropospheric background O₃, temporal variation of precursor emissions (NO_x, NMVOCs, CO, CO₂, CH₄), systematic seasonal changes in transport meteorology as well as the seasonality of photochemical oxidation and removal processes. Emissions of O₃ precursors from anthropogenic and biomass burning sources have driven up tropospheric O₃ concentrations since the pre-industrial era (Lamarque *et al.*, 2010). Apart from anthropogenic precursor emissions, significant variability in O₃ has also been observed from natural sources of precursor emissions including wetland CH₄, soil and lightning NO_x, and biogenic NMVOCs (Arneth *et al.*, 2010), which may also have changed since the pre-industrial era. Increase in tropospheric O₃ also arises from downward transport of O₃ rich airmasses from the stratosphere (Tang *et al.*, 2011). Interannual variations of sporadically occurring pollution events, e.g., forest fires and meteorological patterns, such as El Nino Southern Oscillation (ENSO), Rossby and gravity waves in the tropics (Randel & Thompson, 2011), as well as the North Atlantic Oscillation in mid-latitudes (Thouret *et al.*, 2006) have been found to impact

6. VALIDATION OF SCIAMACHY TROPOSPHERIC OZONE COLUMNS

tropospheric O₃. Long-term changes in stratospheric O₃ and short-term stratospheric anomalies of O₃ due to volcanic eruptions also influence the tropospheric O₃ amount (WMO, 2010). Additionally, the interannual variability of tropospheric O₃ is influenced by the interannual variability in stratospheric O₃ (Hess & Zbinden, 2013; Tarasick *et al.*, 2005). Ozone and its precursors are also transported between continents. Trans – Pacific transport of Asian pollution affects North America (e.g., Jaffe *et al.*, 1999; Parrish *et al.*, 2012; Yienger *et al.*, 2000), the trans-Atlantic transport of North American pollution influences pollution over Europe (Derwent *et al.*, 1998; Logan *et al.*, 2012), and trans-Eurasian transport of European pollution affects Asia (Liu *et al.*, 2002; Parrish *et al.*, 2012). O₃ enhancements can also occur over downwind regions from the decomposition of NO_x reservoirs such as PAN and HNO₃. Therefore, the TOC over a particular region depends on local, regional and import of air masses from upwind emissions (HTAP, 2010; Law *et al.*, 2010). The increase in tropospheric O₃ concentrations since industrialisation has been quantified from atmospheric chemistry, transport, surface exchange, emission estimates and climate coupled models (e.g., Gauss *et al.*, 2006b; Wang & Jacob, 1998). Low O₃ amounts are observed in some regions, which may have resulted from different O₃ removal or loss processes, including chemical, physical and biological means. These are a result of reduction in anthropogenic O₃ precursors emissions, changes in O₃ distribution as well as changes in HO_x (Stevenson *et al.*, 2006). Dry deposition of O₃ at the surface and mostly to vegetation has been influenced by change in land-use as well as change in climate and CO₂ abundance (e.g., Wu *et al.*, 2012).

Figures 6.3 – 6.12 show the global distributions of tropospheric O₃ from SCIAMACHY for the four seasons. Winter (DJF), spring (MAM), summer (JJA) and autumn (SON) for each year from December 2002 to November 2011, which are overlaid with tropospheric O₃ from ozonesondes (filled circles). SCIAMACHY TOC values at high latitudes is flagged as missing data involving polar night latitudes (regions where there are no SCIAMACHY measurements) and additional data flagging such as SCIAMACHY scenes with solar zenith angles greater than 85° or arguable TOC values at high latitudes. Similar pollution features can be observed in the same season from year to year throughout the entire period investigated. Significant differences between the northern and southern hemispheres as well as differences between the seasons are observed. The SCIAMACHY TOC shows annual variability and regional patterns. The seasonal distribution of TOC in both hemispheres shows good correlation with its precursors (Liu *et al.*, 2008; Logan & Kirchhoff, 1986). High levels of TOC in the NH mid-latitudes are observed over the eastern part of the North American continent and across the Atlantic Ocean. High TOC values are also observed over the eastern part of the Asian continent extending across the Pacific Ocean. Elevated TOCs are observed over the tropical southern Atlantic as well as at SH mid-latitudes and over the Indian Ocean. As the tropospheric O₃ budget is strongly linked with NO_x and considering

6.1 Tropospheric ozone columns retrieved from SCIAMACHY measurements and intercomparison with ozonesondes and other satellite instruments

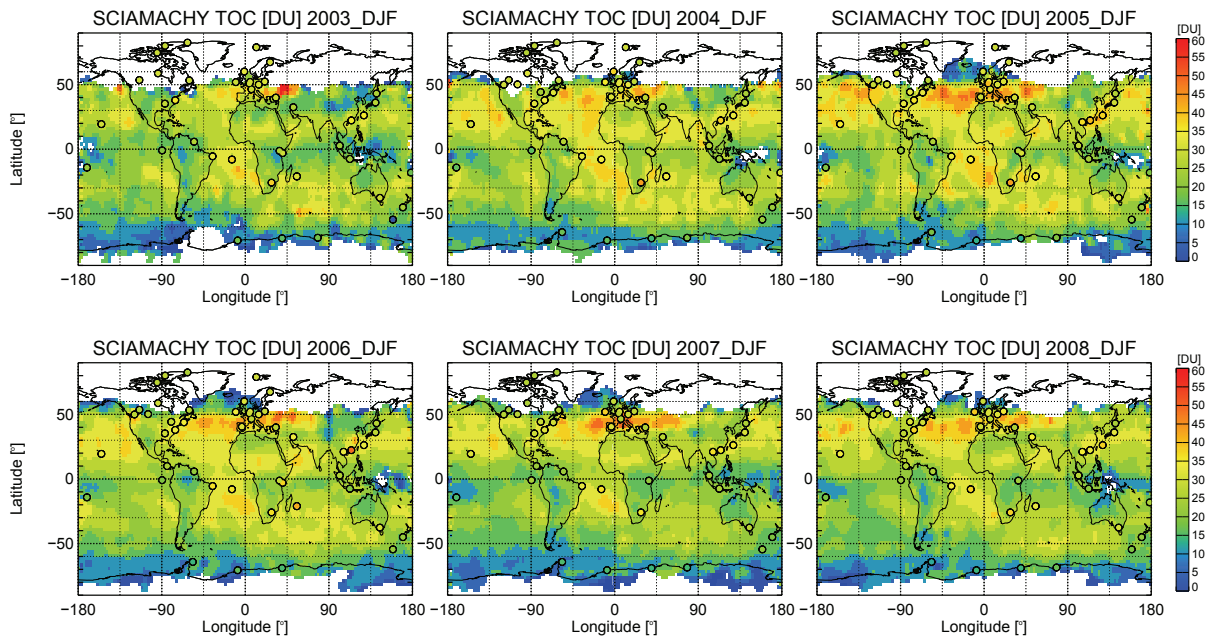
that the lifetime of NO_x with respect to oxidation to HNO_3 is of the order of days, it would be expected that NO_x concentrations would decay rapidly downwind of the continents. However, enhanced TOC values over the ocean are due to chemical recycling of NO_x from HNO_3 and other non-radicals reservoirs in the free troposphere such as PAN, which play major roles in maintaining NO_x concentrations over the oceans. Also of importance in maintaining NO_x level over the ocean is the fast conversion of HNO_3 to NO_x in aerosols (Jacob *et al.*, 2002; Singh *et al.*, 1994). The change of the North Atlantic Oscillation from the predominantly high positive phase to alternating between negative, neutral or positive phases has resulted in an increased flow of the westerlies in the mid-latitudes and subtropical North Atlantic. This promotes the transport of O_3 and its precursors from North America as well as higher frequency of storms over the North Atlantic, with possibly a higher incidence of STS processes in the mid-latitudes. These processes result in an increase of tropospheric O_3 in the subtropical North Atlantic region.

The tropospheric O_3 wave-one feature, which is persistent in the southern tropics with higher TOC values over the southern Atlantic tropics than the Pacific as reported elsewhere (e.g., Chandra *et al.*, 2003; Edwards *et al.*, 2003), is observed in all the seasons. Nearly zonal bands of enhanced TOC of 35 – 45 DU at 20°S – 50°S during austral spring and 35 – 55 DU at 20°N – 50°N during boreal spring and summer are displayed in the global distribution of TOC from SCIAMACHY. The TOC values derived from SCIAMACHY are in good agreement with the values derived from the local/regional in-situ measurements obtained from the ozonesonde instrument. In the southern mid-latitudes, TOC maximizes during boreal autumn and minimizes during boreal spring while in the northern mid-latitudes, TOC maximizes during boreal spring and minimizes during boreal winter season. The TOC values at the northern high latitudes (>60°N) are larger and show more scatter than the TOC at the southern high latitudes. For example, TOC values of 30 – 50 DU are observed during MAM and JJA above 60°N except the persistent low TOC values over the high-terrain Greenland, while TOC values of less than 30 DU are observed above 60°S during austral spring and summer.

Tropospheric O_3 features in the different seasons are summarized as follows. In DJF (figures 6.3), a local maximum in SCIAMACHY TOC is observed in the southern Atlantic region, which is explained by emissions from extensive biomass burning, upper tropospheric O_3 production from lightning NO_x and continuous subsidence due to the Walker circulation (e.g., Fishman *et al.*, 2003; Moxim & Levy II, 2000; Thompson *et al.*, 2000). O_3 precursors produced during petroleum extraction activities can contribute to tropospheric O_3 formation in this region (Jaffe, 1991; Schnell *et al.*, 2011). TOC values in the southern tropical Atlantic are higher than those in the northern tropical Atlantic (30 – 45 DU versus 20 – 35 DU, tropospheric O_3 Atlantic paradox) (Thompson *et al.*, 2000). The prevalence of easterly winds in the lower troposphere, which transit to westerly

6. VALIDATION OF SCIAMACHY TROPOSPHERIC OZONE COLUMNS

winds at pressure levels lower than 500 hPa play a great role in the outflow from West Africa. The persistent anticyclone over West Africa at about 700 hPa leads to strong easterly winds, which causes a net outflow of O_3 and its precursors from biomass burning in West Africa across the Atlantic Ocean towards South America. Transport of O_3 and its precursors from South America especially from the Brazilian coast also contribute to the enhancement of O_3 in the southern tropics. Lightning over land areas in Central Africa and South America as well as convective systems in the Gulf of Guinea can also contribute to enhanced O_3 levels in the upper troposphere especially over the Southern tropical Atlantic during boreal winter season (Jenkins & Ryu, 2004; Thompson *et al.*, 2000). Elevated tropospheric O_3 amounts observed over the northern Atlantic and Pacific mid-latitudes are due to long-range transport of photochemically generated O_3 from North America, Europe and East Asia as well as systematic downward transport from the stratosphere, which is associated with the strong jet stream off the east coast of Asia (e.g., Chandra *et al.*, 2004; Parrish *et al.*, 2012; Stohl *et al.*, 2007, 2003). There are no ozonesonde measurements over the northern Atlantic, but the TOC values derived from ozonesondes over the NH continents and northern Pacific during the boreal winter season are in agreement with those derived from SCIAMACHY (i.e., 15 - 30 DU versus 15 - 35 DU). Also during this season, the tropospheric O_3 distribution exhibits laminar structures with latitudinal gradients where TOC values decreases from the mid-latitudes to the polar regions. During boreal winter, there is a transition in TOC values, whereby the high TOC values that occur in the SH during SON are substantially reduced. These low O_3 values are clearly observed in January and February with pronounced hemispheric symmetry, which can be attributed to seasonal minimum in biomass burning (e.g., de Laat *et al.*, 2005; Duncan *et al.*, 2003).



6.1 Tropospheric ozone columns retrieved from SCIAMACHY measurements and intercomparison with ozonesondes and other satellite instruments

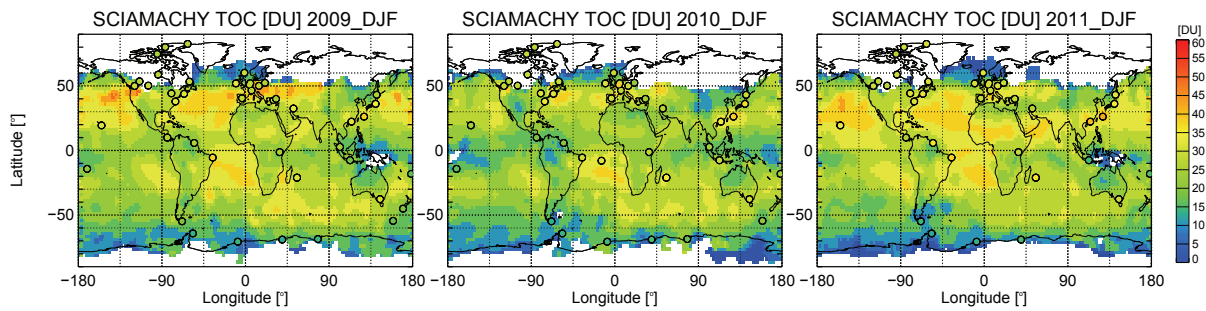


Figure 6.3: Tropospheric O_3 distributions (in Dobson Units (DU)) for December-January-February (DJF) in 2003 – 2011 from SCIAMACHY. The colors in the panels going from blue to red represent smallest to largest values, respectively.

During the boreal winter season, the lowest tropospheric O_3 values are found at the southern polar latitudes.

During northern spring (Figure 6.6), the tropospheric O_3 distribution from SCIAMACHY in both hemispheres shows similar local/regional features when compared to the in-situ measurements from ozonesondes. Enhanced pollution is observed from North America over the Atlantic ocean, central China, downwind of south east Asia and towards the Northern Pacific with tropospheric O_3 values of about 50 DU. The high tropospheric O_3 values in the northern subtropics and mid-latitudes are associated primarily to STE processes, which assume an annual maximum in this zonal band (Chandra *et al.*, 2004). Also of importance to the enhancement of O_3 in this zonal band are tropospheric O_3 production sources including lightning, combustion of fossil fuels, biomass burning and soil emissions (Pfister *et al.*, 2008; Thompson *et al.*, 2007a, 2008). The high TOC in the northern mid-latitudes over the Atlantic and Pacific Oceans is as large as the TOC over industrial emission regions (Chandra *et al.*, 2004). In most of the years, the springtime O_3 maximum in the northern subtropics is on average more pronounced in the Eastern Pacific than the Western. This is due to the Eastern Pacific being a dominant location for stratospheric intrusions (Waugh & Polvani, 2000). The high O_3 values over Southeast Asia is a combination from downward transport of stratospheric O_3 rich air masses, photochemical production in the upper troposphere as well as Southeast Asia biomass burning in the lower troposphere (Parrish *et al.*, 2012; Stohl *et al.*, 2007, 2003). Lowest TOC values (5 - 15 DU) are observed in the tropical pacific during boreal spring season. These low O_3 values are associated with photochemical sink and convection in this region (Kley *et al.*, 1997). In MAM, the low TOC values are more pronounced in the Western tropical pacific than in the Eastern pacific due to the prevailing deep convection (Folkins *et al.*, 2002). Low O_3 values observed over the Andes are well pronounced during boreal spring.

6. VALIDATION OF SCIAMACHY TROPOSPHERIC OZONE COLUMNS

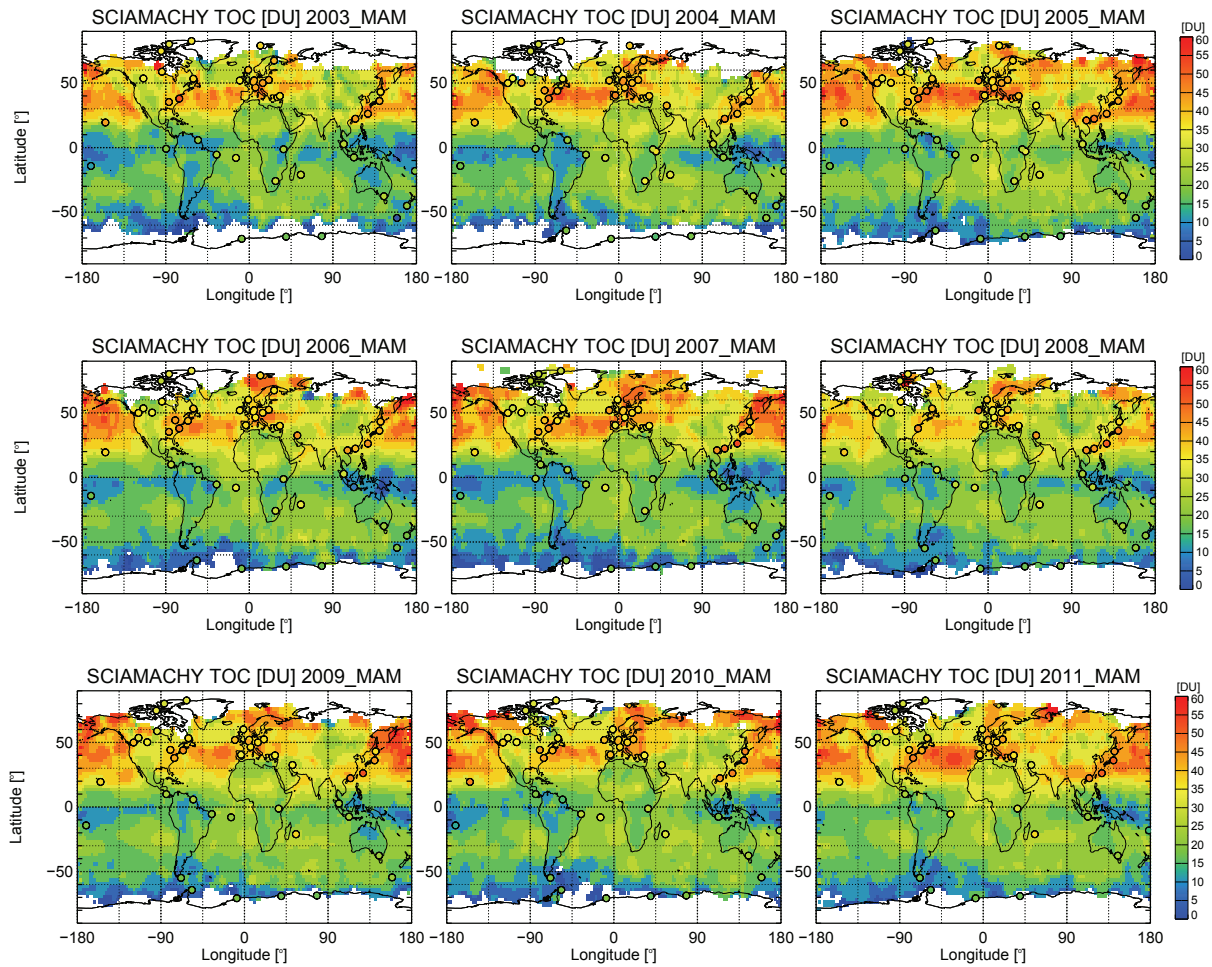


Figure 6.6: Same as Figure 6.3 but for March-April-May (MAM).

In boreal summer (Figure 6.9), large values of TOC occur in the northern subtropics and mid-latitudes. SCIAMACHY captured plumes of high tropospheric O_3 of about 35 – 50 DU in the northern subtropics and over eastern United States, the Mediterranean, eastern Asia, Russia, North Atlantic and North Pacific with the TOC values from SCIAMACHY in close agreement with the local or regional in-situ measurements from ozonesondes. The high level of tropospheric O_3 during boreal summer is primarily photochemically produced from anthropogenic pollution, biogenic VOCs and NO_x (Chandra *et al.*, 2004). Pollution effects with sources from STE, biomass burning, lightning also play a role during this season of the year (Pfister *et al.*, 2008; Thompson *et al.*, 2008). The maximum summertime O_3 values in the northern extratropics are due to a combination of different effects including STE, lightning, biomass burning, and pollution from fossil fuel combustion (James *et al.*, 2003; Oltmans *et al.*, 1996b). Strong photochemical production with O_3 precursors from Asian pollution plays a key role for the O_3 enhancement in this region (e.g., Liu *et al.*, 2002; Oltmans *et al.*, 2004). Enhanced values of TOC are also observed over northern Africa and the

6.1 Tropospheric ozone columns retrieved from SCIAMACHY measurements and intercomparison with ozonesondes and other satellite instruments

Middle East. These can be attributed to the prevailing summer northwesterlies over the eastern Mediterranean (Dayan, 1986), which transport anthropogenic O₃ from Europe into the Middle East and northern Africa. Lower O₃ values in the northern subtropics are found along the Himalayas.

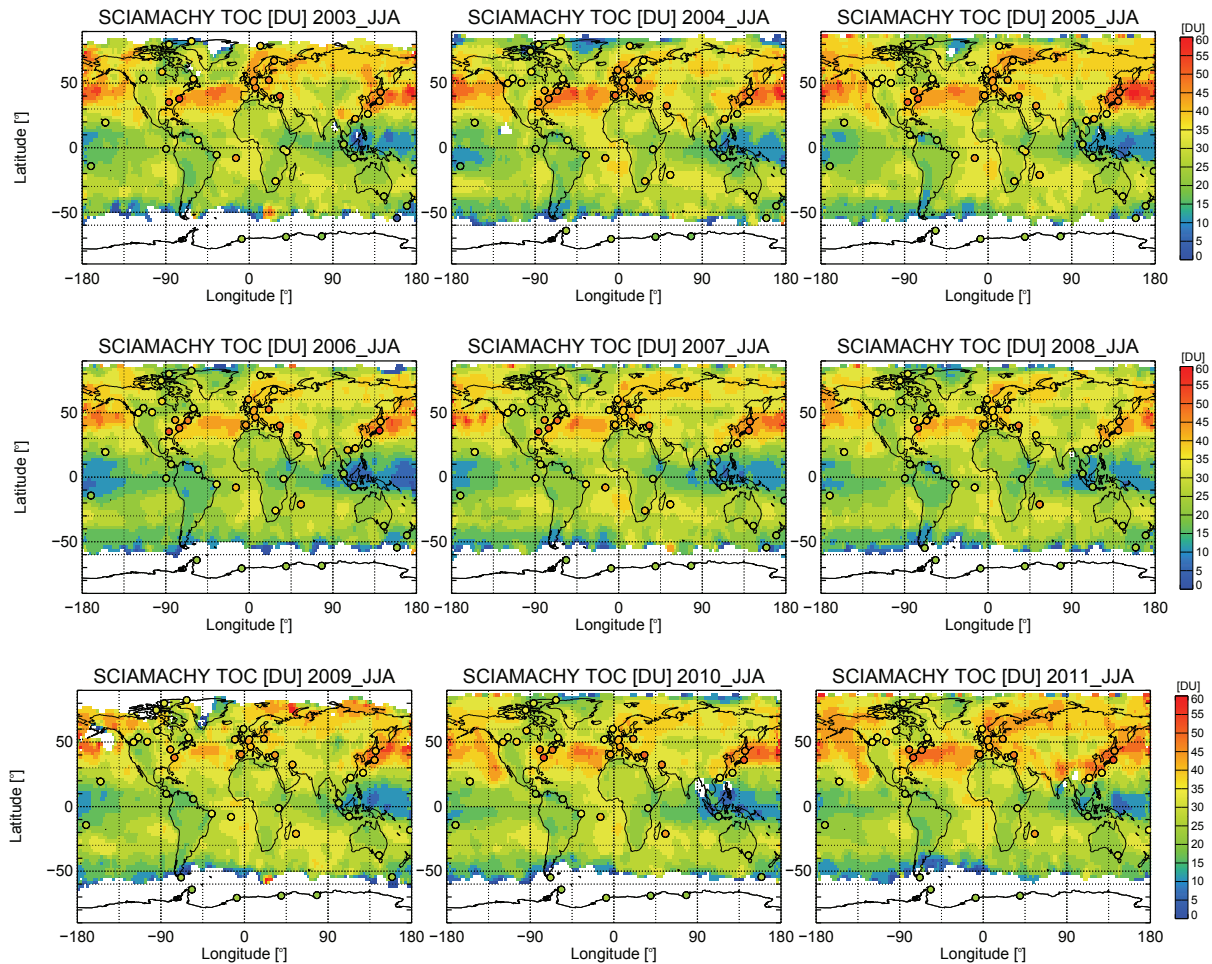


Figure 6.9: Same as Figure 6.3 but for June-July-August (JJA).

In boreal autumn (Figure 6.12), the pollution plumes observed by SCIAMACHY in both hemispheres are in close agreement with in-situ measurements from ozonesondes. The high TOC values that lie along a zonal band of approximately 30°S – 40°S in the SH are similar to the high values observed at the mid-latitudes in the NH during summer and spring. These seasonal enhancements in TOC are of dynamical origin caused by STE (de Laat *et al.*, 2005). SCIAMACHY observations show a broad O₃ maximum (30 – 45 DU) over the Southern Atlantic, the coast of South Africa and Madagascar. Transport along the Indian ocean towards Australia and plumes emanating from eastern Australia are also observed. Similar features have been reported elsewhere (e.g., Fishman *et al.*, 2003). The high O₃ values over the tropical Atlantic and Pacific are due to advection of

6. VALIDATION OF SCIAMACHY TROPOSPHERIC OZONE COLUMNS

subtropical high O_3 air into the tropics as well as from biomass burning, lightning, and continuous downward flow of O_3 rich air masses as part of the Walker circulation (Moxim & Levy II, 2000). Also during boreal autumn, relatively high TOC values of 30 - 40 DU occur over Southeastern US, as well as over the region of US outflow to the North Atlantic towards Southern Europe. High TOC values are also observed over the Middle East and the region of East Asia outflow to the North Pacific. The TOC values obtained in these regions are similar to those from ozonesondes and are in agreement with results given elsewhere (Liu *et al.*, 2002; Parrish *et al.*, 2012). SCIAMACHY values over Southern Europe, the Pacific and the middle east are also similar to the values observed by the ozonesondes in this region. Low O_3 values are found around the Eastern and Western pacific with some changes over the southeastern Pacific. This could be due to the shift of convection from the Western Pacific to the Central and Eastern Pacific during this season (Chandra *et al.*, 1998).

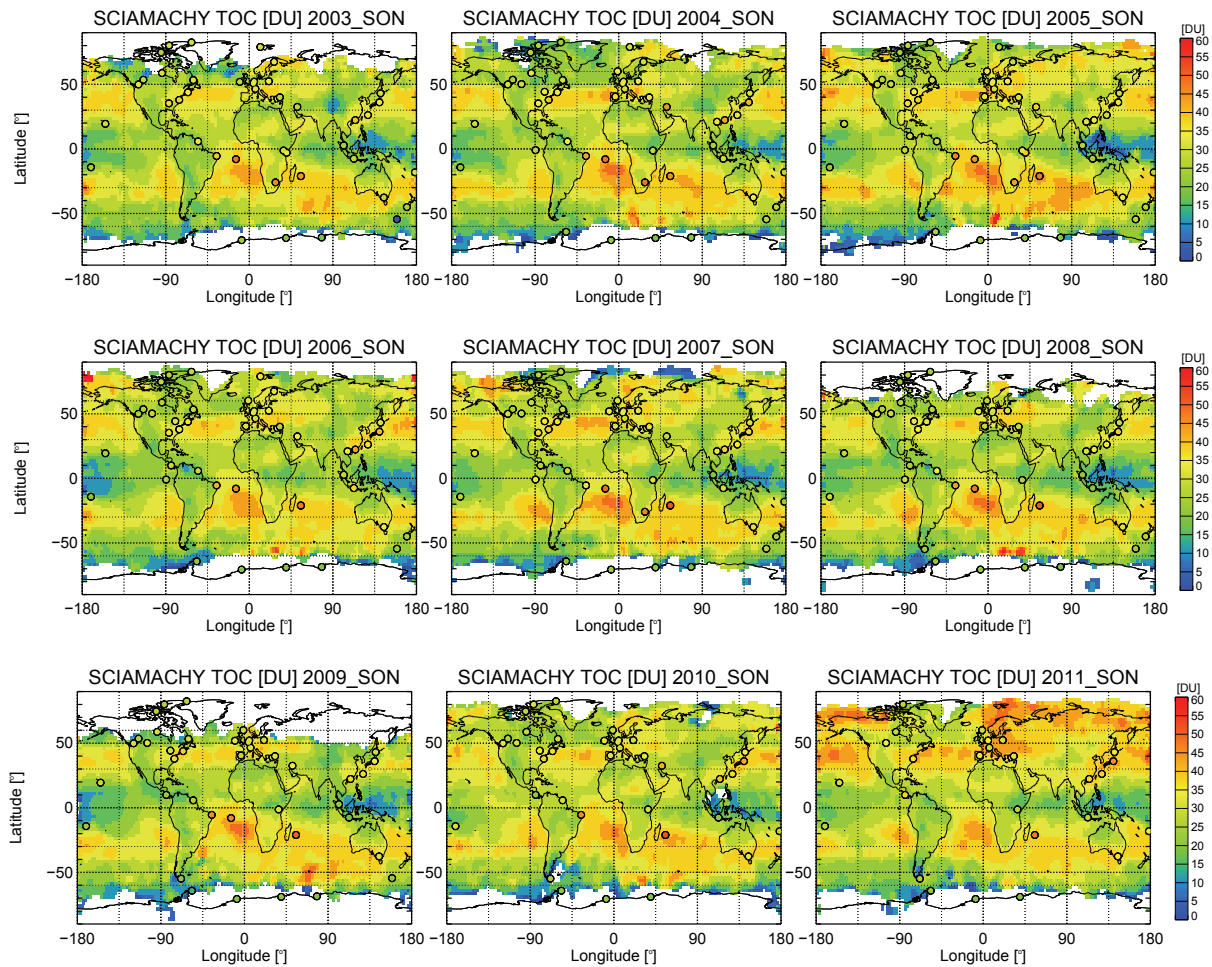


Figure 6.12: Same as Figure 6.3 but for September-October-November (SON).

Another interesting features observed during boreal autumn are the low TOCs over the Sahara

6.2 Intercomparison of tropospheric ozone columns from SCIAMACHY with TES, OMI/MLS and ozonesondes

Desert and the Andes Mountains in South America as previously reported by Fishman *et al.* (2003). These features are highly pronounced during boreal spring and summer.

6.2 Intercomparison of tropospheric ozone columns from SCIAMACHY with TES, OMI/MLS and ozonesondes

The accuracy of the TOC retrieved from SCIAMACHY was investigated by comparing with the TOCs measured by balloon-borne ozonesondes and those retrieved from TES and the combined OMI/MLS data products. The comparison of the TOCs retrieved from SCIAMACHY or other satellite instruments with those from the ozonesondes requires care. This is because the latter provide O_3 measurements along the trajectory paths of the sonde. These are different from satellite's measurements that yield averages above a ground scene. However, the quality of the ozonesonde measurements is well established (WOUDC, 2007). Furthermore, the determination of TOC from ozonesonde measurements does not require *a-priori* information. Therefore, ozonesonde measurements are used as a benchmark in this study to validate SCIAMACHY TOC (Ebojje *et al.*, 2014).

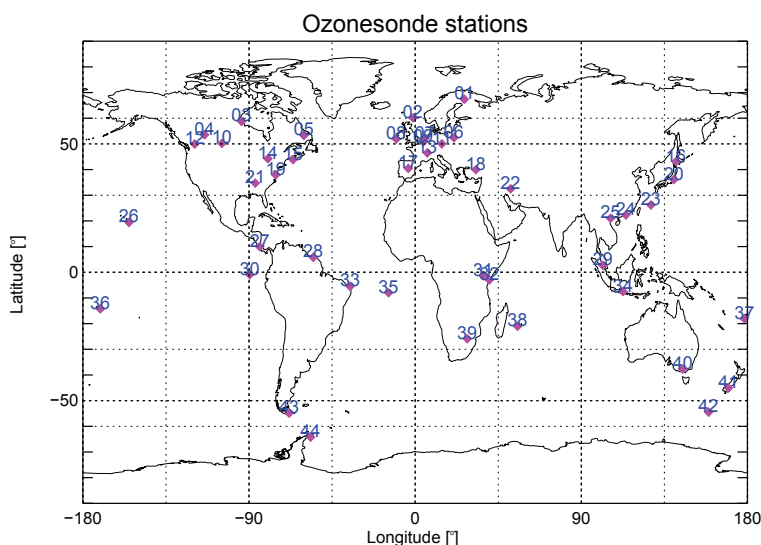


Figure 6.13: World map showing ozonesonde stations (station numbers are listed in Table 4) used in this study.

SCIAMACHY TOCs are validated using ozonesonde data from the Southern Hemisphere Additional OZonesondes (SHADOZ) and the World Ozone and Ultraviolet Radiation Data Centre (WOUDC) (see Figure 6.13), which are listed in Table 6.1. The table shows the SCIAMACHY results determined with a cloud fraction threshold of 10 %. Similar analyses were performed with different cloud fraction thresholds: 0 % (Appendix, Table 7.1), 5 % (Appendix, Table 7.2), 15 %

6. VALIDATION OF SCIAMACHY TROPOSPHERIC OZONE COLUMNS

(Appendix, Table 7.3), and 30 % (Appendix, Table 7.4). This was used to select the optimal cloud fraction threshold as discussed in section 5.4.3.1. Monthly means and standard deviations of SCIAMACHY TOCs were compared with collocated monthly means TOCs from ozonesondes, TES and OMI/MLS using the collocation criteria of $\pm 5^\circ$ in latitude and $\pm 10^\circ$ in longitude. The 1-sigma standard deviation represents an aggregate of the variability of tropospheric O_3 values and associated measurements errors. The ozonesonde data sets overlapping in time with the SCIAMACHY observation period extend from August 2002 to December 2011. However, due to the unavailability of measurements from TES and OMI/MLS before September 2004, the comparisons were limited to the period 2004 – 2011 for which all measurements were available.

Figures 6.14, 6.16 and 6.17, show the TOC time series for some selected ozonesonde stations (see Figure 6.13), while figures 6.15, 6.18, and 6.19 are the corresponding TOC anomaly (TOCA) plots. The anomalies were determined by subtracting from each individual time series, the mean TOC values calculated over the considered period. This approach removes inter-instrumental biases, thus allowing the seasonal variations to be compared more easily. The instruments are assigned the same color code and symbols in both plots for easy identification and comparison. TOC time series from the four instruments, SCIAMACHY (black), ozonesonde (red), TES (violet), and OMI/MLS (green) show a pronounced seasonal cycle with maximum values during spring and summer with slightly different amplitudes.

Figures 6.14 and 6.15 show the TOC and TOC anomaly (TOCA) time series, respectively for some selected tropical ozonesonde stations. The investigated stations in the southern tropics include Nairobi (1.27°S, 36.80°E), Natal (5.49°S, 35.26°W), Java (7.50°S, 112.60°E), Ascension Island (7.98°S, 14.42°W), Samoa (14.23°S, 170.56°W), Fiji (18.13°S, 178.40°E) and Reunion Island (21.06°S, 55.48°E). The southern tropical troposphere is dominated by convective overturning from December – June and strong subsidence, biomass burning as well as lightning NO_x from July – November (Thompson *et al.*, 2003). Depending on the station and the year, the minimum TOC values observed by all instruments occur between January and May while the maximum TOC values are observed between July and December, except above Nairobi, where there is weak seasonality in TOC. Over these regions, the three satellite instruments show similar TOC values and seasonal patterns, which differ slightly in magnitude. Ozonesonde measurements show generally lower minima and higher maxima TOCA values over these regions (Figure 6.15). For example, over Nairobi, ozonesondes recorded high TOCA values of >8 DU in September 2007 and lowest TOCA values of <-6 DU in December 2006 and November 2011. SCIAMACHY TOCA values are lower than those of the other instruments between February and June 2006 while TES shows lower TOCA values between January and March 2010. Above Natal, Java, Ascension Island, Samoa, Fiji and Reunion Island the seasonal behaviour of the satellite data sets is similar. Ozonesonde measurements show

6.2 Intercomparison of tropospheric ozone columns from SCIAMACHY with TES, OMI/MLS and ozonesondes

lowest/highest TOCA values of about -17 DU/16 DU over these regions. The northern tropical stations investigated include San Cristobal (0.92°N, 89.60°W), Sepang Airport (2.73°N, 101.70°E), Paramaribo (5.81°N, 55.21°W), Costa Rica (9.98°N, 84.21°W) and Hilo (19.72°N, 155.07°W).

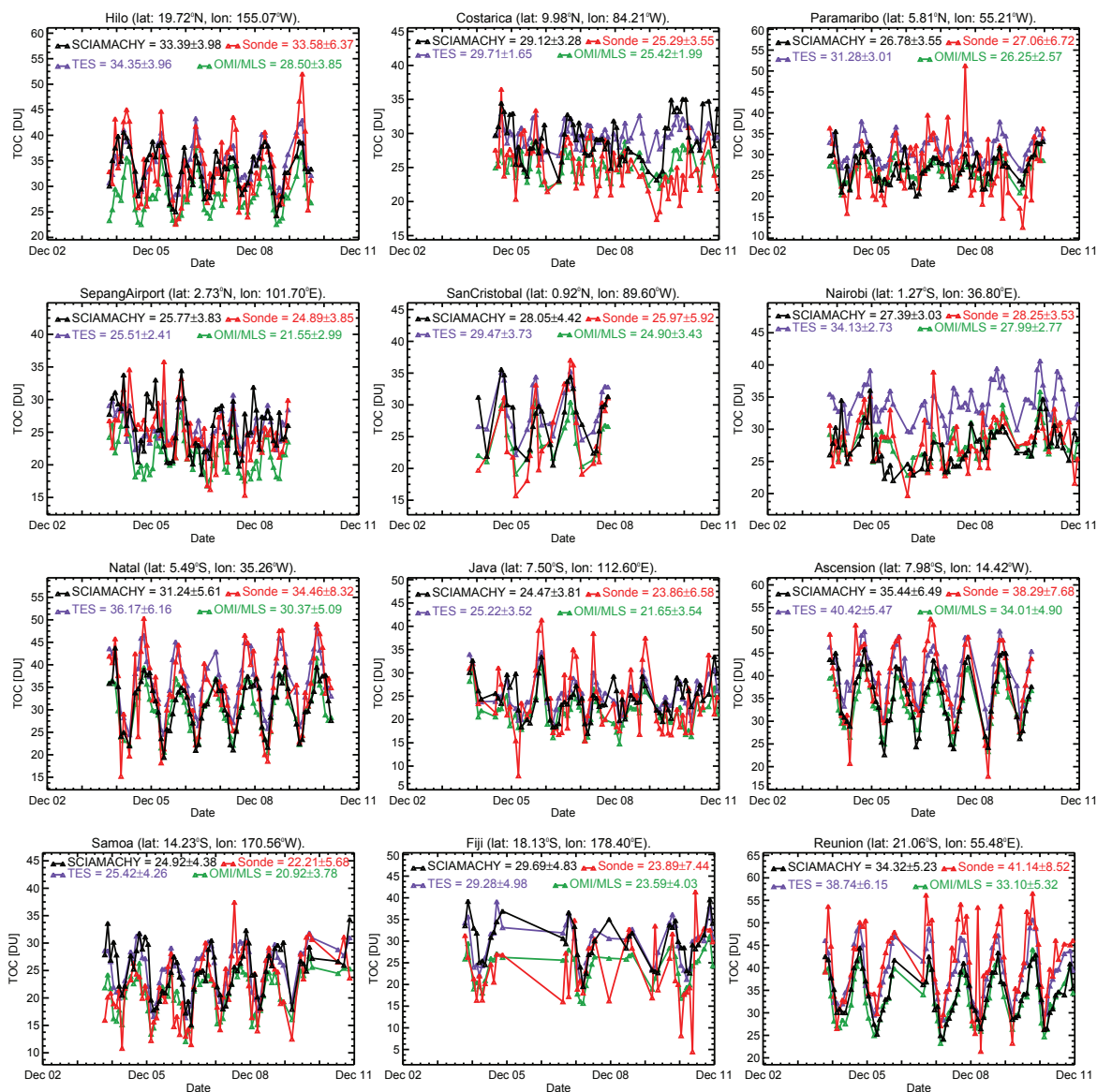


Figure 6.14: Monthly mean tropospheric O₃ column (TOC) in Dobson Units (DU) of tropical stations from SCIAMACHY (black), ozonesondes (red), TES (violet), and OMI/MLS (green).

Similar to the southern tropical stations, the seasonal pattern of the TOCA from all satellite measurements show good agreement except over Costa Rica in 2010. Ozonesonde measurements over these regions show minima and maxima TOCA values. Comparisons of the mean TOC values from SCIAMACHY, TES, OMI/MLS and ozonesondes in the southern Atlantic (Natal, Ascension

6. VALIDATION OF SCIAMACHY TROPOSPHERIC OZONE COLUMNS

Island, Nairobi) with the TOC values of the southern tropical pacific stations (Java, Fiji, Samoa) reveal the evidence of the tropospheric wave-one feature, with TOC values of southern tropical Atlantic stations higher than those at the southern tropical pacific stations. The tropospheric O_3 seasonal cycle in the tropical region is primarily governed by two processes: the annual migration of the inter-tropical convergence zone (ITCZ), which influences the vertical redistribution of O_3 through convection and subsidence as part of the Walker circulation (Moxim & Levy II, 2000).

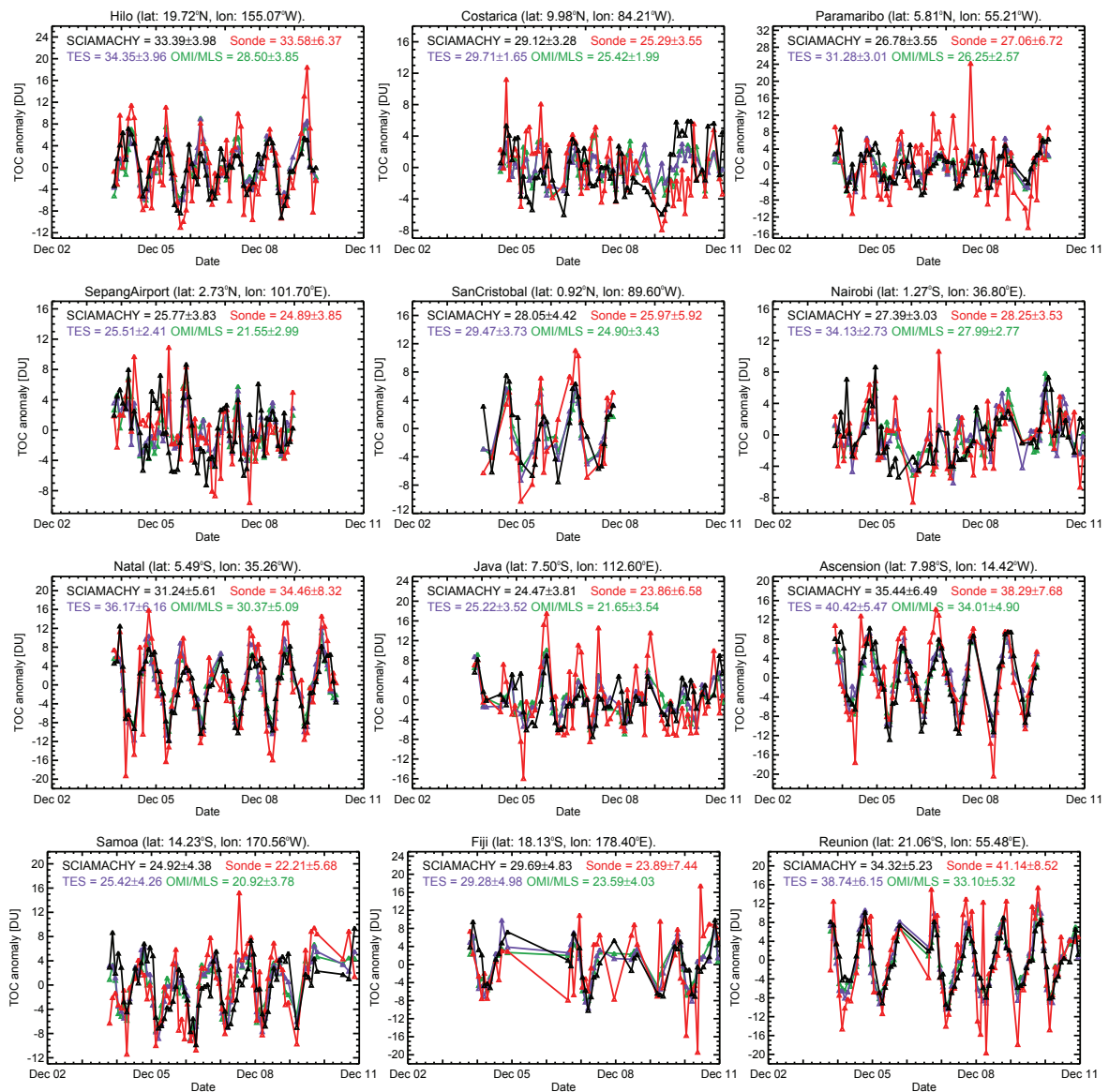


Figure 6.15: Monthly mean tropospheric O_3 column anomaly (TOCA) in Dobson Units (DU) of tropical station from SCIAMACHY (black), ozonesondes (red), TES (violet), and OMI/MLS (green).

The second process is the photochemical production of O_3 from biomass burning and lightning

6.2 Intercomparison of tropospheric ozone columns from SCIAMACHY with TES, OMI/MLS and ozonesondes

activity (Thompson *et al.*, 2000). These processes lead to vertical layers with strongly enhanced O₃ volume mixing ratios and hence the TOCs. The ITCZ determines the wet and dry seasons. During the dry season (August - November), the ITCZ is located over the northern equatorial Atlantic (Hastenrath, 1977), while it travels southwards and back during the wet season (December - July). Therefore, during the first months of the year, the ITCZ is in a southerly position, thus leading to reduction of convection at the NH side of the equator, and also allowing relatively ozone-rich air masses from NH mid-latitudes to be transported to the northern tropics. In the latter half of the year (August - November), the ITCZ takes a more northerly position, thus, allowing all the northern tropical stations to behave similarly to the southern tropical stations.

Observations over the extratropical stations in both hemispheres (Figures 6.16 - 6.19), show tropospheric O₃ seasonality, which corresponds to the precursor elements including STE processes, fossil fuel combustion, biofuel and biomass burning, lightning, biogenic and soil emissions, as well as oceanic emissions. In the NH, largest TOC/TOCA values obtained from all the instruments occur during summer and spring months. Above Sodankyla (67.39°N, 26.65°E) and Lerwick (60.13°N, 1.18°W), SCIAMACHY shows lower TOCA minima (< -12 DU), which are observed in winter. The peak TOC values observed from SCIAMACHY during summer and spring months over both stations are higher than those of the other instruments except over Lerwick in 2006, where ozonesonde measurements are highest. Lower TOCA minima are also recorded by SCIAMACHY over Churchill (58.75°N, 94.07°W), Edmonton (53.55°N, 114.10°W) and Goosebay (53.32°N, 60.30°W). Above these stations SCIAMACHY TOCs exhibit higher anomalies during spring and summer than the other instruments except in 2006 where ozonesonde anomalies are higher. Ozonesonde TOCs show higher anomalies in the spring and summer of 2008 over Churchill and Goosebay while TES TOCs show higher anomalies over Edmonton and Goosebay in the summer of 2010. Above Legionowo (52.40°N, 20.97°E), ozonesonde measurements show generally lower minima with TOCA values less than -11 DU. They exhibit higher anomalies of up to +12 DU compared to those from satellite instruments, mostly during spring. SCIAMACHY and OMI/MLS TOCA values are strange in autumn 2006 and winter of 2011, respectively. TES TOCA values are higher than those of the other instruments in summer of 2010. Ozonesondes measurements over DeBilt (52.10°N, 5.18°E), show higher maxima TOCA of up to +12 DU in spring of 2006 and 2011. TES TOCA values are higher than those of the other instruments in summer of 2010 over DeBilt. Over Valentia (51.93°N, 10.25°W), all the instruments behave differently before December 2006. Ozonesonde TOCA values are higher than those of the other instruments in spring and summer of 2008. SCIAMACHY shows lowest TOCA values of <-10 DU in December 2010. Above Uccle (50.80°N, 4.35°E), ozonesonde measurements show generally lower minima. They exhibit larger anomalies with values up to +12 DU, essentially during spring and summer of 2006 and 2009, respectively and early summer

6. VALIDATION OF SCIAMACHY TROPOSPHERIC OZONE COLUMNS

months of 2011. The ozonesonde TOCA values are strange in winter of 2010. Over Bratt's Lake (50.20°N, 104.70°W), ozonesonde measurements show generally lower minima. They exhibit higher anomalies of up to +13 DU compared to those from satellite instruments, mostly during early spring of 2005 and early summer months of 2011. The seasonality of OMI/MLS becomes different from those of the other instruments after 2009. The values from SCIAMACHY are too high in winter of 2005 and 2009. TES TOCA values are higher than those of the other instruments during the summer of 2010. Above Praha (50.02°N, 14.45°E), ozonesonde TOCA values are higher than those of the other instruments in spring of 2005. All instruments behave differently in 2009 and SCIAMACHY TOCA values are lower than those of the other instruments in winter of 2011. Above Kelowna (49.93°N, 119.40°W), ozonesondes exhibit higher maxima in spring and summer except in the spring of 2008 and 2010, where SCIAMACHY TOCA values are higher. Over Payerne (46.49°N, 6.57°E), ozonesondes exhibit higher TOCA values, mainly in the summer months. SCIAMACHY TOCA values are too high in the winter of 2006 and autumn of 2008. Low TOCA values are observed from SCIAMACHY in late summer of 2009. Over Egbert (44.23°N, 79.78°W) and Yarmouth (43.87°N, 66.11°W), ozonesonde measurements show generally lower minima. They exhibit higher anomalies than the satellite instruments, mostly during spring of 2011 over Egbert and Yarmouth. SCIAMACHY TOCA values are too high in autumn of 2007 over Yarmouth. Above Sapporo (43.10°N, 141.30°E), ozonesondes exhibit higher TOCA values than the satellite measurements, especially in summer and spring of 2007, 2010 and 2011. SCIAMACHY TOCA values are lower than those of the other instruments in December 2009. Over Madrid (40.45°N, 3.72°W), Wallops Island (37.93°N, 75.48°W), Tsukuba (36.10°N, 140.10°E), Huntsville (35.28°N, 86.59°W), Hong Kong (22.31°N, 114.17°E), Naha (26.20°N, 127.70°E) and Hanoi (21.01°N, 105.80°E), ozonesonde measurements show generally lower minima. They exhibit larger anomalies compared to the satellite instruments over Wallops Island, Tsukuba, Huntsville, Naha, Hanoi and Hilo. Over Hong Kong, SCIAMACHY exhibits higher TOCA of up +15 DU in summer 2010 compared to those of the other instruments. Above the low latitude northern stations, including Naha, Hong Kong and Hanoi, largest TOC values occur in late spring. The differences in O₃ seasonal cycles between tropical and extratropical stations in the NH are caused by differing dominant sources of tropospheric O₃ including STE processes and industrial pollution in the extratropics, and biomass burning in the tropics. It has been observed that stratospheric intrusions of O₃ rich air masses contribute significantly to the tropospheric O₃ burden at high latitudes (> 40°) (Chandra *et al.*, 2003). At latitudes of 20° – 40°, the effect of STE processes on tropospheric O₃ abundance is seasonal, which peaks during spring and winter. At latitudes below 20°, STE has little or no contribution to tropospheric O₃ budget (Chandra *et al.*, 2003).

6.2 Intercomparison of tropospheric ozone columns from SCIAMACHY with TES, OMI/MLS and ozonesondes

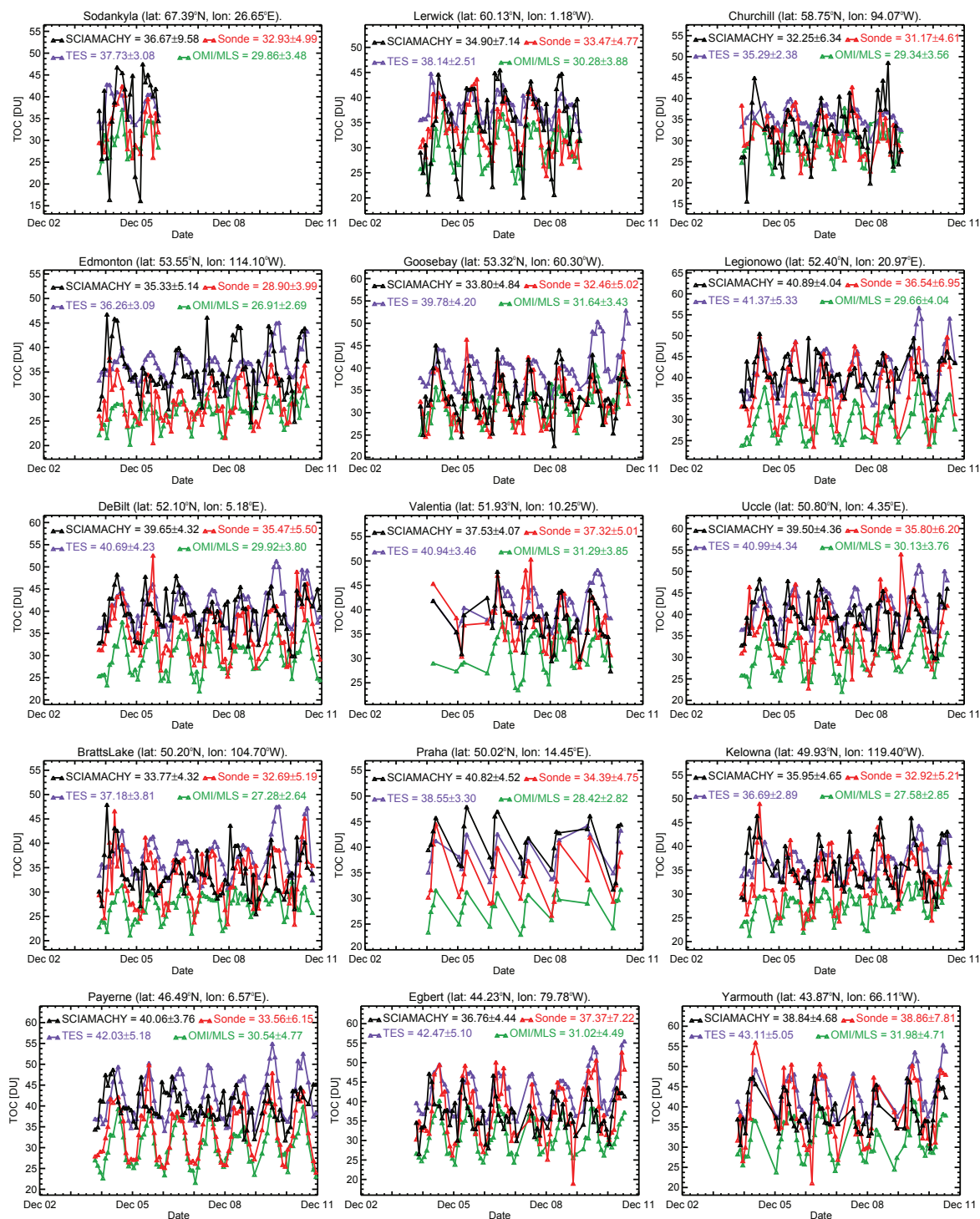


Figure 6.16: Same as Figure 6.14 but for some extratropical ozonesonde stations.

At the southern mid and high latitudes, similar seasonal patterns are observed from all the instruments. The TOC values derived from the instruments are higher during austral spring at the southern mid-latitude stations than above higher southern latitude stations. Generally, above

6. VALIDATION OF SCIAMACHY TROPOSPHERIC OZONE COLUMNS

the southern latitude stations, ozonesonde measurements show lower minima except over Lauder (45.04°S, 169.68°E) where they have similar minima as SCIAMACHY observations.

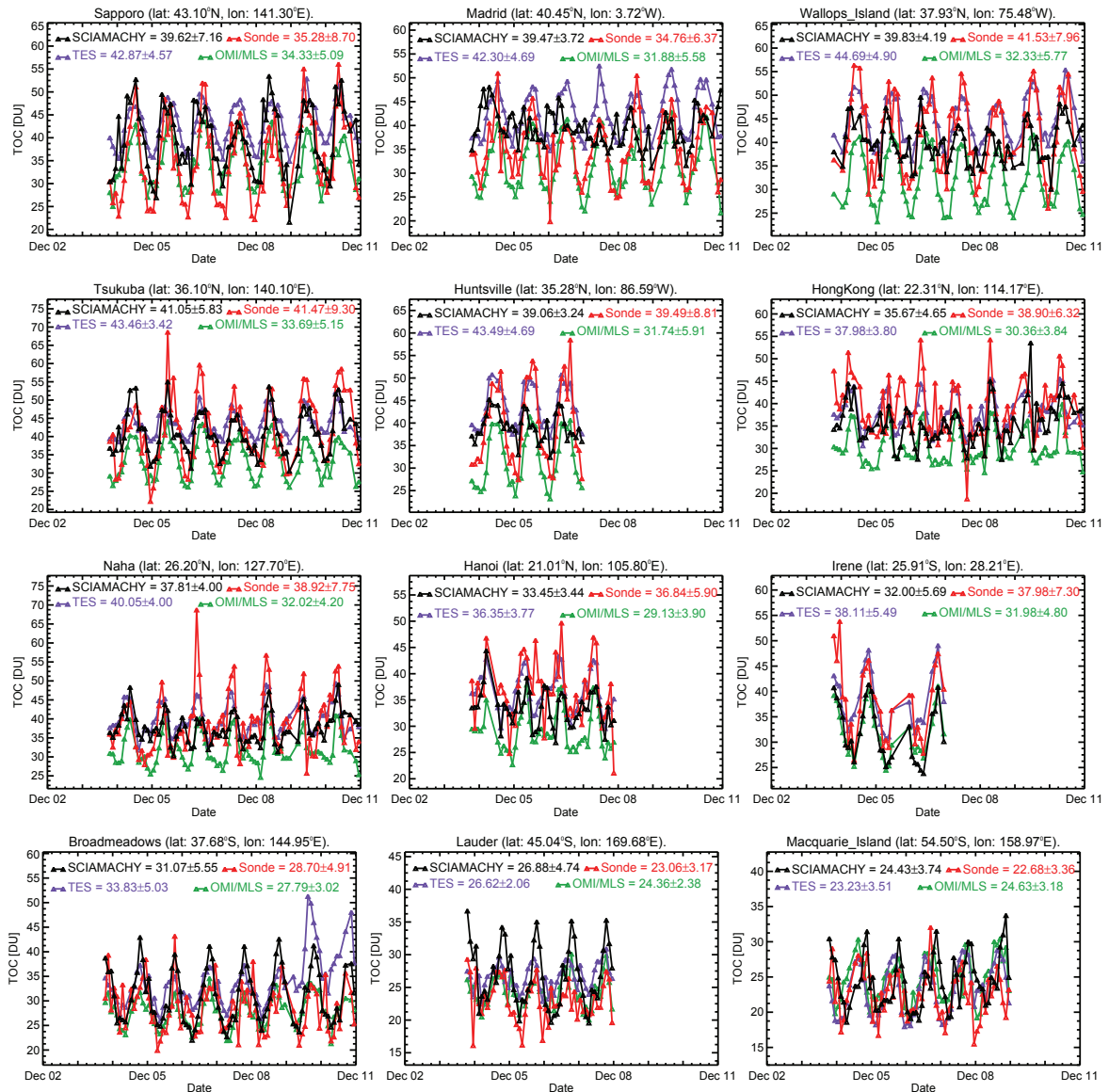


Figure 6.17: Same as Figure 6.14 but for some extratropical ozonesonde stations.

Ozonesondes exhibit higher TOCA maxima over Reunion Island (21.06°S, 55.48°E) and Irene (25.90°S, 28.22°E). Above Broadmeadows (37.68°S, 144.95°E), all the instruments show similar seasonal cycles and maximum values during austral spring except for the years 2010 and 2011 where TES TOCA values are higher and in summer of 2006 where ozonesonde values are higher. Over Lauder, the peak TOC values observed by SCIAMACHY during austral springs are not captured by the other instruments. The low TOC values in the southern high latitudes are an

6.2 Intercomparison of tropospheric ozone columns from SCIAMACHY with TES, OMI/MLS and ozonesondes

indication of low levels of O_3 producing sources in the troposphere and less influence from STE (e.g., de Laat *et al.*, 2005).

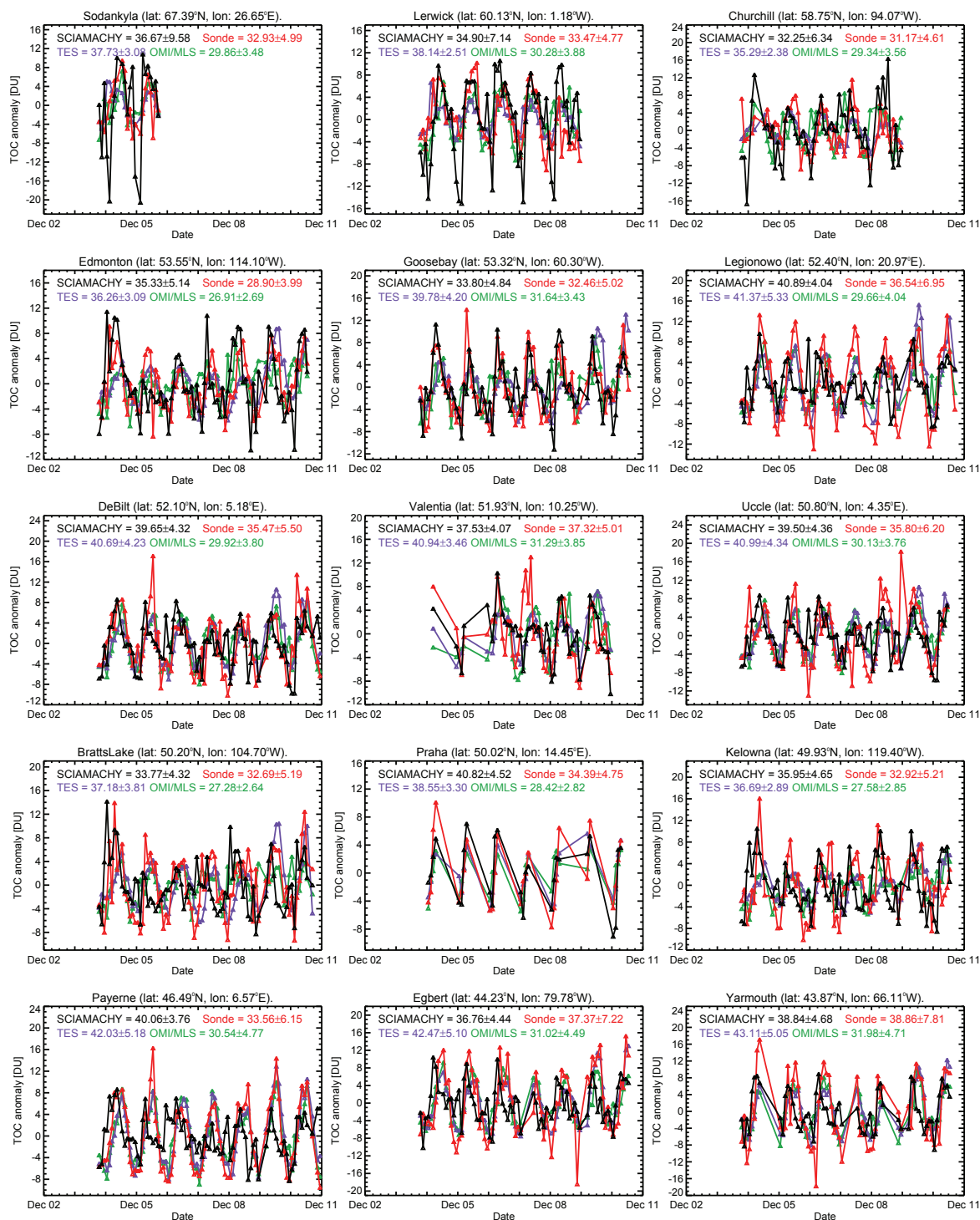


Figure 6.18: Same as Figure 6.15 but for some extratropical ozonesonde stations.

6. VALIDATION OF SCIAMACHY TROPOSPHERIC OZONE COLUMNS

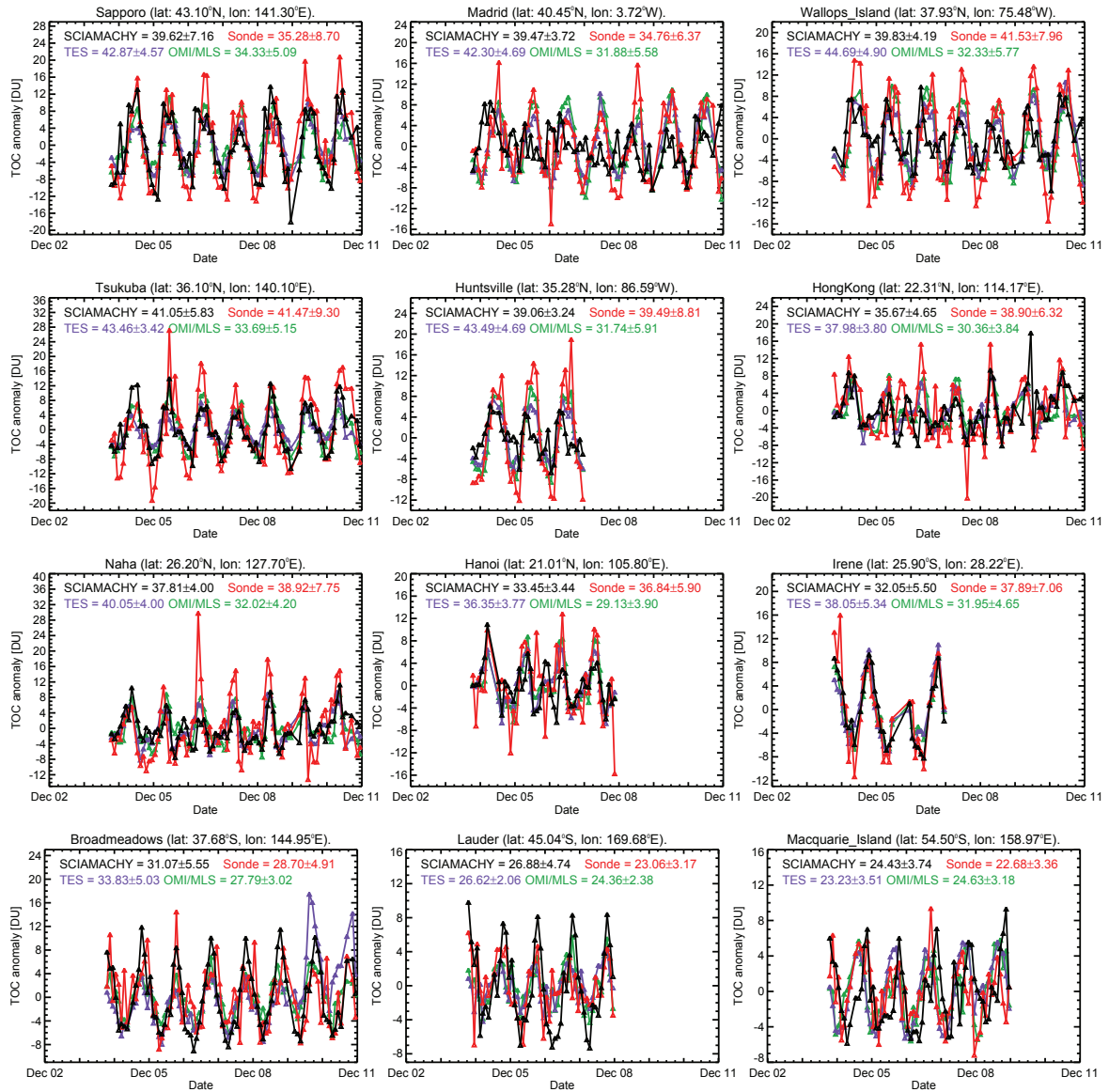


Figure 6.19: Same as Figure 6.15 but for some extratropical ozonesonde stations.

For all satellite data sets, the relative differences with respect to ozonesondes for all considered stations are summarized in Table 6.1. The results show a good agreement for all data sets with mean relative differences of 6 %, 11 % and -6 % for SCIAMACHY, TES and OMI/MLS, respectively. The climatological characteristics exhibited by the ozonesondes may differ due to their location. Therefore, the comparison of the tropospheric O_3 retrieved from SCIAMACHY with both in-situ and other satellite measurements is necessary. For most of the stations in both hemispheres (Figure 6.13), the monthly mean tropospheric O_3 over the entire time series from the four instruments agree in terms of magnitude and annual variation with some differences, which are within the error bars as shown in Table 6.1.

6.2 Intercomparison of tropospheric ozone columns from SCIAMACHY with TES, OMI/MLS and ozonesondes

Station name	No of points	Lat.	Lon.	Mean value and stdev. of TOC from sondes (DU)	Mean value and stdev. of TOC from SCIAMACHY (DU)	Mean value and stdev. of TOC from TES (DU)	Mean value and stdev. of TOC from OMI/MLS (DU)	Mean value of TOC rel. diff. (SCIAMACHY)	Mean value of TOC rel. diff. (TES)	Mean value of TOC rel. diff. (OMI/MLS)
1. Sodankyla	22	67.39	26.65	36.7±9.6	32.9±5.0	37.7±3.1	29.9±3.5	0.11	0.15	-0.09
2. Lerwick	62	60.13	358.82	34.9±7.1	33.5±4.8	38.1±2.5	30.3±3.9	0.04	0.14	-0.10
3. Churchill	57	58.75	265.93	32.3±6.3	31.2±4.6	35.3±2.4	29.3±3.6	0.03	0.13	-0.06
4. Edmonton	79	53.55	245.90	35.3±5.1	28.9±4.0	36.3±3.1	26.9±2.7	0.22	0.25	-0.07
5. Goose Bay	78	53.32	299.70	33.8±4.8	32.5±5.0	39.8±4.2	31.6±3.4	0.04	0.23	-0.03
6. Legionowo	75	52.40	20.97	40.9±4.0	36.5±7.0	41.4±5.3	29.7±4.0	0.12	0.13	-0.19
7. DeBilt	82	52.10	5.18	39.7±4.3	35.5±5.5	40.7±4.2	29.9±3.8	0.12	0.15	-0.16
8. Valentia	49	51.93	349.75	37.5±4.1	37.3±5.0	40.9±3.5	31.3±3.9	0.01	0.10	-0.16
9. Uccle	78	50.80	4.35	39.5±4.4	35.8±6.2	41.0±4.3	30.1±3.8	0.10	0.14	-0.16
10. Bratts Lake	78	50.20	255.30	33.8±4.3	32.7±5.2	37.2±3.8	27.3±2.6	0.03	0.14	-0.17
11. Praha	26	50.02	14.45	40.8±4.5	34.4±4.8	38.6±3.3	28.4±2.8	0.19	0.12	-0.17
12. Kelowna	77	49.93	240.60	36.0±4.7	32.9±5.2	36.7±2.9	27.6±2.9	0.09	0.11	-0.16
13. Payerne	82	46.49	6.57	40.1±3.8	33.6±6.2	42.0±5.2	30.5±4.8	0.19	0.25	-0.09
14. Egbert	74	44.23	280.22	36.8±4.4	37.4±7.2	42.5±5.1	31.0±4.5	-0.02	0.14	-0.17
15. Yarmouth	63	43.87	293.89	38.8±4.7	38.9±7.8	43.1±5.1	32.0±4.7	0.00	0.11	-0.18
16. Sapporo	82	43.10	141.30	39.6±7.2	35.3±8.7	42.9±4.6	34.3±5.1	0.12	0.22	-0.03
17. Madrid	81	40.45	356.28	39.5±3.7	34.8±6.4	42.3±4.7	31.9±5.6	0.14	0.22	-0.08
18. Ankara	78	39.95	32.88	38.1±3.1	35.6±9.9	44.9±7.4	32.6±7.1	0.07	0.26	-0.08
19. Wallops	80	37.93	284.52	39.8±4.2	41.5±8.0	44.7±4.9	32.3±5.8	-0.04	0.08	-0.22
20. Tsukuba	82	36.10	140.10	41.1±5.8	41.5±9.3	43.5±3.4	33.7±5.2	-0.01	0.05	-0.19
21. Huntsville	38	35.28	273.41	39.1±3.2	39.5±8.8	43.5±4.7	31.7±5.9	-0.01	0.10	-0.20
22. Isfahan	50	32.51	51.70	35.2±2.8	37.3±9.1	42.1±5.1	32.2±5.9	-0.06	0.13	-0.14
23. Naha	82	26.20	127.70	37.8±4.0	38.9±7.8	40.1±4.0	32.0±4.2	-0.03	0.03	-0.18
24. Hong Kong	81	22.31	114.17	35.7±4.7	38.9±6.3	38.0±3.8	30.4±3.8	-0.08	-0.02	-0.22
25. Hanoi	47	21.01	105.80	33.5±3.4	36.8±5.9	36.4±3.8	29.1±3.9	0.10	0.10	-0.13
26. Hilo	68	19.72	204.93	33.4±4.0	33.6±6.4	34.4±4.0	28.5±3.9	-0.01	0.02	-0.15
27. Costarica	20	9.98	275.79	29.0±3.7	25.3±3.6	29.7±1.7	25.4±2.0	0.15	0.17	0.01
28. Paramaribo	69	5.81	304.79	26.8±3.6	27.1±6.7	31.3±3.0	26.3±2.6	-0.01	0.16	-0.03
29. Sepang Airport	62	2.73	101.70	25.8±3.8	24.9±3.9	25.5±2.4	21.6±3.0	0.04	0.02	-0.13
30. San Cristobal	27	-0.92	270.40	28.1±4.4	26.0±5.9	29.5±3.7	24.9±3.4	0.08	0.13	-0.04
31. Nairobi	52	-1.27	36.80	26.9±3.0	27.7±3.6	33.8±2.6	27.8±2.8	-0.03	0.22	0.00
32. Malindi	12	-2.99	40.19	29.0±3.5	36.1±5.0	34.0±3.0	28.4±3.7	-0.20	-0.06	-0.21
33. Natal	61	-5.42	324.62	31.2±5.6	34.3±8.6	36.5±6.2	30.6±5.1	-0.09	0.06	-0.11
34. Java	52	-7.57	112.65	24.9±3.8	23.4±6.8	25.1±3.5	21.7±3.7	0.06	0.07	-0.07
35. Ascension	37	-7.58	345.76	35.2±6.3	39.6±7.9	40.2±5.1	34.0±4.5	-0.11	0.01	-0.14
36. Samoa	58	-14.23	189.44	24.5±4.4	21.4±5.4	24.8±4.2	20.3±3.7	0.15	0.16	-0.05
37. Fiji	43	-18.1	178.4	29.7±4.8	23.9±7.4	29.3±5.0	23.6±4.0	0.24	0.23	-0.01
38. La Reunion	61	-21.06	55.48	34.6±5.4	41.1±9.1	39.1±6.4	33.3±5.5	-0.16	-0.05	-0.19
39. Irene	29	-25.91	28.21	32.0±5.7	38.0±7.3	38.1±5.5	32.0±4.8	-0.16	0.00	-0.16
40. Broadmeadows	82	-37.68	144.95	31.1±5.6	28.7±4.9	33.8±5.0	27.8±3.0	0.08	0.18	-0.03
41. Lauder	50	-45.04	169.68	26.9±4.7	23.1±3.2	26.6±2.1	24.4±2.4	0.17	0.15	0.06
42. Macquarie	62	-54.50	158.97	24.4±3.7	22.7±3.4	23.2±3.5	24.6±3.2	0.08	0.02	0.09
43. Ushuaia	21	-54.85	291.69	21.3±4.7	21.0±3.6	24.4±3.0	24.7±3.0	0.01	0.16	0.17
44. Marambio	38	-64.23	303.38	18.6±4.6	18.6±4.1	20.2±5.8	22.1±3.3	0.00	0.09	0.19
Mean value of tropospheric ozone				33.0±4.9	31.6±6.0	35.1±4.1	28.7±4.1	0.06	0.11	-0.06

Table 6.1: Comparisons of tropospheric O₃ columns from SCIAMACHY, ozonesondes, TES and OMI/MLS for some selected stations over the entire time series (2004-2011). Mean value and standard deviation (stdev) as well as the relative difference of each satellite data product using ozonesonde as the reference are shown. The TOC product is for 10 % cloud fraction threshold at 5° latitude × 10° longitude resolution.

Despite an overall good agreement, there are still significant discrepancies between the time series from the different instruments. Possible explanations are as follows. Comparisons of TOC values from satellites with ozonesonde data, which are sparse, are prone to variability in the dynamically active subtropics, where rapid fluctuations in the tropopause heights occur. Such comparisons exhibit a lot of scatter and the regression line may deviate from the line of unity (Ziemke *et al.*, 2006). Differences in the definition of the tropopause height can also contribute to differences in the tropospheric O₃ from the different instruments. Further issues might result from differences in the retrieval algorithms and filtering of data affected by clouds. The comparison of TES tropospheric

6. VALIDATION OF SCIAMACHY TROPOSPHERIC O₃ COLUMNS

O₃ with other data products suffers from a sampling bias because of low number of measurements per month (Toohey *et al.*, 2013). Despite a possible bias (Nassar *et al.*, 2008), the TES data product is valuable, because of a lack of tropospheric O₃ data products from space borne instruments. As a result of the limited vertical resolution of the TES TOC retrieval, information from the stratospheric true state can be smeared into the troposphere. However, the error caused by this effect is included in the error estimate of the TES TOC data product used in this analysis (Osterman *et al.*, 2008). Cloudy data are rejected in both SCIAMACHY and OMI/MLS tropospheric O₃ retrievals (Ziemke *et al.*, 2006) in a similar way. Thus "clear-sky" to "all-sky" biases are not expected. For TES measurements, a "clear-sky" to "all-sky" bias might exist but it is expected to be less significant than the overall sampling bias. The error arising from the time (~7 minutes) between limb and nadir observations for SCIAMACHY as well as for MLS and OMI is assumed to be negligible because of the short time period and the coarse horizontal resolution of the limb measurements.

6.2.1 SCIAMACHY global TOC climatology maps

A global climatology of tropospheric O₃ is useful for evaluating chemistry transport models because it reveals offsets or seasonal differences. It is useful for visualizing and comparing global variations of tropospheric O₃ for different years, seasons and decades. It is also useful for air quality models and can serve as an *a-priori* climatology for O₃ retrievals. The SCIAMACHY tropospheric O₃ climatology exhibits large temporal and spatial variability, which includes O₃ accumulation zones in the tropical south Atlantic all year round and in the subtropical Mediterranean/Asia region in summer months. Persisting elevated amounts of tropospheric O₃ in the NH are observed in mid-latitudes. This is clearly observed over the eastern part of the North American continent, extending across the Atlantic Ocean. Elevated TOC values are also observed over the eastern part of the Asian continent, extending across the Pacific Ocean in boreal spring and summer. A nine-year TOC climatology for SCIAMACHY is shown in Figures 6.20 & 6.21 for each of the months January - December.

The other observed features of the TOC climatology are summarized as follows. The SCIAMACHY tropospheric O₃ climatology exhibits the persistent wave-one feature in the southern tropics, that is, an enhancement of TOC over the Atlantic Ocean between South America and Africa, and a decrease over a wide region in the southern Pacific (Chandra *et al.*, 2002; Thompson *et al.*, 2003). The wave-one feature maximizes in September – November with tropospheric O₃ values greater than 50 DU as compared to TOC values of less than 40 DU over the southern Pacific. The wave-one pattern in TOC originates from different contributing factors including biomass burning and lightning in both Africa and South America, deep convection in the Pacific region coupled with vertical injection of low marine boundary layer tropospheric O₃ into the middle

6.2 Intercomparison of tropospheric ozone columns from SCIAMACHY with TES, OMI/MLS and ozonesondes

and upper troposphere (the large scale Walker Circulation) (e.g., Chandra *et al.*, 2003; Edwards *et al.*, 2003; Martin *et al.*, 2002). At the tropical latitudes, TOC for each month is characterized by low amounts in the Pacific $\sim 20 - 25$ DU with much higher columns $\sim 35 - 50$ DU in the Atlantic.

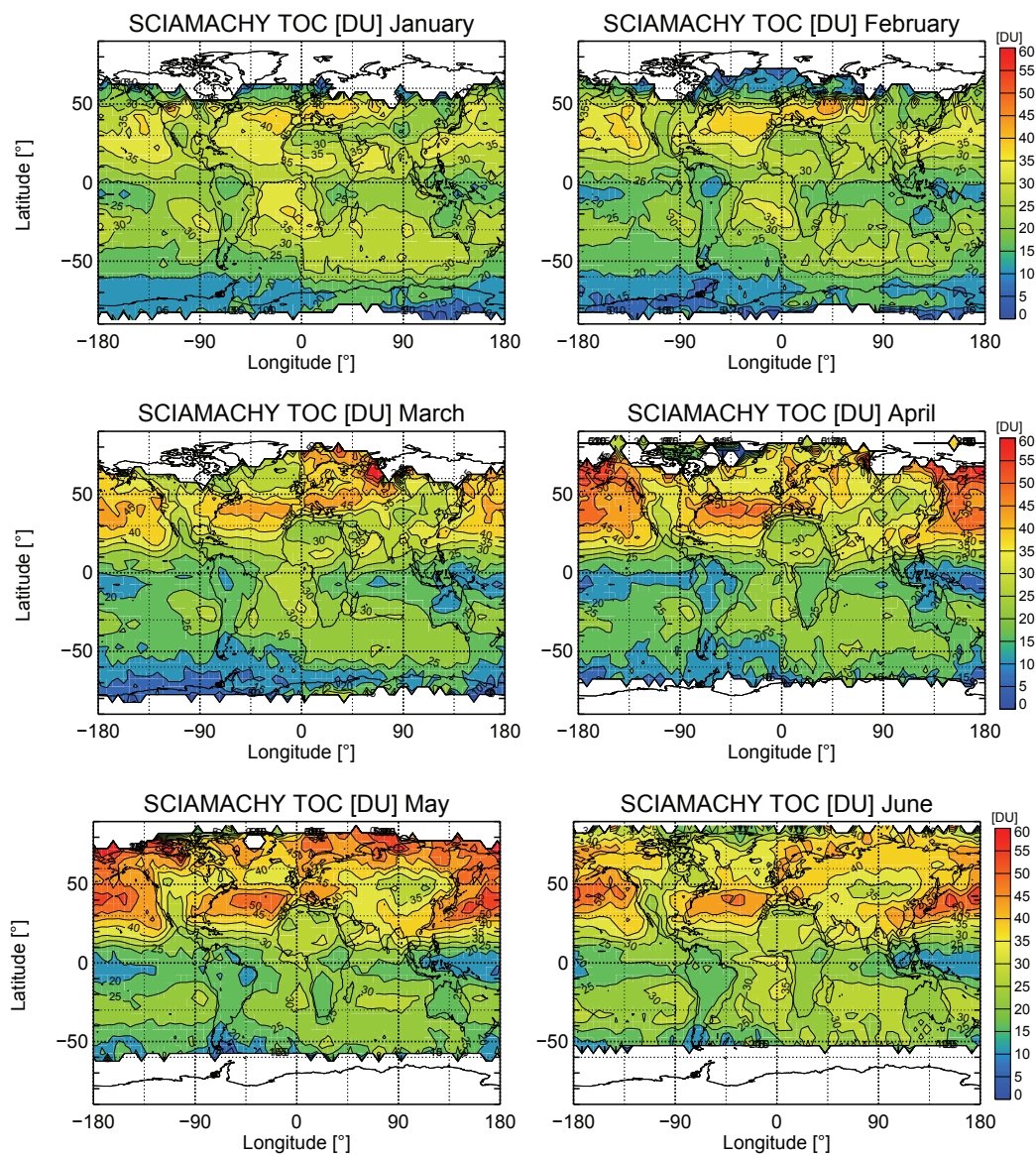


Figure 6.20: Tropospheric O_3 climatology (in DU) for the months, January - June from SCIAMACHY limb-nadir matching measurements. The colours in the panels going from blue to red represent smallest to largest values, respectively.

The lowest TOC in the tropics lies in the western Pacific during June – August with values 15 – 20 DU and in the eastern Pacific during March – May with values less than 20 DU. Low TOC values (< 20 DU) are also observed at the SH high latitudes in December - April. These

6. VALIDATION OF SCIAMACHY TROPOSPHERIC OZONE COLUMNS

low TOC values are associated with less influence of O_3 production sources including STE process and anthropogenic effects (Chandra *et al.*, 2003). Largest TOC in the SH occurs during September - November in the tropical south Atlantic with values greater than 45 DU along a zonal band around $25^\circ\text{S} - 40^\circ\text{S}$. High TOC values are also found in the southern mid-latitudes during September - November with values greater than 40 DU. These are similar to the high TOC values at NH mid-latitudes in summer and spring months. These seasonal enhancements of tropospheric O_3 are associated with the dynamics caused by STE processes (Chandra *et al.*, 2004; de Laat *et al.*, 2005).

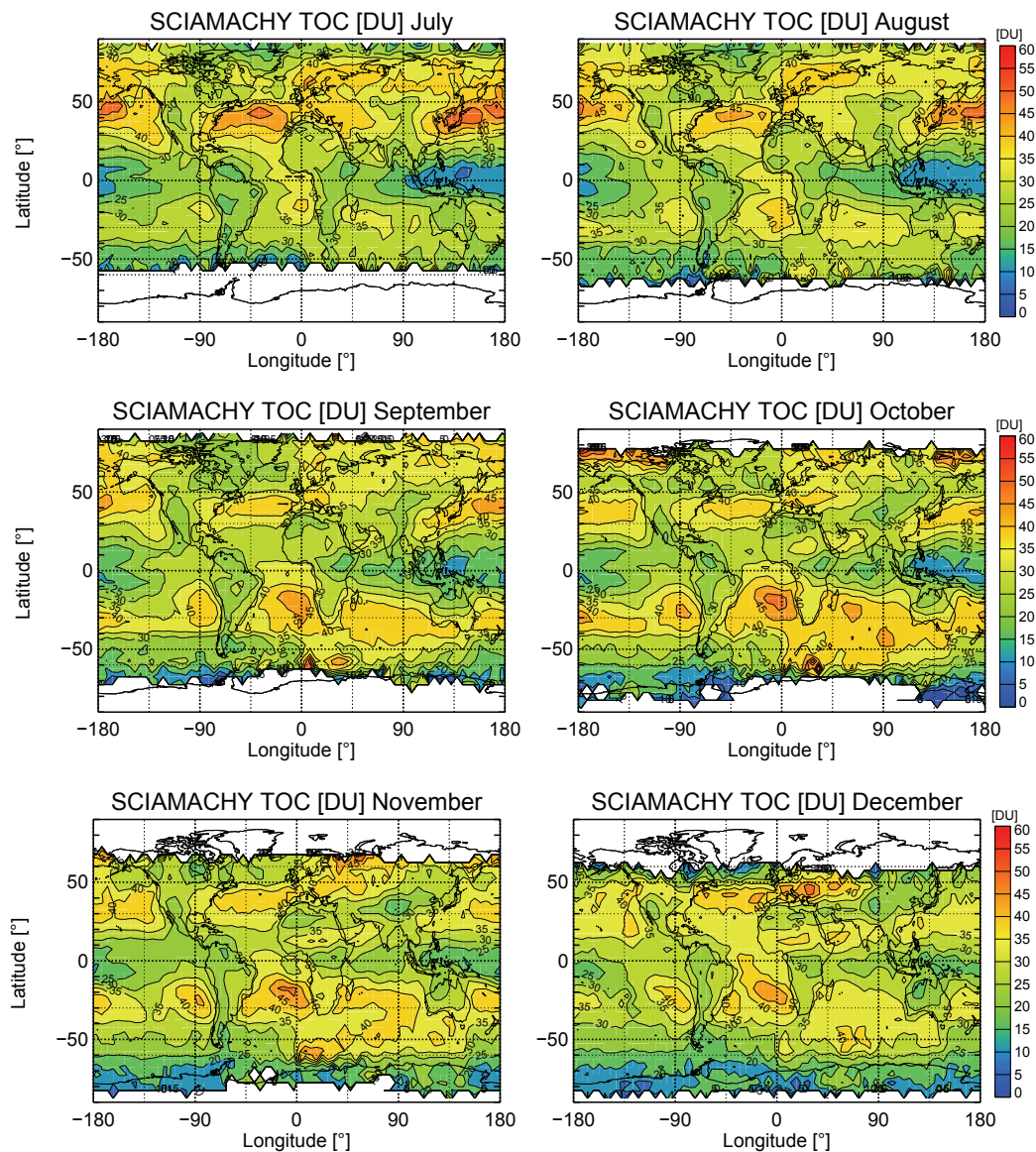


Figure 6.21: Same as Figure 6.20 but for July - December.

The high TOC values at the SH in September - November are substantially reduced in January

and February. January and February months show the most pronounced hemispheric symmetry in TOC of all months, which can be explained partly by a seasonal minimum in biomass burning (Duncan *et al.*, 2003). The largest TOC in the NH occur in the subtropics and mid-latitudes during March – May with values greater than 50 DU in regions of eastern United States extending eastward over North Atlantic. Such high TOC values are also observed over the Mediterranean and eastern Asian continent extending eastward over the Pacific during March – August. The high TOC values in this zonal band are attributed to both anthropogenic and STE processes (Chandra *et al.*, 2004; Lelieveld *et al.*, 2002; Stohl *et al.*, 2007, 2003). During March - June, the observed TOC in the northern mid-latitudes is as large over the Atlantic and Pacific Oceans as it is over industrial emission regions as previously observed by Chandra *et al.* (2004). High TOC values are observed at the northern high latitudes during March – May, which may have resulted from transport of O₃ plumes from the mid-latitudes (Stohl *et al.*, 2007, 2003).

6.2.2 SCIAMACHY zonal mean TOC, TOZ and SOC climatologies

A zonal mean TOC climatology from SCIAMACHY will be useful for the evaluation of 3-D chemistry transport models of the atmosphere. Comparison of a simple model with zonal mean TOC climatology can reveal basic offsets or annual-cycle differences that can aid in initialization and validation of models. It also gives a global view of tropospheric O₃ changes. Figure 6.22 shows the 9-year climatology of zonal mean tropospheric O₃ from SCIAMACHY instrument as a function of the month and latitude averaged over the period from January 2003 to December 2011. The regions shaded white represent places where there are no SCIAMACHY measurements or SCIAMACHY scenes with solar zenith angles greater than 85° or contentious values at high latitudes. Similar plots are made for TOZs (Figure 6.23) and SOCs (Figure 6.24).

In Figure 6.22, the lowest amounts of tropospheric O₃ of less than 20 DU occur in the SH tropics between 0 - 10°S during March - April and in the southern high latitudes (<20 DU) during January - April as well during September - December. In the southern tropics, low O₃ values (<24 DU) occur during February - May and O₃ values of less than 32 DU can be observed throughout the entire time period in the tropics and in the southern mid-latitudes between January and September. The largest TOCs occur in the NH subtropics and mid-latitudes during March - July (>44 DU) and in the SH subtropics during September - November (>40 DU). In the NH, the transition of tropospheric O₃ peak values from the tropical/subtropical region during March - May to peak O₃ values between June - August in the mid-latitudes is observed. This northward shift from spring to summer in the NH is likely related to spring and summer STE with tropospheric O₃ anthropogenically produced during summer months (Chandra *et al.*, 2004; Logan, 1985; Stohl *et al.*, 2007).

6. VALIDATION OF SCIAMACHY TROPOSPHERIC OZONE COLUMNS

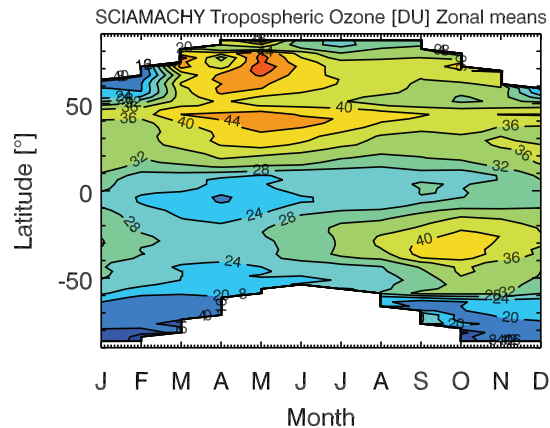


Figure 6.22: Zonal mean tropospheric O_3 column climatology (in DU) derived from January 2003 to December 2011 from SCIAMACHY measurements for 5° latitude bins.

Figure 6.23 shows the SCIAMACHY zonal mean TOZ climatology. TOZ maximizes in the NH between $55^\circ\text{N} - 80^\circ\text{N}$ in February – May (>400 DU) and in the SH between $50^\circ\text{S} - 70^\circ\text{S}$ in September - November (>360 DU). On average, the TOZ values are higher in the NH high latitudes than in the SH high latitudes. Lowest TOZ occurs in December - February and January - August, between latitudes $0 - 20^\circ\text{N}$ (<260 DU). Low TOZ values are observed between latitudes $0 \pm 30^\circ$ all year round (<280 DU). The Low TOZ values in the tropical and subtropical regions, and the high TOZ values in the extratropics during winter/spring are due to O_3 transport as a result the Brewer-Dobson circulation (e.g., Weber *et al.*, 2011).

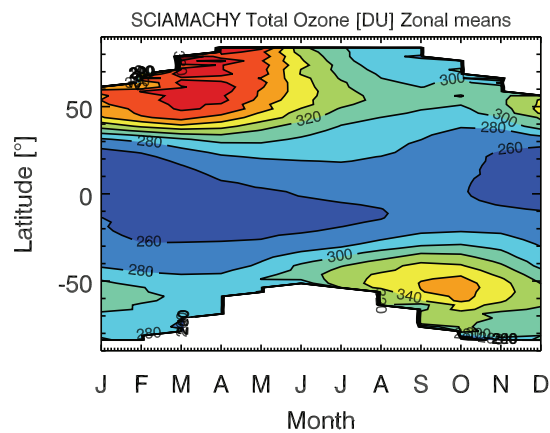


Figure 6.23: Same as Figure 6.22 but for total O_3 column (TOZ).

In Figure 6.24, largest SOC_s occur in the NH at latitudes between $55^\circ\text{N} - 80^\circ\text{N}$ from January to late April (>360 DU) and in the SH between latitudes of $50^\circ\text{S} - 70^\circ\text{S}$ during September - November (>320 DU). The high SOC in the NH is associated with high O_3 over North America and central Asia. Lowest SOC_s occur between $0^\circ - 20^\circ\text{N}$ in December - February (<220 DU). SOC values of

6.2 Intercomparison of tropospheric ozone columns from SCIAMACHY with TES, OMI/MLS and ozonesondes

less than 260 DU are located at the tropics and subtropics all year round. The BDC plays a role in influencing SOC amounts in the tropical and extratropical regions (e.g., Garcia & Randel, 2008; Weber *et al.*, 2011).

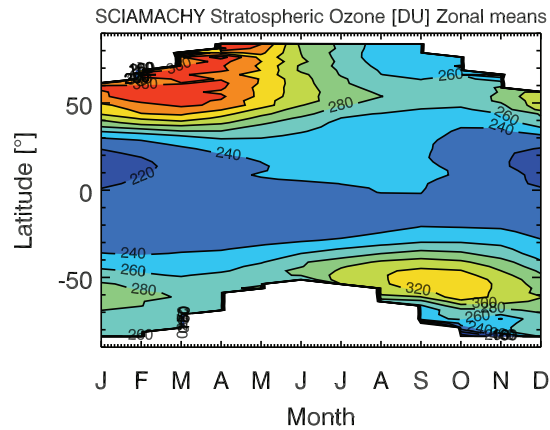


Figure 6.24: Same as Figure 6.22 but for stratospheric O₃ column (SOC)

6.2.3 Zonal distribution of tropospheric ozone columns from SCIAMACHY

Figure 6.25 shows plots of a SCIAMACHY TOC climatology as a function of longitude for 10°S – 0° in October and 30°N – 40°N in April as well as in July. These latitude bands and months were chosen to show several large annually recurring features present in global TOC. Also included in the plots are $\pm 2\sigma$ vertical bars where σ is the calculated 9-year RMS standard error of the mean. TOCs in these two latitude bands have large spatial variability. The left panel (October 10°S - 0) shows large contrast of TOC from low values in the tropical Pacific and high values in the tropical Atlantic (i.e., 18 DU against 42 DU, respectively). In the middle panel (April 30°N - 40°N), zonal variability caused by North Atlantic accumulation (between 30°W and 60°W), the plateau of Tibet (centered about 90°E) and Colorado Plateau (centered about 100°W) are observed. At the right panel (July 30°N - 40°N), in addition to zonal variability observed in the middle panel, is the zonal variability caused by the mediterranean-Asian accumulation (between 20°E and 40°E).

Plots of SCIAMACHY TOC climatology as a function of longitude for 60°S - 40°S, 20°S - 20°N and 40°N - 60°N are shown in Figure 6.26. Spatial variability, the summertime tropospheric O₃ maximum in the NH, the wintertime tropospheric O₃ minimum in the SH, and seasonally reoccurring features present in global TOCs are observed. This kind of plot reveals some of the features that might be hidden or amplified in colour maps, which could result from the resolution or changes in the colour scale. Observations over 60°S - 40°S in the left panel of Figure 6.26 show the zonal variability due to enhancements of O₃ over the Southern Atlantic Ocean and O₃ accumulation

6. VALIDATION OF SCIAMACHY TROPOSPHERIC OZONE COLUMNS

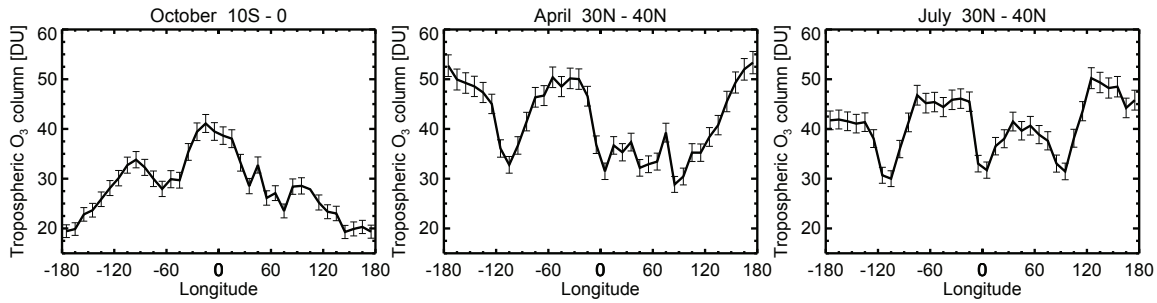


Figure 6.25: Tropospheric O₃ climatology from 2002 - 2011 as a function of longitude from SCIAMACHY for the latitude bands 10°S - 0, 30°S - 40°N and 30°N - 40°N for October, April and July, respectively. Also included in the plots are $\pm 2\sigma$ vertical bars used as estimates of the combination of errors and real atmospheric variability, where σ is the calculated 9-year RMS standard deviation of the individual values.

over the Indian Ocean, which is enhanced during austral spring and summer. In this latitude band, perturbations related to the ozone hole (Wolfram *et al.*, 2008) are observed between 60°S - 70°S. This could be as a result of the extension of the polar vortex and dilution processes during winter and late spring, respectively. In the middle panel of Figure 6.26, corresponding to 20°S - 20°N, the persistent wave-one feature of the tropical tropospheric O₃ is clearly revealed in all seasons. The enhanced O₃ in this zonal band is as a result of biomass burning, lightning and enhanced convection, which is connected to the large scale Walker Circulation (Chandra *et al.*, 2002; Martin *et al.*, 2002). Enhanced TOC is observed over the tropical eastern Pacific Ocean with a maximum during austral spring/summer and minimum during austral autumn. The high O₃ in this region may have been transported from South America (Kim & Newchurch, 1996). In the right panel of Figure 6.26, which corresponds to the 40°N - 60°N latitude band, the zonal variability caused by northern Pacific accumulation and the Gobi desert (between 100°E and 140°E) are observed.

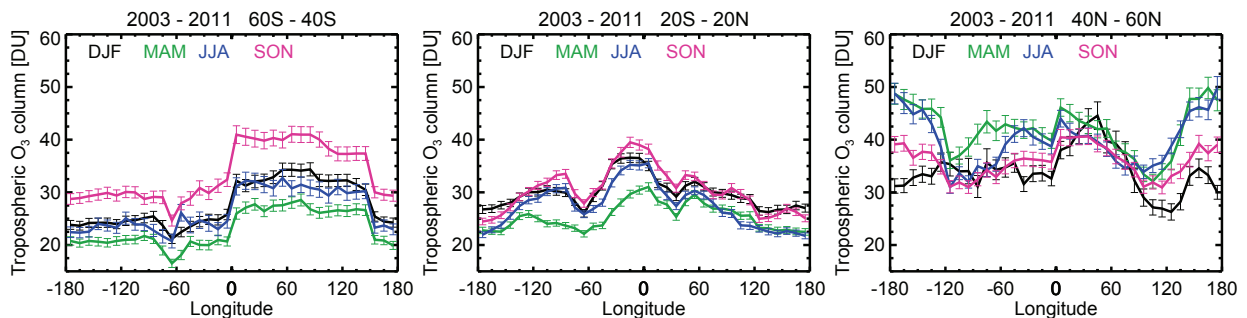


Figure 6.26: Tropospheric O₃ column as a function of longitude from SCIAMACHY for the latitude bands 60°S - 40°S, 20°S - 20°N and 40°N - 60°N for the different seasons between December 2002 and November 2011. Also included in the plots are $\pm 2\sigma$ vertical bars used as estimates of the combination of errors and natural variability of monthly zonal means, where σ is the calculated 9-year RMS standard deviation of the individual values.

6.2 Intercomparison of tropospheric ozone columns from SCIAMACHY with TES, OMI/MLS and ozonesondes

The calculated zonal mean TOC climatology as a function of latitude at three-month intervals (January, April, July, and October) from January 2003 to December 2011 is shown in Figure 6.27. The plot shows high (low) O_3 values during October (April) and April (January) at the southern and northern mid-latitudes, respectively. The high O_3 values during October in the SH mid-latitudes and in April in the NH mid-latitudes are a result of enhancement of O_3 precursors during these periods of the year as discussed in section 6.1.

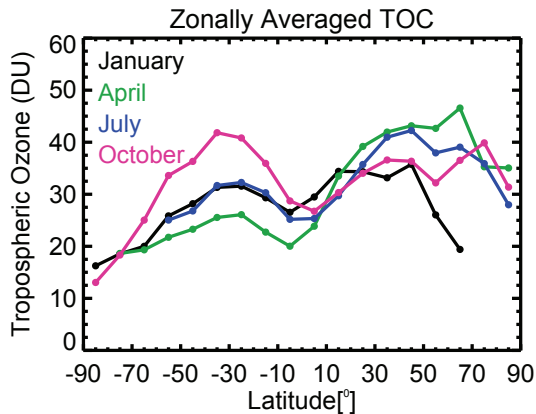


Figure 6.27: Calculated zonal mean TOC climatology as a function of latitude at three-month intervals (January, April, July, and October) from January 2003 to December 2011. The zonal mean values are derived from the 10° latitude \times 10° longitude gridded TOCs.

6.2.4 Intercomparison plots of the zonal distribution of TOCs from SCIAMACHY, TES and OMI/MLS

Figures 6.28 – 6.30 show intercomparison plots between OMI/MLS, SCIAMACHY and TES TOC values as functions of longitude for different latitude bands, $60^\circ\text{S} - 40^\circ\text{S}$, $20^\circ\text{S} - 20^\circ\text{N}$, and $40^\circ\text{N} - 60^\circ\text{N}$, in different seasons in the NH, winter (DJF), summer (JJA), spring (MAM), and autumn (SON), averaged over a period of 6 years from December 2005 to November 2011.

In Figure 6.28 the zonal distribution of TOCs from SCIAMACHY, TES and OMI/MLS for $60^\circ\text{S} - 40^\circ\text{S}$ are shown. The spatial variability of SCIAMACHY and OMI/MLS is similar especially during MAM while TES shows less variation in all seasons. The zonal variability caused by the Andes mountains, which is highly pronounced during boreal spring and summer is captured by SCIAMACHY. The zonal variability, which could be due to the influence STE processes (Pfister *et al.*, 2008; Thompson *et al.*, 2007b) during winter is also captured by SCIAMACHY but the spa-

6. VALIDATION OF SCIAMACHY TROPOSPHERIC OZONE COLUMNS

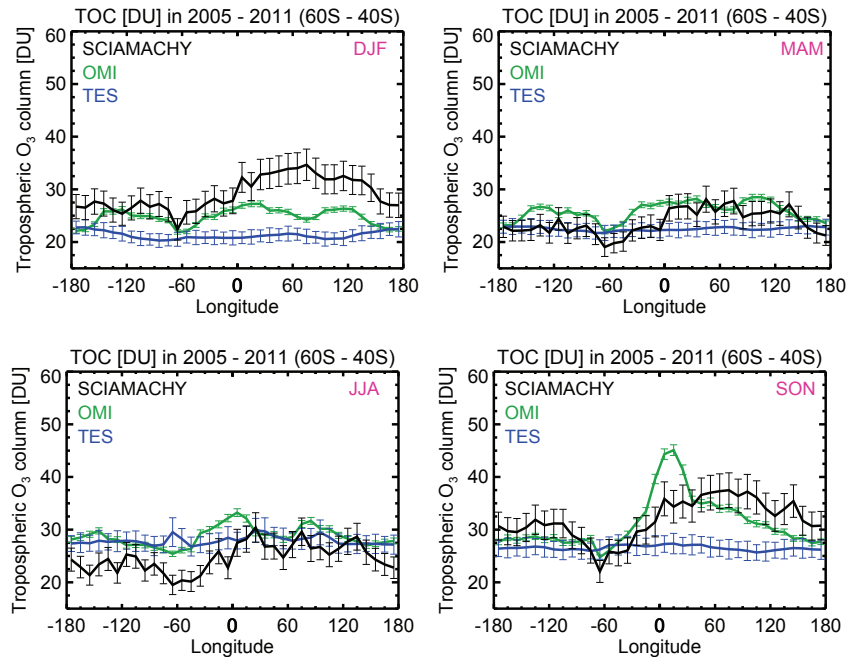


Figure 6.28: Plots of TOC (in DU) as a function of longitude from OMI/MLS, SCIAMACHY and TES for the latitude bins 60°S – 40°S between December 2005 and November 2011; from the top panels, left to right: December-January-February, March-April-May, from the bottom panels, left to right: June-July-August and September-October-November. Also included in the plots are $\pm 2\sigma$ vertical bars used as estimates of the combination of errors and real atmospheric variability, where σ is the calculated 9-year RMS standard deviation of the individual values.

tial variability between 20°E and 20°W as observed from OMI/MLS during autumn is higher than that from SCIAMACHY. This variability can be associated with transport of O₃ rich air from the tropical south Atlantic during autumn months.

Figure 6.29 shows the zonal distribution of TOCs from SCIAMACHY, TES and OMI/MLS for 20°S - 20°N. All satellite instruments show the persistent wave-one feature of the tropical troposphere, i.e., TOCs changing from high values in the tropical Atlantic to low values in the tropical Pacific. This feature is mostly evident in all the seasons but it reaches its maximum during autumn. In this latitude band and for all seasons, TES TOC values are higher than those of other satellite instruments in the tropical Atlantic between 20°W and 20°E. Figure 6.30 shows the zonal distribution of TOCs from SCIAMACHY, TES and OMI/MLS for 40°N - 60°N. Similar zonal variability is observed by SCIAMACHY and TES instruments between 140°E and 220°E mostly in the spring and autumn months. The largest tropospheric O₃ values lie in this zonal range in comparison to the other latitude bands. The year round spatial variability in this zonal band is associated with several tropospheric O₃ production sources including STE, lightning, biomass burning, and combustion of fossil fuels.

6.2 Intercomparison of tropospheric ozone columns from SCIAMACHY with TES, OMI/MLS and ozonesondes

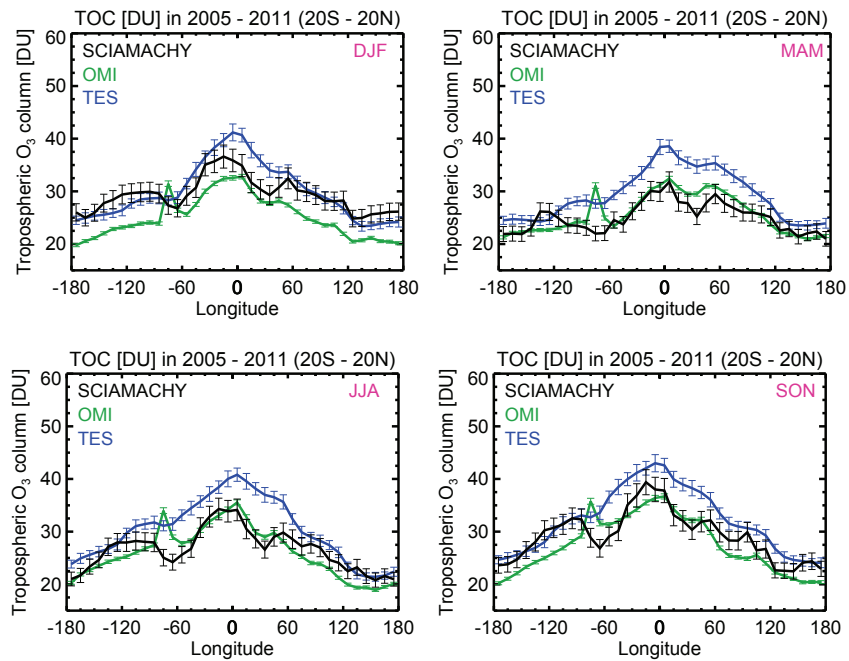


Figure 6.29: Same as figure 6.28 but for the latitude bins 20°S - 20°N.

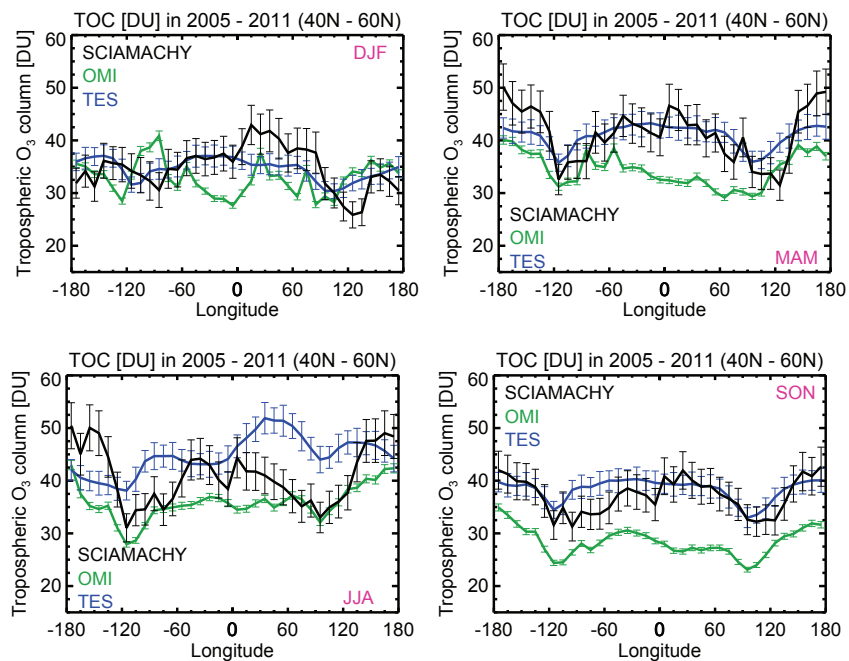


Figure 6.30: Same as figure 6.28 but for the latitude bins 40°N - 60°N.

6.3 Seasonal cycles and trends analysis of SCIAMACHY tropospheric ozone columns

To further evaluate SCIAMACHY tropospheric O₃, eleven cities in the NH mid-latitudes are investigated for the years 2003 - 2011. The results in some of the stations display typical seasonal behaviour of tropospheric O₃, with first maximum occurring in late spring due to the influence of the intrusion of O₃ rich air-masses from the lower stratosphere to the troposphere (Chandra *et al.*, 2004; Logan, 1985), and a continuous increase till summer due to photochemical production of O₃ from both anthropogenic pollution and biogenic VOCs and NO_x (Bojkov, 1986). There is a decrease in TOCs over some of the East Asian cities during monsoon period (June - August). Investigation shows that pollution events are not limited to cities. Typical high O₃ values are found in suburban locations downwind from the urban centers, which can be explained by the O₃-NO_x-VOC sensitivity (Kleinman *et al.*, 2000; Milford *et al.*, 1994).

6.3.1 Seasonal cycles of SCIAMACHY tropospheric O₃

The seasonal cycle of tropospheric O₃ is controlled by several processes including photochemistry, deposition, and transport, which act on local, regional and global scales (Logan, 1985). The seasonal cycle shows a spring to early summer O₃ maximum in the NH mid-latitudes (Derwent *et al.*, 1998; Logan, 1989; Scheel *et al.*, 1990). While the summer O₃ increase is primarily linked to the photochemistry of anthropogenically produced O₃ precursors, and less due to STE processes (Derwent *et al.*, 1998; Hough & Derwent, 1990), the spring O₃ increase is due to a combination of a number of processes. Stratospheric intrusion episodes (Logan, 1985; Oltmans, 1981), which result from the lowering of the tropopause height that permits vertical down-mixing of O₃, are the dominant source of tropospheric O₃ at the mid and high northern latitudes in spring. Photochemical activity resulting from increased solar radiation acting upon the NO_x and other O₃ precursors that have accumulated during winter also play a major role in spring time increase in O₃ (Dibb *et al.*, 2003). Tropospheric O₃ exhibits a slower photochemistry in winter than in spring and summer (e.g., Klonecki & Levy II, 1997). The long photochemical lifetime of tropospheric O₃ in winter (~200 days), allows anthropogenically produced O₃ to accumulate and contribute to spring O₃ increase (Liu *et al.*, 1987).

Figure 6.34 illustrates the seasonal variation of tropospheric O₃ over some cities listed in Table 6.3. Observations over Istanbul, Madrid, New York and Xinglong show a typical seasonal behavior of mid-latitudes tropospheric O₃, with increase in O₃ during boreal spring that could be associated with the downward transport of O₃ from the lower stratosphere (e.g., Logan, 1985). Over New York,

6.3 Seasonal cycles and trends analysis of SCIAMACHY tropospheric ozone columns

Xinglong, Beijing, Teharan, Shanghai, Nam Co, New Delhi and Mexico city, high TOC values are observed during summer months when solar activity is at its peak.

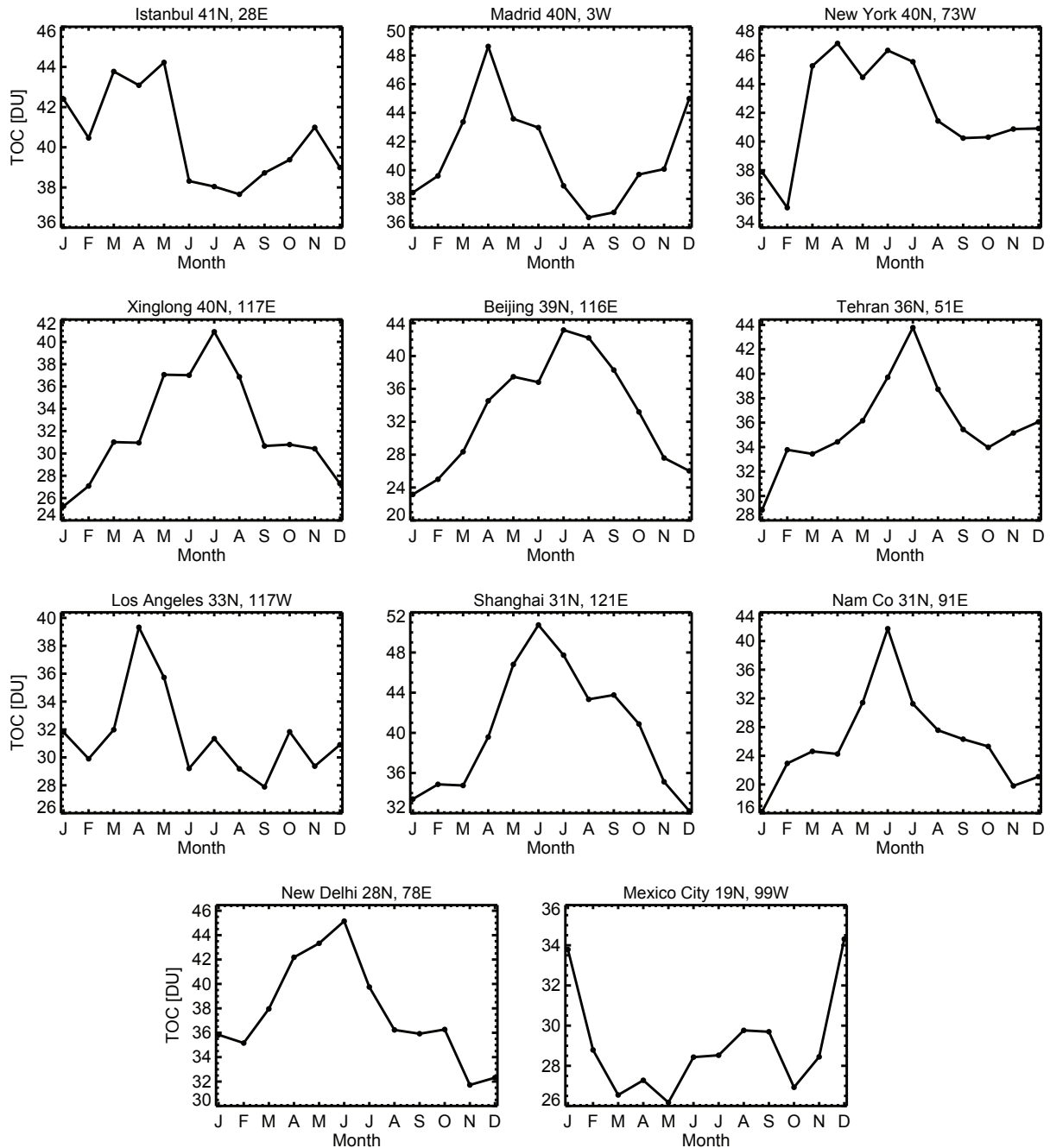


Figure 6.34: Seasonal distribution of the SCIAMACHY TOC from 2003 - 2011 in selected urban regions.

The high O_3 in these regions can be associated with anthropogenic activity (Chandra *et al.*, 2004; Stohl *et al.*, 2007). Lower TOC values observed during summer over Los Angeles, Istanbul and

6. VALIDATION OF SCIAMACHY TROPOSPHERIC OZONE COLUMNS

Madrid can be as a result of photochemical destruction of O₃, a phenomenon that is more prominent in summer than in spring (Derwent *et al.*, 1998). The decrease in O₃ towards end of summer over New Delhi, Nam Co and Shanghai can be associated with the summer monsoon, which starts in mid-June and lasts until end of August (Varshney & Aggarwal, 1992). This brings clean air with lower values of tropospheric O₃. Summer time in these regions is the rainy season. Therefore, there is less photochemical activity due to the presence of clouds and the wet scavenging of O₃ precursors by rains. The East Asian summer monsoon in July – August does not have much influence on the TOC values over Beijing and Xinglong because of the additional downward transport of O₃ from the stratosphere (Stohl *et al.*, 2007). Comparison of the period of Beijing Olympic games in 2008 with the same period in other years shows a slight increase in tropospheric O₃ compared to the other years. The seasonal cycle over Mexico City reflects a typical low latitude station with less influence of STE processes. The high TOC values during winter and summer over Mexico City are due to topography and meteorology. The surrounding mountains and frequent thermal inversions trap O₃ close to the ground (Molina *et al.*, 2007).

6.3.2 SCIAMACHY tropospheric ozone timeseries and trends

The SCIAMACHY tropospheric O₃ trends are determined using a multivariate linear regression with the autocorrelation of consecutive values described by the Cochrane–Orcutt transformation (Cochrane & Orcutt, 1949). It involves first estimating a model and regressing residuals on lagged residuals to estimate the autocorrelation parameter (ρ). ρ is used to transform the variables and an ordinary least square regression is performed on the transformed variables. Detailed discussion on this procedure are included in Cochrane & Orcutt (1949). The approach applied here is similar to that used for stratospheric O₃ trends and variability by Gebhardt *et al.* (2014). The linear regression is unweighted and it accounts for seasonal variations, the quasi-biennial oscillation (QBO), solar cycle signatures (SC), and El Nino-Southern Oscillation (ENSO). The trend model is expressed as:

$$Z_t = \mu + \omega t + S_t + R(t) + \epsilon(t), \quad (6.1)$$

where Z_t is the monthly mean tropospheric O₃ data, t is the month index (1 -108), μ is the intercept, which represent the seasonal fit. ϵ is the error term, ω , which is the gradient or slope, represents the trend. S_t is the seasonal component including annual, semi-annual and the 4 and 3-month terms, which is described as:

$$S_t = \sum_{i=1}^4 \left(\beta_{1i} \sin\left(\frac{2\pi it}{12}\right) + \beta_{2i} \cos\left(\frac{2\pi it}{12}\right) \right), \quad (6.2)$$

6.3 Seasonal cycles and trends analysis of SCIAMACHY tropospheric ozone columns

$R(t)$ represents additional terms including QBO, SC and ENSO, which can be expressed as:

$$R(t) = m\text{QBO50}(t) + n\text{QBO70}(t) + \delta\text{SC}(t) + x \left(N_{34}(t) + \frac{yN_{34}(t)}{dt} \Delta(t) \right). \quad (6.3a)$$

The fitting parameters are μ , ω , β_{11} , β_{12} , ..., β_{23} , β_{24} , m , n , δ , x and y . The harmonics (12, 6, 4, 3-month periods), $i = 1, 2, 3, 4$, a sine and cosine term are used to represent seasonal changes (Weatherhead *et al.*, 2000). The 12 and 6 months correspond to the annual and semi-annual cycles. The terms with 4 and 3 month periods help to improve the fit quality mostly when the cycle shape is not sinusoidal (Stiller *et al.*, 2012). The combination of sine and cosine terms provides a flexible adjustment to any phase of the (semi-)annual variation. The trend uncertainty is 1σ , which is defined by the covariance matrix of regression coefficients. The trends and their uncertainties are presented in relative units of $\% \text{ yr}^{-1}$, i.e. percent per year relative to the mean value of the underlying time series. The trend is significant at the 95 % confidence level if the absolute ratio of the trend to its uncertainty is greater than 2 (Tiao *et al.*, 1990).

6.3.2.1 QBO, solar cycle, and ENSO signatures in ozone

El Niño Southern Oscillation (ENSO) and quasi-biennial oscillation (QBO) modulate the stratospheric circulation (e.g., Simpson *et al.*, 2011), O_3 (e.g., Oman *et al.*, 2013), and STE O_3 flux (e.g., Zheng & Pyle, 2005). QBO dominates the variability of the tropical stratosphere. It is characterized by alternating easterly and westerly wind regimes within a variable period of 2 - 3 years (Pascoe *et al.*, 1948). The QBO directly modulates tropical upwelling through thermal wind balance. Its response to O_3 is driven by vertical transport with maximum influence around 20 – 27 km and 30 – 30 km (Butchart *et al.*, 2003; Chipperfield *et al.*, 1994). Although the QBO is a tropical phenomenon, it influences the entire stratospheric flow by modulating the effects of extratropical waves. It regulates the upwelling branch of the Brewer-Dobson circulation and leads to variation in O_3 VMR mostly at the altitudes of steep O_3 VMR gradient, which is found below and above the maximum in the vertical O_3 VMR profiles. This leads to a vertical squeezing or stretching of the mean vertical O_3 VMR profile during the westerly or easterly QBO phases, respectively (Butchart *et al.*, 2003). During the equinoxes, the QBO circulation cells are of comparable magnitude and are confined to the tropics, with downward (upward) flow in the subtropics to balance the equatorial upwelling (downwelling) during westward (eastward) phase transitions. Thus, they have little impact on the net tropical upwelling or on the large-scale downwelling at mid-latitudes. However, during the solstices, the mean meridional circulation (Hadley circulation) is dominated by a strong winter hemisphere and a very weak or non-existent summer hemisphere. Therefore, the winter hemisphere cell can extend deep into the mid-latitudes, thus, modulating both the mean tropical

6. VALIDATION OF SCIAMACHY TROPOSPHERIC OZONE COLUMNS

upwelling and mean middle and high latitude downwelling with accompanying mass transport (Hsu & Prather, 2009; Voulgarakis *et al.*, 2011). The high-latitude wind anomalies can penetrate the tropopause and provide a mechanism for the QBO to influence the troposphere (Baldwin *et al.*, 2001). In fact, it has been shown that QBO directly has impact on the entire NH tropical to mid-latitude large-scale circulation (Neu *et al.*, 2014). In this study, the 50 and 70 hpa Singapore (1°N, 140°E) winds found at <http://www.geo.fu-berlin.de/en/met/ag/strat/produkte/qbo/> are used as fit proxies. It is smoothed by a 4-month running mean and used between 30 °S - 30 °N in the form of equation 6.4.

$$\text{QBO}(t) = m\text{QBO}_{50}(t) + n\text{QBO}_{70}(t), \quad (6.4)$$

where m and n are fit coefficients, the indices 50 and 70 denote the pressure level of the proxy. A similar approach used for the QBO is implemented for the Mg II index when used as a solar cycle proxy. It is not necessary to de-trend both proxies (Kane & Trivedi, 1986) as smaller periodicities are well revealed.

The 11-year solar cycle leads to a larger magnitude in the variability of the UV irradiance than in the visible and near infrared radiation (Lean *et al.*, 1997). Hence, it influences stratospheric O₃ (Gray *et al.*, 2010). The dynamical perturbations caused by solar flux variability, play a significant role in regulating the chemical state of the atmosphere (Egorova *et al.*, 2005; Gray *et al.*, 2010). Increased solar activity leads to a warmer troposphere, poleward shift of the Hadley circulation and the weakening and poleward expansion of the mid-latitude jets (Gleisner & Thejll, 2003; Haigh, 2003; Labitzke & van Loon, 1995). In this thesis, the solar cycle proxy represented by a multi-instrument monthly average Mg II index based on GOME, SCIAMACHY, and GOME-2 observations is included in the multivariate linear regression in the form of equation 6.5. The data can be obtained from http://www.iup.uni-bremen.de/gome/solar/MgII_composite.dat (Snow *et al.*, 2014).

$$\text{SC}(t) = \delta\text{SC}(t), \quad (6.5)$$

where δ is the fit coefficient for the solar proxy.

Another dominant mode of interannual variability in tropical climate is ENSO. ENSO alters the stratospheric circulation by modulating the propagation and dissipation of the waves that drive it. The waves include not only planetary-scale waves, but also synoptic-scale and gravity waves (e.g., Garcia-Herrera *et al.*, 2006; Simpson *et al.*, 2011). ENSO plays a major role on the interannual variability of the tropospheric chemistry. Response to circulation and convective changes during El Niño lead to decrease in TOC in central and East Pacific and an increase in the West Pacific/Indonesia (Fujiwara *et al.*, 1999, 2000; Thompson *et al.*, 2001). The increase in TOC in

6.3 Seasonal cycles and trends analysis of SCIAMACHY tropospheric ozone columns

the West Pacific/Indonesia is associated with the combination of precursor emission from biomass burning and large-scale circulation processes associated with the shift in the tropical convection pattern (Chandra *et al.*, 2002; Sudo & Takahashi, 2001). Changes in large-scale circulation can either lead to a decrease or increase in TOC. Enhanced convection and upward motion of low O₃ air from the lower troposphere lead to decreases in TOC while suppressed convection and downward motion of O₃ rich air from the upper troposphere lead to increases in TOC. Biomass burning influence on tropospheric O₃ production is confined to the lower troposphere due to suppressed convection. In this study, an ENSO proxy based on the anomalies of the Niño 3.4 index <http://www.cpc.ncep.noaa.gov/data/indices/> is employed to reveal ENSO signatures on tropospheric O₃ timeseries. The combined fit of the proxy and its time derivative account for the time lag as shown in equation 6.6.

$$\text{ENSO}(t) = x \left(N_{34}(t) + \frac{yN_{34}(t)}{dt} \Delta(t) \right), \quad (6.6)$$

where N_{34} is the ENSO proxy and $\Delta(t)$ is the time lag. To account for the non-linearity of $\frac{yN_{34}(t)}{dt}$, the fit starting with a time lag of 2 months, is repeated with the lagged proxy until the remaining time lag approaches zero.

6.3.2.2 Zonal means tropospheric O₃ changes

O₃ trends are mainly caused by long-term changes in both chemistry and dynamics. Uncertainties of O₃ measurements and interannual variability can introduce uncertainties to trends (Logan *et al.*, 2012; Tarasick *et al.*, 2005). Zonal mean time series showing tropospheric ozone changes over three latitude bands (50°S - 30°S, 20°S - 20°N, 30°N - 50°N) are displayed in Figures 6.35 - 6.37. These zonal bands combine mixed data (land, ocean, remote, rural, suburban, and urban). The TOC time series (black) are overlaid with their fitting curves (blue) and linear trend (violet) from the regression model. Below the TOC time series, the fit residuals are shown. The individual terms from the regression including the harmonics, QBO, solar cycle, linear and ENSO terms are shown in corresponding panels below. The harmonic terms comprise all periods (12, 6, 4, and 3 months). The time series of each of the fit parameters are colored, e.g., pink, green, yellow, orange, and brown represent only harmonic, QBO, solar and linear and ENSO terms, respectively, while the overlaid time series in black represents time series with all fit terms removed except the particular fit parameter. The combination of 50 hpa and 70 hpa Singapore winds to fit the QBO as well as the approximation of the semi or annual oscillation with the harmonics appear to be a sufficient approach. Good fit quality is obtained in all three latitude bands. The fit residuals are typically on the order of a few DU in the 3 latitude bands. The harmonic terms show peak values during

6. VALIDATION OF SCIAMACHY TROPOSPHERIC OZONE COLUMNS

hemispheric spring and summer for the 30°N - 50°N and 60°S - 40°S latitude bands. The peak values observed during these seasons of the year are associated both to photochemical production of tropospheric O₃ as well as stratospheric intrusion of O₃ rich air masses into the troposphere. Between 20°S - 20°N, the harmonic terms show peak values mainly during austral spring/summer. The high values in this zonal band are attributed mainly to transport and photochemical production of ozone. Observations at 50°S - 30°S (Figure 6.35), show an insignificant increase in tropospheric O₃ of $0.2 \pm 0.2 \text{ \%yr}^{-1}$. The increase in ozone in this latitude band may be due to the combination of both anthropogenic and natural ozone production including influence of STE processes, biomass burning and fossil fuels combustion. This region is mainly over the ocean with less influence from land, hence there is uniformity in O₃ distributions in this zonal band as observed in Fig. 12 of Ebojie *et al.* (2014). An insignificant decrease in TOCs of $-0.2 \pm 0.5 \text{ \%yr}^{-1}$ is observed between 30°N - 50°N (Figure 6.36). This zonal band is greatly influenced by land-sea contrast in tropospheric O₃ and by anthropogenic activity. Therefore, the decrease in TOC observed over this latitude band could be associated with stronger negative TOC trends over land compared to the ocean, which suggests a decline in tropospheric O₃ and its precursors over this region.

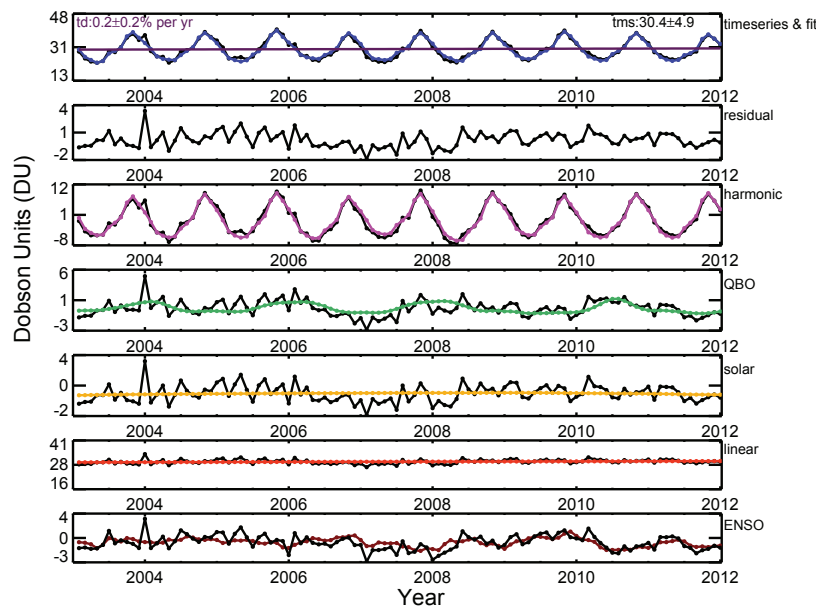


Figure 6.35: Time series of the TOC (in Dobson Units (DU)) from SCIAMACHY for 50°S - 30°S (black) with overlaid fitting curve (blue) in top panel and fit residuals (second panel). Below, the components of the fitting curve are shown individually (from top to bottom): harmonic (pink), QBO (light green), solar cycle (yellow), linear change (orange), and ENSO (brown). Each of these terms is overlaid by the time series with all other components of the fitting curve subtracted, e.g., the harmonic terms by the time series with QBO, solar cycle, and linear terms subtracted.

In the 20°S - 20°N latitudes band (Figure 6.37), an insignificant increase in tropospheric O₃ of

6.3 Seasonal cycles and trends analysis of SCIAMACHY tropospheric ozone columns

$0.5 \pm 0.4 \text{ \%yr}^{-1}$ is observed. The increase in ozone in this region is a contribution of both natural and anthropogenic activities. Biomass burning, forest fires, transport of ozone and its precursors play a major role in enhancing O_3 in this latitude band.

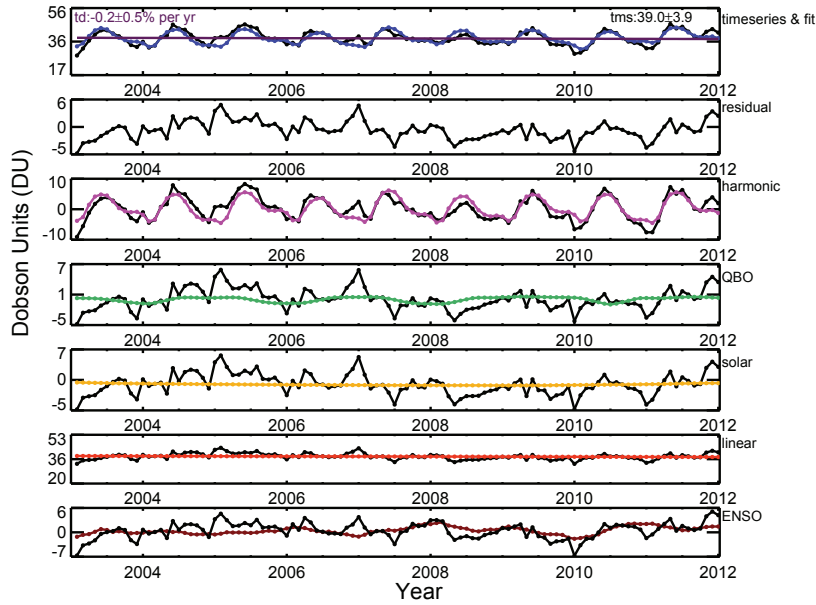


Figure 6.36: Same as Figure 6.35 but for $30^\circ\text{N} - 50^\circ\text{N}$.

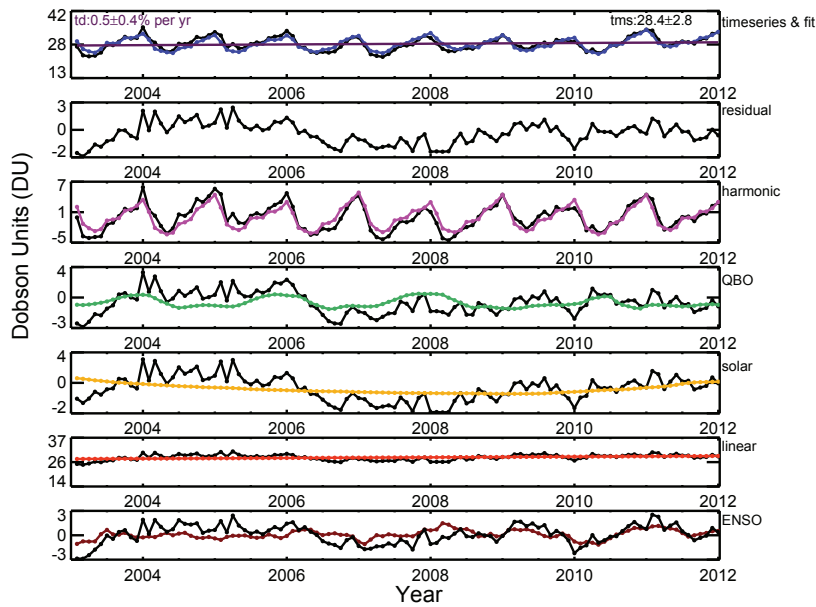


Figure 6.37: Same as Figure 6.35 but for $20^\circ\text{S} - 20^\circ\text{N}$.

6. VALIDATION OF SCIAMACHY TROPOSPHERIC OZONE COLUMNS

Lat. range	Mean value & std. dev. (DU)	Trend (% yr ⁻¹)
1. 50°S - 30°S	30.4±4.9	0.2±0.2
2. 20°S - 20°N	28.4±2.8	0.5±0.4
3. 30°N - 50°N	39.0±3.9	-0.2±0.5

Table 6.2: Trend analysis of SCIAMACHY tropospheric O₃ for different latitude ranges.

6.3.2.3 Timeseries and trends of tropospheric O₃ over megacities

Changes in tropospheric O₃ are best characterized at the downwind side due to O₃-NO_x-VOC sensitivity. Tropospheric O₃ values over rural regions can be higher than the values derived close to region of anthropogenic activities. Generally, rural regions downwind are found to be in a NO_x-limited regime while urban regions are found to be in a NO_x-saturated regime (Duncan *et al.*, 2010; Milford *et al.*, 1989). Downwind of the emission source, there is a transformation from VOC-sensitivity to NO_x-sensitivity as a result of the more rapid removal of NO_x compared to VOCs. Consequently, this leads to an increase in ozone due to the conversion of more NO to NO₂, as well as an increase in the fraction of OH radicals that react with VOCs (Milford *et al.*, 1994). However, as the concentrations of NO_x continue to fall, the air parcel begins to transit from VOC-sensitive to the transitional region and often reaches a NO_x-sensitive regime with resultant decrease in O₃ (Jacob *et al.*, 1995; Kleinman *et al.*, 2000).

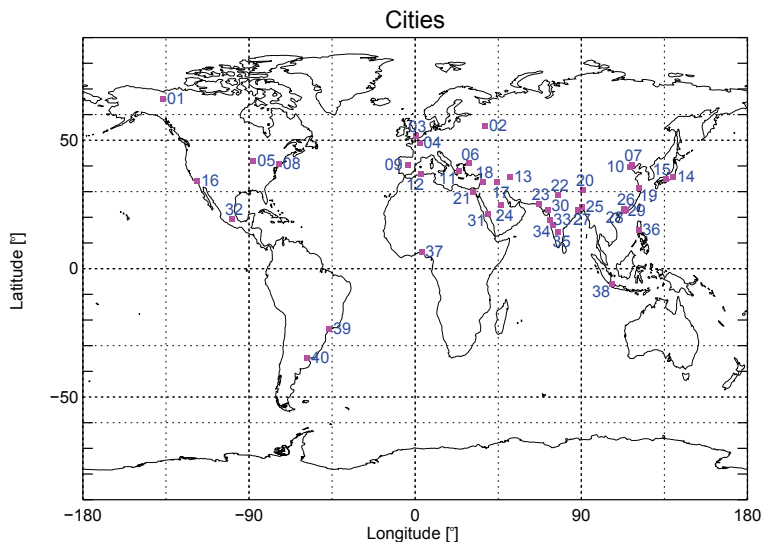


Figure 6.38: World map showing cities (station numbers are listed in Table 6.3) used in trend analysis.

The time series of O₃ from 2003 – 2011 over megacities (see Table 6.3 and Figure 6.38), i.e., large urban agglomerations in excess of 10 million inhabitants are examined to ascertain changes in tropospheric O₃ over the region. These are considered hotspots in terms of pollution due to intensive anthropogenic activities (e.g., Molina & Molina, 2004). The study of changes in tropospheric O₃

6.3 Seasonal cycles and trends analysis of SCIAMACHY tropospheric ozone columns

using satellite instrumentation is efficient as it enables the derivation of both regional and global information on O₃ distributions (e.g., Ebojje *et al.*, 2014; Ziemke *et al.*, 2006). In addition, the combination of satellite measurements with global models of atmospheric chemistry and transport provides information on tropospheric O₃ transport and variability (Chandra *et al.*, 2003; Valks *et al.*, 2003). Temporal changes in continental influence including in-situ tropospheric O₃ production from locally emitted precursors, transport of air masses with varying histories, deposition to the ground and other surfaces, reaction of O₃ with local emissions, etc., contribute to the significant regional differences found in O₃ trends, particularly at the northern mid latitudes (e.g., Oltmans *et al.*, 2006).

Figures 6.39 - 6.49 show the plots of some of the cities investigated in this analysis. The two cities in Europe, Istanbul (Figure 6.39) and Madrid (Figure 6.40), show an insignificant decrease in O₃ time series of $-1.5 \pm 0.8 \text{ \%yr}^{-1}$ and $-0.7 \pm 0.9 \text{ \%yr}^{-1}$, respectively. A similar decrease in tropospheric O₃ over some regions in Europe has been observed in previous studies (e.g., Logan *et al.*, 2012). The decrease in tropospheric O₃ over Europe can be associated with reduction in NO_x emissions (Vestreng *et al.*, 2009). Observations over North America show different signs and magnitude in tropospheric O₃ trends. While an insignificant decrease in TOC is observed over New York ($-0.1 \pm 0.8 \text{ \%yr}^{-1}$, Figure 6.41), an insignificant increase in TOC is derived for Los Angeles ($0.5 \pm 0.5 \text{ \%yr}^{-1}$, Figure 6.42). Observations over Mexico City (Figure 6.43), show a significant negative TOC trend ($-2.0 \pm 0.9 \text{ \% yr}^{-1}$). The negative TOC trends over New York and Mexico cities can be associated with reduction in O₃ precursors emissions (e.g., Zavala *et al.*, 2009), while the insignificant increase observed over Los Angeles may be due to combination of anthropogenic influence, physical setting as well as weather patterns over the region (Milford *et al.*, 1989). Two of the cities investigated in Asia, i.e., Shanghai (Figure 6.44) and Tehran (Figure 6.47), show significant positive TOC trends of $1.9 \pm 0.8 \text{ \%yr}^{-1}$ and $2.0 \pm 0.9 \text{ \%yr}^{-1}$, respectively. Observations over Nam Co (Figure 6.45), Beijing (Figure 6.48) and Xinglong (figures 6.46) show insignificant positive TOC trends of $1.8 \pm 1.9 \text{ \%yr}^{-1}$, $1.3 \pm 1.5 \text{ \%yr}^{-1}$ and $0.5 \pm 0.8 \text{ \%yr}^{-1}$, respectively. The behaviour of TOC trends over these cities can be attributed to an increase in anthropogenically produced O₃ precursor emissions, which can

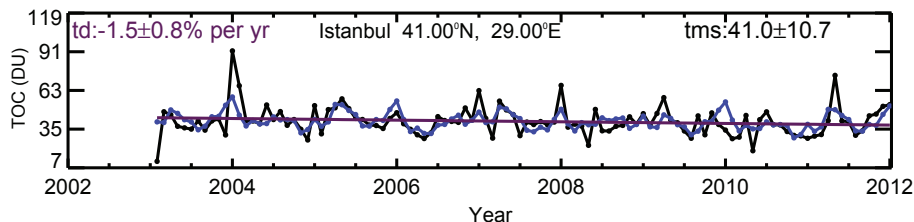


Figure 6.39: Time series of the TOC (in DU) from SCIAMACHY in black with overlaid fitting curve in blue and linear trend in violet over Istanbul (41°N, 28°E). The x-axis label represents the start of each year.

6. VALIDATION OF SCIAMACHY TROPOSPHERIC OZONE COLUMNS

be explained by O_3 - NO_x -VOC sensitivity (e.g., Duncan *et al.*, 2010; Milford *et al.*, 1989). Over New Delhi (Figure 6.49), a significant positive increase in TOC of $2.3 \pm 0.8 \text{ \%yr}^{-1}$ is observed. The increase in TOC over this region can be associated with increased anthropogenic emissions resulting from power stations, road transport, industry and fossil fuel combustion (Gurjar *et al.*, 2004, 2008).

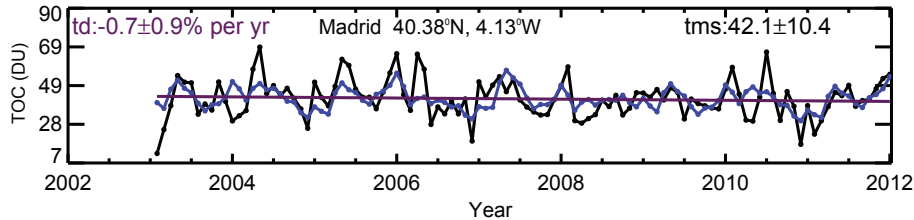


Figure 6.40: Same as Figure 6.39 but for Madrid (40°N, 3°W)

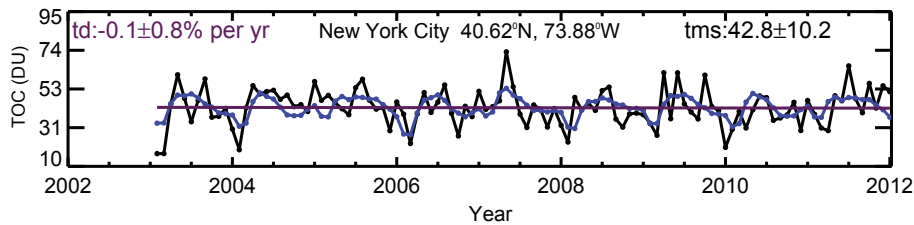


Figure 6.41: Same as Figure 6.39 for New York (40°N, 73°W)

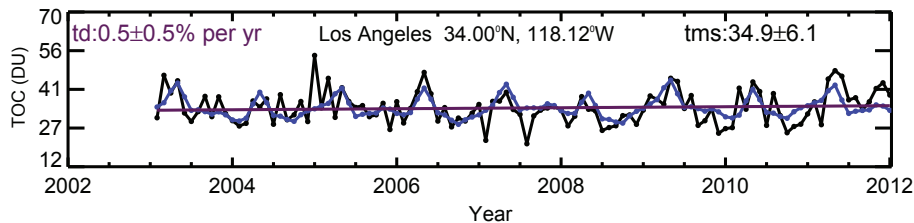


Figure 6.42: Same as Figure 6.39 for Los Angeles (33°N, 117°W)

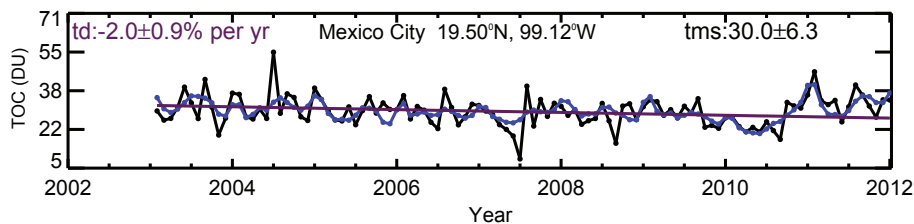


Figure 6.43: Same as Figure 6.39 for Mexico City (19°N, 99°W)

6.3 Seasonal cycles and trends analysis of SCIAMACHY tropospheric ozone columns

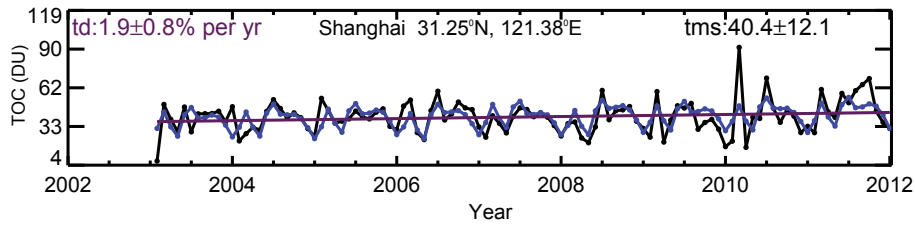


Figure 6.44: Same as Figure 6.39 for Shanghai (31°N, 121°E)

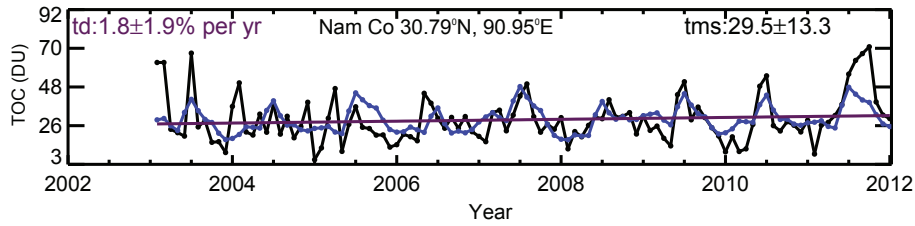


Figure 6.45: Same as Figure 6.39 for Nam Co (31°N, 91°E)

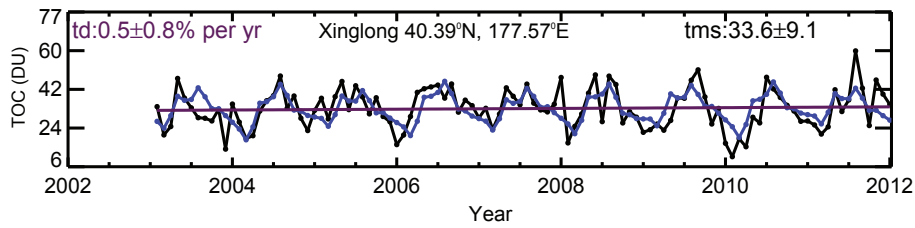


Figure 6.46: Same as Figure 6.39 for Xinglong (40°N, 117°E)

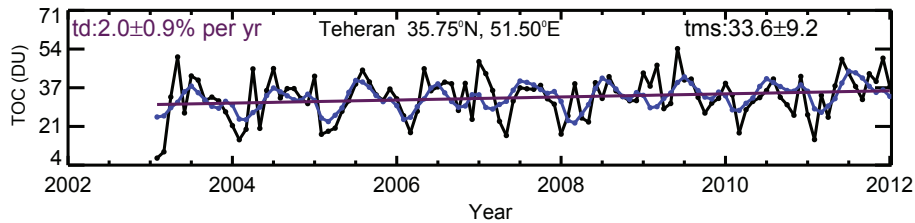


Figure 6.47: Same as Figure 6.39 for Tehran (36°N, 51°E)

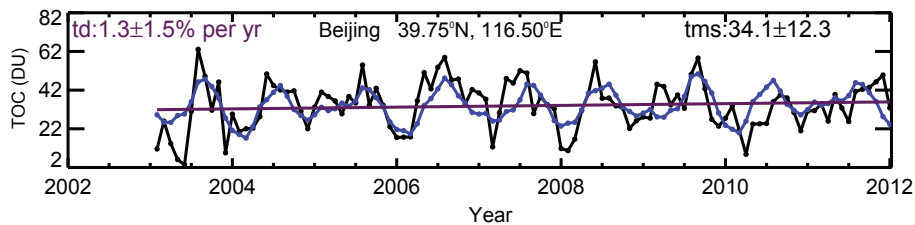


Figure 6.48: Same as Figure 6.39 for Beijing (39°N, 116°E)

6. VALIDATION OF SCIAMACHY TROPOSPHERIC OZONE COLUMNS

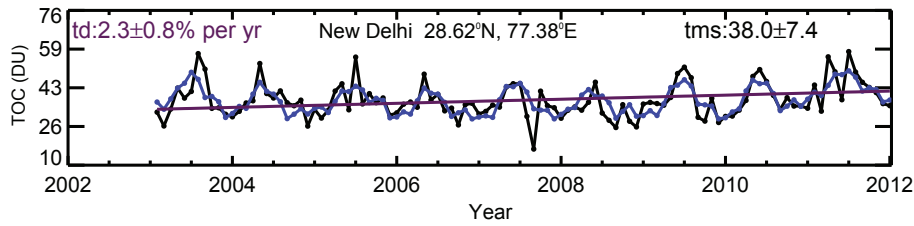


Figure 6.49: Same as Figure 6.39 for New Delhi (28°N, 78°E)

The TOC trends in Table 6.3 are grouped into tropical and extratropical regions. In the tropics (20°N - 20°S), a significant negative TOC trend is observed over Mexico City. While a significant positive TOC trend is recorded over Bangalore an insignificant TOC trends are observed over the other tropical cities (Manila, Mumbai, Pune, Lagos and Jakarta). The significant negative O₃ trend over Mexico City can be associated with reduction in anthropogenically produced O₃ precursors (Zavala *et al.*, 2009), while the observed significant increase in O₃ over Bangalore can be attributed to increase O₃ precursor emissions as a result of economic growth (Dalvi *et al.*, 2006; Sheel *et al.*, 2010).

In the SH subtropics and extratropics, observations over Buenos Aires show a significant positive TOC trend while an insignificant decrease is recorded over Sao Paulo. The significant increase in TOC over Buenos Aires is of anthropogenic origin associated with increasing fossil fuel combustion from thermal power plants mostly during winter as well as photochemically produced O₃ precursors from industry, vehicles and other combustion processes (Mazzeo *et al.*, 2010). The insignificant negative TOC trends over Sao Paulo can be attributed to reduction in O₃ precursors emission as well as the shift in convection pattern over the region (Jacobi *et al.*, 1999; Sudo & Takahashi, 2001).

In the NH subtropical and extratropical regions, significant decrease in TOC trend is observed over London, which could be attributed to the decrease in O₃ precursors (Logan *et al.*, 2012; Vestreng *et al.*, 2009). Observations over Alaska, Teheran, Osaka, Shanghai, New Dehli, Riyadh and Dhaka show significant increase in TOC trends. The significant increase in TOC trends over these cities is mainly of anthropogenic origin (e.g., Molina & Molina, 2004; Ohara *et al.*, 2007). Transport of O₃ and its precursors as well as the prevailing weather phenomenon may also play a role in TOC changes over the cities (e.g., Parrish *et al.*, 2012; Stevenson *et al.*, 2013). Other cities investigated in the NH extratropics show insignificant change in TOC trends as summarized in Table 6.3.

6.3 Seasonal cycles and trends analysis of SCIAMACHY tropospheric ozone columns

Station	Latitude range (°N)		Longitude range (°E)		Trend (% yr ⁻¹)	Mean value & stdev. (DU)
1. Alaska	60.00	72.00	-170.00	-103.00	2.1 ±1.0	38.1±10.5
2. Moscow	55.25	56.25	37.00	38.75	1.3 ±1.8	40.9 ± 10.1
3. London	51.25	52.00	-0.50	1.00	-2.9±0.8	39.8 ± 8.3
4. Paris	48.50	49.25	1.75	3.00	-1.8±1.1	39.3 ± 10.2
5. Chicago	41.87	42.37	-87.64	-87.58	1.7 ±1.1	38.7 ± 10.1
6. Istanbul	40.75	41.25	28.50	29.50	-1.5±0.8	41.0 ± 10.7
7. Xinglong	40.39	40.39	117.57	117.58	0.5±0.8	33.60±9.10
8. New York	40.25	41.00	-74.50	-73.25	-0.1±0.8	42.8 ± 10.2
9. Madrid	40.00	40.75	-4.00	-3.25	-0.7±0.9	42.1 ± 10.4
10. Beijing	39.50	40.00	116.00	117.00	1.3 ±1.5	34.1 ± 12.3
11. Athens	37.75	38.25	23.50	24.00	-1.4±0.7	42.7 ± 8.3
12. Algiers	36.50	37.00	2.50	3.50	-1.4±0.8	31.1 ± 7.5
13. Teheran	35.50	36.00	51.00	52.00	2.0 ±0.9	33.6 ± 9.2
14. Tokyo	35.25	36.25	139.25	140.50	1.1 ±0.8	39.5 ± 12.3
15. Osaka	34.65	35.15	135.60	135.66	1.4 ±0.6	40.5 ± 11.5
16. Los Angeles	33.75	34.25	-118.50	-117.75	0.5 ±0.5	34.9 ± 6.1
17. Baghdad	33.50	33.75	43.75	45.00	0.6 ±0.6	33.9 ± 5.6
18. Dimashq	33.38	33.88	36.25	36.75	1.4 ±0.8	36.7 ± 8.9
19. Nam Co	30.79	30.76	90.97	90.95	1.8 ±1.9	29.5 ± 13.3
20. Shanghai	30.75	31.75	120.75	122.00	1.9 ±0.8	40.4 ± 12.1
21. Cairo	29.50	30.50	30.75	32.00	-0.8±0.7	30.0 ± 4.3
22. New Delhi	28.25	29.00	76.75	78.00	2.3 ±0.8	38.0 ± 7.4
23. Karachi	24.89	25.39	67.05	67.11	0.6 ±0.7	36.4 ± 4.9
24. Riyadh	24.25	25.12	46.25	47.00	0.9 ±0.4	32.6 ± 4.4
25. Dhaka	23.70	24.20	90.38	90.44	3.2 ±1.3	37.2 ± 9.7
26. Guangzhou	23.13	23.63	113.27	113.33	1.9 ±1.0	39.4 ± 10.9
27. Kolkata	22.57	23.07	88.37	88.43	1.3 ±0.9	36.0 ± 6.7
28. Shenzhen	22.55	23.05	114.10	114.16	1.9 ±1.0	39.4 ± 10.9
29. Hong Kong	22.00	23.25	112.75	113.75	1.9 ±1.0	39.4 ± 10.9
30. Ahmedabad	21.43	24.28	70.31	73.12	1.4 ±0.9	36.6±6.3
31. Jeddah	21.00	21.88	38.88	39.62	0.5 ±0.4	35.6 ± 4.8
32. Mexico City	19.25	19.75	-99.50	-98.75	-2.0±0.9	30.0 ± 6.3
33. Mumbai	18.75	19.25	72.50	73.25	-0.4±0.9	34.3 ± 6.4
34. Pune	15.71	18.57	73.12	75.94	0.7 ±0.7	34.3±4.9
35. Bangalore	12.86	15.71	75.94	78.75	2.3 ±1.0	30.6±5.8
36. Manila	14.60	15.60	121.00	121.07	1.8 ±1.3	32.8 ± 8.6
37. Lagos	6.25	7.00	3.00	4.00	-1.5±1.0	33.5 ± 6.5
38. Jakarta	-6.50	-5.75	106.25	107.25	-0.2±1.6	24.6 ± 8.2
39. Sao Paulo	-24.00	-23.25	-47.00	-46.25	-1.6±1.0	32.0 ± 8.0
40. Buenos Aires	-35.00	-34.25	-58.75	-58.00	2.6 ±1.1	28.5 ± 9.3

Table 6.3: Trends in SCIAMACHY tropospheric O₃ in %yr⁻¹ over megacities. Bold text signifies statistically significant changes in TOC.

6.3.2.4 Timeseries and trends of tropospheric O₃ comparison between SCIAMACHY and ozonesondes

This section discusses the comparison of TOCs trends as observed by SCIAMACHY and ozonesonde instruments. The SCIAMACHY TOC data used in this analysis are binned at 5° latitude and 5° longitude. Therefore, differences in the comparison are inevitable. Both instruments show significant decrease in TOC trends over Sodankyla, De Bilt, Bratt's Lake Huntsville, Hanoi, Costarica, Sepang Airport and Kuala. The observed decrease in TOC trends over these regions can be associated with reduction in O₃ precursor emissions as well as meteorological changes (Oltmans *et al.*, 2006).

6. VALIDATION OF SCIAMACHY TROPOSPHERIC OZONE COLUMNS

Station	Lat. (°N)	Lon. (°E)	Sonde		SCIAMACHY	
			Trend (% yr ⁻¹)	Mean value & stdev.(DU)	Trend (% yr ⁻¹)	Mean value & stdev.(DU)
Alert	82.50	297.70	0.2 ±0.6	29.8±4.4	0.6 ±4.4	24.0±8.2
Eureka	80.05	273.58	0.2 ±0.3	29.7±3.5	0.6 ±3.6	31.0±10.0
Ny-alesund	78.93	11.88	-0.2±0.5	33.0±3.2	-3.7±1.4	39.8±7.6
Resolute	74.72	265.02	-0.5±0.5	28.9±4.2	-0.7±2.0	35.2±10.6
Scoresbysund	70.50	338.00	-1.0±0.6	30.5±2.9	-4.0±1.4	33.5±6.9
Sodankyla	67.39	26.65	-1.3±0.5	33.0±3.9	-2.9±1.4	37.8±8.0
Lerwick	60.13	358.82	-2.7±0.4	34.5±5.0	0.2 ±1.0	34.3±9.4
Churchill	58.75	265.93	-0.9±0.4	32.1±4.8	-1.3±1.2	33.1±7.8
Edmonton	53.55	245.90	-0.6±0.4	29.6±4.3	1.3 ±1.1	32.4±8.2
Goosebay	53.32	299.70	0.2 ±0.3	32.7±4.7	2.0 ±1.0	33.0±8.1
Legionowo	52.40	20.97	-0.9±0.3	36.9±7.3	0.7 ±0.8	40.5±8.2
De Bilt	52.10	5.18	-1.0±0.3	36.0±5.9	-1.7±0.6	40.8±8.7
Valentia	51.93	349.75	-1.7±0.9	37.0±5.1	-0.7±1.5	30.9±7.2
Uccle	50.80	4.35	0.0 ±0.6	36.7±6.4	-0.3±0.7	39.8±8.7
Bratt's Lake	50.20	255.30	-1.8±0.7	34.3±6.2	-2.4±1.1	36.5±8.1
Praha	50.02	14.45	-1.4±0.3	39.0±4.8	4.7 ±4.3	38.0±14.4
Kelowna	49.93	240.60	-0.8±0.7	34.1±5.6	1.0 ±1.7	33.1±9.9
Payerne	46.49	6.57	-1.0±0.3	34.3±6.6	-0.3±0.5	44.4±7.3
Egbert	44.23	280.22	2.7 ±0.7	36.7±7.6	0.8 ±0.9	38.5±7.9
Yarmouth	43.87	293.89	3.4 ±2.1	37.8±11.0	-0.1±0.7	42.4±8.8
Sapporo	43.10	141.30	1.4 ±0.4	35.3±8.6	1.3 ±0.6	41.4±10.8
Madrid	40.45	356.28	0.3 ±0.6	35.0±6.8	1.0 ±0.8	41.5±6.9
Ankara	39.95	32.88	-0.2±0.4	35.8±9.6	-0.5±0.5	38.2±4.9
Wallops Island	37.93	284.52	-0.7±0.3	42.0±8.2	-0.3±0.6	41.7±7.4
Tsukuba	36.10	140.10	2.1 ±0.4	40.9±8.9	0.6 ±0.5	41.6±9.5
Huntsville	35.28	273.41	-5.2±1.4	34.6±8.8	-2.7±0.5	36.5±5.2
Isfahan	32.51	51.70	0.8 ±1.0	35.2±8.9	2.5 ±0.7	32.9±4.8
Kagoshima	31.60	130.60	1.5 ±0.6	41.6±4.2	1.5 ±0.6	46.1±4.5
Naha	26.20	127.70	2.0 ±0.5	38.1±7.4	0.2 ±0.8	44.3±8.2
Hong Kong	22.31	114.17	-1.0±0.8	39.5±7.4	2.2 ±0.6	39.8±6.3
Hanoi	21.01	105.80	-8.0±1.6	30.3±8.3	-4.8±1.0	37.1±7.5
Hilo	19.72	204.93	-1.0±0.6	32.9±6.1	1.0 ±0.6	33.1±4.7
Costarica	9.98	275.79	-8.2±1.2	30.5±9.4	-6.3±1.2	34.9±9.5
Paramaribo	5.81	304.79	0.5 ±1.0	27.7±7.2	0.3 ±0.8	27.1±4.9
Sepang Airport	2.73	101.70	-4.5±0.6	23.9±4.0	-4.7±1.1	23.8±5.7
Kuala	2.73	101.70	-8.1±0.7	23.1±5.0	-3.7±1.1	24.1±5.5
San Cristobal	-0.92	270.40	5.9±1.1	26.4±5.2	3.9 ±1.0	29.5±5.0
Nairobi	-1.27	36.80	0.3 ±0.8	28.7±3.5	1.2 ±0.6	26.3±3.4
Malindi	-2.99	40.19	0.5 ±1.1	33.5±5.3	-3.6±0.8	24.2±4.3
Natal	-5.42	324.62	4.3±1.3	36.0±9.1	1.7 ±0.6	30.3±6.4
Java	-7.50	112.60	-0.3±1.1	24.2±6.2	-0.8±1.5	26.6±7.9
Watukosek	-7.57	112.65	-5.2±1.6	22.1±6.7	-2.0±1.7	25.9±7.8
Ascension	-7.98	345.58	0.3 ±0.8	39.5±7.5	1.5 ±0.6	34.6±5.4
Samoa	-14.23	189.44	4.7 ±1.0	21.9±6.1	1.5 ±1.1	23.4±5.7
Suva	-18.10	178.20	0.0 ±1.0	26.7±3.6	2.8 ±0.6	34.3±4.4
Fiji	-18.13	178.40	-2.3±1.1	24.6±6.3	0.0 ±0.7	28.7±5.0
La Reunion	-21.06	55.48	1.7 ±0.9	40.5±8.6	-1.7±0.6	37.4±6.2
Irene	-25.90	28.22	1.8 ±0.7	38.1±4.9	1.6 ±0.7	30.6±3.9
Broadmeadows	-37.68	144.95	-0.2±0.5	28.6±4.7	0.0 ±0.3	31.2±7.1
Lauder	-45.04	169.68	-2.6±0.4	21.8±2.9	1.9 ±0.7	26.0±5.3
Macquarie Island	-54.50	158.97	1.8 ±1.0	23.8±3.8	-0.5±1.2	23.4±6.3
Ushuaia	-54.85	291.69	-9.8±2.1	33.2±10.9	-2.0±2.9	26.2±10.6
Marambio	-64.23	303.38	-5.1±0.9	20.0±4.9	-3.4±5.0	22.6±14.0
Davis	-68.58	77.97	1.3 ±0.6	19.2±3.1	5.5 ±1.0	24.3±5.8
Syowa	-69.00	39.58	0.2 ±0.4	18.2±3.9	0.2 ±1.1	22.5±4.6
Neumayer	-70.65	351.74	-1.1±0.2	19.5±3.8	-0.9±2.1	18.8±5.1

Table 6.4: Trends in SCIAMACHY and ozonesondes tropospheric O₃ in %yr⁻¹. SCIAMACHY TOC data are binned in 5° latitude and 5° longitude. Bold text indicates statistically significant changes in TOC.

6.3 Seasonal cycles and trends analysis of SCIAMACHY tropospheric ozone columns

Significant increase in TOC trends are derived from both instruments over Sapporo, Kagoshima, San Cristobal, Natal, Irene, and Devis. The increase in O_3 over these regions can be associated with increasing O_3 precursor emissions from fossil fuel combustion and Biomass burning. Regional and Inter continental transport of polluted air masses also play a major role in the observed increased in O_3 trend over these regions (e.g., Naja & Akimoto, 2004; Oltmans *et al.*, 2004). Observation shows that there exist some differences in the derived O_3 trends from the two instruments in terms of significance and signs. Over Ny-alesund and Scoresbysund, the derived TOC trends obtained from SCIAMACHY measurements show significant decrease while those derived from ozonesonde instrument show a small insignificant decrease over the two stations. The TOC trends values derived from ozonesonde measurements over Churchill, Payerne, Wallops Island, Ushuaia and Marambio show significant decrease while those of SCIAMACHY show decrease in TOC trends which are not significant. Over Lauder, SCIAMACHY TOC trend is significantly positive while that of ozonesonde is significantly negative. Similar positive increase in TOC trend was derived by Oltmans *et al.* (2006) over Lauder. The increase in trend over this region can be associated with increase in O_3 at the middle and lower troposphere (Oltmans *et al.*, 2006). Over Samoa, the TOC trend derived from ozonesonde showed a significant increase while the increased TOC trend derived from SCIAMACHY over the region is insignificant. SCIAMACHY TOC trends over Hong Kong and Ascension Island is positively significant while the values derived from ozonesonde over these regions are not significant. Over Malindi and La Reunion, SCIAMACHY TOC trends show significant reduction while the trends observed from ozonesonde over both regions are insignificantly positive. The observed trends from both instruments over the other stations show insignificant change in O_3 as summarized in table 6.4.

6.3.2.5 Timeseries and trends of tropospheric O_3 over regions and countries

This section discusses changes in tropospheric O_3 over some regions and countries (Table 6.5). The data sets are gridded on a 2.5° latitude \times 2.5° longitude resolution. Trends range between -0.7 to 1.9 \%yr^{-1} with a significant decrease in TOC of $-0.7 \pm 0.3 \text{ \%yr}^{-1}$ observed over Western Europe. The observed significant negative TOC trend over Western Europe can be attributed to a reduction in NO_x and other tropospheric O_3 precursors (Logan *et al.*, 2012; Vestreng *et al.*, 2009). Observation over some regions and countries in both hemispheres show significant positive TOC trends. These regions include Eastern China ($0.9 \pm 0.4 \text{ \%yr}^{-1}$), Northern India ($1.8 \pm 0.6 \text{ \%yr}^{-1}$), the Indo-Gangetic plain ($1.9 \pm 0.6 \text{ \%yr}^{-1}$), East Asia ($0.7 \pm 0.3 \text{ \%yr}^{-1}$), subtropical North Eastern Pacific ($1.0 \pm 0.4 \text{ \%yr}^{-1}$), Southern China ($1.8 \pm 0.6 \text{ \%yr}^{-1}$), Amazonia ($0.9 \pm 0.3 \text{ \%yr}^{-1}$), Northern Australia ($1.1 \pm 0.4 \text{ \%yr}^{-1}$), Brazil ($0.8 \pm 0.3 \text{ \%yr}^{-1}$) and Southern South America ($1.0 \pm 0.2 \text{ \%yr}^{-1}$).

6. VALIDATION OF SCIAMACHY TROPOSPHERIC OZONE COLUMNS

Station	Latitude range (°N)		Longitude range (°E)		Trend (% yr ⁻¹)	Mean value & stdev.(DU)
Arctic	60.00	90.00	-180.00	180.00	-0.3±0.7	36.0±9.5
Northern Asia	50.00	70.00	40.00	180.00	0.3±0.4	36.4±7.2
Poland	50.00	54.00	15.00	24.00	0.5±1.2	37.3±9.9
Northern Europe	48.00	75.00	-10.00	40.00	-0.4±0.4	37.9±6.8
Atlantic	45.00	55.00	-60.00	-10.00	-0.1±0.3	36.6±4.3
Eastern Europe	40.00	60.00	20.00	50.00	-0.7±0.4	42.5±5.9
North Eastern USA	40.00	50.00	-90.00	-60.00	-0.4±0.5	39.4±7.3
Northern Japan	40.00	50.00	115.00	170.00	0.3 ±0.4	38.9±7.6
Western Europe	40.00	60.00	-15.00	15.00	-0.7±0.3	40.4±4.7
Europe	35.00	75.00	-10.00	40.00	-0.3±0.3	40.9±4.2
Japan	31.00	45.00	129.00	144.00	0.4 ±0.3	40.6±8.6
Central Asia	30.00	50.00	40.00	75.00	0.8 ±0.5	36.7±4.1
Central Eastern China	30.00	40.00	110.00	130.00	0.9 ±0.4	38.0±8.4
Central North America	30.00	50.00	-103.00	-85.00	0.1 ±0.4	35.9±4.4
Mediterranean Basin	30.00	45.00	-5.00	35.00	-0.4±0.4	38.0±3.5
Midlatitude N. E. Pacific	30.00	50.00	-160.00	-125.00	-0.1±0.3	43.1±5.0
South Europe & Mediterranean	30.00	48.00	-10.00	40.00	-0.2±0.4	38.9±3.5
Southern Japan	30.00	40.00	115.00	170.00	0.4 ±0.4	41.7±7.4
Tibetan Plateau	30.00	75.00	50.00	100.00	0.9 ±0.5	35.0±4.8
Western North America	30.00	75.00	-125.00	-105.00	0.5 ±0.5	34.4±4.4
Western USA	30.00	50.00	-125.00	-105.00	0.2 ±0.5	33.5±4.4
Eastern North America	25.00	50.00	-85.00	-50.00	-0.1±0.3	41.3±4.2
Northern India	25.00	30.00	76.00	80.00	1.8 ±0.6	37.0±6.8
Indo-Gangetic plain	21.00	31.00	74.00	92.00	1.9 ±0.6	34.4±5.4
East Asia	20.00	50.00	100.00	145.00	0.7 ±0.3	37.5±4.9
Sahara	18.00	30.00	20.00	65.00	0.1 ±0.4	34.4±2.8
Caribbean	10.00	25.00	-85.00	-60.00	0.6 ±0.4	32.8±3.3
Central America	10.00	30.00	-116.00	-83.00	0.2 ±0.4	32.3±3.0
Subtropical N. E. Pacific	10.00	30.00	-180.00	-125.00	1.0 ±0.4	35.5±3.9
South Asia	5.00	50.00	64.00	100.00	0.5 ±0.5	33.3±3.5
South China	5.00	25.00	90.00	130.00	1.8 ±0.6	32.3±4.5
Southern India	5.00	20.00	60.00	90.00	0.6 ±0.4	32.7±3.3
North Pacific Ocean	0.00	40.00	-120.00	150.00	0.4 ±0.4	33.8±2.3
Northern Hemisphere	0.00	90.00	-180.00	180.00	0.5 ±0.4	35.5±2.7
Tropical Northeast Atlantic	0.00	40.00	-30.00	-10.00	0.5 ±0.3	37.6±2.6
South eastern Asia	-11.00	20.00	95.00	115.00	0.1 ±0.6	27.5±4.2
East Africa	-12.00	18.00	22.00	52.00	0.8 ±0.5	29.4±3.0
West Africa	-12.00	22.00	-20.00	18.00	0.5 ±0.3	34.1±2.9
Amazonia	-20.00	12.00	-82.00	-34.00	0.9 ±0.3	27.5±4.0
Northern Australia	-30.00	-11.00	110.00	155.00	1.1 ±0.4	27.5±4.3
Brazil	-33.73	5.27	-73.75	-28.85	0.8 ±0.3	28.9±4.3
Indian Ocean	-35.00	17.50	50.00	100.00	0.4 ±0.4	31.4±3.3
South Africa	-35.00	-12.00	10.00	52.00	0.2 ±0.4	32.6±5.0
Southern Australia	-45.00	-30.00	110.00	155.00	0.3 ±0.2	31.6±6.1
Southern Pacific Ocean	-55.00	0.00	-80.00	150.00	0.6 ±0.3	31.2±4.6
Southern South America	-56.00	-20.00	-76.00	-40.00	1.0 ±0.2	27.5±4.3
Antarctic	-90.00	-60.00	-180.00	180.00	1.2 ±1.1	20.0±4.3
Southern Hemisphere	-90.00	0.00	-180.00	180.00	0.3 ±0.2	29.5±4.3

Table 6.5: Trends in SCIAMACHY tropospheric O₃ in %yr⁻¹ over some regions and countries of the world. Bold text indicates statistically significant changes in TOC.

The observed significant increase in TOC over these regions can be attributed mainly to increase in precursor emissions, which are of anthropogenic origin (Lal *et al.*, 2012; Parrish *et al.*, 2012). Transport of O₃ and its precursors as well as the prevailing weather patterns have also been identified to influence TOC changes over these regions (e.g., Parrish *et al.*, 2012; Stevenson *et al.*, 2013).

6.3 Seasonal cycles and trends analysis of SCIAMACHY tropospheric ozone columns

Table 6.5 also shows some regions where insignificant TOC trends are observed. The insignificant TOC trends can be attributed to changes in different factors including both anthropogenic and natural phenomena.

6.3.2.6 Changes in SCIAMACHY global tropospheric O₃ columns

Figures 6.50 and 6.51 show changes in SCIAMACHY TOC derived from 2003 - 2011 for 5° latitude × 5° longitude bins in %/yr and DU/yr relative to the mean of the first month, respectively. The contour colors range from blue to red, representing decreasing to increasing TOCs from 2003 - 2011. The white coloured area represents places with no TOC data due to the applied data screening criteria (Ebojie *et al.*, 2014). The errors are estimated at 1-sigma and are shown in Figures 6.52a and 6.52b in units of %/yr and DU/yr, respectively. The regions marked with cross signs represent changes in tropospheric O₃ at the 95 % confidence level. In Figures 6.50 and 6.51, changes in TOC are observed along the outflow from continents to oceanic regions, particularly in the SH. Statistically significant changes in tropospheric O₃ are observed over the regions of North America, Europe, East and south East Asia, South America, part of Africa, part of Australia and over the Middle East, particularly around Saudi Arabia. TOC trends are also significant over the marine region including the Pacific Ocean, Indian Ocean and the Atlantic Ocean. Significant negative TOC trends (-1 to -2 %/yr) are observed over some parts of North America and Europe, which can be attributed to decrease in anthropogenic NO_x and VOCs emissions as well as reduction in other tropospheric O₃ precursors (e.g., Cooper *et al.*, 2012; Hogrefe *et al.*, 2011; Logan *et al.*, 2012; Novelli *et al.*, 1998; Parrish *et al.*, 2012; Vestreng *et al.*, 2009).

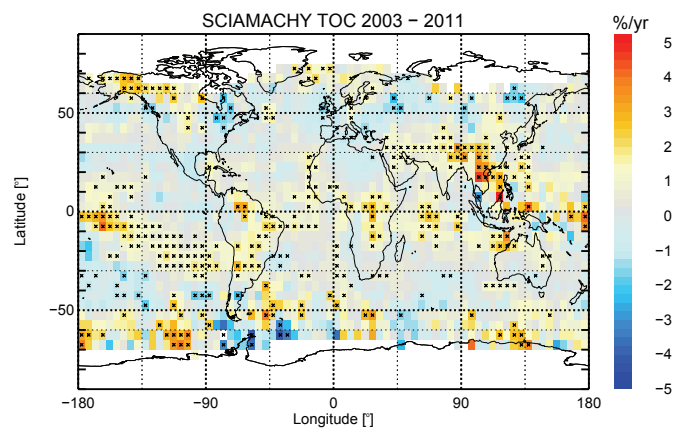


Figure 6.50: Changes in SCIAMACHY tropospheric O₃ columns (%/yr) derived from 2003 - 2011 for 5° latitude × 5° longitude resolution. The regions with cross signs describe statistically significant change and the white colored areas represent places with no trend data.

Similar significant negative TOC trends (-1 to -3 %/yr) are also observed over the southern marine

6. VALIDATION OF SCIAMACHY TROPOSPHERIC OZONE COLUMNS

regions of the Atlantic Ocean, the Pacific Ocean and the Indian Ocean. The observed negative TOC trends over these regions can be associated with increased photochemical sink and dilution processes due to meteorological changes (e.g., Edwards *et al.*, 2006; Jacob & Winner, 2009; Kley *et al.*, 1997; Wai *et al.*, 2014). The significant positive trends observed over South America (up to 2 %/yr), south Asia (1 - 4 %/yr), part of Africa and over the marine regions (up to 2 %/yr), can be attributed to increasing anthropogenic precursor emissions and changes in meteorology or natural emissions (e.g., Beig & Singh, 2007; Lelieveld *et al.*, 2004; Stevenson *et al.*, 2013; Thompson *et al.*, 1996). Studies have shown that intercontinental transport plays a role in ozone trends (Parrish *et al.*, 2012; Zhang *et al.*, 2009). Significant positive TOC trends (1 - 3 %/yr) are observed over the Pacific Ocean. In previous studies, Ziemke *et al.* (2005) derived significant positive trends (5 - 9 %/decade) in the mid-latitude Pacific of both hemispheres during 1979 - 2003. The observed trends over the Pacific Ocean can be attributed to tropospheric O₃ and its precursors transported by the prevailing westerly winds from biomass burning regions in southern Africa and South America (e.g., Sauvage *et al.*, 2006, 2007; Wai *et al.*, 2014). The trans-Pacific transport of Asian pollution also contributes to the enhancement of O₃ over the Pacific Ocean. The prevalence of storm and frontal activity in Asia as well as strong westerly transport of Asian pollution across the North Pacific have been observed to alter the composition of the remote Pacific Ocean (Berntsen *et al.*, 1999; Hoell *et al.*, 1996; Levy & Moxim, 1989). The significant change in O₃ observed over the coast of West Africa, Southern Atlantic and over the regions of South America can be attributed to transport and increase of anthropogenic emissions of NO_x and other O₃ precursors, which have added to emissions from biomass burning and natural sources (e.g., Lelieveld *et al.*, 2004; Moxim & Levy II, 2000; Schultz *et al.*, 1999; Thompson *et al.*, 1996; Wai *et al.*, 2014). Plumes of O₃ and its precursors from savanna burning in northern/western Africa are transported westward/southwestward toward South America and over the Atlantic Ocean by the Harmattan and African Easterly Jet flows. These contribute to changes in TOC trends over these regions (Sauvage *et al.*, 2005, 2006). In southern Africa, the widespread combustion events in Angola, Zambia and the Democratic Republic of Congo, particularly during July - September lead to the formation of O₃ precursors. The transport of O₃ and its precursors by the prevailing wind systems over these regions lead to significant change in TOC (Sauvage *et al.*, 2005, 2007). For instance, the persistent low-level easterlies/southeasterlies in these regions facilitate the westward transport of tropospheric O₃ and its precursors. The prevailing descending airmasses and relatively low wind speeds over southern Africa, South America, Atlantic Ocean and Indian Ocean limit the dispersion of tropospheric O₃ and its precursors produced from burning plumes in Africa and South America. The prevailing high-pressure system over southern Africa leads to the recirculation of plumes of tropospheric O₃ and its precursors over the continent before exiting from the southern or western part of the

6.3 Seasonal cycles and trends analysis of SCIAMACHY tropospheric ozone columns

continent to the Indian Ocean or the Atlantic Ocean south of the ITCZ, respectively (e.g., Edwards *et al.*, 2006; Wai *et al.*, 2014).

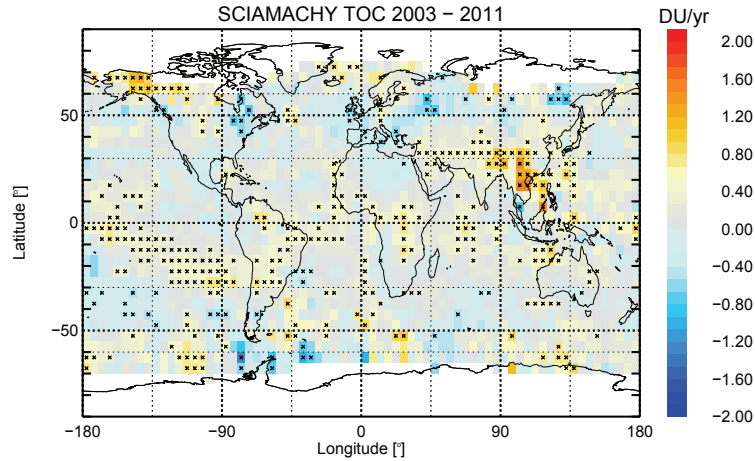


Figure 6.51: Changes in SCIAMACHY tropospheric O₃ columns (DU/yr) derived from 2003 - 2011 for 5° latitude × 5° longitude resolution. The regions marked with crosses describe statistically significant trends and the white colored areas represent places with no trend data.

Biomass burning activities in South America, which peak from August - October, lead to the formation of tropospheric O₃ and its precursors over the region. O₃ and its precursors can remain in the planetary boundary layer before they are transported to the upper troposphere via deep convective processes (e.g., Sauvage *et al.*, 2006; Wu *et al.*, 2011). In the free troposphere, the O₃ plumes can be effectively transported by westerlies through the continental outflows located at the southeast of South America. From the south eastern and north western parts of South America, tropospheric O₃ plumes are transported across the Atlantic and Pacific Oceans toward South Africa, respectively. Tropospheric O₃ and its precursors are transported across the Indian Ocean towards Australia and over the Pacific Ocean, thus leading to the significant positive trend in the TOC over the marine region of the Pacific Ocean (e.g., Edwards *et al.*, 2006; Wai *et al.*, 2014). The significant increase in O₃ (up to 1 %/yr) observed over the South Australia outflow region can be associated with the recurrent southern winter and spring O₃ maximum over the region due to the deep trough residing over the southeastern Indian Ocean, mostly during austral winter and spring, which leads to the trapping of O₃ over the region (Rogal *et al.*, 2010). The observed significant increase in tropospheric O₃ over the Indian Ocean extending towards Australia (up to 2 %/yr), can also be associated with advective transport. This can be explained by the dynamical coupling between the NH's Tibetan High and SH synoptic wave regime (Tibetan High-Australian High coupling) (Rodwell & Hoskins, 1996), which is consistent with the dynamical structure forced by transient off-equatorial heating associated with monsoon convection (Rogal *et al.*, 2010). Statistically significant

6. VALIDATION OF SCIAMACHY TROPOSPHERIC OZONE COLUMNS

increase in TOC observed over the Bay of Bengal (1 - 2 %/yr), can also be attributed to horizontal advection of O₃ and its precursor-rich airmasses. The prevailing large scale wind systems over this region, cause massive transport of continental pollutants to the region (Beig & Singh, 2007). The significant increase in TOC over south Asia (1 - 4 %/yr) is associated mainly with anthropogenically produced O₃ precursors from both domestic and industrial combustion as well as biomass burning (Liu *et al.*, 2002; Logan *et al.*, 2012; Parrish *et al.*, 2012). The O₃ produced over these region is transported towards the western Pacific Ocean by large-scale dynamics controlled by the prevailing wind systems, thus leading to the significant positive trend in O₃ over the western Pacific Ocean.

Figures 6.52a and 6.52b show the contour plots of the %/yr and DU/yr trend uncertainties for 5° latitude × 5° longitude resolution, respectively. The uncertainties are determined from the covariance matrix of the regression. The uncertainty in SCIAMACHY TOC has been discussed in detail by Ebojje *et al.* (2014). Additionally, the uncertainty in tropospheric O₃ trends can arise from scanning mirror degradation and tropopause height information, but the impact of their effects on SCIAMACHY TOC is small (Bramstedt *et al.*, 2009; Ebojje *et al.*, 2014). Inspection of Figures 6.52a and 6.52b shows that the uncertainty in O₃ trend is mostly less than 2 %/yr and 0.5 DU/yr, respectively, on a global basis.

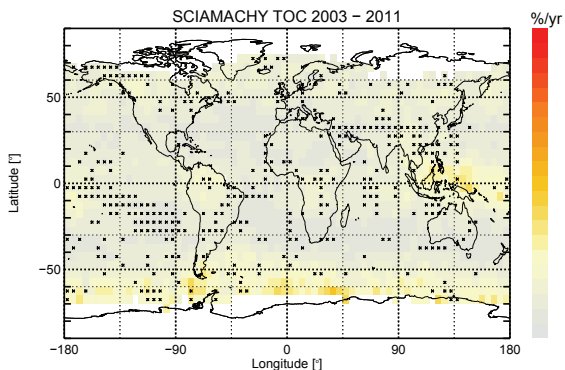


Figure 6.52(a): Same as 6.50 but for the uncertainty in percent per year.

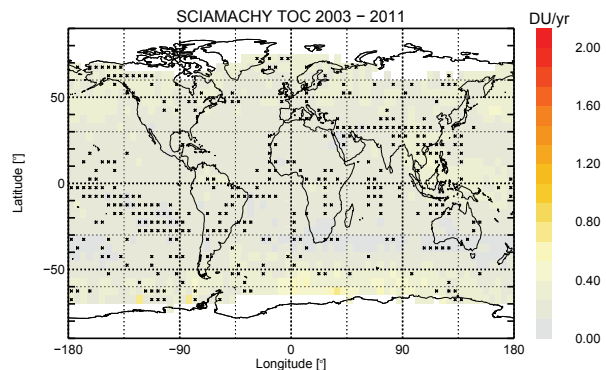


Figure 6.52(b): Same as 6.51 but for the absolute uncertainty per year.

Chapter 7

Summary and conclusion

In this work, an algorithm for retrieving tropospheric O₃ columns (TOCs) from the combined limb and nadir observations (limb-nadir-matching (LNM)) of the SCIAMACHY instrument was presented. The study also included the development of algorithm to derive the tropopause heights from the European Center for Medium Range Weather Forecasts (ECMWF) reanalyses (ERA)-Interim data as well as from the in-situ temperature profile measurements from ozonesonde. A detailed error analysis of the SCIAMACHY TOC data products as well as comparisons of SCIAMACHY TOC with the TOCs from both in-situ and satellite instruments were presented. This work also covered the study of SCIAMACHY TOCs global morphology as well as trend analysis. It examined pollution over countries, regions, cities, megacities and continents, and discussed seasonal variations in tropospheric O₃. The retrieval algorithm is a residual approach, which is similar in concept to that developed in the late 1980s (Fishman & Larsen, 1987), where the TOCs were obtained by subtracting the stratospheric O₃ columns (SOCs) retrieved from SAGE (Stratospheric Aerosol and Gas Experiment) measurements from the total O₃ columns (TOZs) derived from TOMS (Total Ozone Mapping Spectrometer) observations. One unique aspect of the retrieval of TOCs using the SCIAMACHY LNM technique is that total column (nadir) and stratospheric profile (limb) data from the same instrument are used. This reduces some of the uncertainties due to instrumental issues and SCIAMACHY provided a dense sampling of tropospheric O₃ on a global scale. The SCIAMACHY LNM technique subtracts SOCs, retrieved from the limb observations, from the TOZs derived from the nadir observations. The technique requires accurate knowledge of the SOCs, TOZs, tropopause height, and their associated errors.

The SCIAMACHY limb measurements yielded to a first approximation, the stratospheric vertical profiles of trace gases above the region of the nadir mode measurements of total columns. The stratospheric O₃ profiles were retrieved in the Hartley and Chappius bands while the TOZs were derived using the Weighting Function Differential Optical Absorption Spectroscopy (WFDOAS)

7. SUMMARY AND CONCLUSION

technique in the Huggins band. To determine the SOC, the tropopause heights were determined from the ECMWF reanalyses (ERA)-Interim data, using the dynamical (potential vorticity) and the thermal (lapse rate) definitions of the tropopause. Integrating the coincident stratospheric profiles from the tropopause upwards provided the SOCs above the target area. The subtraction of the SOCs from the TOZs yielded the TOCs. The spatial resolution of the SCIAMACHY TOCs determined from the collocated limb and nadir resolution is about 60 km (along track) x 240 km (across track). Comparisons of the tropopause heights computed from ozonesonde temperature profile measurements and the ECMWF dataset showed good agreement with a mean difference of less than 500 m in both hemispheres for the stations considered in this study (see Figure 6.13).

Sensitivity studies were performed to explore the impact of uncertainties in the knowledge of several atmospheric, surface, and geometrical parameters on the retrieved SOCs, TOZs and TOCs. The error contribution from the SOCs, which originated from the retrieval of stratospheric O₃ profiles was computed from errors resulting from uncertainties in the assumed surface albedo, aerosol extinction profile, O₃ absorption cross section, pressure profile, tangent height information and temperature profile. Analysis of the uncertainty parameters in zonal bands, 20°S - 20°N, 60°S - 30°S and 30°N - 60°N, showed that the uncertainty from each of the parameters in a zonal band are nearly constant throughout the year. While the uncertainty contributions from some of the parameters between the zonal bands, 60°S - 30°S and 30°N - 60°N vary, others showed similar values. The sensitivity studies on the SOC showed the contributions from the different parameter uncertainties. The temperature uncertainty (-0.8 DU (-0.3 %)), the uncertainty due to errors in O₃ absorption cross sections (0.2 DU (0.1 %)), the albedo uncertainty (~-1.4 DU (-0.5 %)), and pressure uncertainty (~1.9 DU (0.7 %)) exhibited similar values in both 60°S - 30°S and 30°N - 60°N zonal bands. The uncertainty contribution from tangent height registration showed higher values in the SH than in the NH (2.8 DU (1 %)) versus (1.45 DU (0.5 %)). Conversely, the aerosol uncertainty exhibited higher values in the NH than in the SH (1.4 DU (0.5 %)) versus (-0.9 DU (-0.3 %)). The aerosol uncertainty depends on the scattering phase function and hence on the scattering angle. The largest contribution to the error in TOZ was identified to come from the a-priori errors associated with the O₃ climatology and from the uncertainty in the derived effective scene albedo. For SZA less than 75° and with the inclusion of both ozone and temperature weighting function in the fit, a total error of less than 2 % was estimated. The effective albedo errors contributed to about 1.5 % in the error of the retrieved O₃ column and an assumed effective height of 1 km resulted to an error of 1 % error in the TOC. The interpolation errors from a look-up-table comprising the effective parameters and for SZA less than 80 % was below 0.3 % but may reach 1.5 % for SZA greater than 80°. The error from the ghost vertical column was found to be less than 0.2 %. In summary, the precision of the TOC retrieval was estimated to be about 1 % for

SZA less than 80° and better than 3 % up to SZA of 88° . Investigation on the nadir cloud fraction thresholds showed that an increase by 10 % can on average reduce SCIAMACHY tropospheric O_3 by about 1 DU. This occurred mostly where pollution increased tropospheric O_3 to values above the climatological O_3 . A sensitivity analysis on the zonally averaged monthly means and errors in TOC, SOC, TOZ and the effect of tropopause height (TPH) from $20^\circ S - 20^\circ N$, $60^\circ S - 30^\circ S$ and $30^\circ N - 60^\circ N$, showed that the mean value of the SOC in the tropics was lower than those from the northern and southern hemispheres but it exhibited a higher mean error in comparison to those from the northern and southern zonal bands. The mean SOCs and their error for the southern and northern zonal bands were similar, i.e., approximately 276.9 DU and 4.3 DU (1.6 %), respectively. The similarity in the error values from both zonal bands may be associated with the difference in the uncertainty contribution from aerosol and tangent height registration, which showed a maxima in the NH and SH, respectively. For the TOZ, the mean value and error were lower in the tropics than at the northern and southern hemispheres. The mean TOZ value in the NH was higher than in the SH but the TOZ error in both zonal bands were similar i.e., 3.0 DU (1 %). The rather small errors in TOZs and SOCs still resulted in fairly large errors in the retrieved TOCs. The mean TOC is higher in the NH but has a lower mean absolute error compared to the other zonal bands. The highest mean TOC error (5.6 DU (20.1 %)) was located in the SH. Comparisons of the resulting TOC data set with the TOCs determined from ozonesondes showed a good agreement to within 3 DU. Time series plots of TOCs retrieved from SCIAMACHY and other satellite instruments showed good agreement in capturing the seasonal variations between all instruments. However, some disagreements on the amplitude of the seasonal variations were identified. Global maps of TOC showed the expected seasonal and spatial patterns. The spatial distributions of tropospheric O_3 in the SCIAMACHY LNM TOC product showed characteristic variations related to stratosphere-troposphere exchange (STE) processes, anthropogenic activities and biospheric emissions. Comparisons with TOCs retrieved from TES and OMI/MLS showed similar global morphology and seasonal variations in many regions but differed in others. The zonal time series showed a persistent zonal wave-one pattern in tropospheric O_3 over the southern tropics. Latitudinal and seasonal variations were observed from the time series over megacities, countries and regions. The tropospheric O_3 over different cities in the NH showed consistent seasonal behaviour over the entire time period. Main features with peak O_3 during spring, which can be associated with either O_3 build up during winter, which get photolyzed during spring or influx of O_3 rich stratospheric air masses were observed. Another peak was observed during summer, which can be associated with photochemical production of O_3 from its precursors. Trend analysis of SCIAMACHY global TOC using multivariate regression model showed positive trends significant at the 95 % level over South Asia (1 - 4 %/yr), the South American continent (up to 2

7. SUMMARY AND CONCLUSION

%/yr), North America, especially around Alaska (1 - 3 %/yr), the Australian outflow region (1 - 2 %/yr) as well as over the central African and west African coast (up to 2 %/yr). Over the marine regions, significant positive TOC trends were derived over the South East Pacific region (up to 3 %/yr), the Indian Ocean (1 - 2 %/yr) and the Atlantic Ocean (up to 2 %/yr). Significant negative TOC trends were observed over some regions of Europe and the North American continent (2 - 4 %/yr), which were attributed to reduction in NO_x and other tropospheric O_3 precursors over the regions. Over the Oceanic regions including the Pacific, Atlantic and Indian Oceans, significant decrease in TOC (1 - 5 %/yr) are observed. The observed increase in TOC at the higher latitudes is not large which may be related to the slowing down of the Brewer Dobson circulation as reported from observation study by Weber *et al.* (e.g., 2011). In summary, these results allow the conclusion that the reported TOC data set retrieved by using SCIAMACHY limb-nadir matching observations provides a valuable data record from 2003 to 2012. These data can be used to gain understanding of the spatial and temporal variability of tropospheric O_3 as well as in model comparisons.

7.1 Outlook

The work presented in this PhD thesis showed that accurate knowledge of the stratospheric O_3 columns (SOCs), total O_3 columns (TOZs), tropopause height, and their associated errors are pivotal for the retrieval of SCIAMACHY tropospheric O_3 columns (TOCs). The usage of radiance profiles in UV and triplet in the visible to retrieve stratospheric ozone profiles provided reasonable SOCs in the tropics and mid-latitudes but could not properly account for SOCs at the higher latitudes. The implementation of the DOAS, 0-th order polynomial in UV and 3-rd order polynomial in visible may help account for this problem. The computation of the tropopause heights sometimes fails at the high latitudes and close to the jet streams as a result of the folding of the tropopause. The precise determination of the value of the potential vorticity to separate the tropospheric wind from the stratospheric wind will help in improving the quality of the SOCs. Precise determination of the nadir cloud fraction will improve the derived TOZs. The choice of the right cloud fraction depends on the events to be studied. Increasing or decreasing the cloud fraction threshold can alter tropospheric O_3 column amounts, mostly in cases where pollution increases tropospheric O_3 to values above the climatological O_3 . Discussion on the role of seasonal, interannual, and decadal climate variability on SCIAMACHY TOCs amount and trends, started in section 6.3 of Chapter 6 should be continued. Detailed analysis of tropospheric O_3 seasonality and changes will aid the understanding of its distribution and proffer solutions to the air quality problem. Evaluation of regional and global chemical transport models with SCIAMACHY tropospheric O_3 should be carried out to understand the formation, distribution, accumulation, transport, destruction and deposition

of O₃. Further analysis of SCIAMACHY tropospheric O₃ with its precursors will not only provide insight into pollution hotspots but also enhance policy development and emission management strategies that would aid both air quality and climate.

7. SUMMARY AND CONCLUSION

Appendix

Station name	No of points	Lat.	Lon.	Mean value and stdev. of trop. O ₃ from sondes (DU)	Mean value and stdev. of trop. O ₃ from SCIA-MACHY (DU)	Mean value and stdev. of trop. O ₃ from TES (DU)	Mean value and stdev. of trop. O ₃ from OMI/MLS (DU)	Mean value of trop. O ₃ rel. diff. (SCIA-MACHY)	Mean value of trop. O ₃ rel. diff. (TES)	Mean value of trop. O ₃ rel. diff. (OMI/MLS)
1. Sodankyla	21	67.39	26.65	42.2±5.3	33.1±5.1	37.5±2.9	29.9±3.6	0.28	0.13	-0.10
2. Lerwick	62	60.13	358.82	40.4±4.9	33.5±4.8	38.1±2.5	30.3±3.9	0.21	0.14	-0.10
3. Churchill	59	58.75	265.93	36.8±6.4	31.2±4.5	35.3±2.4	29.4±3.5	0.18	0.13	-0.06
4. Edmonton	79	53.55	245.90	36.3±5.2	28.9±4.0	36.3±3.1	26.9±2.7	0.26	0.25	-0.07
5. Goosebay	78	53.32	299.70	36.2±5.9	32.5±5.0	39.8±4.2	31.6±3.4	0.11	0.23	-0.03
6. Legionowo	75	52.40	20.97	41.3±4.3	36.5±7.0	41.4±5.3	29.7±4.0	0.13	0.13	-0.19
7. DeBilt	82	52.10	5.18	41.0±4.5	35.5±5.5	40.7±4.2	29.9±3.8	0.16	0.15	-0.16
8. Valentia	49	51.93	349.75	38.6±3.9	37.3±5.0	40.9±3.5	31.3±3.9	0.03	0.10	-0.16
9. Uccle	78	50.80	4.35	40.9±4.6	35.8±6.2	41.0±4.3	30.1±3.8	0.14	0.14	-0.16
10. Bratt's Lake	78	50.20	255.30	35.0±4.5	32.7±5.2	37.2±3.8	27.3±2.6	0.07	0.14	-0.17
11. Praha	26	50.02	14.45	41.3±6.0	34.4±4.8	38.6±3.3	28.4±2.8	0.20	0.12	-0.17
12. Kelowna	77	49.93	240.60	35.8±4.3	32.9±5.2	36.7±2.9	27.6±2.9	0.09	0.11	-0.16
13. Payerne	82	46.49	6.57	40.6±4.3	33.6±6.2	42.0±5.2	30.5±4.8	0.21	0.25	-0.09
14. Egbert	74	44.23	280.22	37.5±4.6	37.4±7.2	42.5±5.1	31.0±4.5	0.00	0.14	-0.17
15. Yarmouth	63	43.87	293.89	39.7±5.0	38.9±7.8	43.1±5.1	32.0±4.7	0.02	0.11	-0.18
16. Sapporo	82	43.10	141.30	40.3±6.4	35.3±8.7	42.9±4.6	34.3±5.1	0.14	0.22	-0.03
17. Madrid	81	40.45	356.28	38.5±3.7	34.8±6.4	42.3±4.7	31.9±5.6	0.11	0.22	-0.08
18. Ankara	78	39.95	32.88	37.8±3.8	35.6±9.9	44.9±7.4	32.6±7.1	0.06	0.26	-0.08
19. Wallops	80	37.93	284.52	40.2±4.2	41.5±8.0	44.7±4.9	32.3±5.8	-0.03	0.08	-0.22
20. Tsukuba	82	36.10	140.10	41.8±5.2	41.5±9.3	43.5±3.4	33.7±5.2	0.01	0.05	-0.19
21. Huntsville	38	35.28	273.41	40.5±3.7	39.5±8.8	43.5±4.7	31.7±5.9	0.02	0.10	-0.20
22. Isfahan	50	32.51	51.70	35.6±3.5	37.3±9.1	42.1±5.1	32.2±5.9	-0.05	0.13	-0.14
23. Kagoshima	6	31.60	130.60	36.1±1.9	36.9±4.5	41.0±2.6	29.9±2.6	-0.02	0.11	-0.19
24. Naha	82	26.20	127.70	37.9±4.2	38.9±7.8	40.1±4.0	32.0±4.2	-0.03	0.03	-0.18
25. HongKong	81	22.31	114.17	35.4±4.2	38.9±6.3	38.0±3.8	30.4±3.8	-0.09	-0.02	-0.22
26. Hilo	68	19.72	204.93	33.7±3.8	33.6±6.4	34.4±4.0	28.5±3.9	0.00	0.02	-0.15
27. Alajuela	20	9.98	275.79	28.4±3.6	26.2±3.3	29.6±1.5	25.5±2.0	0.08	0.13	-0.03
28. Paramaribo	69	5.81	304.79	28.2±3.1	27.1±6.7	31.3±3.0	26.3±2.6	0.04	0.16	-0.03
29. Sepang	62	2.73	101.70	26.1±3.3	24.9±3.9	25.5±2.4	21.6±3.0	0.05	0.02	-0.13
30. San Cristobal	27	-0.92	270.40	28.0±4.8	26.0±5.9	29.5±3.7	24.9±3.4	0.08	0.13	-0.04
31. Nairobi	52	-1.27	36.80	26.7±2.7	27.7±3.6	33.8±2.6	27.8±2.8	-0.04	0.22	0.00
32. Malindi	12	-2.99	40.19	29.3±2.8	36.1±5.0	34.0±3.0	28.4±3.7	-0.19	-0.06	-0.21
33. Natal	61	-5.42	324.62	30.9±5.8	34.3±8.6	36.5±6.2	30.6±5.1	-0.10	0.06	-0.11
34. Watukosek	52	-7.57	112.65	25.0±3.5	23.4±6.8	25.1±3.5	21.7±3.7	0.07	0.07	-0.07
35. Ascension	37	-7.58	345.76	32.1±8.1	39.6±7.9	40.2±5.1	34.0±4.5	-0.19	0.01	-0.14
36. Samoa	58	-14.23	189.44	25.2±4.5	21.4±5.4	24.8±4.2	20.3±3.7	0.18	0.16	-0.05
37. Suva	9	-18.10	178.20	30.8±4.6	21.7±4.0	28.6±5.6	22.6±3.6	0.42	0.32	0.04
38. La Reunion	61	-21.06	55.48	35.1±5.5	41.1±9.1	39.1±6.4	33.3±5.5	-0.15	-0.05	-0.19
39. Irene	29	-25.91	28.21	32.4±5.6	38.0±7.3	38.1±5.5	32.0±4.8	-0.15	0.00	-0.16
40. Broadmeadows	82	-37.68	144.95	31.1±5.9	28.7±4.9	33.8±5.0	27.8±3.0	0.08	0.18	-0.03
41. Lauder	50	-45.04	169.68	28.9±5.3	23.1±3.2	26.6±2.1	24.4±2.4	0.25	0.15	0.06
42. Macquarie	62	-54.50	158.97	25.0±4.2	22.7±3.4	23.2±3.5	24.6±3.2	0.10	0.02	0.09
43. Ushuaia	21	-54.85	291.69	27.8±2.8	21.0±3.6	24.4±3.0	24.7±3.0	0.32	0.16	0.17
44. Marambio	45	-64.23	303.38	21.3±2.3	19.1±4.0	21.5±6.2	22.7±3.4	0.12	0.13	0.19
Mean value of tropospheric ozone				34.4±4.8	32.5±6.0	36.2±4.1	28.8±3.93	0.07	0.12	-0.10

Table 7.1: Same as table 6.1 but for 0 % cloud fraction threshold.

APPENDIX

Station name	No of points	Lat.	Lon.	Mean value and stdev. of trop. O ₃ from sondes (DU)	Mean value and stdev. of trop. O ₃ from SCIA-MACHY (DU)	Mean value and stdev. of trop. O ₃ from TES (DU)	Mean value and stdev. of trop. O ₃ from OMI/MLS (DU)	Mean value of trop. O ₃ rel. diff. (SCIA-MACHY)	Mean value of trop. O ₃ rel. diff. (TES)	Mean value of trop. O ₃ rel. diff. (OMI/MLS)
1. Sodankyla	21	67.39	26.65	41.4±6.5	33.0±5.0	37.4±2.9	29.8±3.5	0.26	0.13	-0.10
2. Lerwick	62	60.13	358.82	39.4±4.9	33.5±4.8	38.1±2.5	30.3±3.9	0.18	0.14	-0.10
3. Churchill	59	58.75	265.93	35.9±6.8	31.1±4.6	35.2±2.4	29.4±3.6	0.15	0.13	-0.06
4. Edmonton	79	53.55	245.90	36.1±5.2	28.9±4.0	36.3±3.1	26.9±2.7	0.25	0.25	-0.07
5. Goosebay	78	53.32	299.70	35.9±5.5	32.5±5.0	39.8±4.2	31.6±3.4	0.11	0.23	-0.03
6. Legionowo	75	52.40	20.97	41.0±3.9	36.5±7.0	41.4±5.3	29.7±4.0	0.12	0.13	-0.19
7. DeBilt	82	52.10	5.18	40.6±4.2	35.5±5.5	40.7±4.2	29.9±3.8	0.15	0.15	-0.16
8. Valentia	49	51.93	349.75	38.2±3.3	37.3±5.0	40.9±3.5	31.3±3.9	0.02	0.1	-0.16
9. Uccle	78	50.80	4.35	40.5±4.2	35.8±6.2	41.0±4.3	30.1±3.8	0.13	0.14	-0.16
10. Bratt's Lake	78	50.20	255.30	34.2±4.0	32.7±5.2	37.2±3.8	27.3±2.6	0.05	0.14	-0.17
11. Praha	26	50.02	14.45	40.8±5.5	34.4±4.8	38.6±3.3	28.4±2.8	0.19	0.12	-0.17
12. Kelowna	77	49.93	240.60	35.2±4.0	32.9±5.2	36.7±2.9	27.6±2.9	0.07	0.11	-0.16
13. Payerne	82	46.49	6.57	40.4±4.0	33.6±6.2	42.0±5.2	30.5±4.8	0.20	0.25	-0.09
14. Egbert	74	44.23	280.22	37.3±4.6	37.4±7.2	42.5±5.1	31.0±4.5	0.00	0.14	-0.17
15. Yarmouth	63	43.87	293.89	39.3±5.3	38.9±7.8	43.1±5.1	32.0±4.7	0.01	0.11	-0.18
16. Sapporo	82	43.10	141.30	40.0±6.5	35.3±8.7	42.9±4.6	34.3±5.1	0.13	0.22	-0.03
17. Madrid	81	40.45	356.28	38.1±3.6	34.8±6.4	42.3±4.7	31.9±5.6	0.10	0.22	-0.08
18. Ankara	78	39.95	32.88	37.3±3.3	35.6±9.9	44.9±7.4	32.6±7.1	0.05	0.26	-0.08
19. Wallops	80	37.93	284.52	4 40.1±4.4	41.5±8.0	44.7±4.9	32.3±5.8	-0.04	0.08	-0.22
20. Tsukuba	82	36.10	140.10	41.3±5.4	41.5±9.3	43.5±3.4	33.7±5.2	0.00	0.05	-0.19
21. Huntsville	38	35.28	273.41	40.4±4.0	39.5±8.8	43.5±4.7	31.7±5.9	0.02	0.10	-0.20
22. Isfahan	50	32.51	51.70	35.1±3.3	37.3±9.1	42.1±5.1	32.2±5.9	-0.06	0.13	-0.14
23. Kagoshima	6	31.60	130.60	36.4±3.1	36.9±4.5	41.0±2.6	29.9±2.6	-0.01	0.11	-0.19
24. Naha	82	26.20	127.70	37.5±4.2	38.9±7.8	40.1±4.0	32.0±4.2	-0.04	0.03	-0.18
25. HongKong	81	22.31	114.17	35.2±4.3	38.9±6.3	38.0±3.8	30.4±3.8	-0.10	-0.02	-0.22
26. Hilo	68	19.72	204.93	33.1±3.9	33.6±6.4	34.4±4.0	28.5±3.9	-0.01	0.02	-0.15
27. Alajucla	20	9.98	275.79	27.2±3.4	26.2±3.3	29.6±1.5	25.5±2.0	0.04	0.13	-0.03
28. Paramaribo	69	5.81	304.79	27.7±3.3	27.1±6.7	31.3±3.0	26.3±2.6	0.02	0.16	-0.03
29. Sepang	62	2.73	101.70	25.7±3.2	24.9±3.9	25.5±2.4	21.6±3.0	0.03	0.02	-0.13
30. San Cristobal	27	-0.92	270.40	27.1±4.4	26.0±5.9	29.5±3.7	24.9±3.4	0.04	0.13	-0.04
31. Nairobi	52	-1.27	36.80	26.3±2.9	27.7±3.6	33.8±2.6	27.8±2.8	-0.05	0.22	0.00
32. Malindi	12	-2.99	40.19	29.1±2.8	36.1±5.0	34.0±3.0	28.4±3.7	-0.19	-0.06	-0.21
33. Natal	61	-5.42	324.62	30.9±5.8	34.3±8.6	36.5±6.2	30.6±5.1	-0.10	0.06	-0.11
34. Watukosek	52	-7.57	112.65	24.6±3.7	23.4±6.8	25.1±3.5	21.7±3.7	0.05	0.07	-0.07
35. Ascension	37	-7.58	345.76	31.8±8.2	39.6±7.9	40.2±5.1	34.0±4.5	-0.20	0.01	-0.14
36. Samoa	58	-14.23	189.44	24.7±4.5	21.4±5.4	24.8±4.2	20.3±3.7	0.16	0.16	-0.05
37. Suva	9	-18.10	178.20	30.3±4.6	21.7±4.0	28.6±5.6	22.6±3.6	0.40	0.32	0.04
38. La Reunion	61	-21.06	55.48	34.8±5.5	41.1±9.1	39.1±6.4	33.3±5.5	-0.15	-0.05	-0.19
39. Irene	29	-25.91	28.21	32.2±5.6	38.0±7.3	38.1±5.5	32.0±4.8	-0.15	0.00	-0.16
40. Broadmeadows	82	-37.68	144.95	31.1±5.8	28.7±4.9	33.8±5.0	27.8±3.0	0.08	0.18	-0.03
41. Lauder	50	-45.04	169.68	28.8±5.4	23.1±3.2	26.6±2.1	24.4±2.4	0.25	0.15	0.06
42. Macquarie	62	-54.50	158.97	24.7±4.7	22.7±3.4	23.2±3.5	24.6±3.2	0.09	0.02	0.09
43. Ushuaia	21	-54.85	291.69	26.9±3.3	21.0±3.6	24.4±3.0	24.7±3.0	0.28	0.16	0.17
44. Marambio	45	-64.23	303.38	22.6±2.6	19.1±4.0	21.5±6.2	22.7±3.4	0.18	0.13	0.19
Mean value of tropospheric ozone				34.0±4.5	32.5±6.0	36.2±4.1	28.8±3.9	0.06	0.12	-0.10

Table 7.2: Same as table 6.1 but for 5 % cloud fraction threshold.

Station name	No of points	Lat.	Lon.	Mean value and stdev. of trop. O ₃ from sondes (DU)	Mean value and stdev. of trop. O ₃ from SCIA-MACHY (DU)	Mean value and stdev. of trop. O ₃ from TES (DU)	Mean value and stdev. of trop. O ₃ from OMI/MLS (DU)	Mean value of trop. O ₃ rel. diff. (SCIA-MACHY)	Mean value of trop. O ₃ rel. diff. (TES)	Mean value of trop. O ₃ rel. diff. (OMI/MLS)
1. Sodankyla	21	67.39	26.65	39.9±5.9	32.9±4.9	37.6±3.1	29.8±3.4	0.21	0.14	-0.09
2. Lerwick	62	60.13	358.82	39.0±5.0	33.5±4.8	38.1±2.5	30.3±3.9	0.17	0.14	-0.10
3. Churchill	59	58.75	265.93	35.6±6.4	31.1±4.6	35.2±2.4	29.4±3.6	0.15	0.13	-0.05
4. Edmonton	79	53.55	245.90	36.0±5.0	28.9±4.0	36.3±3.1	26.9±2.7	0.25	0.25	-0.07
5. Goosebay	78	53.32	299.70	35.6±5.1	32.5±5.0	39.8±4.2	31.6±3.4	0.10	0.23	-0.03
6. Legionowo	75	52.40	20.97	40.9±3.5	36.5±7.0	41.4±5.3	29.7±4.0	0.12	0.13	-0.19
7. DeBilt	82	52.10	5.18	40.2±4.1	35.5±5.5	40.7±4.2	29.9±3.8	0.13	0.15	-0.16
8. Valentia	49	51.93	349.75	37.5±3.9	37.3±5.0	40.9±3.5	31.3±3.9	0.00	0.10	-0.16
9. Uccle	78	50.80	4.35	40.1±4.2	35.8±6.2	41.0±4.3	30.1±3.8	0.12	0.14	-0.16
10. Bratt's Lake	78	50.20	255.30	34.1±3.8	32.7±5.2	37.2±3.8	27.3±2.6	0.04	0.14	-0.17
11. Praha	26	50.02	14.45	41.0±5.0	34.4±4.8	38.6±3.3	28.4±2.8	0.19	0.12	-0.17
12. Kelowna	77	49.93	240.60	35.1±3.9	32.9±5.2	36.7±2.9	27.6±2.9	0.07	0.11	-0.16
13. Payerne	82	46.49	6.57	39.9±4.2	33.6±6.2	42.0±5.2	30.5±4.8	0.19	0.25	-0.09
14. Egbert	74	44.23	280.22	37.2±4.2	37.4±7.2	42.5±5.1	31.0±4.5	0.00	0.14	-0.17
15. Yarmouth	63	43.87	293.89	38.8±4.9	38.9±7.8	43.1±5.1	32.0±4.7	0.00	0.11	-0.18
16. Sapporo	82	43.10	141.30	39.2±6.6	35.3±8.7	42.9±4.6	34.3±5.1	0.11	0.22	-0.03
17. Madrid	81	40.45	356.28	37.7±3.9	34.8±6.4	42.3±4.7	31.9±5.6	0.08	0.22	-0.08
18. Ankara	78	39.95	32.88	37.1±3.3	35.6±9.9	44.9±7.4	32.6±7.1	0.04	0.26	-0.08
19. Wallops	80	37.93	284.52	439.7±4.1	41.5±8.0	44.7±4.9	32.3±5.8	-0.05	0.08	-0.22
20. Tsukuba	82	36.10	140.10	40.5±5.6	41.5±9.3	43.5±3.4	33.7±5.2	-0.02	0.05	-0.19
21. Huntsville	38	35.28	273.41	40.3±3.5	39.5±8.8	43.5±4.7	31.7±5.9	0.02	0.10	-0.20
22. Isfahan	50	32.51	51.70	34.9±3.3	37.3±9.1	42.1±5.1	32.2±5.9	-0.07	0.13	-0.14
23. Kagoshima	6	31.60	130.60	35.6±2.6	36.9±4.5	41.0±2.6	29.9±2.6	-0.04	0.11	-0.19
24. Naha	82	26.20	127.70	36.7±4.1	38.9±7.8	40.1±4.0	32.0±4.2	-0.06	0.03	-0.18
25. HongKong	81	22.31	114.17	34.6±4.0	38.9±6.3	38.0±3.8	30.4±3.8	-0.11	-0.02	-0.22
26. Hilo	68	19.72	204.93	32.5±3.9	33.6±6.4	34.4±4.0	28.5±3.9	-0.03	0.02	-0.15
27. Alajuela	20	9.98	275.79	26.3±3.3	26.2±3.3	29.6±1.5	25.5±2.0	0.00	0.13	-0.03
28. Paramaribo	69	5.81	304.79	27.4±3.4	27.1±6.7	31.3±3.0	26.3±2.6	0.01	0.16	-0.03
29. Sepang	62	2.73	101.70	25.1±3.4	24.9±3.9	25.5±2.4	21.6±3.0	0.01	0.02	-0.13
30. San Cristobal	27	-0.92	270.40	26.0±4.5	26.0±5.9	29.5±3.7	24.9±3.4	0.00	0.13	-0.04
31. Nairobi	52	-1.27	36.80	26.1±2.8	27.7±3.6	33.8±2.6	27.8±2.8	-0.06	0.22	0.00
32. Malindi	12	-2.99	40.19	28.6±2.7	36.1±5.0	34.0±3.0	28.4±3.7	-0.21	-0.06	-0.21
33. Natal	61	-5.42	324.62	30.5±5.8	34.3±8.6	36.5±6.2	30.6±5.1	-0.11	0.06	-0.11
34. Watukosek	52	-7.57	112.65	23.9±3.5	23.4±6.8	25.1±3.5	21.7±3.7	0.02	0.07	-0.07
35. Ascension	37	-7.58	345.76	31.2±8.1	39.6±7.9	40.2±5.1	34.0±4.5	-0.21	0.01	-0.14
36. Samoa	58	-14.23	189.44	24.0±4.5	21.4±5.4	24.8±4.2	20.3±3.7	0.12	0.16	-0.05
37. Suva	9	-18.10	178.20	29.8±4.4	21.7±4.0	28.6±5.6	22.6±3.6	0.37	0.32	0.04
38. La Reunion	61	-21.06	55.48	34.3±5.5	41.1±9.1	39.1±6.4	33.3±5.5	-0.17	-0.05	-0.19
39. Irene	29	-25.91	28.21	31.9±5.6	38.0±7.3	38.1±5.5	32.0±4.8	-0.16	0.00	-0.16
40. Broadmeadows	82	-37.68	144.95	30.8±5.5	28.7±4.9	33.8±5.0	27.8±3.0	0.07	0.18	-0.03
41. Lauder	50	-45.04	169.68	28.5±5.3	23.1±3.2	26.6±2.1	24.4±2.4	0.24	0.15	0.06
42. Macquarie	62	-54.50	158.97	24.9±4.0	22.7±3.4	23.2±3.5	24.6±3.2	0.10	0.02	0.09
43. Ushuaia	21	-54.85	291.69	24.6±3.4	21.0±3.6	24.4±3.0	24.7±3.0	0.17	0.16	0.17
44. Marambio	45	-64.23	303.38	22.0±2.9	19.1±4.0	21.5±6.2	22.7±3.4	0.16	0.13	0.19
Mean value of tropospheric ozone				33.5±4.4	32.5±6.0	36.2±4.1	28.8±3.9	0.04	0.12	-0.10

Table 7.3: Same as table 6.1 but for 15 % cloud fraction threshold.

APPENDIX

Station name	No of points	Lat.	Lon.	Mean value and stdev. of trop. O ₃ from sondes (DU)	Mean value and stdev. of trop. O ₃ from SCIA-MACHY (DU)	Mean value and stdev. of trop. O ₃ from TES (DU)	Mean value and stdev. of trop. O ₃ from OMI/MLS (DU)	Mean value of trop. O ₃ rel. diff. (SCIA-MACHY)	Mean value of trop. O ₃ rel. diff. (TES)	Mean value of trop. O ₃ rel. diff. (OMI/MLS)
1. Sodankyla	21	67.39	26.65	39.8±5.8	32.9±4.9	37.6±3.1	29.8±3.4	0.21	0.14	-0.09
2. Lerwick	62	60.13	358.82	39.1±4.8	33.5±4.8	38.1±2.5	30.3±3.9	0.17	0.14	-0.10
3. Churchill	59	58.75	265.93	36.2±5.1	31.1±4.6	35.2±2.4	29.4±3.6	0.16	0.13	-0.05
4. Edmonton	79	53.55	245.90	35.1±4.4	28.9±4.0	36.3±3.1	26.9±2.7	0.21	0.25	-0.07
5. Goosebay	78	53.32	299.70	35.5±4.7	32.5±5.0	39.8±4.2	31.6±3.4	0.09	0.23	-0.03
6. Legionowo	75	52.40	20.97	41.2±3.1	36.5±7.0	41.4±5.3	29.7±4.0	0.13	0.13	-0.19
7. DeBilt	82	52.10	5.18	40.3±3.7	35.5±5.5	40.7±4.2	29.9±3.8	0.14	0.15	-0.16
8. Valentia	49	51.93	349.75	37.4±4.1	37.3±5.0	40.9±3.5	31.3±3.9	0.00	0.10	-0.16
9. Uccle	78	50.80	4.35	40.2±3.7	35.8±6.2	41.0±4.3	30.1±3.8	0.12	0.14	-0.16
10. Bratt's Lake	78	50.20	255.30	33.8±3.6	32.7±5.2	37.2±3.8	27.3±2.6	0.03	0.14	-0.17
11. Praha	26	50.02	14.45	41.4±4.0	34.4±4.8	38.6±3.3	28.4±2.8	0.20	0.12	-0.17
12. Kelowna	77	49.93	240.60	34.9±4.1	32.9±5.2	36.7±2.9	27.6±2.9	0.06	0.11	-0.16
13. Payerne	82	46.49	6.57	39.8±3.8	33.6±6.2	42.0±5.2	30.5±4.8	0.19	0.25	-0.09
14. Egbert	74	44.23	280.22	36.9±4.1	37.4±7.2	42.5±5.1	31.0±4.5	-0.01	0.14	-0.17
15. Yarmouth	63	43.87	293.89	38.8±4.9	38.9±7.8	43.1±5.1	32.0±4.7	0.00	0.11	-0.18
16. Sapporo	82	43.10	141.30	38.5±6.9	35.3±8.7	42.9±4.6	34.3±5.1	0.09	0.22	-0.03
17. Madrid	81	40.45	356.28	37.4±3.6	34.8±6.4	42.3±4.7	31.9±5.6	0.08	0.22	-0.08
18. Ankara	78	39.95	32.88	37.1±3.3	35.6±9.9	44.9±7.4	32.6±7.1	0.04	0.26	-0.08
19. Wallops	80	37.93	284.52	4 39.1±4.0	41.5±8.0	44.7±4.9	32.3±5.8	-0.06	0.08	-0.22
20. Tsukuba	82	36.10	140.10	39.9±6.2	41.5±9.3	43.5±3.4	33.7±5.2	-0.04	0.05	-0.19
21. Huntsville	38	35.28	273.41	39.7±3.6	39.5±8.8	43.5±4.7	31.7±5.9	0.01	0.10	-0.20
22. Isfahan	50	32.51	51.70	34.6±3.4	37.3±9.1	42.1±5.1	32.2±5.9	-0.07	0.13	-0.14
23. Kagoshima	6	31.60	130.60	35.2±2.8	36.9±4.5	41.0±2.6	29.9±2.6	-0.05	0.11	-0.19
24. Naha	82	26.20	127.70	36.3±4.3	38.9±7.8	40.1±4.0	32.0±4.2	-0.07	0.03	-0.18
25. HongKong	81	22.31	114.17	34.4±4.1	38.9±6.3	38.0±3.8	30.4±3.8	-0.12	-0.02	-0.22
26. Hilo	68	19.72	204.93	32.0±4.0	33.6±6.4	34.4±4.0	28.5±3.9	-0.05	0.02	-0.15
27. Alajuela	20	9.98	275.79	25.6±3.3	26.2±3.3	29.6±1.5	25.5±2.0	-0.02	0.13	-0.03
28. Paramaribo	69	5.81	304.79	27.1±3.4	27.1±6.7	31.3±3.0	26.3±2.6	0.00	0.16	-0.03
29. Sepang	62	2.73	101.70	24.8±3.5	24.9±3.9	25.5±2.4	21.6±3.0	0.00	0.02	-0.13
30. San Cristobal	27	-0.92	270.40	25.6±4.1	26.0±5.9	29.5±3.7	24.9±3.4	-0.01	0.13	-0.04
31. Nairobi	52	-1.27	36.80	25.9±2.8	27.7±3.6	33.8±2.6	27.8±2.8	-0.07	0.22	0.00
32. Malindi	12	-2.99	40.19	28.7±2.9	36.1±5.0	34.0±3.0	28.4±3.7	-0.21	-0.06	-0.21
33. Natal	61	-5.42	324.62	30.4±5.7	34.3±8.6	36.5±6.2	30.6±5.1	-0.11	0.06	-0.11
34. Watukosek	52	-7.57	112.65	23.6±3.4	23.4±6.8	25.1±3.5	21.7±3.7	0.01	0.07	-0.07
35. Ascension	37	-7.58	345.76	30.8±8.1	39.6±7.9	40.2±5.1	34.0±4.5	-0.22	0.01	-0.14
36. Samoa	58	-14.23	189.44	23.6±4.5	21.4±5.4	24.8±4.2	20.3±3.7	0.10	0.16	-0.05
37. Suva	9	-18.10	178.20	29.5±4.5	21.7±4.0	28.6±5.6	22.6±3.6	0.36	0.32	0.04
38. La Reunion	61	-21.06	55.48	34.0±5.5	41.1±9.1	39.1±6.4	33.3±5.5	-0.17	-0.05	-0.19
39. Irene	29	-25.91	28.21	31.8±5.6	38.0±7.3	38.1±5.5	32.0±4.8	-0.16	0.00	-0.16
40. Broadmeadows	82	-37.68	144.95	30.5±5.4	28.7±4.9	33.8±5.0	27.8±3.0	0.06	0.18	-0.03
41. Lauder	50	-45.04	169.68	28.2±4.9	23.1±3.2	26.6±2.1	24.4±2.4	0.22	0.15	0.06
42. Macquarie	62	-54.50	158.97	24.6±3.5	22.7±3.4	23.2±3.5	24.6±3.2	0.08	0.02	0.09
43. Ushuaia	21	-54.85	291.69	22.4±3.5	21.0±3.6	24.4±3.0	24.7±3.0	0.06	0.16	0.17
44. Marambio	45	-64.23	303.38	21.7±2.8	19.1±4.0	21.5±6.2	22.7±3.4	0.14	0.13	0.19
Mean value of tropospheric ozone				33.3±4.3	32.5±6.0	36.2±4.1	28.8±3.9	0.03	0.12	-0.10

Table 7.4: Same as table 6.1 but for 30 % cloud fraction threshold.

References

- ANCELLET, G., BEEKMAN, N.M. & PAPAYANNIS, A. (1994). Impact of a cutoff low development on downward transport of ozone in the troposphere. *J. Geophys. Res.*, **99**, 3451–3468. 37
- ANDREAE, M.O., FERREK, R.J., BERMOND, F., BYRD, K.P., ENGSTROM, R.T., HARDIN, S., HOUMERE, P.D., LEMARREC, F., RAEMDONCK, H. & CHATFIELD, R.B. (1985). Dimethyl sulfide in the marine atmosphere. *J. Geophys. Res.*, **90(D7)**, 2891 – 2900. 22
- APPENZELLER, C. & DAVIES, H.C. (1992). Structure of stratospheric intrusions into the troposphere. *Nature*, **358**, 570–572. 36
- ARNETH, A., SITCH, S., BONDEAU, A., BUTTERBACH-BAHL, K., FOSTER, P., GEDNEY, N., DE NOBLET-DUCOUDRÉ, N., PRENTICE, I.C., SANDERSON, M., THONICKE, K., WANIA, R. & ZAEHLE, S. (2010). From biota to chemistry and climate: towards a comprehensive description of trace gas exchange between the biosphere and atmosphere. *Biogeosciences*, **7**, 121–149. 81
- ASHMORE, M.R. (2005). Assessing the future global impacts of ozone on vegetation. *Plant Cell and Env.*, **28**, 949–964. 2
- ATKINSON, R. (1979). Atmospheric reactions of alkoxy and α -hydroxyalkoxy radicals. *Znt. J. Chern. Kinet.*, **29**, 99 – 111. 24
- ATTICKS, M.G. & ROBINSON, G.D. (1983). Some features of the structure of the tropical tropopause. *Quart. J. Roy. Meteorol. Soc.*, **109**, 295–308. 34
- AUMANN, H.H., CHAHINE, M.T., GAUTIER, C., GOLDBERG, M.D., KALNAY, E., MCMILLIN, L.M., REVERCOMB, H., ROSENKRANZ, P.W., SMITH, W.L., STAELIN, D.H., STROW, L.L. & SUSSKIND, J. (2003). AIRS/AMSU/HSB on the Aqua mission: Design, science objectives, data products and processing systems. *IEEE T. Geosci. Remote*, **41**, 253–264. 60
- AUSTIN, J. & BUTCHART, N. (1992). A three-dimensional modeling study of the influence of planetary wave dynamics on polar ozone photochemistry. *J. Geophys. Res.*, **97**, 10165–10186. 35

REFERENCES

- BALDWIN, M.P., GRAY, L.J., DUNKERTON, T.J., HAMILTON, K., HAYNES, P.H., RANDEL, W.J., HOLTON, J.R., ALEXANDER, M.J., HIROTA, I., HORINOUCHE, T., JONES, D.B.A., KINNERSLEY, J.S., MARQUARDT, C., SATO, K. & TAKAHASHI, M. (2001). The quasi-biennial oscillation. *Rev. Geophys.*, **39**, 179–230. 114
- BALIS, D., KROON, M., KOUKOULI, M.E., BRINKSMA, E.J., LABOW, G., VEEFKIND, J.P. & MCPETERS, R.D. (2007). Validation of Ozone Monitoring Instrument total ozone column measurements using Brewer and Dobson spectrophotometer ground-based observations. *J. Geophys. Res.*, **112**, 9901 – 9914. 66
- BARAY, J.L., DANIEL, V., ANCELLET, G. & LEGRAS, B. (1993). The Upper Atmosphere Research Satellite Microwave Limb Sounder instrument. *J. Geophys. Res.*, **98(D6)**, 10751–10762. 15
- BATES, D.R. (1994). *The effects of ozone on plants and people; In: Chemistry of the Atmosphere: Its Impact on Global Change.* edited by: Calvert, Blackwell, J., Scientific Publications, Oxford. 2
- BATES, D.R. & NICOLET, M. (1950). The photochemistry of atmospheric water vapor. *J. Geophys. Res.*, **55(3)**, 301–327. 31
- BEER, R. (2006). TES on the Aura mission: Scientific objectives, measurements, and analysis overview. *IEEE T. Geosci. Remote*, **44**, 1102 – 1105. 20, 60
- BEER, R., GLAVICH, T.A. & RIDER, D.M. (2001). Tropospheric Emission Spectrometer for the Earth Observing System’s Aura satellite. *Appl. Optics*, **40**, 2356 – 2367. 20
- BEIG, G. & SINGH, V. (2007). Trends in tropical tropospheric column ozone from satellite data and MOZART model. *Geophys. Res. Lett.*, **34**, L17801. 128, 130
- BEIRLE, S., KÜHL, S., PUKITE, J. & WAGNER, T. (2010). Retrieval of tropospheric column densities of NO₂ from combined SCIAMACHY nadir/limb measurements. *Atmos. Meas. Tech.*, **3**, 283–299. 61
- BELL, M.L., GOLDBERG, R., HOGREFE, C., KINNEY, P.L., KNOWLTON, K. & LYNN, B. (2007). Climate change, ambient ozone, and health in 50 US cities. *Clim. Change*, **82**, 61–76. 2
- BENKOVITZ, C.M., SCHOLTZ, M.T., PACYNA, J., TARRASON, L., DIGNON, J., VOLDNER, E.C., SPIRO, P.A., LOGAN, J.A. & GRAEDEL, T.E. (1996). Global gridded inventories of anthropogenic emissions of sulfur and nitrogen. *J. Geophys. Res.*, **101(D22)**, 29239–29253. 21

- BERNTSEN, T.K., KARLSDÓTTIR, S. & JAFFE, D.A. (1999). Influence of Asian emissions on the composition of air reaching the North Western United States. *Geophys. Res. Lett.*, **26**, 2171–2174. 128
- BERTAUX, J., MÉGIE, G., WIDEMANN, T., CHASSEFIÈRE, E., PELLINEN, R., KYRÖLÄ, E., KORPELA, S. & SIMON, P. (1991). Monitoring of ozone trend by stellar occultations: The GOMOS instrument. *Adv. Space Res.*, **11(3)**, 237–242. 15
- BETHAN, S.G., VAUGHAN, G. & REID, S.J. (1996). A comparison of ozone and thermal tropopause heights and the impact of tropopause definition on quantifying the ozone content of the troposphere. *Quart. J. Roy. Meteorol. Soc.*, **122**, 929–944. 42, 47
- BHARTIA, P.K., MCPETERS, R.D., MATEER, C.L., FLYNN, L.E. & WELLEMAYER, C. (1996). Algorithm for the estimation of vertical ozone profiles from the backscattered ultraviolet technique. *J. Geophys. Res. Atmos.*, **101**, 18793 – 18806. 60
- BHARTIA, P.K., MCPETERS, R.D., FLYNN, L.E., TAYLOR, S., KRAMAROVA, N.A., FRITH, S., FISHER, B. & DELAND, M. (2013). Solar Backscatter UV (SBUV) total ozone and profile algorithm. *Atmos. Meas. Tech.*, **6**, 2533 – 2548. 60
- BIRNER, T. & BÖNISCH, H. (2011). Residual circulation trajectories and transit times into 309 the extratropical lowermost stratosphere. *Atmos. Chem. Phys.*, **11**, 817–827. 35
- BOGUMIL, K., ORPHAL, J., HOMANN, T., VOIGT, S., SPIETZ, P., FLEISCHMANN, O., VOGEL, A., HARTMANN, M., BOVENSMANN, H., FRERICK, J. & BURROWS, J. (2003). Measurements of molecular absorption spectra with the SCIAMACHY pre-flight model: instrument characterization and reference data for atmospheric remote-sensing in the 230–2380 nm region. *J Atmos. Photochem.*, **157**, 167–184. 71
- BOJKOV, R.D. (1986). Surface ozone during the second half of the nineteenth century. *J. Climate Appl. Meteor.*, **25**, 343–352. 110
- BOVENSMANN, H., BURROWS, J.P., BUCHWITZ, M., FRERICK, J., NOËL, S., ROZANOV, V.V., CHANCE, K.V. & GOEDE, A.P.H. (1999). SCIAMACHY: Mission Objectives and Measurement Modes. *J. Atmos. Sci.*, **56**, 127–150. 3, 15, 16, 17
- BOWMAN, K.W., RODGERS, C.D., KULAWIK, S.S., WORDEN, J., SARKISSIAN, E., OSTERMAN, G., STECK, T., LOU, M., ELDERING, A., SHEPHARD, M., WORDEN, H., LAMPEL, M., CLOUGH, S., BROWN, P., RINSLAND, C., GUNSON, M. & BEER, R. (2006). Tropospheric

REFERENCES

- emission spectrometer: Retrieval method and error analysis. *IEEE T. Geosci. Remote*, **44**(5), 1297 – 1307. 65
- BOXE, C.S., WORDEN, J.R., BOWMAN, K.W., KULAWIK, S.S., NEU, J.L., FORD, W.C., OSTERMAN, G.B., HERMAN, R.L., ELDERING, A., TARASICK, D.W., THOMPSON, A.M., DOUGHTY, D.C., HOFFMANN, M.R. & OLTMANS, S.J. (2010). Validation of northern latitude Tropospheric Emission Spectrometer stare ozone profiles with ARC-IONS sondes during ARCTAS: sensitivity, bias and error analysis. *Atmos. Chem. Phys.*, **10**, 9901 – 9914. 66
- BRACHER, A., BOVENSMANN, H., BRAMSTEDT, K., BURROWS, J.P., VON CLARMANN, T., EICHMANN, K.U., FISCHER, H., FUNKE, B., GIL-LÓPEZ, S., GLATTHOR, N., GRABOWSKI, U., HÖPFNER, M., KAUFMANN, M., KELLMANN, S., KIEFER, M., KOUKOULI, M.E., LINDEN, A., LÓPEZ-PUERTAS, M., TSIDU, G.M., MILZ, M., NOËL, S., ROHEN, G., ROZANOV, A., ROZANOV, V.V., VON SAVIGNY, C., SINNHUBER, M., SKUPIN, J., STECK, T., STILLER, G.P., WANG, D.Y., WEBER, M. & WUTTKE, M.W. (2005). Cross comparisons of O_3 and NO_2 measured by the atmospheric ENVISAT instruments GOMOS, MIPAS, and SCIAMACHY. *Adv. Space Res.*, **36**, 855–867. 58, 74
- BRAMSTEDT, K., NOËL, S., BOVENSMANN, H., BURROWS, J.P., LEROT, C., TILSTRA, L.G., LICHTENBERG, A., G. DEHN & FEHR, T. (2009). *SCIAMACHY monitoring factors: Observation and end-to-end correction of instrument performance degradation*, in *Proceedings of the 2009 Atmospheric Science Conference [CD-ROM]*. edited by H. Sawaya-Lacoste, Eur. Space Agency Spec. Publ. 130
- BRASSEUR, G.P., COX, R.A., HAUGLUSTAINE, D., ISAKSEN, I., LELIEVELD, J., LISTER, D.H., SAUSEN, R., SCHUMANN, U., WAHNER, A. & WIESEN, P. (1998). European scientific assessment of the atmospheric effects of aircraft emissions. *Atmos. Environ.*, **32**, 2329–2418. 65
- BRASSEUR, G.P., ORLANDO, J.J. & TYNDALL, G.S. (1999a). *Atmospheric Chemistry and Global Change*. Oxford Univ. Press, New York.
- BRASSEUR, G.P., ORLANDO, J.J. & TYNDALL, G.S. (1999b). *Trace gas exchanges and biochemical cycles*, in *Atmospheric Chemistry and Global Change*, edited by G. P. Brasseur, J. J. Orlando, and G. S. Tyndall. Oxford Univ. Press, New York. 22
- BREWER, A.W. (1949). Evidence for a world circulation provided by the measurements of helium and water vapour distribution in the stratosphere. *Q. J. Roy. Meteorol. Soc.*, **75**, 351–363. 35

- BREWER, A.W. & MILFORD, J. (1960). The Oxford Kew ozonesonde. *Proc. Roy. Soc. London, Ser. A*, **256**, 470. 14, 66
- BREWER, A.W. & ROY, Q.J. (1949). Evidence for a world circulation provided by the measurements of helium and water vapour distribution in the stratosphere. *Meteor. Soc.*, **75**, 351–363. 34
- BRIOUDE, J., CAMMAS, J.P., COOPER, O.R. & NEDELEC, P. (2008). Characterization of the composition, structure, and seasonal variation of the mixing layer above the extratropical tropopause as revealed by MOZAIC measurements. *J. Geophys. Res.*, **113**, D00B01. 36
- BURROWS, J., WEBER, M., BUCHWITZ, M., ROZANOV, V.V., LADSTÄDTER-WEISSENMAYER, A., RICHTER, A., DE BEEK, R., HOOGEN, R., BRAMSTEDT, K., EICHMANN, K.U., EISINGER, M. & PERNER, D. (1999). The Global Ozone Monitoring Experiment (GOME): Mission concept and first scientific results. *J. Atmos. Sci.*, **56**, 151–175. 16, 71
- BURROWS, J.P., HOLZLE, E., GOEDE, A.P.H., VISSER, H. & FRICKE, W. (1995). SCIAMACHY—Scanning imaging absorption spectrometer for atmospheric cartography. *Acta Astronautica*, **35**, 445–451. 3, 17
- BURROWS, J.P., BOVENSMANN, H., BERGAMETTI, G., FLAUD, J.M., ORPHAL, J., NOËL, S., MONKS, P.S., CORLETT, G.K., GOEDE, A.P.H., VON CLARMANN, T., STECK, T., FISCHER, H., & FRIEDL-VALLON, F. (2004). The geostationary tropospheric pollution explorer (GeoTROPE) missions: objects, requirements and mission concept. *Adv. space Res.*, **34**(4), 682–687. 60
- BUSS, S., HERZOG, A., HOSTETTLER, C., BUI, T.P., LÜTHI, D. & WERNLI, H. (2004). Analysis of a jet stream induced gravity wave associated with an observed stratospheric ice cloud over Greenland. *Atmos. Chem. Phys.*, **4**, 1183–1200. 38
- BUTCHART, N., SCAIFE, A.A., AUSTIN, J., HARE, S.H.E. & KNIGHT, J.R. (2003). Quasi-biennial oscillation in ozone in a coupled chemistry-climate model. *J. Geophys. Res.*, **108**, 4486. 113
- BUTCHART, N., CIONNI, I., EYRING, V., SHEPHERD, T.G., WAUGH, D.W., AKIYOSHI, H., AUSTIN, J., BRÜHL, C., CHIPPERFIELD, M.P., CORDERO, E., DAMERIS, M., DECKERT, R., DHOMSE, S., FRITH, S.M., GARCIA, R.R., GETTELMAN, A., GIORGETTA, M.A., KINNISON, D.E., LI, F., MANCINI, E., McLANDRESS, C., PAWSON, S., PITARI, G., PLUMMER, D.A.,

REFERENCES

- ROZANOV, E., SASSI, F., SCINOCCA, J.F., SHIBATA, K., STEIL, B. & W., T. (2010). ChemistryClimate Model Simulations of Twenty-First Century Stratospheric Climate and Circulation Changes. *J. Climate*, **23**, 5349–5374. 35
- CADBURY, D. (2006). *Space Race: An Epic Battle Between America and the Soviet Union for Dominion of Space*. New York City: HarperCollins. 15
- CALLIES, J., CORPACCIOLI, E., EISINGER, M., HAHNE, A. & LEFEBVRE, A. (2000). GOME-2 - METOP's second-generation sensor for operational ozone monitoring. *ESA Bull.*, **102**, 28–36. 16
- CHAMEIDES, W.L. & DAVIS, D.D. (1982). Chemistry in the troposphere. *Chem. Eng. News*, **60**, 38–52. 22
- CHANCE, K.V., BURROWS, J.P. & SCHNEIDER, W. (1997). Satellite measurements of atmospheric ozone profiles, including tropospheric ozone, from ultraviolet/visible measurements in the nadir geometry: A potential method to retrieve tropospheric ozone. *J. Quant. Spectr. Rad. Trans.*, **57**, 4, 461–476. 16
- CHANCE, K.V., PALMER, P.I., SPURR, R.J.D., MARTIN, R.V., KUROSU, T.P. & JACOB, D.J. (2000). Satellite observations of formaldehyde over North America from GOME. *Geophys. Res. Lett.*, **27**, 3461–3464. 60
- CHANDRA, S., ZIEMKE, J.R., MIN, W. & READ, W.G. (1998). Effects of 1997-1998 El Nino on tropospheric ozone and water vapor. *Geophys. Res. Lett.*, **25(20)**, 3867 – 3870. 88
- CHANDRA, S., ZIEMKE, J.R., BHARTIA, P.K. & MARTIN, R.V. (2002). Tropical tropospheric ozone: Implications for dynamics and biomass burning. *J. Geophys. Res.*, **107(D14)**, 4188. 100, 106, 115
- CHANDRA, S., ZIEMKE, J.R. & MARTIN, R.V. (2003). Tropospheric ozone at tropical and middle latitudes derived from TOMS/MLS residual: Comparison with a global model. *J. Geophys. Res.*, **108, D9**, 4291. 83, 94, 101, 102, 119
- CHANDRA, S., ZIEMKE, J.R., TIE, X. & BRASSEUR, G. (2004). Elevated ozone in the troposphere over the Atlantic and Pacific oceans in the Northern Hemisphere. *Geophys. Res. Lett.*, **31**, L23102. 84, 85, 86, 102, 103, 110, 111
- CHEN, P. (1995). Isentropic cross-tropopause mass exchange in the extratropics. *J. Geophys. Res.*, **100 D8**, 1666116673. 35

- CHIPPERFIELD, M.P., GRAY, L.J., KINNERSLEY, J.S. & ZAWODNY, J. (1994). Two-Dimensional Model Study of the QBO Signal in SAGE II NO₂ and O₃. *Geophys. Res. Lett.*, **21**, 589–592. 113
- CLAUDE, H., HARTMANNGRUBER, R. & KÖHLER, U. (1987). Measurement of atmospheric ozone profiles using the Brewer/Mast sonde – Preparation, procedure, evaluation. *WMO Global Ozone Res. and Monit. Proj.*, **17**. 67
- COCHRANE, D. & ORCUTT, G.H. (1949). Application of least squares regression to relationships containing autocorrelated error terms. *J. Amer. Stat. Assoc.*, **44**, 32 – 61. 112
- COFALA, J., AMANN, M., KLIMONT, Z., KUPIAINEN, K. & HÖGLUNDISAKSSON, L. (2007). Scenarios of global anthropogenic emissions of air pollutants and Methane until 2030. *Atmos. Environ.*, **41**, 8486–8499. 1
- COLDEWEY-EGBERS, M., WEBER, M., LAMSAL, L.N., DE BEEK, R., BUCHWITZ, M. & BURROWS, J.P. (2005). Total ozone retrieval from GOME UV spectral data using the weighting function DOAS approach. *Atmos. Chem. Phys.*, **5**, 5015 – 5025. 55, 56, 57, 58, 73
- COLLINS, W.J., DERWENT, R.G., JOHNSON, C.E. & STEVENSON, D.S. (2002). The oxidation of organic compounds in the troposphere and their global warming potentials. *Clim. Change*, **52(4)**, 453479. 24
- COLLINS, W.J., DERWENT, R.G., GARNIER, B., JOHNSON, C.E., SANDERSON, M.G. & STEVENSON, D.S. (2003). Effect of stratosphere-troposphere exchange on the future tropospheric ozone trend. *J. Geophys. Res.*, **108(D12)**, 8528. 29, 32, 35
- COOPER, O.R., GAO, R.S., TARASICK, D., LEBLANC, T. & SWEENEY, J. (2012). Long-term ozone trends at rural ozone monitoring sites across the United States, 1990–2010. *J. Geophys. Res.*, **117**, D22307. 127
- CORFIDI, S.F., MERITT, J.H. & FRITSCH, J.M. (1996). Predicting the Movement of Mesoscale Convective Complexes. *Wea. Forecasting*, **11(No. 1)**, 41–46. 37
- CORNÚ, M.A. (1879). Sur la limite ultra-violette du spectre solaire. *Comptes Rendus* **88**, 1101–1108. 12
- CREILSON, J.K., FISHMAN, J. & WOZNIAK, A.E. (2003). Intercontinental transport of tropospheric ozone: a study of its seasonal variability across the North Atlantic utilizing tropospheric ozone residuals and its relationship to the North Atlantic Oscillation. *Atmos. Chem. Phys.*, **3**, 2053–2066. 81

REFERENCES

- CREILSON, J.K., FISHMAN, J. & WOZNIAK, A.E. (2005). Arctic Oscillation-induced variability in satellite-derived tropospheric ozone. *Geophys. Res. Lett.*, **32**, L14822. 81
- CRISTOFANELLI, P., BONASONI, P., COLLINS, W., FEICHTER, J., FORSTER, C., JAMES, P., KENTARCHOS, A., KUBIK, P.W., LAND, C., MELOEN, J., ROELOFS, G.J., SIEGMUND, P., SPRENGER, M., SCHNABEL, C., STOHL, A., TOBLER, L., TOSITTI, L., TRICKL, T. & P., Z. (2003). Stratosphere-to-troposphere transport: A model and method evaluation. *J. Geophys. Res.*, **108(D12)**, 8525. 32
- CRUTZEN, P.J. (1970). The influence of nitrogen oxides on the atmospheric ozone content. *Q. J. Roy. Meteor. Soc.*, **96**, 320–325. 22, 31
- CRUTZEN, P.J. (1971). Ozone production rates in oxygen-hydrogen-nitrogen oxide atmosphere. *J. Geophys. Res.*, **76**, 7311–7327. 1
- CRUTZEN, P.J. (1973). A discussion of the chemistry of some minor constituents in the stratosphere and troposphere. *Pure App. Geophys.*, **106-108**, 1385–1399. 2
- CRUTZEN, P.J. (1974). Photochemical reactions initiated by and influencing ozone in unpolluted tropospheric air. *Tellus*, **26**, 47–57. 26
- CRUTZEN, P.J. (1995). Overview of tropospheric chemistry: Developments during the past quarter century and a look ahead. *Faraday Disc.*, **100**, 1–21. 2
- CRUTZEN, P.J. & ANDREAE, M.O. (1990). Biomass burning in the tropics: Impact on atmospheric chemistry and biogeochemical cycles. *Science*, **250**, 1669–1678. 21
- CUESTA, J., EREMENKO, M., LIU, X., DUFOUR, G., CAI, Z., HÖPFNER, M., VON CLARMANN, T., SELBITTO, P., FORET, G., GAUBERT, B., BEEKMANN, M., ORPHAL, J., CHANCE, K., SPURR, R. & FLAUD, J.M. (2013). Satellite observation of lowermost tropospheric ozone by multispectral synergism of IASI thermal infrared and GOME-2 ultraviolet measurements over Europe. *Atmos. Chem. Phys.*, **13(19)**, 9675–9693. 60
- DALVI, M., BEIG, G., PATIL, U., KAGINALKAR, A., SHARMA, C. & MITRA, A.P. (2006). A GIS based methodology for gridding large scale emission inventories: application to carbon-monoxide emissions over Indian region. *Atmos. Environ.*, **40**, 2995–3007. 122
- DANIELSEN, E.F. (1968). Stratospheric-Tropospheric Exchange Based on Radioactivity, Ozone and Potential Vorticity. *J. Atmos. Sci.*, **25**, 502–518. 35

- DAVE, J.V. & MATEER, C.L. (1967). A Preliminary Study on the Possibility of Estimating Total Atmospheric Ozone from Satellite Measurements. *J. Atmos. Sci.*, **24**, 414–427. 16
- DAVIS, C.A. & TRIER, S.B. (2007). Mesoscale Convective Vortices Observed during BAMEX. Part I: Kinematic and Thermodynamic Structure. *Mon. Wea. Rev.*, **135**, 2029–2049. 37
- DAYAN, U. (1986). Climatology of back trajectories from Israel based on synoptic analysis. *J. Clim. Appl. Meteorol.*, **25**, 591–595. 87
- DE LAAT, A.T.J., ABEN, I. & ROELOFS, G.J. (2005). A model perspective on total tropospheric O₃ column variability and implications for satellite observations. *J. Geophys. Res.*, **110**, D13303. 84, 87, 97, 102
- DEE, D.P., UPPALA, S.M., SIMMONS, A.J., BERRISFORD, P., POLI, P., KOBAYASHI, S., ANDRAE, U., BALMASEDA, M.A., BALSAMO, G., BAUER, P., BECHTOLD, P., BELJAARS, A.C.M., VAN DE BERG, L., BIDLOT, J., BORMANN, N., DELSOL, C., DRAGANI, R., FUENTES, M., GEER, A.J., HAIMBERGER, L., HEALY, S.B., HERSBACH, H., HÓLM, E.V., ISAKSEN, L., KÄLLBERG, P., KÖHLER, M., MATRICARDI, M., MCNALLY, A.P., MONGE-SANZ, B.M., MORCRETTE, J.J., PARK, B.K., PEUBEY, C., DE ROSNAY, P., TAVOLATO, C., THÉPAUT, J.N. & VITART, F. (2012). The ERA-Interim reanalysis: configuration and performance of the data assimilation system. *Q.J.R. Meteorol. Soc.*, **137**, 553–597. 43
- DELON, C., REEVES, C.E., STEWART, D.J., SERÇA, D., DUPONT, R., MARI, C., CHABOUREAU, J.P. & TULET, P. (2008). Biogenic nitrogen oxide emissions from soils impact on NO_x and ozone over West Africa during AMMA (African Monsoon Multidisciplinary Experiment): modelling study. *Atmos. Chem. Phys.*, **8**, 2351–2363. 21
- DERWENT, R., SIMMONDS, P., SEURING, S. & DIMMER, C. (1998). Observation and interpretation of the seasonal cycles in the surface concentrations of ozone and carbon monoxide at Mace Head, Ireland from 1990 to 1994. *Atmos. Environ.*, **32**, 145–157. 82, 110, 112
- DESSLER, A.E., HINTSA, E.J., WEINSTOCK, E.M., ANDERSON, J.G. & CHAN, K.R. (1995). Mechanisms controlling water vapor in the lower stratosphere: A tale of two stratospheres. *J. Geophys. Res.*, **100(D11)**, 2316723172. 34, 36
- DETHOF, A., O’NEILL, A. & SLINGO, J. (2000). Quantification of the isentropic mass transport across the dynamical tropopause. *J. Geophys. Res.*, **105**, 12279–12294. 35

REFERENCES

- DI NOIA, A., SELBITTO, P., DEL FRATE, F. & DE LAAT, J. (2013). Global tropospheric ozone column retrievals from OMI data by means of neural networks. *Atmos-meas-tech.*, **6**, 895–915. 61
- DIBB, J.E., TALBOT, R.W., SCHEUER, E., SEID, G., DEBELL, L., LEFER, B. & RIDLEY, B. (2003). Stratospheric influence on the northern North American free troposphere during TOPSE: 7 Be as a stratospheric tracer. *J. Geophys. Res.*, **108 (D4)**, 8363. 110
- DIGNON, J. (1992). NO_x and SO_x Emissions from Fossil Fuels: A Global Distribution. *Atmos. Environ.*, **26A**, 1157–1163. 21
- DOBSON, G.M.B. (1931). A photoelectric spectrometer for measuring the amount of atmospheric ozone. *Proc. Phys. Soc.*, **43**, 324–339. 13
- DOBSON, G.M.B. (1956). Origin and Distribution of the Polyatomic Molecules in the Atmosphere. *R. Soc. Lond. Proc. A.*, **236**, 187–193. 35
- DOBSON, G.M.B. (1973). The laminated structure of the ozone in the atmosphere. *Q. J. R. Meteorol. Soc.*, **99**, 599–607. 37
- DOBSON, G.M.B. & HARISON, D.D. (1926). Measurements of the amount of ozone in the Earth's atmosphere and its relation to other geophysical conditions. *Proc. R. Soc. London A.*, **110**, 660–693. 13
- DÖRNBRACK, A., BIRNER, T., FIX, A., FLENTJE, H., MEISTER, A., SCHMID, H., BROWELL, E. & MAHONEY, M. (2002). Evidence for inertia gravity waves forming polar stratospheric clouds over Scandinavia. *J. Geophys. Res.*, **197(D20)**, 8287. 38
- DOUGHTY, D.C., THOMPSON, A.M., SCHOEBERL, M.R., STAJNER, I., WARGAN, K. & HUI, W.C.J. (2011). An intercomparison of tropospheric ozone retrievals derived from two Aura instruments and measurements in western North America in 2006. *J. Geophys. Res.*, **116**, D06303. 60
- DUNCAN, B.N., MARTIN, R.V., STAUDT, A.C., YEVICH, R. & LOGAN, J.A. (2003). Interannual and seasonal variability of biomass burning emissions constrained by satellite observations. *J. Geophys. Res.*, **108(D2)**, 4100. 84, 103
- DUNCAN, B.N. *et al.* (2010). Application of OMI observations to a space-based indicator of NO_x and VOC controls on surface ozone formation. *Atmos. Environ.*, **44, 18**, 2213–2223. 118, 120

-
- EBOJIE, F., VON SAVIGNY, C., LADSTÄTTER-WEISSENMAYER, A., ROZANOV, A., WEBER, M., EICHMANN, K., BÖTEL, S., RAHPOE, N., BOVENSMANN, H. & BURROWS, J.P. (2014). Tropospheric column amount of ozone retrieved from SCIAMACHY limb-nadir-matching observations. *Atmos. Meas. Tech. Discuss.*, **6**, 7811–7865. 61, 67, 89, 116, 119, 127, 130
- EDWARDS, D.P. *et al.* (2003). Tropospheric ozone over the tropical Atlantic: A satellite perspective. *J. Geophys. Res.*, **108** (D8), 4237. 83, 101
- EDWARDS, D.P. *et al.* (2006). Satellite observed pollution from Southern Hemisphere biomass burning. *J. Geophys. Res.*, **111**, D14312. 128, 129
- EGOROVA, T., ROZANOV, E., ZUBOV, V., SCHMUTZ, W. & PETER, T. (2005). Influence of solar 11-year variability on chemical composition of the stratosphere and mesosphere simulated with a chemistry-climate model. *Adv. Space Res.*, **35** (3), 451–457. 114
- EICHMANN, K.U., VON SAVIGNY, C., REICHL, P., ROBERT, C., STEINWAGNER, J., BOVENSMANN, H. & BURROWS, J.P. (2009). SCODA: SCIAMACHY CIOud Detection Algorithm from limb radiance measurements Algorithm Theoretical Baseline Document (ATBD). *Institute of Environmental Physics, University of Bremen*. 55
- ELBERN, H., HENDRICKS, J. & A., E. (1998). A climatology of tropopause folds by global analyses. *Theor. Appl. Climatol.*, **59**, 181200. 36
- ELDERING, A., KULAWIK, S.S., WORDEN, J.R., BOWMAN, K.W. & OSTERMAN, G.B. (2008). Implementation of cloud retrievals for Tropospheric Emission Spectrometer atmospheric retrievals: 2. Characterization of cloud top pressures and effective optical depth retrievals. *J. Geophys. Res.*, **113**, D16S37. 66
- FABIAN, P. & PRUCHNIEWICZ, P.G. (1977). Meridional distribution of ozone in the troposphere and its seasonal variation. *J. Geophys. Res.*, **82**, 2063–2073. 22
- FARMAN, J.C., GARDINER, B.G. & SHANKLIN, J.D. (1985). Large losses of total ozone in Antarctica reveal seasonal ClO_x/NO_x interaction. *Nature*, **315**, 207–210. 31
- FEISTER, W. & WARMBT, W. (1987). Long-term measurements of surface ozone in the German Democratic Republic. *J. Atmos. Chem.*, **5**, 1–21. 1
- FINLAYSON-PITTS, B.J. & PITTS JR., J.N. (1986). *Atmospheric Chemistry*. John Wiley & Sons Ltd. 24, 26

REFERENCES

- FINLAYSON-PITTS, B.J. & PITTS JR., J.N. (1997). Tropospheric Air Pollution: Ozone, Airborne Toxics, Polycyclic Aromatic Hydrocarbons, and Particles. *Science*, **276**, 1045. 2
- FISCHER, H. & OELHAF, H. (1996). Remote sensing of vertical profiles of atmospheric trace constituents with MIPAS limb emission spectrometers. *Appl. Opt.*, **35(16)**, 2787–2796. 15
- FISCHER, H., DE REUS, M., TRAUB, M., WILLIAMS, J., LELIEVELD, J., DE GOUW, J., WARNECKE, C., SCHLAGER, H., MINIKIN, A., SCHEELE, R. & SIEGMUND, P. (2000). Tracer correlations in the northern high latitude lowermost stratosphere: Influence of crosstropopause mass exchange. *Geophys. Res. Lett.*, **27(1)**, 97–100. 36
- FISCHER, H., DE REUS, M., TRAUB, M., WILLIAMS, J., LELIEVELD, J., DE GOUW, J., WARNECKE, C., SCHLAGER, H., MINIKIN, A., SCHEELE, R. & SIEGMUND, P. (2003). Deep convective injection of boundary layer air into the lowermost stratosphere at midlatitudes. *Atmos. Chem. Phys.*, **3**, 739745. 34
- FISHMAN, J. & BALOK, A.E. (1999). Calculation of daily tropospheric ozone residuals using TOMS and empirically improved SBUV measurements: Application to an ozone pollution episode over the eastern United States. *J. Geophys. Res.*, **104**, 30319 – 30340. 3, 59
- FISHMAN, J. & CRUTZEN, P.J. (1978). The origin of ozone in the troposphere. *Nature*, **274**, 855–858. 1
- FISHMAN, J. & LARSEN, J.C. (1987). Distribution of total ozone and stratospheric ozone in the tropics: Implication for the distribution of tropospheric ozone. *J. Geophys. Res.*, **92**, 6627–6634. 3, 59, 131
- FISHMAN, J., SOLOMON, S. & CRUTZEN, P.J. (1979). Observational and theoretical evidence in support of a significant in-situ photochemical source of tropospheric ozone. *Tellus*, **31**, 432446. 2, 21
- FISHMAN, J., WATSON, C., LARSEN, J. & LOGAN, J. (1990). Distribution of tropospheric ozone determined from satellite data. *J. Geophys. Res.*, **95**, 3599–3617. 3, 59, 60
- FISHMAN, J., WOZNIAK, A.E. & CREILSON, J.K. (2003). Global distribution of tropospheric ozone from satellite measurements using the empirically corrected tropospheric ozone residual technique: Identification of the regional aspects of air pollution. *Atmos. Chem. Phys.*, **3**, 893–907. 83, 87, 89

- FISHMAN, J., CREILSON, J.K., WOZNIAK, A.E. & CRUTZEN, P.J. (2005). Interannual variability of stratospheric and tropospheric ozone determined from satellite measurements. *J. Geophys. Res.*, **110**, D20306. 81
- FLITTNER, D.E., BHARTIA, P.K. & HERMAN, B.M. (2000). O₃ profiles retrieved from limb scatter measurements: Theory. *Geophys. Res. Lett.*, **27**, 2601–2604. 53, 54
- FLYNN, L.E., SEFTOR, C.J., LARSEN, J.C. & XU, P. (2006). The Ozone Mapping and Profiler Suite, in: Earth Science Satellite Remote Sensing, edited by: Qu, J. J., Gao, W., Kafatos, M., Murphy, R. E., and Salomonson, V. V. *Springer, Berlin*, 279–296. 15
- FOLKINS, I., BRAUN, C., THOMPSON, A.M. & WITTE, J. (2002). Tropical ozone as an indicator of deep convection. *J. Geophys. Res.*, **107**, 4184. 85
- FOSTER, P.M.D.F. & SHINE, K.P. (1997). Radiative forcing and temperature trends from stratospheric ozone changes. *J. Geophys. Res.*, **102(D9)**, 10841–10855. 31
- FREDERICK, J.E., CEBULA, R.P. & HEATH, D.F. (1986). Instrument characterization for the detection of long-term changes in stratospheric ozone: An analysis of the SBUV/2 radiometer. *J. Atmos. Oceanic Technol.*, **3**, 472–480. 16
- FRISK, U. *et al.* (2003). The Odin satellite I: Radiometer design and test. *Astron. Astrophys.*, **402(3)**, L27–L34. 15
- FROIDEVAUX, L. *et al.* (2006). Early validation analyses of atmospheric profiles from EOS MLS on the Aura satellite. *IEEE Trans. Geophys. Remote Sens.*, **44(5)**, 1075 – 1092. 66
- FROIDEVAUX, L. *et al.* (2008). Validation of Aura Microwave Limb Sounder stratospheric ozone measurements. *J. Geophys. Res.*, **113**, D15S20. 66
- FUEGLISTALER, S., DESSLER, A.E., DUNKERTON, T.J., FOLKINS, I., FU, Q. & MOTE, P.W. (2009). Tropical tropopause layer. *Rev. Geophys.*, **47**. 34
- FUENZALIDA, H.A., SANCHEZ, R. & GARREAU, R.D. (2005). A climatology of cutoff lows in the Southern Hemisphere. *J. Geophys. Res.-Atmos.*, **110 (D18)**. 37
- FUJIWARA, M., KITA, K., KAWAKAMI, S., OGAWA, T., KOMALA, N., SARASPRIYA, S. & SURIPTO, A. (1999). Tropospheric ozone enhancements during the Indonesian forest fire events in 1994 and in 1997 as revealed by ground-based observations. *Geophys. Res. Lett.*, **26(16)**, 2417–2420. 114

REFERENCES

- FUJIWARA, M., KITA, K., OGAWA, T., KAWAKAMI, S., KOMALA, N., SANO, T., KOMALA, N., SARASPRIYA, S. & SURIPTO, A. (2000). Seasonal variation of tropospheric ozone in Indonesia revealed by 5-year ground-based observations. *J. Geophys. Res.*, **105**, 1879 – 1888. 114
- FUSCO, A.C. & LOGAN, J.A. (2003). Analysis of 1970-1995 trends in tropospheric ozone at Northern Hemisphere midlatitudes with the GEOS-CHEM model. *J. Geophys. Res.*, **108**, 4449. 21
- FUSSEN, D. & BINGEN, C. (1999). A volcanism dependent model for the extinction profile of stratospheric aerosols in the UV-visible range. *Geophys. Res. Lett.*, **26**, 703–706. 55
- GALETZKA, M. & GLAUNER, P.O. (2012). A correct even-odd algorithm for the point-in-polygon (pip) problem for complex polygons. *CoRR*, **abs/1207.3502**. 63
- GANGULY, N.D. & TZANIS, C. (2011). Study of stratosphere-troposphere exchange events of ozone in India and Greece using ozonesonde ascents. *Meteoro. Appl. in press*. 29
- GARCIA, R.R. & RANDEL, W.J. (2008). Acceleration of the Brewer-Dobson circulation due to increases in greenhouse gases. *J. Atmos. Sci.*, **65**, 2731–2739. 105
- GARCIA-HERRERA, R., CALVO, N., GARCIA, R.R. & GIORGETTA, M.A. (2006). Propagation of ENSO temperature signals into the middle atmosphere: A comparison of two general circulation models and ERA-40 reanalysis data. *J. Geophys. Res.*, **111**, D06101. 114
- GAUSS, M., ISAKSEN, I.S.A., LEE, D.S. & SØVDE, O.A. (2006a). Impact of aircraft NO_x emissions on the atmosphere – tradeoffs to reduce the impact. *Atmos. Chem. Phys.*, **6**, 1529–1548. 21
- GAUSS, M., MYHRE, G., ISAKSEN, I.S.A. *et al.* (2006b). Radiative forcing since preindustrial times due to ozone change in the troposphere and the lower stratosphere. *Atmos. Chem. Phys.*, **6**(3), 575–599. 82
- GEBHARDT, C., ROZANOV, A., HOMMEL, R., WEBER, M., BOVENSMANN, H., BURROWS, J.P., DEGENSTEIN, D., FROIDEVAUX, L. & THOMPSON, A.M. (2014). Stratospheric ozone trends and variability as seen by SCIAMACHY from 2002 to 2012. *Atmos. Chem. Phys.*, **14**, 2, 831–846. 112
- GETTELMAN, A., HOLTON, J.R. & ROSENLOF, K.H. (1997). Mass fluxes of O₃, CH₄, N₂O, and CF₂Cl₂ in the lower stratosphere calculated from observational data. *J. Geophys. Res.*, **102**, D15, 19149–19159. 29
- GETTELMAN, A., HOOR, P., PAN, L.L., RANDEL, W.J., HEGGLIN, M.I. & BIRNER, T. (2011). The extratropical upper troposphere and lower stratosphere. *Rev. Geophys.*, **49**, RG3003. 31

- GILGE, S., PLASS-DUELMER, C., FRICKE, W., KAISER, A., RIES, L., BUCHMANN, B. & STEINBACHER, M. (2010). Ozone, carbon monoxide and nitrogen oxides time series at four alpine GAW mountain stations in central Europe. *Atmos. Chem. Phys.*, **10**, 12295–12316. 1
- GLEISNER, H. & THEJLL, P. (2003). Patterns of tropospheric response to solar variability. *Geophys. Res. Lett.*, **30 (13)**, 1711. 114
- GOERING, M.A., GALLUS JR., W.A., OLSEN, M.A. & STANFORD, J.L. (2001). Role of stratospheric air in a severe weather event: Analysis of potential vorticity and total ozone. *J. Geophys. Res.*, **106 (D11)**, 11813–11823. 37
- GOSSARD, E.E. & MUNK, W. (1954). On gravity waves in the atmosphere. *J. Meteorol.*, **11**, 259–269. 38
- GOTTWALD, M. & BOVENSMANN, H., eds. (2011). *SCIAMACHY - Exploring the Changing Earth's Atmosphere*. Springer Heidelberg Dordrecht London New York, ISBN 978-90-481-9895-5. 3, 17, 18
- GÖTZ, F.W.P., MEETHAM, A.R. & DOBSON, G.M.B. (1934). The vertical distribution of ozone in the atmosphere. *Proc. R. Soc. London, Ser. A*, **145**, 416–443. 13
- GRAY, L.J. *et al.* (2010). Solar influences on climate. *Rev. Geophys.*, **48**, RG4001. 114
- GRYPARIS, A., FORSBERG, B., KATSOUYANNI, K., ANALITIS, A., TOULOUMI, G. & SCHWARTZ, J. (2004). Acute effects of ozone on mortality from the "air pollution and health: a European approach" project. *Am. J. Respir. Crit. Care Med.*, **170**, 1080–1087. 2
- GUENTHER, A.B., ZIMMERMAN, P.R., HARLEY, P.C., MONSON, R.K. & FALL, R. (1993). Isoprene and Monoterpene Emission Rate Variability - Model Evaluations and Sensitivity Analyses. *J. Geophys. Res.-Atmos.*, **98**, 12609–12617. 1
- GURJAR, B.R., VAN AARDENNE, J.A., LELIEVELD, J. & MOHAN, M. (2004). Emission estimates and trends (1990–2000) for megacity Delhi and implications. *Atmos. Environ.*, **38(33)**, 5663–5681. 120
- GURJAR, B.R., BUTLER, T.M., LAWRENCE, M.G. & LELIEVELD, J. (2008). Evaluation of Emissions and Air Quality in Megacities. *Atmos. Environ.*, **42(7)**, 1593–1606. 120
- HAIH, J.D. (2003). The effects of solar variability on the Earth's climate. *Philos. Trans. R. Soc. London*, **A 361**, 95–111. 114

REFERENCES

- HALES, T.C. (2007). Jordans Proof of the Jordan Curve Theorem. *Studies in logic, grammar and rhetoric*, **10** (23). 62
- HALEY, C.S., BROHEDE, S.M., SIORIS, C.E., GRIFFIOEN, E., MURTAGH, D.P., MCDADE, I.C., ERIKSSON, P., LLEWELLYN, E.J., BAZUREAU, A. & GOUTAIL, F. (2004). Retrieval of stratospheric O₃ and NO₂ profiles from Odin Optical Spectrograph and Infrared Imager System (OSIRIS) Limb-Scattered Sunlight Measurements. *J. Geophys. Res.*, **109**, D16303. 53
- HARTLEY, W.N. (1880). On the Probable Absorption of the Solar Ray by Atmospheric Ozone. *Chem. News*, **26**, 268. 12
- HASTENRATH, S. (1977). On the upper-air circulation over the equatorial Americas. *Arch. Meteor. Geophys. Bioklimatol.*, **309 - 321**. 93
- HAYNES, P.H., MCINTYRE, M.E., SHEPHERD, T.G., MARKS, C.J. & SHINE, K.P. (1994). On the downward control of extratropical diabatic circulations by eddy-induced mean zonal forces. *J. Atmos. Sci.*, **48**, 651–680. 35, 38
- HAYNES, P.H., SCINOCCHA, J. & GREENSLADE, M. (2001). Formation and maintenance of the extratropical tropopause by baroclinic eddies. *J. Geophys. Res. (Atmos.)*, **4179-4182**. 41
- HEATH, D.F., KRUEGER, A.J., ROEDER, H.R. & HENDERSON, B.D. (1975). The solar backscatter ultraviolet and total ozone mapping spectrometer (SBUV/TOMS) for Nimbus G. *Optical Engineering*, **14**(4), 323–331. 16
- HECK, W.W., TAYLOR, O.C., ADAMS, R., BINGHAM, G., MILLER, J., PRESTON, E. & WEINSTEIN, L. (1982). Assessment of crop loss from ozone. *J. Air Pollut. Control Assoc.*, **32**, 353361. 2
- HELD, I.M. (1982). On the height of the tropopause and the static stability of the troposphere. *J. Atmos. Sci.*, **39**, 412–417. 42
- HELD, I.M. & B. J. HOSKINS, B.J. (1985). Large-scale eddies and the general circulation of the troposphere. *Adv. Geophys.*, **28A**, 3–31. 35
- HERMAN, J.R. & CELARIER, E.A. (1997). Earth surface reflectivity climatology at 340–380 nm from TOMS data. *J. Geophys. Res.*, **102**, 28003–28011. 57
- HESS, P.G. & ZBINDEN, R. (2013). Stratospheric impact on tropospheric ozone variability and trends: 1990–2009. *Atmos. Chem. Phys.*, **13**, 649–674. 82

- HEWITT, C.N. (1999). *Reactive Hydrocarbons in the Atmosphere*, Edited by: C. Nicholas Hewitt. Elsevier inc., New York. 22
- HIGHWOOD, E.J., HOSKINS, B.J. & BERRISFORD, P. (2000). Properties of the Arctic tropopause. *Quart. J. Roy. Meteor. Soc.*, **126**, 1515–1532. 42, 45
- HILBOLL, A., RICHTER, A., ROZANOV, A., HODNEBROG, O., HECKEL, A., SOLBERG, S., STORDAL, F. & BURROWS, J.P. (2013). Improvements to the retrieval of tropospheric NO₂ from satellite stratospheric correction using SCIAMACHY limb/nadir matching and comparison to Oslo CTM2 simulations. *Atmos. Meas. Tech.*, **6**, 565–584. 61
- HILSENATH, E., CEBULA, R.P., DELAND, M.T., LAAMANN, K., TAYLOR, S., WELLEMAYER, C. & BHARTIA, P.K. (1995). Calibration of the NOAA-11 Solar Backscatter Ultraviolet (SBUV/2) Ozone Data Set from 1989 to 1993 using In-Flight Calibration Data and SSBUV. *J. Geophys. Res.*, **100**, 1351–1366. 16
- HINTSA, E.J., BOERING, K.A., WEINSTOCK, E.M., ANDERSON, J.G., GARY, B.L., PFISTER, L., DAUBE, B.C., WOFSY, S.C., LOEWENSTEIN, M., PODOLSKE, J.R., MARGITAN, J.J. & BUI, T.P. (1998). Troposphere-stratosphere transport in the lowermost stratosphere from measurements H₂O, CO₂, N₂O and O₃. *Geophys. Res. Lett.*, **25**, 2655–2658. xvii, 33, 37
- HOELL, J.M., DAVIS, D.D., LIU, S.C., NEWELL, R., SHIPHAM, M., AKIMOTO, H., MCNEAL, R.J., BENDURA, R.J. & DREWRY, J.W. (1996). Pacific Exploratory Mission-West A (PEM-West A): September-October 1991. *J. Geophys. Res.*, **101(D1)**, 1641–1653. 128
- HOERLING, M.P., SCHAACK, T.K. & LENZEN, A.J. (1991). Global objective tropopause analysis. *Mon. Wea. Rev.*, **119**, 1816–1831. 45
- HOGREFE, C., LYNN, B., CIVEROLO, K., KU, J.Y., ROSENTHAL, J., ROSENZWEIG, A., GOLDBERG, R., GAFFIN, S., KNOWLTON, K. & KINNEY, P.L. (2004). Simulating changes in regional air pollution over the eastern United States due to changes in global and regional climate and emissions. *J. Geophys. Res.*, **109**, D22301. 21
- HOGREFE, C., HAO, W., ZALEWSKY, E.E., KU, J.Y., LYNN, B., ROSENZWEIG, C., SCHULTZ, M.G., RAST, S., NEWCHURCH, M.J., WANG, L., KINNEY, P.L. & SISTLA, G. (2011). An analysis of long-term regional-scale ozone simulations over the northeastern United States: variability and trends. *Atmos. Chem. Phys.*, **11**, 567–582. 127
- HOINKA, K.P. (1997). The tropopause: Discovery, definition and demarcation. *Meteorol. Z.*, **6 (6)**, 281–303. 41

REFERENCES

- HOINKA, K.P. (1998). Statistics of the global tropopause pressure. *Mon. Wea. Rev.*, **16**, 3303–3325. 41
- HOLTON, J.R., HAYNES, P.H., MCINTYRE, M.E., DOUGLASS, A.R., ROOD, R.B. & PFISTER, L. (1995). Stratosphere–troposphere exchange. *Rev. Geophys.*, **33**, 403–439. xvii, 29, 31, 32, 33, 34, 35, 36, 41, 44, 46
- HOOGEN, R., ROZANOV, V.V., BRAMSTEDT, K., EICHMANN, K., WEBER, M., DEBEEK, R., BUCHWITZ, M. & BURROWS, J.P. (1998). Height resolved ozone information from GOME data. *Earth Observation Quarterly*, **58**, 9–10. 60
- HOOGEN, R., ROZANOV, V.V. & BURROWS, J.P. (1999). Ozone profiles from GOME satellite data: algorithm description and first validation. *J. Geophys. Res.*, **14**, 7, 8263–8280. 60
- HOOR, P., GURK, C., BRUNNER, D., HEGGLIN, M.I., WERNLI, H. & FISCHER, H. (2004). Seasonality and extent of extratropical TST derived from insitu CO measurements during SPURT. *Atmos. Chem. Phys.*, **4**, 1427–1442. 36
- HOSKINS, B.J. (1991). Towards a PV- θ view of the general circulation. *Tellus*, **43B**, 27–35. 33, 34, 46
- HOSKINS, B.J., MCINTYRE, M.E. & ROBERTSON, A.W. (1985). On the use and significance of isentropic potential vorticity maps. *Quart. J. Roy. Meteorol. Soc.*, **111**, 887–946. 33, 37
- HOUGH, A.M. & DERWENT, R.G. (1990). Changes in the global concentration of tropospheric ozone due to human activities. *Nature*, **344**, 645–648. 110
- HSU, J. & PRATHER, M.J. (2009). Stratospheric variability and tropospheric ozone. *J. Geophys. Res.*, **114**, D06102. 21, 114
- HTAP (2010). Hemispheric Transport of Air Pollution 2010, Part A: Ozone and Particulate Matter; Air Pollution Studies No. 17, edited by F. Dentener, T. Keating, and H. Akimoto. *United Nations, New York and Geneva*. 82
- IPCC, . (2007). IPCC: Summary for policymakers, in Climate Change 2007: The Physical Science Basis. Contribution of Working Group I to the Fourth Assessment Report of the Intergovernmental Panel on Climate Change [Solomon, S., Qin, D., Manning, M., Chen, Z., Marquis, M., Averyt, K. B., Tignor, M., and Miller, H. L.]. *Geneva, Switzerland*, **2**, 53–57. 1, 26

- IPCC, . (2013). *IPCC, 2013: Climate Change 2013: The Physical Science Basis. Contribution of Working Group I to the Fifth Assessment Report of the Intergovernmental Panel on Climate Change* [Stocker, T. F., Qin, D., Plattner, G.- K., Tignor, M., Allen, S. K., Boschung, J., Nauels, A., Xia, Y., Bex V. and Midgley, P. M., (eds.)]. Cambridge University Press, Cambridge, United Kingdom and New York, NY, USA. 2, 26
- ITO, K., DE LEON, S.F. & LIPPMANN, M. (2005). Associations between ozone and daily mortality: analysis and meta-analysis. *Epidemiology*, **16**, 446–457. 2
- JACOB, D.J. & WINNER, D.A. (2009). Effect of climate change on air quality. *Atmos. Environ.*, **43**, 51 – 63. 128
- JACOB, D.J., HOROWITZ, L.W., MUNGER, J.W., HEIKES, B.G., DICKERSON, R.R., ARTZ, R.S. & KEENE, W.C. (1995). Seasonal transition from NO_x - to hydrocarbon-limited conditions for ozone production over the eastern United States in September. *J. Geophys. Res.*, **100(D5)**, 9315–9324. 118
- JACOB, D.J., LOGAN, J.A. & MURTI, P.P. (1999). Effect of rising Asian emissions on surface ozone in the United States. *Geophys. Res. Lett.*, **26**, 2175–2178. 1, 21
- JACOB, D.J., FIELD, B.D., JIN, E.M., BEY, I., LI, Q., LOGAN, J.A., YANTOSCA, R.M. & SINGH, H.B. (2002). Atmospheric budget of acetone. *J. Geophys. Res.*, **44100**, 107(D10). 83
- JACOBI, P., SEGURA, D.B. & KJELLEN, M. (1999). Governmental responses to air pollution: summary of a study of the implementation of rodízio in São Paulo. *Environ. and Urbanization*, **11 (1)**, 79 – 88. 122
- JAFFE, D.A. (1991). *Local sources of pollution in the Arctic from Prudhoe Bay to the Taz Peninsula*. In: Sturges, W.T. (Ed.), *Arctic Ozone Chemistry, in Pollution of the Arctic Atmosphere*. Elevesier, Essex, England. 83
- JAFFE, D.A., ANDERSON, T., COVERT, D., KOTCHENRUTHER, R., TROST, B., DANIELSON, J., SIMPSON, W., BERTSEN, T., KARLSDOTTIR, S., BLAKE, D., HARRIS, J., CARMICHAEL, G. & UNO, I. (1999). Transport of Asian air pollution to North America. *Geophys. Res. Lett.*, **26**, 711–714. 82
- JAMES, P., STOHL, A., FORSTER, C., ECKHARDT, S., SEIBERT, P. & FRANK, A. (2003). A 15-year climatology of stratosphere-troposphere exchange with a Lagrangian particle dispersion model - 2. Mean climate and seasonal variability. *J. Geophys. Res.*, **108 (D12)**, 8522. 86

REFERENCES

- JENKINS, G.S. & RYU, J.H. (2004). Linking horizontal and vertical transports of biomass fire emissions to the tropical Atlantic ozone paradox during the Northern Hemisphere winter season: climatology. *Atmos. Chem. Phys.*, **4**(2), 449–469. 84
- JOHNSON, B.J., OLTMANS, S.J., VÖMEL, H., SMIT, H.G.J., DESHLER, T. & KÖGER, C. (2002). Electrochemical concentration cell (ECC) ozone sonde pump efficiency measurements and tests on the sensitivity to ozone of buffered and unbuffered ECC sensor cathode solutions. *J. Geophys. Res.*, **107**, 4393. 68
- JOHNSTON, H. (1971). Reduction of stratospheric ozone by nitrogen oxide catalysts from supersonic transport exhaust. *Science*, **173**, 517–522. 31
- JORDAN, C. (1887). *Cours D'Analyse de l'Ecole Polytechnique*. Paris, Gauthier-Villars et fils. 62
- JOURDAIN, L., WORDEN, H.M., BOWMAN, K., LI, Q.B., ELDERING, A., KULAWIK, S.S., OSTERMAN, G., BOERSMA, K.F., FISHER, B., RINSLAND, C.P., BEER, R. & GUNSON, M. (2007). Tropospheric vertical distribution of tropical Atlantic ozone observed by TES during the northern African biomass burning season. *Geophys. Res. Lett.*, **34**, L04810. 65
- KALABOKAS, P.D., VIRAS, L.G., BARTZIS, J. & REPAPIS, C.C. (2000). Mediterranean rural ozone characteristics around the urban area of Athens. *Atmos. Environ.*, **34**, 5199–5208. 1, 2
- KANE, R.P. & TRIVEDI, N.B. (1986). Effects of linear trend and mean value on maximum entropy spectral analysis. *Proc. Indian Acad. Sci. (Earth Planet. Sci.)*, **95** (2), 201–208. 114
- KAYNAK, B., HU, Y., MARTIN, R.V., RUSSELL, A.G., CHOI, Y. & WANG, Y. (2008). The effect of lightning NO_x production on surface ozone in the continental United States. *Atmos. Chem. Phys.*, **8**, 5151–5159. 21
- KIM, J.H. & NEWCHURCH, M.J. (1996). Climatology and trends of tropospheric ozone over the eastern Pacific Ocean: The influences of biomass burning and tropospheric dynamics. *Geophys. Res. Lett.*, **23**, 3723–3726. 81, 106
- KIM, J.H., NEWCHURCH, M.J. & HAN, K. (2001). Distribution of tropical tropospheric ozone determined directly from TOMS measurements. *J. Atmos. Sci.*, **58**, 2699–2708. 60
- KLEINMAN, L.I., DAUM, P.H., IMRE, D.G., LEE, J.H., LEE, Y.N., NUNNERMACKER, L.J., SPRINGSTON, S.R., WEINSTEIN-LLOYD, J. & NEWMAN, L. (2000). Ozone production in the New York City urban plume. *J. Geophys. Res.*, **105**(D11), 14495–14511. 110, 118

- KLEY, D., SMIT, H.G.J., VÓMEL, H., GRASSL, H., RAMANATHAN, V., CRUTZEN, P.J., WILLIAMS, S., J., M. & OLTMANS, S. (1997). Tropospheric water vapour and ozone cross-sections in a zonal plane over the central equatorial Pacific. *Q. J. R. Meteorol.Soc.*, **123**, 2009 – 2040. 85, 128
- KLONECKI, A. & LEVY II, H. (1997). Tropospheric chemical ozone tendencies in CO-CH₄-NO_y-H₂O system: Their sensitivity to variations in environmental parameters and their application to a global chemistry transport model study. *J. Geophys. Res.*, **102(D17)**, 21221–21237. 110
- KOBAYASHI, J. & TOYAMA, Y. (1966). On various methods of measuring the vertical distribution of atmospheric ozone (III) - Carbon iodine type chemical ozonesonde. *Pap. Met. Geophys.*, **17**, 113–126. 14, 67
- KOELEMEIJER, R.B.A., STAMMES, P., HOVENIER, J.W. & DE HAAN, J.F. (2001). A fast method for retrieval of cloud parameters using oxygen A-band measurements from the Global Ozone Monitoring Experiment. *J. Geophys. Res.*, **106**, 3475–3496. 56
- KOKHANOVSKY, A.A. & ROZANOV, V.V. (2004). The physical parameterization of the top-of-atmosphere reflection function for a cloudy atmosphere-underlying surface system: the oxygen A-band case study. *J. Quant. Spectrosc. Radiat. Transfer.*, **85**, 35–55. 58
- KOMHYR, W.D. (1967). Nonreactive gas sampling pump. *Rev. Sci. Instrum.*, **38**, 981–983. 13
- KOMHYR, W.D. (1969). Electrochemical concentration cells for gas analysis. *Ann. Geoph.*, **25**, 203–210. xvii, 14, 66
- KOMHYR, W.D. (1986). *Operations handbook—Ozone measurements to 40-km altitude with model 4A electrochemical concentration cell (ECC) ozonesondes (used with 1680 MHz radiosondes)*. Air Resour. Lab., Boulder, Colo. 67
- KOMHYR, W.D. & HARRIS, T.B. (1971). *Development of an ECC-Ozonesonde*. Boulder, Colo. : U.S. Dept. of Commerce, NOAA Techn. Rep. ERL 200-APCL 18ARL-149. 14
- KOMHYR, W.D., BARNES, R.A., BROTHERS, G.B., LATHROP, J.A. & OPPERMAN, D.P. (1995a). Electrochemical concentration cell ozonesonde performance evaluation during STOIC 1989. *J. Geophys. Res.*, **100**, 9231–9244. 67, 68
- KRIEGER, F.J. (1958). *Behind the Sputniks*, vol. 6. Washington, DC: Public Affairs Press. 15

REFERENCES

- KULAWIK, S.S., WORDEN, J. & ELDERING, E.A., A. (2006). Implementation of cloud retrievals for Tropospheric Emission Spectrometer (TES) atmospheric retrievals: 1. Description and characterisation of errors on trace gas retrievals. *J. Geophys. Res.*, **111**, D24204. 66
- LABITZKE, K. & VAN LOON, H. (1995). Connection between the troposphere and the stratosphere on a decadal scale. *Tellus*, **47A**, 275–286. 114
- LADSTÄTTER-WEISSENMAYER, A., MEYER-ARNEK, J., SCHLEMM, A. & BURROWS, J.P. (2004). Influence of stratospheric airmasses on tropospheric vertical O₃ columns based on GOME (Global Ozone Monitoring Experiment) measurements and backtrajectory calculation over the Pacific. *Atmos. Chem. Phys.*, **4**, 903–909. 3, 60
- LAL, D.M., GHUDE, S.D., PATIL, S.D., KULKARNI, S.H., JENA, C., TIWARI, S. & SRIVASTAVA, M.K. (2012). Tropospheric ozone and aerosol long-term trends over the Indo-Gangetic Plain (IGP), India. *Atmos. Res.*, **116**, 82 – 92. 126
- LAMARQUE, J.F., LANGFORD, A.O. & PROFITT, M.H. (1996). Crosstropopause mixing of ozone through gravity wave breaking: Observation and modeling. *J. Geophys. Res.*, **101(D17)**, 22969–22976. 36
- LAMARQUE, J.F., BOND, T.C., EYRING, V., GRANIER, C. *et al.* (2010). Historical (1850-2000) gridded anthropogenic and biomass burning emissions of reactive gases and aerosols: methodology and application. *Atmos. Chem. Phys.*, **10(15)**, 7017–7039. 81
- LAW, K.S., FIERLI, F., CAIRO, F., SCHLAGER, H., BORRMANN, S., STREIBEL, M., REAL, E., KUNKEL, D., SCHILLER, C., RAVEGNANI, F., ULANOVSKY, A., D'AMATO, F., VICIANI, S. & VOLK, C.M. (2010). Air mass origins influencing TTL chemical composition over West Africa during 2006 summer monsoon. *Atmos. Chem. Phys.*, **10**, 10753–10770. 82
- LEAN, J., ROTTMAN, G., KYLE, H.L., WOODS, T.N., HICKEY, J.R. & PUGA, L.C. (1997). Detection and parameterization of variations in solar mid-and near-ultraviolet radiation (200-400 nm). *Geophys. Res. Lett.*, **102**, 29939–29956. 114
- LEEDS, A.R. (1880). Lines of Discovery in the History of Ozone. *Annals of the New York Academy of Sciences*, **1 (3)**, 363–391. 12
- LELIEVELD, J., VAN AARDENNE, J., FISCHER, H., DE REUS, M., WILLIAMS, J. & WINKLER, P. (2004). Increasing ozone over the Atlantic Ocean. *Science*, **304**, 1483 – 1487. 128

- LELIEVELD, J.A. *et al.* (2002). Global air pollution crossroads over the Mediterranean. *Science*, **298**(5594), 794 – 799. 103
- LEMIEUX, P.M., LUTES, C.C. & SANTOIANNI, D.A. (2004). Emissions of organic air toxics from open burning: a comprehensive review. *Progress in Energy and Combustion. Science*, **30**, 1–32. 22
- LEUE, C., WENIG, M., WAGNER, T., PLATT, U. & JÄHNE, B. (2001). Quantitative analysis of NO_x emissions from GOME satellite image sequences. *J. Geophys. Res.*, **106**, 5493–5505. 60
- LEVELT, P.F., VAN DEN OORD, G.H.J., DOBBER, M.R., MÄLKKI, A., VISSER, H., DE VRIES, J., STAMMES, P., LUNDELL, J. & SAARI, H. (2006). The Ozone Monitoring Instrument (OMI). *IEEE T. Geosci. Remote*, **44**(5), 1093–1101. 16, 20
- LEVY, H.I. (1971). Normal atmosphere: Large radical and formaldehyde concentrations predicted. *Science*, **173**, 141–143. 2, 32
- LEVY, I.H. & MOXIM, W.J. (1989). Influence of long-range transport of combustion emissions on the chemical variability of the background atmosphere. *Nature*, **338**, 326 – 328. 128
- LEVY, I.H., MAHLMAN, J.D. & MOXIM, W.J. (1980). A stratospheric source of reactive nitrogen in the unpolluted troposphere. *Geophys. Res. Lett.*, **7**(9), 441–444. 32, 33
- LI, F., AUSTIN, J. & J., W.R. (2008). The strength of the BrewerDobson circulation in a changing climate: Coupled chemistryclimate model simulations. *Atmos. Chem. Phys.*, **21**, 40–57. 35
- LI, F., STOLARSKI, R.S. & NEWMAN, P.A. (2009). Stratospheric ozone in the post-CFC era. *Atmos. Chem. Phys.*, **9**, 2207–2213. 35
- LIN, C.Y., JACOB, D., MUNGER, J. & FIORE, A. (2000). Increasing background ozone in surface air over the United States. *Geophys. Res. Lett.*, **27**, 3465–3468. 32
- LINDZEN, R.S. (1993). Baroclinic neutrality and the tropopause. *J. Atmos. Sci.*, **50**, 1148–1151. 42
- LIPPMANN, M. (1989). Health effects of ozone: a critical review. *J. Air Pollut. Contr. Assoc.*, **39**, 672–695. 1
- LIU, C., PENNING DE VRIES, M., BEIRLE, S., HOOR, P., MARBACH, T., FRANKENBERG, C., PLATT, U. & WAGNER, T. (2008). Relationship between ATSR fire counts and CO vertical column densities retrieved from SCIAMACHY onboard ENVISAT, Remote Sens. of Fire. *Sc. and App., Proc. of SPIE*, **7089**, 70890I. 82

REFERENCES

- LIU, H., JACOB, D.J., CHAN, L.Y., OLTMANS, S.J., BEY, I., YANTOSCA, R.M., HARRIS, J.M., DUNCAN, B.N. & MARTIN, R.V. (2002). Sources of tropospheric ozone along the Asian Pacific Rim: An analysis of ozonesonde observations. *J. Geophys. Res.*, **107(D21)**, 4573. 82, 86, 88, 130
- LIU, S., TRAINER, M., FEHSENFELD, F., PARRISH, D., WILLIAMS, E., FAHEY, D., HUBLER, G. & MURPHY, P. (1987). Ozone production in the rural troposphere and the implication for regional and global ozone distributions. *J. Geophys. Res.*, **92**, 4191–4207. 110
- LIU, X., CHANCE, K., SIORIS, C.E., KUROSU, T.P., SPURR, R.J.D., MARTIN, R.V., FU, T.M., LOGAN, J.A., JACOB, D.J., PALMER, P.I., NEWCHURCH, M.J., MEGRETSKAIA, I.A. & CHATFIELD, R. (2006). First directly retrieved global distribution of tropospheric column ozone from GOME: Comparison with the GEOS-CHEM model. *J. Geophys. Res.*, **111**, D02308. 60
- LIU, X., BHARTIA, P.K., CHANCE, K., SPURR, R.J.D. & KUROSU, T.P. (2010). Ozone profile retrievals from the Ozone Monitoring Instrument. *Atmos. Chem. Phys.*, **10**, 2521–2537. 60
- LIVESEY, N.J., READ, W.G., FROIDEVAUX, L., LAMBERT, A., MANNEY, G.L., PUMPHREY, H.C., SANTEE, M.L., SCHWARTZ, M.J., WANG, S., COFIELD, R.E., CUDDY, D.T., FULLER, R.A., JARNOT, R.F., JIANG, J.H., KNOSP, B.W., STEK, P.C., WAGNER, P.A. & WU, D.L. (2011). EOS MLS Version 3.3 Level 2 data quality and description document. *Tech. rep., Jet Propulsion Laboratory*. 66
- LLEWELLYN, E., LLOYD, N.D., DEGENSTEIN, D.A., GATTINGER, R.L., PETELINA, S.V., BOURASSA, A.E., WIENSZ, J.T., IVANOV, E.V., MCDADE, I.C., SOLHEIM, B.H., MCCONNELL, J.C., HALEY, C.S., VON SAVIGNY, C., SIORIS, C.E., MCLINDEN, C.A., GRIFFOEN, E., KAMINSKI, J., EVANS, W.F.J., PUCKRIN, E., STRONG, K., WEHRLE, V., HUM, R.H., KENDALL, D.J.W., MATSUSHITA, J., MURTAGH, D.P., BROHEDE, S., STEGMAN, J., WITT, G., BARNES, G., PAYNE, W.F., PICHE, L., SMITH, K., WARSHAW, G., DESLAUNIERS, D.L., MARCHAND, P., RICHARDSON, E.H., KING, R.A., WEVERS, I., MCCREATH, W., KYRÖLÄ, E., OIKARINEN, L., LEPPELMEIER, G.W., AUVINEN, H., MEGIE, G., HAUCHECORNE, A., LEFEVRE, F., DE LA NOË, J., RICAUD, P., FRISK, U., SJOBERG, F., VON SCHEELE, F. & NORDH, L. (2004). The OSIRIS instrument on the Odin spacecraft. *Can. J. Phys.*, **82**, 411–422. 15
- LOGAN, J.A. (1985). Tropospheric ozone: Seasonal behaviour, trends and anthropogenic influence. *J. Geophys. Res.*, **90**, 10463–10482. 103, 110

- LOGAN, J.A. (1989). Ozone in rural areas of the United States. *J. Geophys. Res.*, **94 (D6)**, 8511–8532. 110
- LOGAN, J.A. & KIRCHHOFF, V.W.J.H. (1986). Seasonal variations of tropospheric ozone at Natal, Brazil. *J. Geophys. Res.*, **91(D7)**, 7875–7881. 82
- LOGAN, J.A., PRATHER, M.J., WOFSY, S.C. & MCELROY, M.B. (1981). Tropospheric chemistry: A global perspective. *J. Geophys. Res.*, **86**, 7210–7255. 2
- LOGAN, J.A. *et al.* (2012). Changes in ozone over Europe: Analysis of ozone measurements from sondes, regular aircraft (MOZAIC) and alpine surface sites. *J. Geophys. Res.*, **117, D09301**. 82, 115, 119, 122, 125, 127, 130
- LUCKE, R.L., KORWAN, D.R., BEVILACQUA, R.M., HORNSTEIN, J.S., SHETTLE, E.P., CHEN, D.T., DAEHLER, M., LUMPE, J.D., FROMM, M.D., DEBRESTIAN, D., NEFF, B., SQUIRE, M., KÖNIG-LANGLO, G. & DAVIES, J. (1999). The polar ozone and aerosol measurement (POAM) III instrument and early validation result. *J. Geophys. Res.*, **104(D15)**, 18785–18799. 15
- MADDOX, R.A. (1980). Mesoscale convective complexes. *Bull. Amer. Meteor. Soc.*, **61**, 1374–1387. 37
- MAHLMANN, J.D. (1997). Dynamics of transport processes in the upper troposphere. *Science*, **276 (5315)**, 1079–1083. 37
- MARENCO, A., GOUGET, H., NEDELEC, P., P., P.J. & KARCHER, F. (1994). Evidence of a long-term increase in tropospheric ozone from Pic du Midi data series: Consequences: Positive radiative forcing. *J. Geophys. Res.*, **99(D8)**, 16,617–16,632. 29
- MARTIN, R.V. *et al.* (2002). Interpretation of TOMS observations of tropical tropospheric ozone with a global model and in situ observations. *J. Geophys. Res.*, **107(D18)**, 4351. 101, 106
- MATEER, C.L., HEATH, D.F. & KRUEGER, A.J. (1971). Estimation of total ozone from satellite measurements of backscattered ultraviolet earth radiance. *J. Atmos. Sc.*, **28**, 1307–1311. 16
- MATTHEWS, E. (1983). Global vegetation and land use: new high resolution data bases for climate studies. *J. Appl. Meteorol.*, **22**, 474–487. 55
- MAZZEO, N.A., PINEDA ROJAS, A.L.Y. & VENEGAS, L.E. (2010). Carbon monoxide emitted from the city of Buenos Aires and transported to neighbouring districts. *Lat. Am. appl. res.*, **40 (3)**, 267–273. 122

REFERENCES

- MCCORMICK, M.P., CHU, W.P., ZAWODNY, J.M., MAULDIN III, L.E. & MCMASTER, L.R. (1991). TStratospheric Aerosoland Gas ExperimentIII (SAGE III) aerosol and trace gas measurements for Earth observingsystem (EOS). *Proc. SPIE Int. Soc. Opt. Eng.*, **1491**, 125–141. 15
- MCPETERS, R.D., LABOW, G.J. & JOHNSON, B.J. (1997). A satellite-derived ozone climatology for balloonsonde estimation of total column ozone. *J. Geophys. Res.*, **102(D7)**, 8875–8885. 14
- MCPETERS, R.D., JANZ, S.J., HILSENATH, E., BROWN, T.L., FLITTNER, D.E. & HEATH, D.F. (2000). The retrieval of O₃ profiles from limb scatter measurements: Results from the Shuttle Ozone Limb Sounding Experiment. *Geophys. Res. Lett.*, **27**, 2597–2600. 15, 53
- MENARD, R.D. & FRITSCH, J.M. (1989). A Mesoscale Convective Complex-Generated Inertially Stable Warm Core Vortex. *Mon. Wea. Rev.*, **117,6**, 1237–1261. 37
- MIERUCH, S., WEBER, M., VON SAVIGNY, C., ROZANOV, A., BOVENSMANN, H., BURROWS, J.P., BERNATH, P.F., BOONE, C.D., FROIDEVAUX, L., GORDLEY, L.L., MLYNCZAK, M.G., RUSSELL III, J.M., THOMASON, L.W., WALKER, K.A. & AND ZAWODNY, J.M. (2012). Global and long-term comparison of SCIAMACHY limb ozone profiles with correlative satellite data (2002–2008). *Atmos. Meas. Tech.*, **5**, 771 – 788. 55
- MILFORD, J.B., RUSSELL, A.G. & MCRAE, G.J. (1989). A new approach to photochemical pollution control: implications of spatial patterns in pollutant responses to reductions in nitrogen oxides and reactive organic gas emissions. *Env. Sci. Tech.*, **23 (10)**, 1290–1301. 118, 119, 120
- MILFORD, J.B., GAO, D., SILLMAN, S., BLOSSEY, P. & RUSSEL, A. (1994). Total Reactive Nitrogen (NO_y) as an Indicator of the Sensitivity of Ozone to Reduction in Hydrocarbons and NO_x Emissions. *J. Geophys. Res.*, **99**, 3533 – 3542. 110, 118
- MOLINA, L.T., KOLB, C.E., DE FOY, B., LAMB, B.K., BRUNE, W.H., JIMENEZ, J.L., RAMOS-VILLEGAS, R., SARMIENTO, J., PARAMO-FIGUEROA, V.H., CARDENAS, B., GUTIERREZ-AVEDOY, V. & MOLINA, M.J. (2007). Air quality in North America’s most populous city – overview of the MCMA-2003 campaign. *Atmos. Chem. Phys.*, **7**, 2447–2473. 112
- MOLINA, M.J. & MOLINA, L.T. (2004). Megacities and atmospheric pollution. *J. Air Waste Manag. Assoc.*, **54**, 644–680. 118, 122
- MOXIM, W.J. & LEVY II, H. (2000). A model analysis of the tropical South Atlantic Ocean tropospheric ozone maximum: The interaction of transport and chemistry. *J. Geophys. Res.*, **105(D13)**, 17393 – 17415. 83, 88, 92, 128

- MUDWAY, I.S. & KELLY, F.J. (2000). Ozone and the lung: a sensitive issue. *Mol Aspects Med.*, **21**, 1–48. 2
- MUNRO, R., SIDDANS, R., REBURN, W.J. & KERRIDGE, B. (1998). Direct measurement of tropospheric ozone from space. *Nature*, **392**, 168–171. 60
- NAJA, M. & AKIMOTO, H. (2004). Contribution of regional pollution and long-range transport to the Asia-Pacific region: analysis of long-term ozonesonde data over Japan. *J. Geophys. Res.*, **109**, D21306. 125
- NAJA, M., AKIMOTO, H. & STAEHELIN, J. (2003). Ozone in background and photochemically aged air over central Europe: Analysis of long-term ozonesonde data from Hohenpeissenberg and Payerne. *J. Geophys. Res.*, **108**, 4063. 32
- NASSAR, R. *et al.* (2008). Validation of tropospheric emission spectrometer (TES) Nadir ozone profiles using ozonesonde measurements. *J. Geophys. Res.*, **113**, D15S17. 66, 100
- NATRAJ, V., LIU, X., KULAWIK, S.S., CHANCE, K., CHATFIELD, R., EDWARDS, D.P., ELDERING, A., FRANCIS, G., KUROSU, T., PICKERING, K., SPURR, R. & WORDEN, H. (2011). Multispectral sensitivity studies for the retrieval of tropospheric and lowermost tropospheric ozone from simulated clear sky GEO-CAPE measurements. *Atmos. Environ.*, **45**, 7151–7165. 60
- NEU, J.L., FLURY, T., MANNEY, G.L., SANTEE, M.L., LIVESEY, N.J. & WORDEN, J. (2014). Tropospheric ozone variations governed by changes in stratospheric circulation. *Nature Geosci.* 114
- NOVELLI, P.C., MASARIE, K.A. & LANG, P.M. (1998). Distributions and recent changes of carbon monoxide in the lower troposphere. *J. Geophys. Res.*, **103(D15)**, 19015–19033. 127
- OHARA, T., AKIMOTO, H., KUROKAWA, J., HORII, N., YAMAJI, K., YAN, X. & HAYASAKA, T. (2007). An Asian emission inventory of anthropogenic emission sources for the period 1980–2020. *Atmos. Chem. Phys.*, **7**, 4419–4444. 122
- OLIVIER, J.G.J., BOUWMAN, A.F., VENDER HOEK, K.W. & BERDOWSKI, J.J.M. (1998). Global air emission inventories for anthropogenic sources of NO_x, NH₃ and N₂O in 1990. *Env. poll.*, **102(S1)**, 135–148. 1
- OLSEN, M.A., DOUGLASS, A.R. & SCHOEBERL, M.R. (2002). Estimating downward cross-tropopause ozone flux using column ozone and potential vorticity. *J. Geophys. Res.*, **107(D22)**, 4636. 36

REFERENCES

- OLSEN, S.C., MCLINDEN, C.A. & PRATHER, M.J. (2001). Stratospheric N₂O-NO_y system: Testing uncertainties in a three-dimensional framework. *J. Geophys. Res.*, **106**, 28771–28784. 29
- OLSZYK, D.M., THOMPSON, C.R. & POE, M.P. (1988b). Crop loss assessment for California: modeling losses with different ozone standard scenarios. *Env. poll.*, **53**, 303–311. 2
- OLTMANS, S.J. (1981). Surface ozone measurements in clean air. *J. Geophys. Res.*, **86**, 1174–1180. 110
- OLTMANS, S.J., HOFMANN, L., HARRIS, J.M., KOMHYR, W.D. & KUNIYUKI, D. (1996a). Tropospheric ozone during Mauna Loa Observatory Photochemistry Experiment 2 compared to long-term measurements from surface and ozonesonde observations. *J. Geophys. Res.*, **101 (D9)**, 14569–14580. 1
- OLTMANS, S.J., LEVY II, H., HARRIS, J., MERRILL, J., MOODY, J., LATHROP, J., CUEVAS, E., TRAINER, M., Ø’NEILL, M., PROSPERO, J., VÖMEL, H. & JOHNSON, B. (1996b). Summer and spring ozone profiles over the North Atlantic from ozonesonde measurements. *J. Geophys. Res.*, **101**, 29179–29200. 86
- OLTMANS, S.J., LEFOHN, A.S., HARRIS, J.M., GALBALLY, I., SCHEEL, H.E., BODEKER, G., BRUNKE, E., CLAUDE, H., TARASICK, D.W., JOHNSON, B.J., SIMMONDS, P., SHADWICK, D., ANLAUF, K., HAYDEN, K., SCHMIDLIN, F., FUJIMOTO, T., AKAGI, K., MEYER, C., NICHOL, S., DAVIES, J., REDONDAS, A. & CUEVAS, E. (2006). Long-term changes in tropospheric ozone. *Atmos. Environ.*, **40**, 3156–3173. 1, 119, 123, 125
- OLTMANS, S.J. *et al.* (2004). Tropospheric ozone over the North Pacific from ozonesonde observations. *J. Geophys. Res.*, **109**, D15S01. 86, 125
- OMAN, L.D., WAUGH, D.W., PAWSON, S., STOLARSKI, R.S. & NEWMAN, P.A. (2009). On the influence of anthropogenic forcings on changes in the stratospheric mean age. *J. Geophys. Res.*, **114**, D03105. 35
- OMAN, L.D. *et al.* (2013). The ozone response to ENSO in Aura satellite measurements and a chemistry–climate simulation. *J. Geophys. Res. Atmos.*, **118**, 965–976. 113
- O’ROURKE, J. (1998). *Computational geometry in C*. Cambridge University Press New York, NY, USA. 63
- OSTERMAN, G., BOWMAN, K., ELDERING, A. *et al.* (2009). TES Level 2 Data User’s Guide, last access: 12 January 2010. *JPL*, **4**, D–38042. 65, 66

- OSTERMAN, G. *et al.* (2008). Validation of Tropospheric Emission Spectrometer (TES) Measurements of the Total, Stratospheric and Tropospheric Column Abundance of Ozone. *J. Geophys. Res.*, **113**, D15S16. 65, 100
- PAN, L.L., RANDEL, W.J., GARY, B.L., MAHONEY, M.J. & HINTSA, E.J. (2004). Definitions and sharpness of the extratropical tropopause: A trace gas perspective. *J. Geophys. Res.*, **109**, D23103. 42, 46
- PARRISH, D.D., LAW, K.S., STAEHELIN, J., DERWENT, R., COOPER, O.R., TANIMOTO, H., VOLZ-THOMAS, A., GILGE, S., SCHEEL, H.E., STEINBACHER, M. & CHAN, E. (2012). Long-term changes in lower tropospheric baseline ozone concentrations at northern mid-latitudes. *Atmos. Chem. Phys.*, **12**, **23**, 11485–11504. 82, 84, 85, 88, 122, 126, 127, 128, 130
- PASCOE, C.L., GRAY, L.J., CROOKS, S.A., JUCKES, M.N. & BALDWIN, M.P. (1948). The quasi-biennial oscillation: Analysis using ERA-40 data. *J. Geophys. Res.*, **110**, D08105. 113
- PFISTER, G.G., EMMONS, L.K., HESS, P.G., LAMARQUE, J.F., THOMPSON, A.M. & YORKS, J.E. (2008). Analysis of the Summer 2004 ozone budget over the United States using Intercontinental Transport Experiment Ozonesonde Network Study (IONS) observations and Model of Ozone and Related Tracers (MOZART-4) simulations. *J. Geophys. Res.*, **113**, D23306. 1, 85, 86, 107
- PIERCE, R.B. *et al.* (2009). Impacts of background ozone production on Houston and Dallas, Texas, air quality during the Second Texas Air Quality Study field mission. *J. Geophys. Res.*, **114**, D00F09. 21
- PIERCE, T., GERON, C., BENDER, L., DENNIS, R., TONNESEN, G. & GUENTHER, A. (1998). Influence of increased isoprene emissions on regional ozone modeling. *J. Geophys. Res.*, **103**(D19), 25611–25629. 22
- PLATT, U. (1985). *The origin of nitrous and nitric acid in the atmosphere*. W. Jaeschke, Springer Verlag. 24
- PLATT, U., LEBRAS, G., POULET, G., BURROWS, J.P. & MOORTGAT, G. (1990). Peroxy radicals from night-time reaction of NO₃ with organic compounds. *Nature*, **348**, 147–149. 24
- PLÖGER, F., KONOPKA, P., GÜNTHER, G., GROOSS, J.U. & MÜLLER, R. (2009). Impact of the vertical velocity scheme on modeling transport in the tropical tropopause layer. *J. Geophys. Res.*, **115**, D03301. 34

REFERENCES

- POULIDA, O., DICKERSON, R.R. & HEYMSFIELD, A. (1996). Stratospheretroposphere exchange in a midlatitude mesoscale convective complex. 1. observations. *J. Geophys. Res.*, **101**, 68236836. 34, 36, 38
- PRATHER, M.J. & REMSBERG, E.E. (1993). The atmospheric effects of stratospheric aircraft: Report of the 1992 models and measurements workshop, NASA reference publication 1292. *National Aeronautics and Space Administration, Washington, DC, USA*, **1–3**. 55
- PRICE, C., PENNER, J. & PRATHER, M. (1997). NO_x from lightning: 1. Global distribution based on lightning physics. *J. Geophys. Res.*, **102(D5)**, 5929–5941. 21
- PRICE, J.D. & VAUGHAN, G. (1992). Statistical studies of cut-off-low systems. *Annales Geophys.-Atm. Hydro. and Space Sc.*, **10 (1-2)**, 96102. 37
- PRICE, J.D. & VAUGHAN, G. (1993). The potential for stratosphere troposphere exchange in cut-off-low systems. *Quart. J. Roy. Meteorol. Soc.*, **119 (510)**, 343–365. 36, 37
- QUENEY, P. (1948). The problem of airflow over mountains: A summary of theoretical studies. *Bull. Amer. Meteor. Soc.*, **29**, 16–26. 38
- RAHPOE, N., VON SAVIGNY, C., WEBER, M., ROZANOV, A.V., BOVENSMANN, H. & BURROWS, J.P. (2013). Error budget analysis of SCIAMACHY limb ozone profile retrievals using the SCIATRAN model. *Atmos. Meas. Tech.*, **6**, 2825 – 2837. 70
- RAMANATHAN, V. & DICKINSON, R.E. (1979). The role of stratospheric ozone in the zonal and seasonal radiative energy balance of the Earth-troposphere system. *J. Atmos. Chem.*, **36**, 10841104. 2
- RAMASWAMY, V., SCHWARZKOPF, M.D. & SHINE, K.P. (1992). Radiative forcing of climate from halocarbon-induced global stratospheric ozone loss. *Nature*, **355**, 810–812. 32
- RAMASWAMY, V., CHANIN, M.L., ANGELL, J., BARNETT, J., SEIDEL, D., GELMAN, M., KECKHUT, P., KOSHLEKOV, Y., LABITZKE, K., LIN, J.J., O’NEILL, A., NASH, J., RANDEL, W., ROOD, R., SHINE, K., SHIOTANI, M. & SWINBANK, R. (2001). Stratospheric temperature trends: Observations and model simulations. *Rev. Geophys.*, **39**, 71–122. 2
- RANDEL, W. & THOMPSON, A. (2011). Interannual variability and trends in tropical ozone derived from SAGE II satellite data and SHADOZ ozonesondes. *J. Geophys. Res.*, **116**, D07303. 81

- RANDEL, W.J., WU, F. & GAFFEN, D.J. (2000). Interannual variability of the tropical tropopause derived from radiosonde data and NCEP reanalyse. *J. Geophys. Res.*, **105(D12)**, 15509–15524. 42
- RANDEL, W.J., WU, F., OLTMAS, S.J., ROSENLOF, K. & NEDOLUHA, G.E. (2004). Interannual changes of stratospheric water vapor and correlations with tropical tropopause temperatures. *J. Atmos. Sci.*, **61**, 2133–2148. 41
- RAO, T.N., ARVELIUS, J. & KIRKWOOD, S. (2008). Climatology of tropopause folds over a European Arctic station (Esrang). *J. Geophys. Res.*, **113, D00B03**. 36
- RAULT, D.F. (2005). Ozone profile retrieval from Stratospheric Aerosol and Gas Experiment (SAGE III) limb scatter measurements. *J. Geophys. Res. (Atmos.)*, **110**, D09309. 53
- RAY, E.A., MOORE, F.L., ELKINS, J.W., DUTTON, G.S., FAHEY, D.W., VÖMEL, H., OLTMANS, S.J. & ROSENLOF, K.H. (1999). Transport into the Northern Hemisphere lowermost stratosphere revealed by in situ measurements. *J. Geophys. Res.*, **104(D21)**, 26565–26580. 38
- REED, R.J. (1955). A study of a characteristic type of upper-level frontogenesis. *J. Meteor.*, **12**, 226237. 42
- REID, G.C. & GAGE, K.S. (1981). On the annual variation in the height of the tropical tropopause. *J. Atmos. Sci.*, **38**, 1928–1938. 42
- RODGERS, C.D. (2000). *Inverse methods for atmospheric sounding: Theory and practice*. World Scientific Publishing Co. Ltd, Singapore, F. W. Taylor ,ed, (university of Oxford). 65
- RODWELL, M.J. & HOSKINS, B.J. (1996). Monsoons and the dynamics of deserts. *Q.J.R. Meteorol. Soc.*, **122**, 1385–1404. 129
- ROELOFS, G.J. & LELIEVELD, J. (1997). Model study of the influence of cross-tropopause O₃ transports on tropospheric O₃ levels. *Tellus B.*, **49**, 38–55. 1, 21
- ROELOFS, G.J., KENTARCHOS, A.S., TRICKL, T., STOHL, A., COLLINS, W.J., CROWTHER, R.A., HAUGLUSTAINE, D., KLONECKI, A., LAW, K.S., LAWRENCE, M.G., VON KUHLMANN, R. & VAN WEELE, M. (2003). Intercomparison of tropospheric ozone models: ozone transports in a complex tropopause folding event. *J. Geophys. Res-A.*, **108D12**, (Art No. 8529). 29, 32
- ROGAL, M., HITCHMAN, M.H., BUKER, M.L., TRIPOLI, G.J., STAJNER, I. & HAYASHI, H. (2010). Modeling the effects of Southeast Asian monsoon outflow on subtropical anticyclones and midlatitude ozone over the Southern Indian Ocean. *J. Geophys. Res.*, **115**, D20101. 129

REFERENCES

- ROHEN, G.J., VON SAVIGNY, C., LLEWELLYN, E.J., KAISER, J.W., EICHMANN, K.U., BRACHER, A., BOVENSMANN, H. & BURROWS, J.P. (2006). First results of ozone profiles between 35 and 65 km retrieved from SCIAMACHY limb spectra and observations of ozone depletion during the solar proton events in October/November 2003. *Adv. Space Res.*, **37**, 2263–2268. 53, 54
- ROSCOE, H.K. (2004). Possible descent across the Tropopause in Antarctic winter. *Adv. Space Res.*, **33**, 1048–1052. 42
- ROTH, C.Z., DEGENSTEIN, D.A., BOURASSA, A.E. & LLEWELLYN, E.J. (2007). The retrieval of vertical profiles of ozone number density using Chappuis band absorption information and a multiplicative algebraic reconstruction technique. *Can. J. Phys.*, **85**, 1225–1243. 53
- ROWLAND, F.S. & MOLINA, M.J. (1975). Chlorofluoromethanes in the Environment. *Rev. Geophys. Space Phys.*, **13**, 1–15. 31
- ROZANOV, A., EICHMANN, K.U., VON SAVIGNY, C., BOVENSMANN, H., BURROWS, J.P., VON BARGEN, A., DOICU, A., HILGERS, S., GODIN-BEEKMANN, S., LEBLANC, T. & MCDERMID, I.S. (2007). Comparison of the inversion algorithms applied to the ozone vertical profile retrieval from SCIAMACHY limb measurements. *Atmos. Chem. Phys.*, **7**, 4763–4779. 53
- ROZANOV, V.V., KUROSU, T. & BURROWS, J.P. (1998). Retrieval of Atmospheric Constituents in the UV Visible: A New Quasi-Analytical Approach for the Calculation of Weighting Functions. *J. Quant. Spectrosc. Radiat. Transfer*, **60**, 277–299. 56
- RUSCH, D.W., MOUNT, G.H., BARTH, C.A., THOMAS, R.J. & CALLAN, M.T. (1984). Solar mesospheric explorer ultraviolet spectrometer: Measurements of ozone in the 1.0–0.1 mbar region. *J. Geophys. Res.*, **89**, 11677–11687. 15, 53
- RUSSELL III, J.M., GORDLEY, L.L., PARK, J.H., DRAYSON, S.R., HESKETH, W.D., CICERONE, R.J., TUCK, A.F., FREDERICK, J.E., HARRIES, J.E. & CRUTZEN, P.J. (1993). The Halogen Occultation Experiment. *J. Geophys. Res.*, **98**(D6), 10777–10797. 15
- SANKEY, D. & SHEPHERD, T.G. (2003). Correlations of longlived chemical species in a middle atmosphere general circulation model. *J. Geophys. Res.*, **108**. 35
- SANTER, B.D., WEHNER, M.F., WIGLEY, T.M.L., SAUSEN, R., MEEHL, G.A., TAYLOR, K.E., AMMANN, C., ARBLASTER, J., WASHINGTON, W.M., BOYLE, J.S. & BRÜGGEMANN, W. (2003a). Contributions of anthropogenic and natural forcing to recent tropopause height changes. *Science*, **301**(5632), 479–483. 51

- SANTER, B.D., SAUSEN, R., WIGLEY, T.M.L., BOYLE, J.S., ACHUTARAO, K., DOUTRIAUX, C., HANSEN, J.E., MEEHL, G.A., ROECKNER, E., RUEDY, R., SCHMIDT, G. & TAYLOR, K.E. (2003b). Behavior of tropopause height and atmospheric temperature in models, reanalyses, and observations: decadal changes. *J. Geophys. Res.*, **108(D1)**, 4002. 42
- SANTER, B.D., WIGLEY, T.M.L., SIMMONS, A.J., ALLBERG, G.A., UPPALA, A.M., AMMANN, C., BOYLE, J.S., BRÜGGEMANN, W., DOUTRIAUX, C., FIORINO, M., MEARS, C., MEEHL, G.A., SAUSEN, R., TAYLOR, K.E., WASHINGTON, W.M., WEHNER, M.F. & WENTZ, F.J. (2004). Identification of anthropogenic climate change using a second-generation reanalysis. *J. Geophys. Res.*, **109**, D21104. 42
- SAUSEN, R. & SANTER, B.D. (2003). Use of changes in tropopause height to detect human influences on climate. *Meteorol. Z.*, **12(3)**, 131–136. 51
- SAUVAGE, B., THOURET, V., CAMMAS, J.P., GUEUSI, F., ATHIER, G. & NÉDÉLEC, P. (2005). Tropospheric ozone over equatorial Africa: Regional aspects from the MOZAIC data. *Atmos. Chem. Phys.*, **5**, 311–335. 128
- SAUVAGE, B., THOURET, V., THOMPSON, A.M., WITTE, J.C., CAMMAS, J.P., NÉDÉLEC, P. & ATHIER, G. (2006). Enhanced view of the tropical Atlantic ozone paradox and zonal wave one from the in situ MOZAIC and SHADOZ data. *J. Geophys. Res.*, **111**, D01301. 128, 129
- SAUVAGE, B., GHEUSI, F., THOURET, V., CAMMAS, J.P., DURON, J., ESCOBAR, J., MARI, C., MASCART, P. & PONT, V. (2007). Medium-range mid-tropospheric transport of ozone and precursors over Africa: two numerical case studies in dry and wet seasons. *Atmos. Chem. Phys.*, **7**, 5357–5370. 128
- SAWYER, J.S. (1959). The introduction of the effects of topography into methods of numerical forecasting. *Quart. J. R. Met. Soc.*, **85**, 31–43. 38
- SCHEEL, H.E. (2003). *Ozone climatology studies for the Zugspitze and neighboring sites in the German Alps*. In: Lindskog, A. (Ed.), TOR-2 Final Report. EUROTRAC-2 ISS. GSF Research Center, Munich, Germany.
- SCHEEL, H.E., BRUNKE, E.G. & SEILER, W. (1990). Trace gas measurements at the monitoring station, Cape Point, South Africa between 1978 and 1988. *J. Atmos. Chem.*, **11**, 197–210. 110
- SCHNELL, R.C., OLTMANS, S.J., NEELY, R.R., ENDRES, M.S., MOLENAR, J.V. & WHITE, A.B. (2011). Rapid photochemical production of ozone at high concentrations in a rural site during winter. *Nat. Geosci.*, **2**, 120–122. 83

REFERENCES

- SCHOEBERL, M.R. *et al.* (2007). A trajectory based estimate of the tropospheric column ozone column using the residual method. *J. Geophys. Res.*, **112**, D24S49. 3, 59
- SCHÖNBEIN, C.F. (1858). On the Various Conditions of Oxygen. *Philos. Mag. IV*, **15**, 24–27. 12
- SCHULTZ, M.G. *et al.* (1999). On the origin of tropospheric ozone and NO_x over the tropical South Pacific. *J. Geophys. Res.*, **104**, 5829–5843. 128
- SEIDEL, D.J., ROSS, R.J., ANGELL, J.K. & REID, G.C. (2001). Climatological characteristics of the tropical tropopause as revealed by radiosondes. *J. Geophys. Res.*, **106**, 7857–7878. 44
- SELLITTO, P., BOJKOV, B.R., LIU, X., CHANCE, K. & DEL FRATE, F. (2011). Tropospheric ozone column retrieval from the Ozone Monitoring Instrument by means of neural networks algorithms. *Atmos. Meas. Tech.*, **4**, 2375 – 2388. 61
- SEO, K.H. & BOWMAN, K.P. (2001). A climatology of isentropic cross-tropopause exchange. *J. Geophys. Res.*, **106**, 28159–28172. 32, 35
- SEO, K.H. & BOWMAN, K.P. (2002). Lagrangian estimate of global stratosphere-troposphere mass exchange. *J. Geophys. Res.*, **107**, (D21),4555. 36
- SHAPIRO, M.A. (1978). Further evidence of the mesoscale and turbulent structure of upper level jet stream-frontal zone systems. *Mon. Weather Rev.*, **106**, 1100–1110. 42
- SHAPIRO, M.A. (1980). Turbulent mixing within tropopause folds as a mechanism for the exchange of chemical constituents between the stratosphere and the troposphere. *J. Atmos. Sci.*, **37**, 994–1004. 35, 36
- SHEEL, V., LAL, S., RICHTER, A. & BURROWS, J.P. (2010). Comparison of satellite observed tropospheric NO₂ over India with model simulations. *Atmos. Environ.*, **44**, 3314–3321. 122
- SHEPHERD, T.G. (2002). Issues in Stratosphere-troposphere Coupling. *J. Meteor.Soc. Japan.*, **80**, 769–792. 31
- SHEPHERD, T.G. (2007). Transport in the middle atmosphere. *J. Meteorol. Soc. Jpn.*, **85B**, 165–191. 32, 35
- SHINDELL, D.T., FALUVEGI, G., UNGER, N., AGUILAR, E., SCHMIDT, G.A., KOCH, D., BAUER, S.E. & MILLER, R.L. (2006b). Simulations of preindustrial, presentday, and 2100 conditions in the NASA GISS composition and climate model G-PUCCINI. *Atmos. Chem. Phys.*, **6**, 4427–4459. 29

- SIERK, B., RICHTER, A., ROZANOV, A., VON SAVIGNY, C., SCHMOLTNER, A.M., BUCHWITZ, M., BOVENSMANN, H. & BURROWS, J.P. (2006). Retrieval and Monitoring of Atmospheric Trace Gas Concentrations in Nadir and Limb Geometry using the Space-Borne SCIAMACHY Instrument. *Environmental Monitoring and Assessment*, **120**, 65–77. 61
- SILLMAN, S., LOGAN, J.A. & WOFSY, S.C. (1990). The sensitivity of ozone to nitrogen oxides and hydrocarbons in regional ozone episodes. *J. Geophys. Res.*, **95(D2)**, 1837–1851.
- SIMPSON, I.R., SHEPHERD, T.G. & SIGMOND, M. (2011). Dynamics of the lower stratospheric circulation response to ENSO. *J. Atmos. Sci.*, **68**, 2537–2556. 113, 114
- SINGER, S.F. & WENTWORTH, R.C. (1957). A method for the determination of the vertical ozone distribution from a satellite. *J. Geophys. Res.*, **62(2)**, 299–308. 15, 60
- SINGH, H.B., OHARA, D., HERLTH, D., SACHSE, W., BLAKE, D.R., BRADSHAW, J.D., KANAKIDOU, M. & CRUTZEN, P.J. (1994). Acetone in the atmosphere: distribution, sources, and sinks. *J. Geophys. Res.*, **99**, 18051819. 25, 29, 83
- SINGH, H.B., KANAKIDOU, M., CRUTZEN, P.J. & JACOB, D.J. (1995). High concentrations and photochemical fate of oxygenated hydrocarbons in the global atmosphere. *Nature*, **378**, 50–54. 25, 29
- SINGH, H.B., SALAS, L.J., CHATFIELD, R.B., CZECH, E., FRIED, A., WALEGA, J., EVANS, M.J., FIELD, B.D., JACOB, D.J., BLAKE, D., HEIKES, B., TALBOT, R., SACHSE, G., CRAWFORD, J.H., AVERY, M.A., SANDHOLM, S. & FUELBERG, H. (2004). Analysis of the atmospheric distribution, sources, and sinks of oxygenated volatile organic chemicals based on measurements over the Pacific during TRACE-P. *J. Geophys. Res.*, **109**, D15S07. 24
- SIORIS, C.E., KUROSU, T.P., MARTIN, R.V. & K., C. (2004). Stratospheric and tropospheric NO₂ observed by SCIAMACHY: First results. *Adv. in Space Res. Special issue: Trace Constituents in the Troposphere and Lower Stratosphere*, **34/4**, 780–785. 61
- SMIT, H.G.J. (2002). Ozonesondes, in *Encyclopedia of Atmospheric Sciences*, edited by J. Holton, J. Pyle, and J. Curry. *Academic Press, London.*, 1469–1476. xvii, 14, 15, 67
- SMIT, H.G.J. & STRAETER, W. (2004b). JOSIE-2000, Jülich Ozone Sonde Intercomparison Experiment 2000, The 2000 WMO international intercomparison of operating procedures for ECC-ozonesondes at the environmental simulation facility at Jülich. *WMO Global Atmos. Watch Rep.*, 158. 15

REFERENCES

- SMIT, H.G.J., STRAETER, W., JOHNSON, B.J., OLTMANS, S.J., DAVIES, J., TARASICK, D.W., HOEGGER, B., STUBI, R., SCHMIDLIN, F.J., NORTHAM, T., THOMPSON, A.M., WITTE, J.C., BOYD, I. & POSNY, F. (2007). Assessment of the performance of ECCozonesondes under quasiflight conditions in the environmental simulation chamber: Insights from the Juelich Ozone Sonde Intercomparison Experiment (JOSIE). *J. Geophys. Res.*, **112**, D19306. 15, 67
- SMIT, H.G.J. *et al.* (2011). Quality Assurance and Quality Control for Ozonesonde Measurements in GAW. *WMO Global Atmos. Watch Rep.*, **20**. xviii, 68, 69
- SNOW, M., WEBER, M., MACHOL, J., VIERECK, R. & RICHARD, E. (2014). Comparison of Magnesium II core-to-wing ratio observations during solar minimum 23/24. *J. Space Weather Space Clim.*, **4**, A04, 3695–3716. 114
- SOLOMON, S. (1999). Stratospheric ozone depletion: A review of concepts and history. *Rev. Geophys.*, **37**, 275–316. 35
- SOLOMON, S., GARCIA, R.R., ROWLAND, F.S. & WUEBBLES, D.J. (1986). On the depletion of Antarctic ozone. *Nature.*, **321**, 755–758. 31
- SOLOMON, S., SCHMELTEKOPF, A.L. & SANDERS, R.W. (1987). On the interpretation of zenith-sky absorption measurements. *Rev. Geophys.*, **92**, 8311–8319. 57
- SONKAEW, T., ROZANOV, V.V., VON SAVIGNY, C., ROZANOV, A., BOVENSMANN, H. & BURROWS, J.P. (2009). Cloud sensitivity studies for stratospheric and lower mesospheric ozone profile retrievals from measurements of limb-scattered solar radiation. *Atmos. Meas. Tech.*, **2**, 653–678. 53, 54
- SPRENGER, M., MASPOLI, M.C. & WERNLI, H. (2003). Tropopause folds and crosstropopause exchange: A global investigation based upon ECMWF analyses for the time period March 2000 to February 2001. *J. Geophys. Res.-Atm.*, **108** (D12). 35, 36, 46
- SPRENGER, M., WERNLI, H. & BOURQUI, M. (2007). Stratosphere Troposphere exchange and its relation to potential vorticity streamers and cutoffs near the extratropical tropopause. *J. Atmos. Sci.*, **64**, 15871604. 29, 36
- STAEHELIN, J., THUDIUM, J., BUEHLER, R., VOLZ-THOMAS, A. & GRABER, W. (1994). Trends in surface ozone concentrations at Arosa (Switzerland). *Atmos. Env.*, **28** (1), 75–87. 1
- STEVENSON, D.S. *et al.* (2006). Multimodel ensemble simulations of present-day and near-future tropospheric ozone. *J. Geophys. Res.*, **111**, D08301. 3, 82

- STEVENSON, D.S. *et al.* (2013). Tropospheric ozone changes, radiative forcing and attribution to emissions in the Atmospheric Chemistry and Climate Model Intercomparison Project (ACCMIP). *Atmos. Chem. Phys.*, **13**, 6, 3063–3085. 122, 126, 128
- STEWART, D.J., TAYLOR, C.M., REEVES, C.E. & MCQUAID, J.B. (2008). Biogenic nitrogen oxide emissions from soils: impact on NO_x and ozone over west Africa during AMMA (African Monsoon Multidisciplinary Analysis): observational study. *Atmos. Chem. Phys.*, **8**, 2285–2297. 21
- STILLER, G.P., VON CLARMANN, T., HAENEL, F., FUNKE, B., GLATTHOR, N., GRABOWSKI, U., KELLMANN, S., KIEFER, M., LINDEN, A., LOSSOW, S. & LÓPEZ-PUERTAS, M. (2012). Observed temporal evolution of global mean age of stratospheric air for the 2002 to 2010 period. *Atmos. Chem. Phys.*, **12**, 3311–3331. 113
- STOHL, A. & TRICKL, T. (1999). A textbook example of long-range transport: Simultaneous observation of ozone maxima of stratospheric and North American origin in the free troposphere over Europe. *J. Geophys. Res.*, **104**, 30445–30462. 37
- STOHL, A., JAMES, P., FORSTER, C., SPICHTINGER, N., MARENCO, A., THOURET, V. & SMIT, H.G.J. (2001). An extension of MOZAIC ozone climatologies using trajectory statistics. *J. Geophys. Res.*, **106**, 27757–27768. 37, 38
- STOHL, A., FORSTER, C., HUNTRIESER, H., MANNSTEIN, H., MCMILLAN, W.W., PETZOLD, A., SCHLAGER, H. & WEINZIERL, B. (2007). Aircraft measurements over Europe of an air pollution plume from South-east Asia – aerosol and chemical characterization. *Atmos. Chem. Phys.*, **7**, 913–937. 84, 85, 103, 111, 112
- STOHL, A. *et al.* (2003). Stratosphere-troposphere exchange: A review, and what we have learned from STACCATO. *J. Geophys. Res.*, **108(D12)**, 8516. 32, 46, 84, 85, 103
- STOLARSKI, R.S. & CICERONE, R.J. (1974). Stratospheric chlorine: A possible sink for ozone. *Can. J. Chem.*, **52**, 1610–1615. 31
- SUDO, K. & TAKAHASHI, M. (2001). Simulation of tropospheric ozone changes during 1997–1998 El Niño: Meteorological impact on tropospheric photochemistry. *Geophys. Res. Lett.*, **28(21)**, 4091 – 4094. 115, 122
- SUDO, K., TAKAHASHI, M. & AKIMOTO, H. (2003). Future changes in stratosphere-troposphere exchange and their impacts on future tropospheric ozone simulations. *Geophys. Res. Lett.*, **30(24)**, 2256. 32

REFERENCES

- TANG, Q. & PRATHER, M.J. (2012). Tropospheric column ozone: matching individual profiles from Aura OMI and TES with a chemistry-transport model. *Atmos. Chem. Phys.*, **12**, 10441–10452. 65
- TANG, Q., PRATHER, M.J. & HSU, J. (2011). Stratosphere-troposphere exchange ozone flux related to deep convection. *Geophys. Res. Lett.*, **38**, L03806. 81
- TARASICK, D.W., FIOLETOV, V.E., WARDLE, D.I., KERR, J.B. & DAVIES, J. (2005). Changes in the vertical distribution of ozone over Canada from ozonesondes: 1980–2001. *J. Geophys. Res.*, **110**, D02304. 82, 115
- TERAO, M., LOGAN, J., DOUGLASS, A. & STOLARSKI, R. (2008). Contribution of stratospheric ozone to the interannual variability of tropospheric ozone in the northern extratropics. *J. Geophys. Res.*, **113**, 4063. 32
- THOMPSON, A.M. & HUDSON, R.D. (1999). Tropical tropospheric ozone (TTO) maps from Nimbus 7 and Earth Probe TOMS by the modified-residual method: Evaluation with sondes, ENSO signals, and trends from Atlantic regional time series. *J. Geophys. Res.*, **104** (D21), 26961–26975. 3, 59
- THOMPSON, A.M., WITTE, J.C., HUDSON, R.D., GUO, H., HERMAN, J.R. & FUJIWARA, M. (2001). Tropical tropospheric ozone and biomass burning. *Science*, **291**, 2128 – 2132. 114
- THOMPSON, A.M., STONE, J.B., WITTE, J.C., MILLER, S.K., OLTMANS, S.J., KUCSERA, T.L., ROSS, K.L., PICKERING, K.E., MERRILL, J.T., FORBES, G., TARASICK, D.W., JOSEPH, E., SCHMIDLIN, F.J., McMILLAN, W.W., WARNER, J., HINTSA, E.J. & JOHNSON, J.E. (2007a). Intercontinental chemical transport experiment Ozonesonde Network Study (IONS) 2004: 2. Tropospheric ozone budgets and variability over northeastern North America. *J. Geophys. Res.*, **112**, D12S13. 85
- THOMPSON, A.M., STONE, J.B., WITTE, J.C., MILLER, S.K., PIERCE, R.B., CHATFIELD, R.B., OLTMANS, S.J., COOPER, O.R., LOUCKS, A.L., TAUBMAN, B.F., JOHNSON, B.J., JOSEPH, E., KUCSERA, T.L., MERRILL, J.T., MORRIS, G.A. & HERSEY, S. (2007b). Intercontinental chemical transport experiment Ozonesonde Network Study (IONS) 2004: 1. Summer-time upper troposphere/lower stratosphere ozone over northeastern North America. *J. Geophys. Res.*, **112**, D12S12. 1, 107
- THOMPSON, A.M., YORKS, J.E., MILLER, S.K., WITTE, J.C., MORRIS, G.A., BAUMGARDNER, D., LADINO, L. & RAPPENGLUECK, B. (2008). Tropospheric ozone sources and wave

- activity over Mexico City and Houston during Milagro/ Intercontinental Transport Experiment (INTEX]B) Ozonesonde Network Study, 2006 (IONS]06). *Atmos. Chem. Phys.*, **8**, 5113–5125. 85, 86
- THOMPSON, A.M. *et al.* (1996). Where did tropospheric ozone over southern Africa and the tropical Atlantic come from in October 1992? Insights from TOMS, GTE TRACE A and SAFARI 1992. *J. Geophys. Res.*, **101**, 24251–24278. 128
- THOMPSON, A.M. *et al.* (2000). A Tropical Atlantic Paradox: Shipboard and Satellite Views of a Tropospheric Ozone Maximum and Wave-one in January–February 1999. *Geophys. Res. Lett.*, **27**, 3317–3320. 83, 84, 93
- THOMPSON, A.M. *et al.* (2003). Southern Hemisphere Additional Ozonesondes (SHADOZ) 1998–2000 tropical ozone climatology: 1. Comparison with Total Ozone Mapping Spectrometer (TOMS) and ground-based measurements. *J. Geophys. Res.*, **108(D2)**, 8238. 67, 90, 100
- THOURET, V., CAMMAS, J.P., SAUVAGE, B., ATHIER, G., ZBINDEN, R., NÉDÉLEC, P., SIMON, P. & KARCHER, F. (2006). Tropopause referenced ozone climatology and inter-annual variability (1994–2003) from the MOZAIC programme. *Atmos. Chem. Phys.*, **6**, 1033–1051. 81
- TIAO, G.C., REINSEL, G.C., XU, D., PEDRICK, J.H., ZHU, X., MILLER, A.J., DELUISI, J.J., MATEER, C.L. & WUEBBLES, D.J. (1990). Effects of autocorrelation and temporal sampling schemes on estimates of trend and spatial correlation. *J. Geophys. Res.*, **95**, 20507–20517. 113
- TILMES, S., GARCIA, R.R., KINNISON, D.E., GETTELMAN, A. & RASCH, P.J. (2009). Impact of geoengineered aerosols on the troposphere and stratosphere. *J. Geophys. Res.*, **114**, D12305. 33
- TILMES, S., KINNISON, D.E., GARCIA, R.R., SALAWITCH, R., CANTY, T., LEE-TAYLOR, J., MADRONICH, S. & CHANCE, K. (2012). Impact of very short-lived halogens on stratospheric ozone abundance and UV radiation in a geo-engineered atmosphere. *Atmos. Chem. Phys.*, **12**, 10945–10955. 33
- TOOHEY, M. *et al.* (2013). Characterizing sampling biases in the trace gas climatologies of the SPARC Data Initiative. *J. Geophys. Res. Atmos.*, **118**, 11847 – 11862. 100
- TOUMI, R., BEKKI, S. & LAW, K.S. (1994). Indirect influence of ozone depletion on climate forcing by clouds. *Nature*, **372**, 348–351. 32

REFERENCES

- TVERBERG, H. (1980). A proof of the Jordan curve theorem. *Bulletin of the London Mathematical Society*, **12** (1), 34–38. 62
- USEPA (1986). Air quality criteria for ozone and other photochemical oxidants. *Office of Research and Development, Washington, DC, USA 20460, EPA 600-84/020dF*. 2
- VALKS, P., KOELEMMEIJER, R.B.A., VAN WEELE, M., VAN VELTHOVEN, P., FORTUIN, J.P.F. & KELDER, H. (2003). Variability in tropical tropospheric ozone: Analysis with Global Ozone Monitoring Experiment observations and a global model. *J. Geophys. Res.*, **108**(D11), 4328. 81, 119
- VAN HAVER, P., DE MUER, D., BEEKMANN, M. & MANCIER, C. (1996). Climatology of tropopause folds at midlatitudes. *Geophys. Res. Lett.*, **23** (9), 1033–1036. 36
- VARSHNEY, C. & AGGARWAL, M. (1992). Ozone pollution in the urban atmosphere of Delhi. *Atmos. Environ.*, **26**(3), 291–294. 112
- VAUGHAN, G. & PRICE, J.D. (1991). On the relation between total ozone and meteorology. *Q. J. R. Meteorol. Soc.*, **117**, 1281–1298. 41
- VESTRENG, V., NTZIACHRISTOS, L., SEMB, A., REIS, S., ISAKSEN, I.S.A. & TARRASON, L. (2009). Evolution of NO_x emissions in Europe with focus on road transport control measures. *Atmos. Chem. Phys.*, **9**, 1503–1520. 1, 119, 122, 125, 127
- VOLZ, A. & KLEY, D. (1988). Evaluation of the Montsouris series of ozone measurements made in the nineteenth century. *Nature*, **332**, 240–242. 1, 29
- VÖMEL, H. & DIAZ, K. (2010). Ozone sonde cell current measurements and implications for observations of near-zero ozone concentrations in the tropical upper troposphere. *Atmos. Meas. Tech.*, (2), **3**, 495–505. 68
- VON SAVIGNY, C., HALEY, C.S., SIORIS, C.E., MCDADE, I.C., LLEWELLYN, E.J., DEGENSTEIN, D., EVANS, W.F.J., GATTINGER, R.L., GRIFFIOEN, E., KYRÖLÄ, E., LLOYD, N.D., MCCONNELL, J.C., MCLINDEN, C.A., MÉGIE, G., MURTAGH, D.P. & SOLHEIM, B. (2003). Stratospheric ozone profiles retrieved from limb scattered sunlight radiance spectra measured by the OSIRIS instrument on the Odin satellite. *Geophys. Res. Lett.*, **30**, 14, 1755–1758. 53, 54
- VOULGARAKIS, A., HADJINICOLAOU, P. & PYLE, J.A. (2011). Increases in global tropospheric ozone following an El Nio event: Examining stratospheric ozone variability as a potential driver. *Atmos. Sci. Lett.*, **12**, 228–232. 114

- VOUNTAS, M., DINTER, T., BRACHER, A., BURROWS, J.P. & SIERK, B. (2007). Spectral studies of ocean water with space-borne sensor SCIAMACHY using Differential Optical Absorption Spectroscopy (DOAS). *Ocean Sci.*, **3**, 429–440. 60
- WAI, K.M., WU, S., KUMAR, A. & LIAO, H. (2014). Seasonal variability and long-term evolution of tropospheric composition in the tropics and Southern Hemisphere. *Atmos. Chem. Phys.*, **14**, 4859–4874. 128, 129
- WALLACE, J. & HOBBS, P. (2006). Atmospheric Science: An Introductory Survey. *Acad. Press Burlington Mass.*, 483. 43
- WANG, X. & MAUZERALL, D.L. (2004). Characterising distributions of surface ozone and its impacts on grain production in China, Japan and South Korea. *Atm. Env.*, **38**, 4383–4402. 2
- WANG, Y. & JACOB, D.J. (1998). Anthropogenic forcing on tropospheric ozone and OH since preindustrial times. *J. Geophys. Res.*, **103**, 31123–31135. 82
- WANG, Y., JACOB, D. & LOGAN, J.A. (1998). Global simulation of tropospheric $O_3 - NO_x$ -hydrocarbon chemistry: 3. Origin of tropospheric ozone and its effects on nonmethane hydrocarbons. *J. Geophys. Res.*, **103(D9)**, 10757–10767. 21
- WARNEKE, C., MCKEEN, S.A., DE GOUW, J.A., GOLDAN, P.D., KUSTER, W.C., HOLLOWAY, J.S., WILLIAMS, E.J., LERNER, B.M., PARRISH, D.D., TRAINER, M., FEHSENFELD, F.C., KATO, S., ATLAS, E.L., BAKER, A. & BLAKE, D.R. (2007). Determination of urban volatile organic compound emission ratios and comparison with an emissions database. *J. Geophys. Res.*, **112**, D10S47. 22
- WARSHAW, G., DESAULNIERS, D. & DEGENSTEIN, D. (1998). Optical design and performance of the Odin UV/visible spectrograph and infrared imager instrument, paper presented at 12th Annual AIAA/USU Conference on Small Satellites. *Am. Inst. of Aeronaut. and Astronaut., Logan, Utah*. 15
- WATERS, J.W. *et al.* (2006). The Earth Observing System Microwave Limb Sounder (EOS MLS) on the Aura satellite. *IEEE Trans. Geosci. Remote Sens.*, **44(5)**, 1075 – 1092. 20
- WAUGH, D.W. & POLVANI, L.M. (2000). Climatology of intrusions into the tropical upper troposphere. *Geophys. Res. Lett.*, **27**, 3857–3860. 85
- WAYNE, R.P. (2000). *Chemistry of Atmospheres*. Oxford University Press. 21, 22

REFERENCES

- WEATHERHEAD, E.C. *et al.* (2000). Detecting the recovery of total column ozone. *J. Geophys. Res.*, **105(D17)**, 22201–22210. 113
- WEBER, M., LAMSAL, L.N., COLDEWEY-EGBERS, M., BRAMSTEDT, K. & BURROWS, J.P. (2005). Pole-to-pole validation of GOME WFDOAS total ozone with groundbased data. *Atmos. Chem. Phys.*, **5**, 1341 – 1355. 55, 58, 74
- WEBER, M., LAMSAL, L.N. & BURROWS, J.P. (2007). Improved SCIAMACHY WFDOAS total ozone retrieval: Steps towards homogenising long-term total ozone datasets from GOME, SCIAMACHY, and GOME2, Proc. "Envisat Symposium 2007", Montreux, Switzerland. *ESA SP-636*. 58
- WEBER, M., DIKTY, S., BURROWS, J.P., GARNY, H., DAMERIS, M., KUBIN, A., ABALICHIN, J. & LANGEMATZ, U. (2011). The Brewer-Dobson circulation and total ozone from seasonal to decadal time scales. *Atmos. Chem. Phys.*, **11**, 11221 – 11235. 104, 105, 134
- WEBER, M., CHEHADE, W., FIOLETOV, V.E., FRITH, S.M., LONG, C.S., STEINBRECHT, W. & WILD, J.D. (2013). Stratospheric Ozone, in State of the Climate in 2012. *Bull. Amer. Meteor. Soc.*, **94**, S36 – S37. 74
- WELLEMAYER, C.G., TAYLOR, S.L., SEFTOR, C.J., MCPETERS, R.D. & BHARTIA, P.K. (1997). A correction for the Total Ozone Mapping Spectrometer profile shape errors at high latitude. *J. Geophys. Res.*, **102**, 9029–9038. 56
- WERNLI, H. & BOURQUI, M. (2002). A Lagrangian 1-year climatology of (deep) cross-tropopause exchange in the extratropical Northern Hemisphere. *J. Geophys. Res.-Atm.*, **107 (D1-D2)**. 32, 38, 46
- WILD, O. (2007). Modelling the global tropospheric ozone budget: exploring the variability in current models. *Atmos. Chem. Phys.*, **7**, 2643–2660. 29
- WIRTH, V. (1995). Diabatic heating in an axisymmetric cut-off cyclone and related stratosphere-troposphere exchange. *Quart. J. Roy. Meteor. Soc.*, **121**, 127–147. 36
- WIRTH, V. (2001). Cyclone-anticyclone asymmetry concerning the height of the thermal and the dynamical tropopause. *J. Atm. Sci.*, **58(1)**, 26–37. 42, 46
- WMO (1957). World Meteorological Organization, Definition of the tropopause. *Tech. rep.*. 43, 44, 66, 67

- WMO (1986). World Meteorological Organization, Atmospheric ozone 1985. *Tech. Rep. WMO Rep.*, **16**, 42, 43, 46
- WMO (1999). World Meteorological Organization, Scientific Assessment of Ozone Depletion: 1998, Global Ozone Research and Monitoring Project - Report No. 44, Geneva. *WMO 44, Geneva, Switzerland*.
- WMO (2003). World Meteorological Organization, Health Aspects of Air Pollution with Particulate Matter, Ozone And Nitrogen Dioxide. *Report EUR/03/5042688*, 7–30. 2
- WMO (2007). World Meteorological Organization, Scientific Assessment of Ozone Depletion: 2006, Global Ozone Research and Monitoring Project, Geneva, Switzerland. *Report No. 50*, 572. 33
- WMO (2010). Scientific assessment of ozone depletion: 2010, Global Ozone Research and Monitoring Project-Report No. 51. *Geneva, Switzerland*. 82
- WOLFRAM, E.A. *et al.* (2008). New differential absorption lidar for stratospheric ozone monitoring in Patagonia, South Argentina. *J. Opt. A: Pure Appl. Opt.*, **10**, 104021. 106
- WORDEN, J., LIU, X., BOWMAN, K., CHANCE, K., BEER, R., ELDERING, A., GUNSON, M. & WORDEN, H. (2007). Improved tropospheric ozone profile retrievals using OMI and TES radiances. *Geophys. Res. Lett.*, **34**(1), L01809. 60
- WOUDC (2007). *WOUDC: User Guide to the WMO/GAW World Ozone Data Centre Version 3.0*. WOUDC. 67, 89
- WU, L., SU, H. & JIANG, J.H. (2011). Regional simulations of deep convection and biomass burning over South America: 1. Model evaluations using multiple satellite data sets. *J. Geophys. Res.*, **116**, D17208. 129
- WU, S., MICKLEY, L.J., KAPLAN, J.O. & JACOB, D.J. (2012). Impacts of changes in land use and land cover on atmospheric chemistry and air quality over the 21st century. *Atmos. Chem. Phys.*, **12**, 1597–1609. 82
- YIENGER, J.J., GALANTER, M., HOLLOWAY, T.A., PHADNIS, M.J., GUTTIKUNDA, S.K., CARMICHAEL, G.R., MOXIM, W.J. & LEVY II, H. (2000). The episodic nature of air pollution transport from Asia to North America. *J. Geophys. Res.*, **105**(D22), 26931–26945. 82
- YOUNG, P.J. *et al.* (2013). Pre-industrial to end 21st century projections of tropospheric ozone from the Atmospheric Chemistry and Climate Model Intercomparison Project (ACCMIP). *Atmos. Chem. Phys.*, **13**, 4, 2063–2090. 21

REFERENCES

- ZAHN, A. & BRENNINKMEIJER, C.A.M. (2003). New directions: a chemical tropopause defined. *Atmos. Environ.*, **37**, 439–440. 42
- ZANGL, G. & HOINKA, K.P. (2001). The tropopause in the polar regions. *J. Clim.*, **14** (14), 3117–3139. 42, 43, 45
- ZAVALA, M., LEI, W., MOLINA, M.J. & MOLINA, L.T. (2009). Modeled and observed ozone sensitivity to mobile-source emissions in Mexico City. *Atmos. Chem. Phys.*, **9**, 39–55. 119, 122
- ZHANG, L., JACOB, D.J., KOPACZ, M., HENZE, D.K., SINGH, K. & JAFFE, D.A. (2009). Intercontinental source attribution of ozone pollution at western U.S. sites using an adjoint method. *Geophys. Res. Lett.*, **36**, L11810. 128
- ZHENG, G. & PYLE, J.A. (2005). Influence of El Niño Southern Oscillation on stratosphere/troposphere exchange and the global ozone budget. *Geophys. Res. Lett.*, **32**, L01814. 113
- ZHOU, T., GELLER, M.A. & LIN, W. (2012). An observational study on the latitudes where wave forcing drives Brewer-Dobson upwelling. *J. Atmos. Sci.*, **69**, 1916–1935. 35
- ZIEMKE, J.R., CHANDRA, S. & BHARTIA, P.K. (1998). Two new methods for deriving tropospheric column ozone from TOMS measurements: The assimilated UARS MLS/HALOE and convective-cloud differential techniques. *J. Geophys. Res.*, **103**(D17), 22115–22128. 3, 59
- ZIEMKE, J.R., CHANDRA, S. & BHARTIA, P.K. (2003). Upper tropospheric ozone derived from the cloud slicing technique: Implications for large-scale convection. *J. Geophys. Res.*, **108**(D13), 4390. 59
- ZIEMKE, J.R., CHANDRA, S. & BHARTIA, P.K. (2005). A 25-year data record of atmospheric ozone in the Pacific from Total Ozone Mapping Spectrometer (TOMS) cloud slicing: Implications for ozone trends in the stratosphere and troposphere. *J. Geophys. Res.*, **110**, D15105. 128
- ZIEMKE, J.R., CHANDRA, S., DUNCAN, B.N., FROIDEVAUX, L., BHARTIA, P.K., LEVELT, P.F. & WATERS, J.W. (2006). Tropospheric ozone determined from Aura OMI and MLS: Evaluation of measurements and comparison with the Global Modeling Initiatives Chemical Transport Model. *J. Geophys. Res.*, **D19303**, 111. 3, 59, 66, 99, 100, 119
- ZIEMKE, J.R., CHANDRA, S., LABOW, G., BHARTIA, P.K., FROIDEVAUX, L. & WITTE, J.C. (2011). A global climatology of tropospheric and stratospheric ozone derived from Aura OMI and MLS measurements. *Atmos. Chem. Phys.*, **103**, 9237–9251. 3, 59, 66

REFERENCES

ZIERL, B. & WIRTH, V. (1997). The role of radiation for stratosphere-troposphere exchange in an upper tropospheric anticyclone. *J. Geophys. Res.*, **102**, 23883-23894. 37, 38